SAND 95-1003
GRI-95/0080
GRI
RECORD COPY
C.1
RETAIN HARDCOPY
MICROFICHE

Annual Report

SANDIA NATIONAL
LABORATORIES
TECHNICAL LIBRARY

Development of Stimulation Diagnostic Technology

Prepared by:
Sandia National Laboratories

Gas Research Institute

Drilling and Completion Group
June 1995

p.162

GRI-95/0080 SAND-95-1003

DEVELOPMENT OF STIMULATION DIAGNOSTIC TECHNOLOGY

ANNUAL REPORT
(January 1994-December 1994)

Prepared by
N. R. Warpinski, J. C. Lorenz,
J. E. Uhl, B. P. Engler, P.M. Drozda
D. J. Holcomb, C.J. Young and R.S. Harding

Sandia National Laboratories
Division 6114
P.O. Box 5800
Albuquerque, New Mexico 87185

For
GAS RESEARCH INSTITUTE
Contract No. 5089-211-2059

GRI Project Manager
Steve Wolhart
Tight Gas Sands Field Evaluation

February 1995

50272-101

REPORT DOCUMENTATION PAGE	1. REPORT NO. GRI-95/0080	2.	3. Recipient's Accession No.
4. Title and Subtitle DEVELOPMENT OF STIMULATION DIAGNOSTIC TECHNOLOGY			5. Report Date 2/24/95 Preparation 6.
7. Author(s) N.R. Warpinski, J.C. Lorenz, J.E. Uhl, B.P. Engler P.M Drozda D.J. Holcomb, C.J. Young and R.S. Harding			8. Performing Organization Rept. No. SAND95-1003
9. Performing Organization Name and Address Sandia National Laboratories Division 6114 P.O. Box 5800 Albuquerque, New Mexico 87185			10. Project/Task/Work Unit No. 11. Contract(C) or Grant(G) No. (C) 5089-211-2059 (G)
12. Sponsoring Organization Name and Address Gas Research Institute 8600 Bryn Mawr Avenue Chicago, Illinois 60631			13. Type of Report & Period Covered 1994 Annual Report, 14.

15. Supplementary Notes

16. Abstract (Limit: 200 words) The approach to stimulation diagnostics is to integrate in situ stress measurements (including microfracs, anelastic strain recovery, circumferential velocity analysis, and coring-induced fractures) with natural fracture characterization, stimulation analyses (including FRACPRO ™, other models, finite-element analyses, and various pressure analyses), and fracture diagnostics in order to validate hydraulic fracture concepts, models and diagnostic capabilities. The M-site "A" sand experiment has provided the time evolution of a hydraulic fracture in a layered sedimentary sequence. These results show an asymmetric fracture that first develops within the sandstone interval, later grows upward in a circular fashion, and finally grows downward in the near wellbore region. Processing codes to automatically perform event detection and location have been developed and are awaiting M-Site testing and optimization. The M-Site monitor well instrumentation has been successfully installed and checked out. Thirty levels of triaxial accelerometers and 6 levels of biaxial tiltmeters are in position for fracture monitoring. Surface noise problems are currently being addressed. Models of hydraulic fracturing show that microseisms develop as a result of two types of stress changes within the reservoir, increased shear stresses around the fracture tip and increased pore pressure due to leakoff. Core-based stress tests made on the M-Site monitor well "C" sand samples showed unexpected behavior, but the results confirm the stress orientation at M-Site. Stress modeling in the Moxa Arch region of the Green River basin is helping to clarify stress relationships and to show the origin of the stress fields that induced natural fractures to form. The modeling results are being included in a topical report on natural fractures within the basin.

17. Document Analysis a. Descriptors
Tight gas sands, in situ stress, stress measurement, natural fractures, Green River basin, hydraulic fracturing, fracture diagnostics

b. Identifiers/Open-Ended Terms
anelastic strain recovery, circumferential velocity anisotropy, coring induced fractures, natural fractures, Green River basin, stimulation, hydraulic-fracture diagnostics, microseisms, seismic analysis.

c. COSATI Field/Group

18. Availability Statement	19. Security Class (This Report)	21. No. of Pages
Release unlimited	unclassified	
	20. Security Class (This Page)	22. Price

GRI DISCLAIMER

LEGAL NOTICE This report was prepared by Sandia National Laboratories as an account of work sponsored by the Gas Research Institute (GRI). Neither GRI, members of GRI, nor any person acting on behalf of either:

a. Makes any warranty or representation, express or implied, with respect to the accuracy, completeness, or usefulness of the information contained in this report, or that the use of any apparatus, method, or process disclosed in this report may not infringe privately owned rights; or

b. Assumes any liability with respect to the use of, or for damages resulting from the use of, any information, apparatus, method, or process disclosed in this report.

Title	Development of Stimulation Diagnostic Technology
Contractor	Sandia National Laboratories GRI Contract Number: 5089-211-2059
Principal Investigator	N. R. Warpinski
Report Period	January 1993-December 1993 Annual Report
Objective	To apply Sandia's expertise and technology towards the development of stimulation diagnostic technology in the areas of in situ stress, natural fracturing, stimulation processes and fracture diagnostics.
Technical Perspective	Large quantities of natural gas exist in low permeability reservoirs throughout the US. Characteristics of these reservoirs, however, make production difficult and often uneconomic. Matrix rock permeabilities are often submicrodarcy, and natural fractures are commonly marginal, being anisotropic and easily damaged. Stimulation is required for these types of reservoirs, with hydraulic fracturing being the primary stimulation option. Understanding stimulation behavior is difficult, however, because of the complex nature of most of these reservoirs. Diagnostics that can map out the fracture length, height, and azimuth are the missing element in hydraulic-fracture analysis. Integrating knowledge of the matrix rock, natural fractures, in situ stresses with stimulation models and diagnostics is required if stimulation effectiveness is to be determined and enhanced.
Results	Activities during 1994 centered on the M-Site experiment, where drilling and instrumenting of the monitor well and analysis of the "A" sand tests were the major focus. Several stress and property tests were run on monitor well core samples in preparation for fracturing tests. Design of the monitor well instrumentation was completed and the instruments were successfully emplaced in October, with all instruments functioning. Fracturing tests were delayed until 1995 to solve surface noise problems that were primarily interfering with the accelerometers, but also the tiltmeters.

Analyses of the "A" sand results were completed in 1994, with the diagnostic data accurate enough to show the time development of the hydraulic fracture. The "A" sand results provided the information needed to optimize design of the M-Site monitor well instrumentation, to begin the development of the software needed to semi-automatically process the monitor well data, and to develop the software needed to process multi-level wireline data.

Modeling of both the seismic data and the mechanical behavior of the reservoir continued during 1994. A seismic processing code to locate events in a complex velocity field was modified for diagnostic use. This code is proving valuable for optimizing the automatic location schemes. Codes to calculate the mechanical response of the reservoir due to a hydraulic fracture have been developed for tiltmeter analysis and for correlation of the mechanical rock behavior with the seismic rock behavior.

Several processing codes are being developed to analyze the M-Site and other data. One code (SEER) has been written to automatically process the accelerometer data from the monitor well. This code has been specially written to interact with the Data Acquisition System used for the monitor well. A second code (READ5) has been written to automatically process 5-level data from widely spaced, multi-level, advanced receivers run in a borehole on a fiber-optic wireline. A third code has been written to process two-level data from advanced receivers run on a 7-conductor wireline.

Technical Approach

The approach to stimulation diagnostics is to integrate in situ stress measurements (including microfracs, anelastic strain recovery, circumferential velocity analysis, and coring-induced fractures) with natural fracture characterization, stimulation analyses (including FRACPRO™ other models, finite-element analyses, and various pressure analyses), and fracture diagnostics in order to validate hydraulic fracture concepts, models and diagnostic capabilities. From now until the end of the project, the emphasis will be on developing a diagnostics system to map out hydraulic-fracture length and other parameters. The ultimate goal is to develop real-time, industry-run, fracture-diagnostics capabilities.

Project Implications

Hydraulic fracturing is a complex process and is difficult to optimize. This project combines reservoir characterization, fracture diagnostics and stimulation analyses to better understand hydraulic fracturing. The missing element, as noted above, is the ability to accurately measure fracture dimensions including length in a practical manner. Measuring fracture dimensions is a key part to analyzing and optimizing stimulation treatments as well as making field development and well spacing decisions. Significant

progress was made toward developing this capability in the past year and this will continue to be the major emphasis of this project. Other key results from this project include the characterization of natural fractures in the Green River Basin, a comparison of fracture models using SFE No. 3 data and a catalog of core-based stress measurement techniques. These results, combined with fracture diagnostics and other stimulation analyses, will help to optimize the process of hydraulic fracturing.

Steve Wolhart
Sr. Technology Manager, Drilling & Completion

TABLE OF CONTENTS

1.0	RESEARCH OBJECTIVES	1
2.0	SUMMARY OF ALL PREVIOUS WORK PERFORMED	3
3.0	SPECIFIC OBJECTIVES OF THE CURRENT YEAR	4
4.0	WORK PLANS FOR THE CURRENT YEAR	5
5.0	IN SITU STRESS	6
6.0	NATURAL FRACTURES	11
7.0	STIMULATION	13
8.0	M-SITE EXPERIMENT	14
9.0	AUTOMATED PROCESSING	30
10.0	MODELING AND INTERPRETATION	32
11.0	OTHER DIAGNOSTIC TASKS	40
12.0	REFERENCES	41
13.0	MAJOR ACHIEVEMENTS	42
14.0	MAJOR PROBLEMS	43
15.0	CONCLUSIONS	44
16.0	OBJECTIVES AND WORK PLANNED FOR NEXT YEAR	45

Tables

Table 1 Rock properties of monitor well core, C sand
Table 2 Sequence of operations
Table 3 Orientation scan azimuths
Table 4. Filter parameters
Table 5 Velocity structure data
Table 6 Reduced velocity structure
Table 7 Accelerometer groupings
Table 8. Parameters for tip shear calculations
Table 9. Additional parameters for leakoff calculations

Figures

Figure 1 ASR data from 4316 ft
Figure 2 ASR data from 4317 ft
Figure 3 ASR data from 4312 ft
Figure 4 P-wave velocity data from sample #1 at 4314 ft
Figure 5 Least-squares fit of sample #1 data
Figure 6 P-wave velocity data from sample #2 at 4314 ft
Figure 7 Least-squares fit of sample #2 data
Figure 8 S-wave velocity data from both samples at 4314 ft
Figure 9 AE onset for uniaxial tests
Figure 10 Polar plot of uniaxial data
Figure 11 AE onset for extensional tests
Figure 12 Polar plot extensional data
Figure 13 Polar plot compressional wave velocities
Figure 14 Well layout at M-Site
Figure 15 Configuration for velocity survey
Figure 16 MWX-2 velocity data
Figure 17 MWX-3 velocity data
Figure 18 P-wave tomogram
Figure 19 Receiver positions in MWX-2
Figure 20 Orientation scan data for vertical axis
Figure 21 Orientation scan data for horizontal-1 axis
Figure 22 Orientation scan data for horizontal-2 axis
Figure 23 Mounting geometry
Figure 24 Example orientation data for level 1, shot at 4930 ft
Figure 25 Example orientation data for level 2, shot at 4930 ft
Figure 26 Example orientation data for level 3, shot at 4930 ft
Figure 27 Example orientation data for level 4, shot at 4930 ft
Figure 28 Orientation results
Figure 29 Orientation of individual axes
Figure 30 Inclination of each level
Figure 31 Histogram of events
Figure 32 Example event (first event)
Figure 33 Traces and hodograms of first event, level 1

Figure 34 Traces and hodograms of first event, level 2
Figure 35 Traces and hodograms of first event, level 3
Figure 36 Traces and hodograms of first event, level 4
Figure 37 Filtered traces and hodograms of first event, level 2
Figure 38 Filtered traces and hodograms of first event, level 3
Figure 39 Second event
Figure 40 Second event, filtered traces
Figure 41 Traces and hodograms of second event, level 1, unfiltered
Figure 42 Traces and hodograms of second event, level 2, unfiltered
Figure 43 Traces and hodograms of second event, level 3, unfiltered
Figure 44 Traces and hodograms of second event, level 4, unfiltered
Figure 45 Traces and hodograms of second event, level 1, filtered
Figure 46 Traces and hodograms of second event, level 2, filtered
Figure 47 Traces and hodograms of second event, level 3, filtered
Figure 48 Traces and hodograms of second event, level 4, filtered
Figure 49 Map of microseisms using average of all four levels
Figure 50. Uncertainty map of microseisms using average of all four levels
Figure 51. Map of microseisms using average of all three levels
Figure 52. Uncertainty map of microseisms using average of all three levels
Figure 53. Map of microseisms using p-s separation only
Figure 54. Map of microseisms using P-wave move out for elevation
Figure 55. Map of microseisms using all levels independently
Figure 56. Map of microseisms using inclination from specified levels
Figure 57. Uncertainty map of microseisms using inclination from specified levels
Figure 58. Map of microseisms using inclination from specified levels, time #1
Figure 59. Map of microseisms using inclination from specified levels, time #2
Figure 60. Map of microseisms using inclination from specified levels, time #3
Figure 61. Map of microseisms using inclination from specified levels, time #4
Figure 62. Map of microseisms using inclination from specified levels, time #5
Figure 63. Map of microseisms using inclination from specified levels, time #6
Figure 64. Refraction tracing plot, event #1
Figure 65. Refraction tracing plot, event #2
Figure 66. Refraction tracing plot, event #3
Figure 67. Refraction tracing plot, event #4
Figure 68. Refraction microseism map
Figure 69. Refraction uncertainty microseism map
Figure 70. Histogram of events for minifrac #2
Figure 71. Example low frequency event from minifrac #2
Figure 72. Trace and hodograms of example event from minifrac #2, level 1
Figure 73. Trace and hodograms of example event from minifrac #2, level 2
Figure 74. Trace and hodograms of example event from minifrac #2, level 3
Figure 75. Trace and hodograms of example event from minifrac #2, level 4
Figure 76. Map of microseisms using average of all four levels, minifrac #2
Figure 77. Map of microseisms using average of three levels, minifrac #2
Figure 78. Map of microseisms using average of three levels, minifrac #2
Figure 79. Uncertainty map of microseisms using average of three levels, minifrac #2
Figure 80. Refraction microseism map, minifrac #2
Figure 81. Refraction uncertainty microseism map, minifrac #2
Figure 82. Histogram of events, minifrac #3

Figure 83. Histogram of events, minifrac #4
Figure 84. H/Z results for minifrac #3
Figure 85. Spectral ratio contour results for minifrac #3
Figure 86. Cable frequency response test
Figure 87. Cable noise characteristics
Figure 88. Noise survey of MWX-3
Figure 89. Parameters for Sneddon stress analysis
Figure 90. Zone of shear slippage around crack tip
Figure 91. Leakoff induced failure function orthogonal to crack face
Figure 92 Wavefront contours for source 900 ft from M-Site receivers
Figure 93. Mislocation vectors for 441 grid points
Figure 94. Effect of noise on location solutions for (a) P-wave only and (b) p and S-wave
Figure 95. Effect of noise on location solutions for wider receiver spacing
Figure 96 Calculated and actual locations for five calibration shots

1.0 RESEARCH OBJECTIVES

The objective of this project is for Sandia National Laboratories to apply its expertise and technology towards the development of stimulation diagnostic technology. Stimulation diagnostic technology, as defined here, contains different areas such as (1) in situ stresses, (2) natural fracture characterization, (3) stimulation modeling, (4) hydraulic-fracture diagnostics, and (5) the design and conduct of field experiments. Integration of these areas can yield a more complete analysis of hydraulic fracture behavior and effectiveness in the reservoir. Beginning in the last quarter of this year, additional efforts were initiated to develop microseismic fracture diagnostics into a reliable, accurate, near-real time service.

In situ stresses, both the direction and the magnitudes, are of vital importance to the production of gas from low permeability reservoirs. Stress data are required for advanced design and analysis of fracture treatments, for completion information, and for understanding of the production mechanisms in tight reservoirs. The specific objective of the in situ stress task is to integrate core, log, and injection stress data into a complete picture of the stress in the reservoir, and to develop a "catalog" of techniques, each with a set of validated procedures, which can be brought to bear on the problem of stress determination.

Many of the tight reservoirs in the US, particularly in western basins, produce primarily from marginal natural fracture systems. Understanding the natural fracture system and the effects of stress, pore pressure, water saturation, etc. are important for any rational decisions on completion and stimulation of wells in these reservoirs. The specific objectives of the natural fracture task are to obtain description and distributions of the fracture systems from core, logs and outcrops, determine the importance of the fracture systems, and integrate these data for use in completion/stimulation design and production operations.

Effective hydraulic fracture stimulation requires a comprehensive design model that can adequately predict fracture behavior and reservoir performance. GRI has such a model (FRACPRO™) that can be used for design, analysis, and real-time control. Confident use of such models requires validation in realistic physical situations, a difficult task since the created fractures are not very accessible. The specific objectives of the stimulation modeling task are to perform analyses of injections using pressure analyses, finite element models, simple fracture models, and other resources in order to obtain a comparison with FRACPRO™ and to aid in its validation.

Information on fracture behavior is currently available only through the use of indirect fracture diagnostic techniques, but these techniques are far from being routine field procedures, nor do they have the universal confidence of industry. The advancement of microseismic (and other seismic) monitoring requires rigorous standards for receivers, recorders, and processing algorithms. Completion of this task requires the application of advanced multi-station receivers that can faithfully record the particle motion induced by the specific events, the use of telemetry and recorders with sufficient dynamic range and band width to transmit and store the data, and the development of analysis techniques that can be applied in real-time or near-real-time modes.

Field experiments are an integral part of GRI's Stimulation & Completion Project and the means by which models, diagnostics, and other procedures can be tested, refined, and verified. Sandia has a lead role in the diagnostic phases of the M-Site tests that are being conducted in the Piceance basin near Rifle, CO. This work includes the design of the instrumentation string of accelerometers and tiltmeters for a newly drilled monitor well and the application of wireline microseismic instrumentation for existing wells. These field experiments will provide the baseline information for developing the hardware and processing algorithms for fracture diagnostic analysis.

In addition to the M-Site activities, Sandia will be jointly conducting other field experiments with interested companies in other locations. These tests will allow for data to be obtained in other formations with different properties, stresses, depths, etc., and they will also serve as test sites for technology developed under this project.

2.0 SUMMARY OF ALL PREVIOUS WORK PERFORMED

2.1 In Situ Stress

Previous work on in situ stresses includes ASR analyses of SFE-4, Canyon Sands, and UPRC Frontier core, and Circumferential Velocity analyses of the same core plus Maxus Cleveland formation and Berea core. These results were important source material for the core-based stress-measurement reports completed last year (GRI-93/0270) and the follow-up stress-azimuth report (GRI-93/0429) and stress-azimuth SPE paper (SPE 27985).

2.2 Natural Fractures

Previous natural fracture studies include Green River basin fieldwork which identified two primary fracture sets and efforts to reconstruct the tectonic development of the basin which led to the development of the fractures. Studies of natural fractures in core were used to develop a theory of the role of diagenesis in fracture development. This theory has proved useful in explaining Frontier fracture systems.

2.3 Stimulation

Previous stimulation activities include most importantly the analysis and documentation of the Fracture Propagation Modeling Forum results. These data were included in an SPE paper (SPE 25890) and GRI report (GRI-93/0109) summarizing the results. Other modeling activities have been conducted to assess site suitability.

2.4 Diagnostics

A considerable effort in fracture diagnostics was conducted in 1992 at the M-Site during the site suitability testing and in 1993 at the M-Site during the "A" sand experiments. These experiments form the basis for all of the M-Site design work and the development of processing codes for fracture diagnostics.

The suitability testing was performed in order to assess whether the M-Site near Rifle was acceptable for fracture diagnostic research. Results from that test were highly positive, indicating that microseisms were generated in large numbers, they were highly analyzable, and they could be used to map fracture progress.

After funding was approved for the M-Site and diagnostic projects, the "A"-sand Multi-Level and Treatment-Well Diagnostic Tests was conducted in October-November of 1993. These tests included a detailed velocity survey and four fracturing experiments monitored with a five-level receiver system in an offset well and a single receiver (or other instrumentation) in the treatment well. Only preliminary analysis of these data was performed in 1993.

3.0 SPECIFIC OBJECTIVES OF THE CURRENT YEAR

Specific objectives of the current year are:

Provide an analysis of the natural fracture distribution in the Green River basin through the study of outcrops, core and logs.

Obtain stress information on the M-Site monitor well by making core-based stress measurements on selected sandstone core from zones to be fractured.

Develop final location maps of the M-Site "A" sand hydraulic fractures and correlate the microseismic results with any other diagnostic and modeling data.

Install monitor well instrumentation at M-Site, including both accelerometers and tiltmeters.

Develop software codes for the automatic processing of microseismic data.

Perform any feasible task to promote the development of a fracture-diagnostics service industry.

4.0 WORK PLANS FOR THE CURRENT YEAR

Work plans for the current year include:

Completion of the Greater Green River basin natural fracture study and the completion of reports documenting those results.

Measurements of stress and mechanical properties on M-Site core retrieved from the monitor well.

Completion of the analysis of the "A" sand fracture experiments including a map of the fracture and the time dependent behavior.

Design of the instrumentation systems for the M-Site monitor well, including accelerometers and tiltmeters.

Emplacement of the instrumentation in the monitor well and check-out of their behavior.

Development of software codes for automatic processing of the monitor well seismic data.

Development of software codes for automatic processing of wireline-run seismic receivers, including a five-level system run on a fiber-optic wireline and a two-level system run on seven conductor wireline.

Development of algorithms and codes for calculating the mechanical response of the reservoir due to hydraulic fracturing for comparison with the seismic behavior.

Development of codes for analyzing the tiltmeter response at M-Site.

Modification of existing seismic codes for use in microseismic location schemes in complex velocity fields typical of gas reservoirs.

Continued involvement in any joint diagnostic tests with industrial partners.

5.0 IN SITU STRESS

Knowledge of the directions and magnitudes of in situ stress are of vital importance to the production of gas from low permeability reservoirs. Stress data are used in the design and analysis of hydraulic fracture stimulations and are necessary for the understanding of parameters affecting production. However, in situ stresses are difficult to measure, and there is no commonly accepted practice for determining the stresses. As a result, there is often a lack of confidence in stress data from any one technique. In light of this reality, it is common sense to develop as many ways as possible to determine stress parameters.

Sandia has previously worked on integrating information from anelastic strain recovery (ASR), differential strain curve analysis (DSCA), circumferential velocity anisotropy (CVA), coring-induced fractures, log-derived wellbore effects, overcoring of archived core and microfrac stress measurements in order to obtain an integrated program to provide the best possible stress measurement. These activities led to the preparation of two reports, Core Based Stress Measurements: A Guide to Their Application[1] (GRI-93/0270) and Techniques for Determining Subsurface Stress Direction and Assessing Hydraulic Fracture Azimuth[2] (GRI-93/0429). As a result of these capabilities, Sandia conducted several core-based measurements on samples from the M-Site monitor well.

5.1 Monitor well stress measurements

5.1.1 Objectives

In order to determine the stress field in the B and C sands, several core-based stress measurements were attempted. The objectives of these measurements were to confirm the orientation of the stress field at this depth and to determine the magnitude of the maximum principal horizontal stress. The magnitude of the minimum principal horizontal stress would be determined later using various hydraulic fracturing techniques.

5.1.2 Experimental Program

Core from the 4314 foot level at the Multiwell site was used to measure anelastic strain recovery, acoustic emissions during relaxation, velocity anisotropy, and acoustic emission onset (Kaiser effect) anisotropy for comparison with the in situ stress orientation. A conventional triaxial test series was also carried out to determine the failure surface parameters.

Anelastic strain recovery (ASR) measurements were performed on three core samples between 4316 and 4321 ft. At the same time, measurements of the acoustic emissions occurring during relaxation were made on a companion sample at 4318 ft.

Velocity measurements were made on two, unpressurized samples, in both the horizontal plane and vertically. Velocities were measured using compressional (V_P), horizontally polarized shear (V_{SH}) and vertically polarized shear (V_{SV}) waves.

A total of 6 conventional triaxial tests $\sigma_{11} > \sigma_{22} = \sigma_{33} = P_c$, 8 extension tests, $\sigma_{11} = \sigma_{22} > \sigma_{33}$, and 8 uniaxial tests were completed, using one inch diameter subcores taken at various orientations to the master core. To study the anisotropy, subcores were cut with axes in the horizontal plane at 25 degree intervals and also with vertical axes.

Triaxial test specimens were instrumented to measure axial (ε_{11}) and radial strains (ε_{22}). All tests were instrumented to detect and count acoustic emission events.

5.1.3 Anelastic Strain Recovery

Anelastic strain measurements were performed at 4316, 4317 and 4321 ft in the B sand. In all three cases, the core was retrieved in good condition with clear scribe lines, good orientation data, and little observable damage to the core. The three samples were selected near the bottom of the core run to minimize the time between cutting and initial instrumentation. As seen in Figures 1-3, only a small amount of strain recovery was measured on each of the tests, a surprising result since much larger recoveries had been observed in the nearby MWX wells when they were cored and tested about 10-12 years earlier. The core was in very good shape so it was not likely that shock effects had already induced complete relaxation. Furthermore, an acoustic emission test was conducted on a sample taken from 4318 ft, and no acoustic emissions were observed during the expected recovery period. Since all crack formation is expected to induce acoustic emissions, it was clear that no relaxation recovery was occurring and the measured strains were most likely thermal, chemical, or pore pressure effects.

To check results, the orientations of the measured strain for each sample were determined. Measured stress orientations were 61°, 120° and 94°, with an average of 92°, but the any apparent agreement between this stress azimuth and that measured during the MWX project (~100-110°) is probably more a matter of coincidence than of accuracy or reliability of these particular ASR results. Previous experience has shown that strain recoveries of less than 30 microstrains will not yield reliable stress azimuth data. Because of the lack of any relaxation recovery (small strain values and particularly because there were no acoustic emissions), no further ASR tests were attempted.

5.1.4 Velocity Anisotropy Measurement

Two measurements of the circumferential velocity anisotropy were made on core samples at a depth of 4314 ft. In both cases, velocity pulses were excited with V_{SV} and V_{SH} transducers, the corresponding P-waves and S-waves were detected, and the appropriate velocities were determined from the time delay.

Figure 4 shows the P-wave velocity of sample #1 using the two different sources, and there is fairly good agreement between the two cases. The P-wave velocity from the V_{SV} source was then fit with the theoretical velocity distribution, as shown in Figure 5. From this fit, the minimum velocity orientation can be quickly deduced, giving an azimuth of N115°E for this sample. This azimuth is the maximum stress direction or the hydraulic fracture azimuth.

Similar data from sample #2 are shown in Figures 6 and 7. For this sample, the maximum velocity azimuth is N106°E. Thus, the general stress orientation appears to be ESE-WNW, in agreement with previous data from this site.

The S-wave velocities, shown in Figure 8, exhibit little anisotropy. Very little work has been performed on the effect of relaxation microcracks on S-waves, but from these results, such data do not appear to be useful for obtaining the stress orientation.

5.1.6 Results Of Triaxial Tests

All triaxial tests were done using subcores cut vertically. Axial strains exhibited significant non-linearity at stresses up to about 15,000 psi, consistent with compaction and crack closure. As a consequence, Young's modulus (E) and Poisson's ratio (v) could not be considered constant. Assuming that the maximum value of Young's modulus corresponds to the actual modulus of the matrix, with most cracks closed, we found E increased from about 5,000,000 psi at confining pressures below 2000 psi to 6,400,000 psi at 10,000 psi, the highest confining pressure used. Poisson's ratio, measured at the same stress as E, showed no clear trend with pressure, varying in the range 0.22 plus or minus 0.05. Results are given in the Table 1 below.

Table 1 Rock properties of monitor well core, C sand

Confining Pressure (psi)	Axial Stress (psi)	Young's Modulus (psi)	Poisson's Ratio
0	22,000	---	---
500	28,500	5,400,000	---
480	29,600	5,400,000	0.22
1,000	30,900	4,700,000	0.28
2,000	36,300	5,100,000	0.23
4,000	49,700	5,900,000	0.22
10,000	74,800	6,400,000	0.16

The sandstone exhibited considerable ductility at all but the lowest confining pressures. Failure parameters were determined by a least squares fit to the maximum stresses observed. The failure surface was essentially linear and well-described by

$$\sigma_{11} = 27{,}000 \text{ psi} + 708\ P_c. \quad (1)$$

The Coulomb failure surface parameters were then calculated to be

$$\tau = 6{,}090 \text{ psi} + 128\sigma \quad (2)$$

5.1.7 Results Of Uniaxial Tests

Uniaxial tests were done to determine the stress required to produce acoustic emissions (AE), the high-frequency bursts of sound emitted by grain scale failures. A popular, although controversial, method for determining in situ stress assumes that the stress required to initiate grain scale failures (AE) in a uniaxially loaded core is the same as the in situ stress along the loading axis. Thus the in situ stress orientation and magnitude could be determined by a series of uniaxial tests on subcores cut at a distribution of angles.

Results for the uniaxial tests are plotted in Figure 9, showing the stress at which the AE rate began to increase as a function of the angle of the subcore axis relative to North. Using the standard interpretation of the Kaiser effect method of determining in situ stress from uniaxial tests, the results imply a maximum horizontal stress of about 46 MPa (6200 psi) at 30 degrees, a minimum horizontal stress of 31 MPa (4500 psi) at 120 degrees and a vertical stress of 56 Mpa (8100 psi), all of which are much too large.

Figure 10 replots the data on a polar plot to emphasize the orientation of the anisotropy. In Figure 10, the minimum onset stress has been subtracted from the stresses in Figure 9. This results in the characteristic figure eight shape of a cos 2θ angular dependence with a phase angle of about 30 degrees.

5.1.8 Results Of Extension Tests

An alternate theory for determining in situ stress from acoustic emissions is based on the use of extensional testing. The underlying idea is that uniaxial testing to determine in situ stresses is flawed because of the rotational invariance of the stress, resulting in the possibility of growth of cracks of many different orientations. Thus the onset of AE, produced by crack growth, is not uniquely linked to the orientation of the uniaxial stress.

Extension tests define a unique plane, i.e., that plane containing the two equal maximum compressive stresses. Thus a series of extension tests on variously oriented subcores to detect the onset of AE is in principle expected to define the orientation of the in situ stress state.

A series of tests, identical to the uniaxial test series, was carried out under extensional test conditions and the stress at which the AE rate began to increase was determined. Figures 11 and 12 show the results in the same manner as Figures 9 and 10 represent the results of the uniaxial tests. As Figure 12 shows, the onset stress was anisotropic, with the axis of maximum onset stress at about 30 degrees. As discussed by Holcomb,[3] this implies that the minimum in situ horizontal stress was at 30 degrees and the maximum in situ horizontal stress was at 120 degrees. The magnitudes of the in situ stresses require additional measurements to determine the pressure dependence of the Kaiser effect for extensional loading. For a complete discussion of the Kaiser effect under various load paths and the implications for its use in determining in situ stress, see Holcomb.[3,4]

5.1.9 Discussion Of In Situ Stress And Core-Based Measurements

Five techniques were applied to the core in an effort to determine the orientation and magnitude of the in situ stress: anelastic strain recovery, monitoring of acoustic emissions during core relaxation, velocity anisotropy measurements, uniaxial Kaiser effect and extensional Kaiser effect. Anelastic strain recovery and the associated acoustic emissions did not give any results. Of the remaining three tests, the most established of these methods is the determination of the orientation of the velocity anisotropy. Assuming that the anisotropy is due to relaxation cracks, then the crack orientation would be anisotropic. Normals to the crack planes would be predominantly parallel to the maximum in situ compressive stress, with correspondingly fewer cracks with normals in the directions of the smaller in situ stresses.

Elastic wave velocities are decreased by cracks that are oriented such that the particle motion induced by the wave tends to open and close the cracks. In the case of compressional waves, where particle motion is parallel to propagation direction, it would be predicted that the wave velocity would be lowest in the direction parallel to the largest number of crack normals. For relaxation cracks, this is the direction of the maximum compressive stress. Figure 13 shows the results for V_P, discussed earlier, plotted on a polar plot with the minimum velocity subtracted off. The axis of maximum velocity is at about 30 degrees, implying a minimum at 120 degrees. Thus the velocity measurements predict the maximum horizontal in situ stress direction to be at 120 degrees. Although not shown, V_P in the vertical direction was about 10 per cent lower than the lowest velocity in the horizontal plane. This implies that the vertical stress is the overall maximum compressive stress.

Comparing Figures 10, 12 and 13, we see that the Kaiser effect and the velocity anisotropy all indicate the anisotropy axis is about 30 degrees. However the usual interpretation of the uniaxial Kaiser effect indicates that the direction of maximum stress required to produce AE is the direction of maximum in situ stress, a prediction that is 90 degrees out of phase with the prediction of the velocity measurements and the extensional Kaiser effect, as well as other known stress information from this site.

The results indicate that the extensional Kaiser effect method produces orientations that are in agreement with those predicted from the velocity anisotropy, although with considerably more effort in testing. However, in theory, the Kaiser effect method yields information on the stress magnitudes which the velocity method can not. In this case, however, the magnitudes from the uniaxial test are clearly wrong.

6.0 NATURAL FRACTURES

Many of the tight sandstones, particularly those in western US basins, have matrix permeabilities of a few microdarcies or less. Economic production from such reservoirs is impossible unless natural fractures or other mechanisms provide additional permeability. Well testing of many of these microdarcy or submicrodarcy reservoirs often yields effective permeabilities of tens or hundreds of microdarcies, substantiating the hypothesis that most of these reservoirs are fractured. Outcrop, log and core studies have also shown the presence of natural fractures. Knowledge of the characteristics and importance of the natural fractures is important because it may affect the stimulation or other completion plan.

6.1 General Activities

John Lorenz has been consulting with and aiding Amoco Production Co. efforts in its horizontal well program in the eastern part of the Green River basin. Another 30-degree deviated pilot hole was drilled and cored through part of the lower Almond Formation in order to assess the presence, character, and orientation of natural fractures at the same location where a vertical well, drilled in about 1980, has produced little gas. Core and FMI logs indicate an east-west to east-northeast-by-west-southwest fracture trend. This is similar to the fractures found in a previous well drilled at the end of last year, which is currently producing gas at an economic rate. The new hole will therefore also be kicked off and drilled horizontally into the Almond Formation.

In order to assess the current state of knowledge of the in situ stress orientations in the Green River basin, 73 Four-Arm Caliper, Fracture Identification, and Dipmeter logs were purchased from Riley's Electric Log, Inc. and analyzed for stress-induced breakouts. Of these logs, only six contain information on the stress state (some were unoriented, some did not display breakouts, some logs had malfunctioned, etc.) However, those logs that do contain information suggest that:

1. stress orientation varies across the basin
2. stress orientation may also vary vertically in certain locations as a function of lithology and/or of tectonically-controlled stress domain

Hugo Harstad (student at NM Tech) is analyzing the fracture patterns that were derived from outcrops for use in reservoir simulators. Enlargements of photos of the best outcrops are being corrected for perspective distortion, and the fractures are being divided into sets for differential treatment in the models.

John Lorenz has been helping Amoco Production Co. assess fractures in core from a deviated well drilled into the Frontier and Dakota Formations on the Moxa Arch. The core contains several natural fractures, and will be invaluable for obtaining unambiguous data on subsurface fracture orientations in the southern part of the arch.

John Lorenz gave a presentation at the GRI-sponsored Green River basin workshop in Denver on Nov. 7th. The presentation covered current efforts to characterize and model the natural fractures and stresses in the deeper parts of the basin, focusing on the Frontier Formation.

Liaison with companies having Green River Basin holdings consisted of 1) visiting the Amoco core library and helping to assess recent Frontier core from the Moxa Arch area as well as core from a Niobrara play, and 2) assisting Union Pacific geologists in assessing deep Frontier core slabs for fractures at the USGS Denver core library. Union Pacific has plans for a deep Frontier project in the western part of the basin.

6.2 Modeling

A two-dimensional, plane-strain, finite-element geomechanical model of the Green River basin has been developed to calculate in situ stresses along a cross-section through the basin. This model is being used to investigate stress and fracture development in the Frontier formation.

A north-south stratigraphic section across the basin, in conjunction with indenter boundary conditions at the edge of the basin, has been modeled to simulate the effects of the thick-skinned thrust of the Uinta and Wind River mountains. The geomechanical model includes (1) an idealization of the geometry, (2) initial and boundary conditions, (3) constitutive models of the behavior of the various rock layers and (4) the discretization of the problem into a finite-element formulation to permit a computational solution.

Although there were no attempts to calibrate the stress magnitudes (the magnitudes of the calculated stresses are not correct, but the ratios and distributions are appropriate), the modeling shows that several of the deeper sedimentary layers must have carried considerably higher stresses than the shallower formations, and the intensity of the stresses increases as the indenters are approached. However, there is also a general trend of increasing stress from north to south across the basin. These results will be incorporated into a topical report on stress and natural fracture development in the Green River basin. This report was in progress at the end of 1994.

7.0 STIMULATION

Some form of stimulation, usually hydraulic fracturing, is required for the economic production of gas from tight reservoirs. A long-sought objective has been comprehensive hydraulic-fracture models that could be used for the design, analysis, and, ultimately, real-time control of the fracturing process. In order to help validate such comprehensive models, Sandia is tasked to (1) analyze appropriate field stimulation and minifrac data in order to obtain an independent assessment of fracture performance, and (2) conduct any advanced activities (e.g., finite element analyses, model comparisons, etc.) which provide independent confirmation of model validity.

Little activity was performed on the stimulation task, as this task awaits the results of the M-Site diagnostic data. When accurate diagnostic data are obtained, the results will be compared with fracture models.

8.0 M-SITE EXPERIMENT

Three of the primary goals of GRI's Stimulation and Completion program are (1) validation of hydraulic-fracture design models, (2) development of hydraulic-fracture length diagnostics, and (3) validation of all fracture-diagnostic technology. Validation implies a confirmation of the predicted results by actual measurement in the field, and thus requires an instrumented facility where fracture behavior can be measured. The effort to develop such a capability is named the M-Site Experiments. Sandia has been involved (along with CER Corp. and RES) in the development and testing at M-Site.

The M-Site location is in the Piceance basin near the town of Rifle, CO, in Mesaverde sandstones at depths from 4000-5000 ft. Two wells, designated MWX-2 and MWX-3, are currently available for testing and fracturing and are shown in Figure 14. During the fall of 1992, a site suitability test was conducted, from which highly positive results were obtained. During 1993, the first of several experiments was conducted in the A sand, and planning for a new monitor well was initiated.

8.1 M-Site "A" Sand Multi-Level and Treatment Well Diagnostic Test

The Multi-Level and Treatment Well Diagnostic Test was a two-week long set of experiments conducted in October-November, 1993 in the "A" sand at M-Site. Although preliminary analyses were conducted in 1993, the bulk of the analysis of these tests were performed throughout 1994

8.1.1 Objectives

1. Monitor fracture geometry from an offset well using the greater accuracy derived from a multi-station receiver.
2. Compare a multi-station monitoring experiment with a single station experiment (i.e., the suitability test).
3. Compare the multi-station results with the treatment-well receiver data.
4. Use the diagnostic information on length and height to begin validating models.
5. Compare height from H/Z logging (Teledyne's technique) to that derived from microseisms (first time validation for this technique).
6. Compare the noise-polarization azimuth (Teledyne's technique) to the azimuth obtained from offset-well microseismic data (first time validation for this technique).
7. Test the data-acquisition systems for bugs and problems.
8. Determine instrument spacing requirements.
9. Obtain a full tomographic survey of the site for velocity structure.
10. Determine the effect of velocity structure on microseismic analysis errors.

8.1.2 Experiment Operations

The A Sand Experiments were conducted during the last week in October and the first week of November, 1993. The A Sand Experiments were a two-well test using MWX-2 and MWX-3. As listed in Table 2, a velocity survey was conducted on October 26-28, 1993 using a multi-level receiver system (5 levels, 10 ft spacing) fielded by Bolt Technology Corporation in MWX-2 and a down-hole Bolt airgun as the source in MWX-3. Subsequently, the receiver system was modified for microseismic use, positioned within MWX-2, and oriented using the Bolt airgun (again, in MWX-3).

Table 2 Sequence of Operations

OPERATION	MWX-2	MWX-3	COMMENTS
Velocity Survey	5-level receivers	Bolt airgun source	10 ft spacing
Orientation	4-level receiver	Bolt airgun source	10 ft spacing
Minifrac #1	Observation well 4-level receiver	Treatment well Bottom-hole pressure	Reference minifrac
Minifrac #2	Observation well 4-level receiver	Treatment well Single receiver + gyro	Oriented H/Z
Minifrac #3	Observation well 4-level receiver	Treatment well Single receiver	Unoriented H/Z
Sand Frac	Observation well 4-level receiver	Treatment well Spectral gamma	Tracer test

During the following week, four hydraulic fracture experiments were conducted with different types of instrumentation in the treatment well (MWX-3), and with a four-level receiver system in the observation well (MWX-2). The first minifrac had a bottom-hole pressure tool in the treatment well for accurate pressure measurements that were needed for model calculations. This minifrac is considered the reference minifrac as it was performed first (least perturbation to the rock or reservoir) and could be accurately compared with model predictions because of the high-quality bottom-hole pressure data. The two subsequent minifracs had single receivers in the treatment well for H/Z analyses as well as microseism analyses. In minifrac #2, the receiver was oriented with a Gyrodata orienting tool. In minifrac #3, no orientation was used because of the negative effect of the orienting tool on receiver resonances. The final test, a sand frac, had a spectral gamma tool in the treatment well for tracer studies.

8.1.3 Equipment

The major seismic equipment used during these experiments consisted of a Bolt multi-level receiver system, a single analog receiver system, a Bolt airgun, and a Gyrodata orienting tool. The multi-level receiver system consists of up to five levels of triaxaial accelerometers designed by Sandia National Labs, manufactured by OYO Geospace Instruments, Inc, and fielded by Bolt Technology Corporation. The receivers[5] were designed using modal analysis to be resonant free up to 2000 Hz by using a new type clamp mechanism. The solid-state accelerometers provide accurate particle motion detection, without spurious modes, phase errors, or high frequency noise limitations, nearly up to the resonant frequency of the accelerometers (typically up to 1800 Hz). The receivers are designed to send electrical signals up to a formatter (situated 10 ft above the receiver array) which digitizes the data, converts the electrical signal to an optical one, and sends the data uphole on a fiber-optic wireline. The fiber-optic wireline used in these tests was one designed and owned by Chevron. Optical transmission of the data was required because of the high data rates required by these tests (almost 4 Megabits/second) over the long wireline. The maximum sampling rate of this system is 0.125 msec, and the anti-aliasing filter is set at 3125 Hz.

The optical signal is converted back to electrical data at the surface and input into a modified OYO DAS-1 data acquisition system, referred to as the BH-DAS. The BH-DAS sends all raw data to a METRUM VLDS (very large data storage) system for full backup of all information. In parallel, an amplitude-triggered event-detection capability has been installed in the BH-DAS to detect and capture event data on SEG-2 files for further analysis. The event detection compares a moving-amplitude window with a

resettable threshold for each channel to determine if events have been recorded. Event detection can be triggered using any number or combination of the channels in the multi-receiver system. For example, if channels 3, 6, 8 and 9 have been set as trigger channels, an event will be declared only if the moving amplitude window exceeds the threshold on all four selected channels. In addition, the threshold can be reset at any time on a graphics screen that shows the current threshold compared to the continuous moving window. This system gives us flexibility to turn off noisy channels, to change the threshold when conditions are noisy (e.g., during pumping), or to bias the search for signals by choosing particular channels.

For these A sand tests, the BH-DAS was connected to the M-Site network and SEG-2 event files were sent across the network for storage in the central computer facility. The event detection position (the sample point where an event was declared) was placed in the center of a 2048 sample window, so sufficient pre-event and post-event data would be taken for future processing. For the velocity survey, the data were written to a 9 track tape for later analysis. Standard trigger mode was used for velocity survey seismic recording.

The single receiver, used in treatment well applications, is the same design as the receivers in the multi-level system, but it sends analog data to the surface over a seven-conductor wireline. The three accelerometers in this triaxial package were driven using battery-operated power supplies to minimize noise from nearby power lines and other on-site equipment, as well as ground loops. The data from the analog receiver were digitized and stored on a Sony DAT recorder at 12000 samples/sec. Playback from the Sony was through a digital interface into a PC over a GPIB interface.

Although the analog receiver does not have an orientation device within it, the tool was modified to interface to a Gyrodata gyro tool so that an oriented H/Z survey could be run. Since the gyro tool is quite long and heavy, it was expected that significant resonances would be induced, and two separate H/Z minifracs were performed to compare the with-gyro and without-gyro results.

The velocity survey was conducted with down-hole receivers and a down-hole source. The source chosen was the Bolt airgun, which uses a hydraulically driven pulse. Spectral data show that considerable energy is emitted up to 600-800 Hz, and both P-wave and S-wave data could be detected in the receiver well. The airgun was deployed in a continuous mode, where the source is lowered downhole at a constant rate and the pulse is fired at set intervals which provide the correct spacing on the source shots.

8.1.4 Velocity Survey

In order to determine the velocity structure of the sand-shale sequence in the vicinity of the A sand, a two-well velocity survey was conducted on October 26-28, 1993. The receivers were located in well MWX-2 and the Bolt airgun was run in MWX-3. The range of shot and receiver locations is shown schematically in Figure 15. Receivers were moved at 10 ft increments between 4500 ft and 5000 ft, while airgun shots were positioned at 5 ft intervals between 4500 ft and 5200 ft. Fill-in receiver data at 5 ft intervals were then conducted between 4800 and 5000 ft. P-wave picks were completed in 1993 and were reported in the 1993 report.

Analysis of the P-wave-arrival first breaks were completed first, as P-wave data required considerably less processing than the S-wave results. Several test tomographic inversion runs were performed to determine proper processing parameters and to winnow poor quality first arrival picks. The tomographic inversion code used a simultaneous iterative reconstruction technique (SIRT) to obtain seismic P-wave velocities

from travel time observations. Acceptable velocity solutions were typically obtained after 5 iterations of the algorithm, with RMS residuals (difference between observed and calculated travel times) between 0.5 and 1 millisecond. The pixel grid used is 24x24. Travel time data were used with source and receivers at 10 ft vertical intervals from 4500 to 5000 ft. The wells MWX-2 and MWX-3 are 211 ft apart in this depth range (there is slight hole deviation from vertical).

In the final tomographic inversion, a starting velocity model was constructed with sonic log data from MWX-2 and MWX-3. These log data are shown in Figures 16 and 17, along with the gamma logs for lithologic reference. Best results were obtained by allowing inversion to proceed with velocities constrained to fit the starting model at the top and bottom of the tomogram. In these areas, pixel velocities are poorly resolved because of the limited ray path coverage. Global velocity constraints were applied to keep tomographic velocities within a few percent of the sonic log velocities. Figure 18 shows a black and white representation of the inversion results. The higher velocity A sand at 4940 ft and B sand at 4530 ft can be clearly seen. The heterogeneous nature of this fluvial environment is also evident in Figure 18.

8.1.5 Receiver Orientation

After completing the velocity survey using the 5-level array, the receivers were pulled out of MWX-2 and re-configured for the fracturing experiments. To obtain the widest possible receiver aperture, it was necessary to reduce the system to 4 levels, with a 10 ft interconnects between the top three receivers and a single 50 ft interconnect between the third and fourth receiver. Because of telemetry issues, it was not possible to use all 5 receivers with a 50 ft interconnect in the system, nor was it possible to use longer interconnects between the other receivers (however, these issues will have been attended to and longer interconnects will be available for future experiments). The receivers were then positioned at 4885, 4895, 4905 and 4955 ft in MWX-2 (the offset well), as shown in the schematic in Figure 19. Note that while there are 4 receivers in this array, the configuration is less than optimal because of the short spacing, especially for the high velocities in this formation. This particular configuration was chosen to position at least one receiver below the sand, one receiver in the sand, and one receiver above the sand, without having any receivers in the thin shale between the two parts of the A sand.

The receivers were oriented by first conducting 7 test shots of the air gun at 4700 ft to assure that the receivers were adequately clamped, and then conducting a full air-gun scan from 4700 to 5150 ft at 10 ft intervals. Figure 20 shows an example of the vertical accelerometer of the 4885-ft receiver, with shot 1 occurring at 4700 ft and shot 45 occurring at 5150 ft. It is clear that the vertical receiver observes a different signal polarity as the shot point passes from above to below, and a compression positive system would have the positive vertical axis pointing downward

The horizontal axes also show useful information as to the direction of the accelerometers. While the actual angular orientation will be given next, as determined from hodograms, the 180° ambiguity can be resolved by examining similar data for the two horizontal channels As an example, Figures 21 and 22 show the x an y channels from the 4895-ft level, with the x channel showing a positive first break (pointing toward the shot) and the y channel showing a negative first break (pointing away from the shot

Figure 23 shows the configuration of the accelerometers within the receiver mount. Historically, data channels have been taken as H2, H1, V, which is a right handed system based on the connector tabs being the positive direction. In this case, however, it is clear that the compressional direction is opposite the tabs, and since our analysis conventions assume that compression is positive, the receiver system is left handed and must be accounted for in the final location schemes.

The hodograms from one of the air-gun scan shots, using unfiltered data, are shown in Figures 24 through 27. Figure 24 gives the important data of the top-level receiver (at 4885 ft) for a shot at 4930 ft depth in MWX-3. At the bottom are the three components, at the top left is the horizontal polarization, and at the top right is the vertical plane polarization. Data associated with the shot, polarization, etc. are given on the far right. For example, the P-wave arrival occurred at sample point 509 which occurs at a relative time of 1.12 msec. The window for the hodogram extends from point 509 to point 537 at a time of 4.63 msec, through approximately four cycles. The horizontal azimuth (H on the plot) is 0.5° with a standard deviation of 11.1°. The inclination (V on the plot) is -11.5° with a standard deviation of 34.5°. For this particular shot and level, the horizontal polarization is very tight, but the inclination is questionable. Many of the test shots had inclination polarizations that were difficult to interpret, presumably because of the layering.

The results of Figure 24, as well as Figures 25-27, however, assume that the receiver system is right handed. Upon factoring in the left-handedness of the system, with the first break results taken from the scan, it is clear that the inclination angle needs to be the negative of the angle given in Figure 24. The left-handedness and the first break direction do not affect the horizontal orientation angle. Using similar considerations for the other levels, it can be determined that the actual inclination for level 2 (4895 ft) is the negative of the one determined with hodograms, while the inclinations for levels 3 and 4 (4905 and 4955 ft) are unchanged. While this redefinition of the angles may seem confusing, it is simpler to deal with the end result than to change an analysis code every time a new receiver configuration is encountered.

The horizontal polarization data from Figures 24-27 show that the receivers have rotated considerably relative to each other, with relative orientations of 0.5°, -74°, 88.3°, and 85.2°. Using a large number of the scan shots, it is possible to obtain statistically accurate orientations for the receivers. Figure 28 and Table 3 show the relative orientations at each of the four receiver levels for shots between 4800 and 5010 ft. The data are clearly consistent, with small standard deviations. Figure 29 shows the orientations of the positive direction of the horizontal receiver channels in an absolute sense, which in this case is the same as the relative numbers since the shot well is due north of the receiver well. However, the 180° ambiguity has been removed, as can be seen in the shifts in levels 1 and 2.

The inclination data are less accurate than the azimuth, but this is primarily due to the velocity structure of the formation. Figure 30 shows the measured inclination compared to the actual inclination of the shot point for all three levels. The one-to-one line, upon which all data should lie in a homogeneous medium with no error in processing, is also given for reference. While all levels have some angular windows through which the errors are sizable, level 4 appears to have the worst vertical response regardless of the inclination of the shot. This is an indication that the clamp on this level may not have been adequate.

8.1.6 Minifrac #1 Seismic Events

Minifrac #1 was conducted on November 1, 1993. The actual injection, described in another section, used a linear gel and lasted approximately 30 min. Two shut-in periods were inserted in the beginning of the treatment to search for near-wellbore problems. For correlation with the seismic data, a bottom-hole pressure tool was inserted in the treatment well.

Figure 31 shows a correlated plot of bottom-hole pressure with seismic signals triggered by the event detector. Initially, the event-detector threshold was set high to minimize pump-noise events, and, thus, few

events were triggered when pumping started. The threshold was subsequently lowered and approximately 5 min into the treatment, events were being detected at an average rate of about 5 per 2 minute interval. While the number of events jumped at shut in, they rapidly declined after shut in to fewer than one event per minute.

Figure 32 shows the first event, which occurs prior to the first shut-in period. This event has clear P-wave arrivals on all channels and good S-wave arrivals on some channels. Each division on this graph is 100 sample points, or 12.5 msec. The traces are all scaled to the maximum amplitude of all channels. The maximum amplitude is given as the "SCALE", which is in bit counts of the A/D system. The maximum bit count for the A/D system is $\pm 2^{20}$, or $\pm 1{,}048{,}576$ bit counts. The high frequency sections of the traces are due to the accelerometer resonances, which have a center frequency of 2200 Hz, but begin to be seen about 1700-1800 Hz. This "ringing" of the accelerometers is, in fact, very useful for determining P-wave arrival times.

Figures 33-36 show the overlain traces and hodograms from each of the four levels of the first event using the raw (unfiltered) data. Given at the bottom are the three traces and a picked location for both the p wave and the s wave. S-wave picks are found by searching for changes in amplitude, polarization, and frequency. At the top are the horizontal and vertical hodograms. The horizontal hodogram is a plot of the y-channel amplitude vs the x-channel amplitude. The vertical hodogram is a plot of the vertical-channel amplitude vs the resultant amplitude of the x and y channels. Given to the right of the hodograms are the associated data, including the P-wave arrival location (P) in sample point numbers and msec, the range (RANGE TO) for the hodogram, the S-wave arrival (S), the horizontal azimuth (H) and its standard deviation (SD), the inclination (V) and its standard deviation, the absolute rms values (RMS H and V) of the angles (positive sign regardless of orientation), the velocity factor (VEL FAC) used in the distance calculation, and the distance calculated from the p-s separation. The distance is given by

$$d = \frac{V_p V_s}{V_p - V_s}\left(t_s - t_p\right), \tag{3}$$

where the velocity factor is

$$\text{velocity factor} = \frac{V_p V_s}{V_p - V_s}, \tag{4}$$

t_p is the P-wave arrival time, and t_S is the S-wave arrival time.

In Figure 33, the P-wave arrival is very clear and the horizontal hodogram is linear over the first cycle with a relative orientation of 2.8° Factoring in the orientation data, the signal is coming from an angle that is about 3° west of north, or essentially from the direction of the treatment well. The vertical hodogram is not nearly as linear (which is usually the case) and suggests that the signal is coming slightly from below. However, at this level the x channel is pointed away from the treatment well, so the signal is actually coming from above. Here again is some of the confusion that can develop as a result of the 180° ambiguity, but which was resolved with the orientation scan data. This particular microseism also gives an example of a case where the S-wave arrival is not immediately obvious from amplitude and frequency alone (which can be determined by eye), and polarization changes were examined to determine its location.

Figure 34 shows the data from the next level down, with a clear P-wave arrival, a poorer quality azimuthal hodogram, a linear inclination hodogram and an S-wave arrival that is not immediately clear from observation alone. The absolute orientation of this signal at this level is about 5° west of north. Figure 35 shows the associated data for the third level, with a clear P-wave arrival, good hodograms, and a relatively clear S-wave arrival (from frequency). The absolute orientation of the impinging signal is about 1° west of north. Figure 36 shows the data from level four, where all necessary results are quite clear. The absolute

orientation of this signal is about 3° west of north. In general, the azimuthal results from all four levels are highly consistent. Such consistency is not always the case with the inclinations. In this example, the inclinations vary from about +11° to -2° after the orientations of the receivers are considered.

Figure 37 shows the results of filtering on the data from Figure 34 (level 2). This example shows one case where the filtering changed the orientation considerably (12°), but the change is probably due to the less than ideal horizontal hodogram that was originally found in the raw data (Figure 34). More often filtering has the effect shown in Figure 38, which corresponds to the level 3 data (Figure 35). In this case, the filtering changes the azimuth by only 1°. The filtering parameters used are given in Table 4

Table 4. Filter parameters

Cutoff frequency (Hz)	1500
Ripple (passband) (dB)	0.3
Stopband attenuation (dB)	60
Stopband edge frequency (Hz)	1800

Figure 39 shows the unfiltered traces for the second automatically triggered event. This example is much different from the first event in that the P-wave amplitude is much smaller than the S-wave amplitude and the S-wave arrivals can be easily discerned. The filtered traces for this event are given in Figure 40, which further enhances the S-wave arrival.

Figures 41-44 show the traces and hodograms for the individual levels of the second event using the unfiltered data. As noted from Figure 39, the P-wave amplitude is much smaller than the S-wave amplitude, with clear arrivals of both the p and s waves. Relative azimuths of the four levels are -9.1, -84.7, 64.9, and 54.5, respectively, which are absolute azimuths of 9°, 16°, 21°, and 28° (degrees clockwise from north). Inclinations of the four levels are 8°, 0°, 21°, and -9°. Clearly, layering and other effects are distorting the inclination of the signals.

Given in Figures 45-48 are the filtered versions of the second event. Relative azimuths for each level are -4 °, 88°, 70°, and 60°, respectively, which translate into absolute azimuths of 4°, 24°, 16°, and 23°. Filtering of the data has only a small effect on the azimuth of most signals on most levels. Inclinations of the four levels from filtered data are 15°, -18°, 22°, and -4°.

Of the 89 events, 78 of them are analyzable, with the rest being noise, electrical spikes, or other signals that are of undetermined origin. These results were then used in several different types of analyses for determining event locations.

8.1.7 Minifrac #1 Event Analyses

The first analysis attempted was a simple half-space model (constant velocity) using straight ray-path tracing with a velocity factor of 22.3 ft/msec, which was derived from the average log p- and S-wave velocities. Locations for all four levels are averaged together and the microseismic origin derived in this way is shown in Figure 49. The left plot is the plan view on a 500 x 500 ft scale, showing the average microseismic locations, the monitor well (MWX-2), the treatment well (MWX-3) and a regression line through the points. The right plot is a side view showing the top and bottom of the A sand (horizontal

lines), the treatment well (double line) and the projection of the receiver well on the regression azimuth along with the location of the four receivers (rectangles). The bottom plot shows the pressure and event markers marking where events occurred relative to the pressure. It is clear from the data that the fracture is asymmetric, with much more growth on the east wing than on the west wing. There is also considerable height growth, but most of the growth is upward.

If ellipses are drawn to the size of the coordinate-axis standard deviations, however, it is clear that this analysis does not give an accurate view of the shape of the fracture. Such an uncertainty plot is shown in Figure 50, using the same format as that given in Figure 49. While the length and azimuth of the fracture do not appear to be affected by the uncertainty in the data, the height of the fracture cannot be determined with any reasonable accuracy. The reason for this problem is the layering of the formation and the resultant variability in inclination angles due to refractions and head waves which cannot be accounted for in a half space model. Such a problem would also be minimized if a wider aperture array were possible, and such an array is being developed for all future use at this site.

Upon examining the original location calculations, it was observed that most events with a large uncertainty are inaccurate because one of the receivers is pointed away from the other three receivers. Without abandoning the half-space simplification, the data were re-analyzed by throwing away the outlier and averaging the information from the remaining three levels. The results from this calculation are shown in Figure 51, and the uncertainty plot is shown in Figure 52. While the uncertainties are much improved using this approach and the length and azimuth estimates would appear acceptable, the uncertainty in the height estimate is still too great.

Another analysis that was attempted was a distance matching routine to find the most likely origin from the intersection of the distances (p-s separation) to each level. This analysis allows the inclination data to be ignored, as the elevation and radial distance away can be directly computed. The azimuth from the hodograms is used, however, to provide the correct azimuthal direction. Figure 53 shows such a calculation, which does little to improve the accuracy of fracture height. However the length and azimuth estimates are very similar to the previous techniques.

Although the P-wave move-out is too small to use move-out data for calculating the elevation and radial distance together, as small amounts of error in picking the arrival will yield negative radial distances or absurdly large ones, the elevation alone is relatively insensitive to these errors and can be independently estimated from the move-out data. Coupled with the distance and azimuth from previous results, it is possible to devise another calculation of the shape of the fracture that is independent of the inclination data. This result is given in Figure 54, but it shows that any error in the arrival times tend to keep all elevation estimates at the level of the receivers. Nevertheless, the length and azimuth results are similar to all previous results.

For comparison with all previous results, Figure 55 shows all of the individual origin points, as if each receiver were an independent station. Locations were calculated using p-s separation for distance and azimuth and inclination from the hodograms. It is in Figure 55 that one can estimate the inaccuracy of the results when attempting to use a single receiver to map hydraulic fractures.

Several other half-space methods were also attempted, but the one that appeared to be the most reasonable approach to dealing with the inclination problem was to use the orientation scan data to choose the levels with the most accurate inclinations and use them for the elevation calculation. Then, discarding the outlier, the distance and the azimuth from the inclination level plus two additional levels were used to determine the origin point. For these data, the best level for shallower origin points was level 3, while the best level for

deeper origin points was level 2. The resulting plot of the fracture image is shown in Figure 56. Fracture length and azimuth are again unchanged by this processing technique, but the height appears to be more reasonable. An uncertainty plot is shown in Figure 57, but no uncertainty in the height can be determined because the elevation is specified by one level (no statistics). This approach appears to be the most accurate way to image the entire fracture using the half-space simplification, because it corrects for most layering effects through the choice of receiver for elevation estimates.

Using this method for further analyses, Figures 58-63 show the development of the microseisms with time. In Figure 58, only about 12 minutes of fracturing has occurred yet the fracture appears to have reached its total length extent in this time. Very little height growth has yet occurred. Ten microseisms later (Figure 59), at about the time that pressure stops increasing and begins to decrease, the situation is still very similar. Ten microseisms farther (Figure 60), during the time when pressure starts decreasing, some height growth upward and downward has begun, as would be expected from the pressure behavior. Figure 61, which shows all the data up to shut-in, has some additional height growth and an increasing width of signals in the horizontal plane. Adding the first ten points after shut-in, as given in Figure 62, additional height growth is observed in the upward direction. With ten more points and farther into shut-in (Figure 63), signals are found at increasing height (both up and down) and increasing offset distances. The final plot, with all of the data, is the one shown in Figure 56.

The next step taken was to use the velocity structure information to trace the rays back to the source using Snell's law. The tomographic grid was linearized into a layered structure with average velocities in the layers given in Table 5. These results were then further refined to give the velocity structure shown in Table 6. Figure 64 shows a summary plot of the first event, comparing the resultant refraction analysis with other previously discussed results. Shown on the left plot are the rays as determined from the hodograms and p-s separation for each level and a marker giving the source location for the various techniques. Shown on the right plot is a side view of the ray paths from the receiver well back to the apparent source using the straight-line half-space results and the refraction results. Also shown are the elevations and distances derived from the various techniques. Note that the P-wave move-out distance calculation is almost always in error. In the bottom box is a summary of the coordinate locations and standard deviations of the various techniques. For this event, it makes little difference whether a straight-line or refracted path is chosen. Three other examples, for events 2-4 and shown in Figures 65-67, also indicate that the straight-line approach gives results that are relatively close to the refraction data.

A plot of the refraction origins is given in Figure 68, and the uncertainty plot is shown in Figure 69. As before, the length and azimuth are little changed by the type of analysis, but the height shows large uncertainties. At this point, there is little advantage in using this type of refraction approach for these data. Although the work is ongoing and is not included in this report, an attempt is being made to use P-wave and S-wave arrival times to determine the source location by finding the shortest travel time for each wave. Such an approach will circumvent the errors associated with using the inclination data in any type of ray tracing scheme.

8.1.8 Minifrac #2 Seismic Events

Minifrac #2 was conducted on November 3, 1993. The actual injection, described in another section, used a linear gel and lasted approximately 40 min. Three shut-in periods were inserted throughout the treatment to search for near-wellbore problems. Figure 70 shows a correlated plot of surface pressure with seismic signals triggered by the event detector. Initially there were a large number events detected, but many of

these were not microseisms and are, thus unanalyzable. Throughout most of the treatment, there were about 5 events per 2 minute interval, with most of these events being analyzable.

While many of the events were similar to those seen in minifrac #1, others had some differences in characteristics. Figure 71 shows one of several events that had considerably lower frequency than all of the events seen in the first minifrac. These results are shown more closely in Figures 72-75, with the hodograms and overlain traces for each level given. These signals are particularly easy to analyze with clear P and S arrivals. Since most of the signals are similar to those seen in minifrac #1, an appendix of events was not included for this or later tests.

8.1.9 Minifrac #2 Event Analyses

Only three of the various event analyses were run on minifrac #2, an average of all four levels, an average of the three closest levels, and a ray-tracing analysis to include velocity structure. Figure 76 shows the average of all four levels and Figure 77 shows the uncertainty associated with the data. As before, the fracture is asymmetric, but in this test the asymmetry is less as there appears to be growth downward and to the west. The band of signals is also somewhat wider, which is what one would suspect would occur if leakoff were responsible for inducing some of the microseisms.[2] The uncertainty in the data, as seen in Figure 77, is greater than that seen for the first minifrac. Some of the difficulty associated with analyzing these data, relative to minifrac #1, may be due to changes in the formation velocities due to the additional leakoff fluids.

The average of three levels, with the outlier discarded, is plotted in Figure 78 and the uncertainty is shown in Figure 79. These results give a very similar picture to that of the four-level average, and indicates that the greater uncertainty in locations for minifrac #2 are probably due to some system changes or perturbations. Figure 80 and 81 show the ray-tracing results, using the same velocity data as that used for minifrac #1. As seen before, when the inclination data are used to begin any ray tracing routine, the results are little different from the half-space results. Other more advanced analyses are being performed on these data but are not included in this report.

8.1.10 Minifracs #3 And #4

The results from minifrac #3 are similar to minifrac #2 and also show a tendency for greater width of signals. A histogram of the events vs surface pressure are shown in Figure 82. Although it appears that there are considerably more signals during the shut-in phase of this minifrac than there was in the two earlier ones, the reason for this increase was a lowering of the threshold for event detection. Consequently, some of the triggered "events" are noise or are signals that cannot be analyzed. Detailed results from this minifrac are not included in this report.

Minifrac #4 had proppant added to it, and it was hoped that it would be possible to listen to the fracture closing on the sand. However, because of technical difficulties with tracer testing, it was not possible to flow the well back and include closure on the prop and it was not clear whether any closure on the sand was observed. Figure 83 shows the histogram of events correlated with the surface pressure. The fracture included three separate pumps with long shut-in periods in between. Many more signals are seen when sand was injected with cross-linked gel in the third pump phase. Detection of seismic signals continued long after shut-in, but some receiver problems developed in the middle of the night and there was no way to fix the problems and continue taking data. Only about 6 hours of shut-in data were obtained.

Although no observation of closure on sand was observed, the fourth minifrac was notable for its excessive amount of non-microseismic signals. The first two minifracs had about 80% analyzable signals, the third minifrac had about 60% analyzable signals (lower threshold), and the last minifrac had about 40%. It is unknown why the sand injection might have caused this behavior, or if it was some cumulative effect of continual pumping. All of the observed microseisms were similar to those shown in previous tests and are not given here.

8.2 H/Z Analyses

H/Z analyses were planned for both the 2nd and 3rd minifracs, by using a single receiver in the treatment well. The receiver in the 2nd minifrac was oriented with a Gyrodata gyro tool and timing of the data was provided by IRIG boards. However, both of these add-ons caused problems with data quality. The Gyrodata tool, a device about 6-ft long and 80-lb weight caused significant resonances in the 400-500 Hz range, and the IRIG board added electrical noise on top of the signals. As a results, the single receiver data from this test are not particularly good quality. In the 3rd minifrac, both the Gyrodata tool and the IRIG timing were omitted, and data quality were considerably improved, with both microseism background and discrete events being detected throughout the fracture. The analysis and results of the fracture height diagnostics for Minifrac #3 are described in this section

8.2.1 H/Z Method

The GRI H/Z fracture height determination technique uses the background motion. The background earth motion following a hydraulic stimulation is a continuum of small events that we have named Continuous Microseismic Radiation (CMR). The level of CMR immediately after a fracture stimulation is about 10 to 100 times larger than the ambient background motion before the stimulation. The method requires recording data at 15 to 20 depths within and beyond the vertical extent of the fracture - both above and below the expected fracture. (The method is described in detail in Fix et al.[6,7] (GRI-91/0031 and GRI-91/0031) and Mahrer[8] (SPE 21834) and will be only outlined here.) The data recorded at depths within the fracturing show a dominance of horizontal energy. Above and below the fracture, the vertical energy is larger than the horizontal energy. The depths of change from horizontal to vertical energy are the top and bottom of the fracture. The background motion data are formed into its two vector components: the horizontal component, H, and the vertical component, Z. An average of the H and Z energy is calculated at each depth and the H/Z ratio is formed. The top and bottom of the fracturing can be found where the H/Z ratio inverts from a vertical dominance to a horizontal dominance. The use of the H/Z ratio accommodates the analysis for the general decrease in the level of microseismic activity with time as the survey traverse is made from one level to another.

Following Mini-Frac No. 3-A, 17 depths were occupied at 50-foot intervals between 4900 and 5300 foot depths. A segment of data was taken at each depth. The rms values were calculated for 200 sample segments. The CMR background segments were extracted between the signals. The average values were calculated for the horizontal and the vertical components. The H/Z ratios are plotted in decibels so that a ratio less than 1 will have the same visual appearance as a ratio greater than 1. Thus, when the bar is positive, the ratio is greater than 1 and the horizontal component is greater than the vertical component and we are in the fracture. Conversely, when the bar is negative, the decibel value is negative and the ratio is less than one and we are outside the fracture. The negative value results from the vertical component being larger than the horizontal component.

The results of the fracture height processing by the H/Z method are presented in Figure 84. In Figure 84, the top of the fracture is interpreted at a depth of 4725 feet halfway between the stations at depths of 4700 and 4750 feet. The bottom of the fracture is interpreted at a depth of 4975 feet halfway between the stations at a depth of 4950 and 5000 feet. This top and bottom give a fracture height of 250 feet. The large positive values at depths of 4750 feet and 4950 feet provide a good confirmation of the fracture extent. An alternate interpretation of the top and bottom depths would be to place them at these 4750 and 4950 foot levels. These depths give a fracture height of 200 feet.

8.2.2 Spectral Ratio Contour Method

Another variation of the H/Z method is to form the H/Z ratio in the frequency domain. The CMR data at each depth selected between the peaks in the rms data are taken as time domain samples. The spectra of these time domain samples are calculated for the horizontal vector and for the vertical vector at each depth. The spectral ratio is then formed. A contour plot is then made of the H/Z spectral ratios. This variation of the H/Z method was first presented in GRI Report No. 93/0031 (Fix et al.[8]) and is described there.

The spectral contours vs. depth are plotted in Figure 85. Frequency in hertz is the abscissa; the frequency range is from 0 to 6000 Hz. (Digitizing was at 12,000 samples per second; therefore, the Nyquist frequency is 6000 Hz. This sampling rate is higher than normally used.) Depth in feet is the ordinate; the range of depth is 4900 feet to 5300 feet in 50-foot increments. The contour intervals are 15, 10, 5, 0, -5, -10, and -15 dB. The corresponding grayscale in the figure is: silver gray (see at 4950 feet depth and 2400 Hz), black, darker gray, light gray (much of the background), darker gray (than number 3), and intermediate gray. The -15 dB level is not evident in the figure. The range of the perforations from 4900 to 4950 feet is plotted as a dark bar on the right vertical margin of the plot.

Interpretation of Figure 85 is in agreement with the interpretation of Figure 84. The top of the fracture is interpreted above 4750 feet along the top of the large amplitude darker gray, black and silver gray contours. The bottom of the fracture is interpreted as being below 4950 feet where there are similar large amplitude contours. The large spectral contours in Figure 85 are in direct correlation with the large bars at these depths in Figure 84. The spectral data suggest that the top and bottom of the fracture are closer to these two depth stations rather than half way between them and the next adjacent depths.

The vertical streak of energy between about 2300 and 2600 Hz in figure 85 is created by resonances of the accelerometers in the sondes. A 3000 Hz antialias filter was used. Therefore, energy is falling off rapidly between 3000 Hz and the 6000 Hz Nyquist frequency. Even with this fall-off, there are large amplitudes in the H/Z ratio at 3900 to 4500 Hz and near 4800 Hz further emphasizing the confirmation of a fracture boundary in the interpretation of this technique.

The top and bottom of the fracture from both the H/Z bar method and the H/Z spectral contour method are in good agreement with the top and bottom of the fracture from the observations made in the remote MWX No. 3 well.

8.3 Monitor Well Design

The major focus of the M-Site experiments is to validate diagnostic techniques and model calculations by accurately imaging a hydraulic fracture. In order to achieve this objective, it is necessary to obtain some reliable ground-truth measurement of the fracture size and shape. The M-site experiment ground truth will

be established through the use of a highly instrumented monitor well, which will include both seismic instruments and downhole tiltmeters (which will also be referred to as inclinometers).

8.3.1 Seismic instrumentation

Accelerometers have been chosen for the seismic transducers in the monitor well. Even though accelerometers are more expensive than geophones, their noise-floor and frequency-response characteristics make them especially well suited for this experiment. The Wilcoxin Research Model 731-20 Seismic accelerometers were chosen and have the following nominal characteristics.

Sensitivity	20 Volts/g
Amplitude range	0.2 g peak
Amplitude nonlinearity	1%
Frequency response	±3 dB from 1.5-1200 Hz
Resonance frequency	>2200 Hz
Transverse sensitivity	<4% of axial
Electrical noise	<1 μg broadband (2 Hz - 20 kHz)
	-158 dB re g/√Hz at 100 Hz
	-163 dB re g/√Hz at 1000 Hz
Temperature range	-40 - 120° C
Vibration limit	50 g peak
Shock limit	200 g peak

Over 100 accelerometers were purchased and then checked for their characteristics. In order to match as closely as possible the three accelerometers in each triaxial package, the entire set of accelerometers were compared first by sensitivity, second by bias output voltage, and third by the resonant frequency of the accelerometers. The triaxial sets that most closely matched were placed in the middle depth locations, while the least matched sets were placed at the far top and bottom. In general, all triaxial packages are adequately matched for these diagnostic purposes. Table 7 shows the sets for each pod and their characteristics. Pod #1 is at the far bottom of the well, while pod #30 is at the top.

8.3.2 Seismic Data Acquisition System

The second major requirement for the seismic instrumentation is a complete data acquisition system. With as many as 32 levels, and each level containing three channels, a high-speed 96 channel data acquisition system (DAS) is required. We have found such a system in the OYO Geospace DAS-1. Particularly impressive is the 24 bits of resolution at which the system can digitize. However, in a continuous mode the DAS has not been able to supply data at the desired rates for more than 48 channels at the present time. This channel limitation is acceptable for initial tests, but we are continuing to investigate if the number of recording channels can be expanded.

8.3.3 Inclinometers

The inclinometers chosen for this application are Applied Geomechanics Model 510 Geodetic Borehole tiltmeters. These gages have the following characteristics:

Resolution	10 nanoradians
Operating tilt range	±900 μradians
Leveling range	±3°
Temperature	70°C
Pressure	>3000 psi (tested at Sandia)

These tiltmeters appear ideal for both small inclinations that are expected during stress tests and large inclinations during fracture treatments. Tiltmeters were ordered and checked out by CER Corporation.

8.3.4 Cabling

Design of the cable systems for both the accelerometer and tiltmeter systems was performed by Sandia and CER in conjunction with TESTCORP, the cable manufacturer. Both cables had significant design questions that needed to be addressed prior to manufacture.

The accelerometer cable required 90 channels plus spares, so to minimize size and cost, the smallest possible gage wire was chosen, in this case AWG 26. However, to insure that the frequency response of the system would be sufficient, several tests were conducted to evaluate the behavior of AWG 26 wire. Figure 86 shows the frequency response of a dummy accelerometer run through 5000 ft of the wire. The amplitude output was measured as a function of frequency and plotted in dB. The critical point is the 3 dB down location, which we required to be at least 2200 Hz, the resonant frequency of the accelerometer. Our tests showed that the 3 dB point was at 3200 Hz and at 2200 Hz the response was less than 2 dB down. Figure 87 shows the noise characteristics of the dummy test. Previous work through seven conductor wireline has given noise levels about -105 dB, and we required similar noise levels for this cable. In this case, noise levels are -105 to -110 dB except at 1550 Hz where they reach -100 dB. In both respects, AWG 26 wire was found to be acceptable for the cable.

As a result of the previous testing, the final cable was specified with 96 twisted pairs of AWG 26 wires, 5100 ft long with 30 accelerometer pods at specified depths. The cable was filled with a water block compound, was given an 1800 lb Kevlar stress core, and bound with a heavy jacket. O.D. of the cable was 0.85 in.

The tiltmeters required considerably more power than the accelerometers to run the gimballing motors, so larger diameter wires were needed for motor control. Since there are two separate sensors in each tiltmeter, and each sensor has motor control, gain switches, temperature and other functions, each tiltmeter required nine AWG 26 and six AWG 18 wires. With six tiltmeters, the total diameter was too large to manufacture a single cable, and, thus, six different cables were manufactured for each tiltmeter. Each tiltmeter cable was 0.415 in O.D., did not have a Kevlar core, was water blocked and covered with a heavy jacket.

8.3.5 Instrument Installation

Initial instrument installation was performed in August by attaching accelerometers, tiltmeters, cables and centralizers to tubing for lowering into position. Locations of each of the instrument pods were marked with radioactive pips. Accelerometer pods were checked for orientation by tap tests. The entire assemblage of equipment and cables was successfully installed, but all of the TESTCORP connectors on the tiltmeters failed, and the all equipment were retrieved.

The source of the malfunction was determined and new connectors were ordered and field spliced to the tiltmeter cables. Finally, in October the instrumentation was re-installed, checked out, and cemented in place. All instrumentation were functioning after this operation.

8.3.6 Check-Out and Noise Suppression

Initial check out of the instrumentation was conducted in early November during perforation and stress testing of zones in MWX-2 and MWX-3. This was the first occasion when the entire instrumentation/data acquisition system was integrated. It was quickly discovered that the seismic instruments were swamped by noise that was much greater than any seismic signals seen in past experiments. During investigation of this problem it was found that the seismic signals coming out of the monitor well were clean, but that the surface instrumentation was picking up large amounts of interference. The sources of the interference were thought to be (1) the ground of the rural power system, (2) the high tension power lines running nearly overhead and (3) the high power switching characteristics of the many nearby drilling rigs that were operating at any time. Several simple fixes were attempted first (such as better isolation transformers), but the noise was only reduced by about a factor of two.

To remedy the noise problem, Sandia began an intensive effort to regain performance of the system. All facets of the accelerometer output, amplifier performance and data acquisition (DAS-1) response were tested and modeled. After several weeks of testing a five-pronged program was put into motion. First, high quality isolation transformers were obtained for all input power. Second, all surface cables were sheathed in both magnetic and electric shielding materials. Third the power supply to the accelerometer amplifiers was redesigned for battery supply. Fourth, the accelerometer amplifiers were redesigned to be true differential capable of high levels of common mode noise rejection. Fifth, the DAS-1 input capacitance was lowered to provide better amplifier performance at typical frequencies of the seismic events. Because of the long lead time of materials and the large number of components, this redesign effort has extended into 1995.

8.4 Observation Well Noise Check

On December 13, 1994, a noise check was conducted on MWX-3 using a single analog triaxial receiver. The purpose of these tests was to investigate the noise levels caused by gas flowing through open stress-test perforations and to identify, if possible, which perforations were responsible for the gas flow. It is important that this well have a low background noise level because the five-level wireline system will be located in this well for most M-Site tests.

The procedure used consisted of:

1. clamping the tool at stations above, below, and in between every set of perforations (depths chosen were 4875, 4835, 4715, 4530, 4460, 4360, 4240, 4120, 3000 and 1500 ft)
2. observing the type of noise on a signal analyzer
3. sampling the spectrum
4. recording the noise amplitude at specific frequencies.

These data were then plotted and compared with noise spectra obtained from the last set of experiments (conducted in during the suitability test). Figure 88 shows the spectral data obtained at the eight levels through the perforations. Just about all data show a peak at about 500-600 Hz that reaches almost -60 dB

(from a reference of 1 volt). This peak is right in the middle of the microseism range and is at least 40 dB (or 100 times) greater than the noise level of the last test. Since signal-to-noise ratios in the last experiment were typically 20:1, this degree of noise would probably make it impossible to accurately locate microseismic signals in the upcoming experiments. Two of the channels do not exhibit this peak, but instead show in increased level of lower frequency noise. One possible reason for this may be the location of the tool relative to the gas bubbles.

The observed 100 times greater noise level makes it difficult to use this well for microseismic monitoring, and it was recommended that some effort be made to reduce noise in this well. This effort will be conducted in 1995.

9.0 AUTOMATED PROCESSING

In order for microseismic diagnostics to become a usable field service, it will be necessary to develop automatic processing algorithms to map event locations on a real-time or near-real-time basis. In addition, the large volume of data that will be obtained at M-Site makes it imperative that the seismic results be handled automatically, with the exception of checks made on selected events or investigations of noise levels or other unknown types of events.

9.1 M-Site Monitor Well Analysis Program

Analysis of the M-Site monitor-well data is critical to the successful development of this project, but with 30 sets of triaxial accelerometers taking data at 8000 samples per second, the amount of data to be processed is overwhelming and could not be completed without automatic routines. A code named SEER has been developed to handle the special requirements associated with processing the monitor well seismic data. This code is written in C++ for speed and flexibility.

SEER is a somewhat complicated code that must interact with a data handler card that accepts data from the DAS. Because of the high data rates, there was no available data acquisition system that could take data continuously, write all of the tape to data for backup, and also send the data to a separate PC for real-time processing. To circumvent this problem, the DAS-1 system was set up to write the backup data to a Fujitsu 3480 tape unit which has a read-after-write(RAW) capability that could be used to send data to a PC. To accomplish this task, OYO Geospace Instruments added a data handler card to interface with the RAW capability of the 3480 and map the data files into extended PC memory. The SEER program uses the same DOS extender model as that used on the data handler and special functions to talk to the data handler and ask for 5-second long files. Only after the event files are mapped into memory can the actual processing of the data take place.

SEER is set up to ask for a data file, process the data by searching for P-wave arrivals of events, calculate horizontal polarizations of the P-wave, write event files to the M-Site network for further analysis, calculate the location of events, and write information files to the M-Site network. When a data file is completed, the program then requests the next incoming file. Because of the time required for processing, it is usually possible to process every other data file, or 50 % of the data, in real time. The rest can be obtained after the test is completed.

The SEER program uses an event-comb architecture to look for P-wave arrivals. Analysis of a data file takes place by first calculating and storing the squared amplitude of the noise at the beginning of each file. Data are then processed point-by-point and compared with the noise record multiplied by an appropriate threshold value. The processing includes squaring of the amplitudes and a check of all seismic levels to find any with apparent events. If an apparent event is found, all surrounding levels are checked at that time and for the next seven samples. If sufficient other channels find events within the seven-second window, an event is declared and an event file is written. The data are then processed for polarization and event location and an information file of these results is written to the M-Site network. The program continues looking through the data file, but only after an appropriate number of quiet samples have been detected (so an event is not found in the coda of the prior event). In this way, the data file is analyzed for events and the necessary results are sent to the M-Site network.

9.2 Five-Level Wireline Receivers

The second major program being developed is currently named READ5 and is built to process data from a multi-level advanced-receiver wireline array such as the one currently being used by BOLT Technologies. This program is also written in C++ for speed and flexibility.

Since the five-level system run by BOLT already has event detection built into it, READ5 starts by checking any network storage location for event files. When a new one is found, the program uses an event comb similar to SEER to determine where the P-wave arrival is located. Like seer, the program also determines horizontal polarization and event locations. In addition this program plots the results on plan-view and side-view screen displays. READ5 can also take information files from SEER or other programs and plot those points as well. Thus READ5 is built to be the final analysis program for fracture diagnostics.

READ5 is different than SEER in that it is also set up to manually change any of the event picks. An operator can scan through the event files, graph them, and examine the P-wave arrivals picks that were automatically chosen. If desired, the operator can change the pick, thus resulting in new event data and locations. READ5 will be a continually developing program that we will use as the backbone of our processing capabilities.

9.3 Two-Level Wireline Receivers

A third program, named MS2LEV, has been developed for a two-level system that cannot entirely process event locations in the straightforward manner used on the other multi-level systems. This program, however, is more of a front end for analysis and quality assurance, although changes are being incorporated into it to expand its capability. The driving impetus for this program was to have some QC information from feasibility-type fracture experiments where only one or two levels might be run on a seven conductor wireline.

MS2LEV is an adaptation of previously developed FORTRAN programs that will read data files from any network storage device, do event detection, and allow graphical checks and analyses of either the event files or the original data files. In this program, however, the checks and analyses are currently done manually by the operator, although automatic processing is being considered. This program was assembled to prepare for a January 1995 Mitchell Energy Company Fracture Monitoring Feasibility test.

10.0 MODELING AND INTERPRETATION

10.1 Microseismic Interpretation

All evidence available suggests that microseisms are generated by shear movement of the rock in the vicinity of the hydraulic fracture.[9,10] Since many reservoir rocks are quite competent, it is most likely that shear movements occur as slippages along natural fractures, bedding planes, planes of weakness, and other low-strength features.

A linear friction law is usually found to adequately represent rock behavior,[11] resulting in a slippage condition of

$$|\tau| \geq \tau_o + \mu(\sigma_n - p) \,, \tag{5}$$

where τ is the shear stress, τ_0 is the inherent shear strength of the sheared feature, μ is the coefficient of friction, σ_n is the net normal stress acting on the fracture, and p is the local pore pressure within the fracture. Examining Eq. 5, we can see three methods by which slippages can be induced by the hydraulic fracture: increasing the shear stress, increasing the local pore pressure, or decreasing the normal stress. It is not likely that τ_0 and μ will change much as a result of the fracturing process. As will be shown, these three possible changes can be induced by two different mechanisms.

10.2.1 Crack Tip Effects

Analytical solutions for the stress around fractures have been developed by Westergaard[12] and Sneddon[13] for 2-D and radial fractures, and these solutions show that shear stresses are increased significantly in the vicinity of the fracture tip and tensile stresses are induced out ahead of the tip (thus reducing the normal stress on any slippage plane). As a result, the induced stresses in the near tip region are conducive to shear movement and the generation of microseismic signals. The size of this region is important, because it should correlate with microseism locations that appear to be some distance orthogonal to the fracture. For a two-dimensional crack, the stresses around the crack are given by Sneddon[13] as

$$\begin{aligned}
\frac{1}{2}(\sigma_x + \sigma_y) &= P_o\left\{\frac{r}{\sqrt{r_1 r_2}}\cos\left[\theta - \frac{1}{2}\theta_1 - \frac{1}{2}\theta_2\right] - 1\right\} \\
\frac{1}{2}(\sigma_y - \sigma_x) &= P_o\left\{\frac{r\sin\theta}{a}\left(\frac{a^2}{r_1 r_2}\right)^{\frac{3}{2}}\sin\left[\frac{3}{2}(\theta_1 + \theta_2)\right]\right\} \\
\tau_{xy} &= P_o\left\{\frac{r\sin\theta}{a}\left(\frac{a^2}{r_1 r_2}\right)^{\frac{3}{2}}\cos\left[\frac{3}{2}(\theta_1 + \theta_2)\right]\right\},
\end{aligned} \tag{6}$$

where the angles θ, θ_1 and θ_2 and the distances r, r_1 and r_2 are shown in Figure 89. The characteristic length dimension, a, may be either a half-height or half-length, P_0 is the net treatment pressure, and σ_x, σ_y and τ_{zy} are the stresses induced by the crack.

The induced stresses, when combined with the existing in situ stresses, can be used to determine the shear stresses on any existing slippage plane oriented at some arbitrary angle, β, and the normal stress on that plane. These stresses are given by

$$\begin{aligned}
\tau_\beta &= \tau_{xy}\left(\sin^2\beta - \cos^2\beta\right) - \left(\sigma_1 + \sigma_x - \sigma_3 - \sigma_y\right)\sin\beta\cos\beta \\
\sigma_\beta &= \left(\sigma_1 + \sigma_x\right)\sin^2\beta + \left(\sigma_3 + \sigma_y\right)\cos^2\beta + 2\tau_{xy}\sin\beta\cos\beta
\end{aligned} \tag{7}$$

If we define a function, F, given by

$$F = |\tau| - \mu(\sigma - P) , \quad (8)$$

then for F_β greater than τ_o, slippage will occur. Since τ_o is typically small for natural fractures and many other weak features, a positive F is a good indication of slippage conditions. For slippage planes not aligned with the crack characteristic length, $\sigma_z = \nu(\sigma_x + \sigma_y)$ and Equation 7 must be modified so that the correct stresses are acting on the slippage plane. For radial fractures, Sneddon[13] provides appropriate stress equations in place of Equations 6.

Results from Equations 6-8 can best be seen by calculating F for an example. Given the parameters in Table 8, for conditions that might be found in a fracture treatment at a depth of 5000 ft, zones of slippage for several β are indicated in Figure 90. The zero point is the crack tip and the internal zone of each curve describes the area where F is greater than τ_o = 100 psi (0.7 MPa). As can be seen in this figure, there are favorable planes at which the slippages occur as far away as 20 ft (6 m). The most favorable slippage planes are located between 30° and 45°, and a minimal slippage zone is found for angles greater than 75 °. In any case, these results show that the microseisms can be induced some distance orthogonal to the fracture, and the orthogonal distance is a function of both reservoir and treatment parameters. This information is important for interpreting microseismic data, since it suggests that the presence of a wide active zone around the fracture tip is normal for a singular fracture and is not necessarily indicative of complex fracture behavior.

Table 8. Parameters for tip shear calculations

σ_{max}	5000 psi	34.5 MPa
σ_{min}	4000 psi	27.6 MPa
P_o	800 psi	5.5 MPa
a	100 ft	61 m
μ	0.6	0.6
P	2200 psi	15.2 MPa

10.1.2 Leakoff Effects

The second method of inducing microseisms (or making F greater than τ_o) is by leakoff of the high-pressure fracturing fluid into the formation or into natural fractures.[9,14] This mechanism is actually more efficient at inducing slippage than the crack-tip effect because the volume of application is orders of magnitude larger (along the entire face, as opposed to near the tip) and the perturbing force is much greater. Changes in crack tip stresses are on the order of the net fracturing pressure, which is generally less than 1000 psi (6.9 MPa). The perturbing leakoff parameter is the increase in pore pressure, which is the total treating pressure minus the pore pressure, the value of which may be several thousand psi (several tens of MPa).

Evaluation of this mechanism requires the calculation of the stress induced by the fracture, the pore pressure perturbation, and the back stresses, if any, as well as a knowledge of the in situ stresses. The stresses induced by the fracture can be estimated from Equations 6 by considering the stress decay along the centerline of the crack. Under such conditions, $\theta_2=\pi-\theta_1=\tan^{-1}(r/a)$ and $r_1=r_2=\sqrt{r^2+a^2}$. These substitutions allow the equations to be reduced to

$$\sigma_z = P_o\left\{1-\frac{2a^2y+y^2}{\left(a^2+y^2\right)^{3/2}}\right\}$$
$$\sigma_y = P_o\left\{1-\frac{y^3}{\left(a^2+y^2\right)^{3/2}}\right\} \qquad (9)$$
$$\sigma_x = \nu\left(\sigma_y+\sigma_z\right),$$

where ν is Poisson's ratio. For most cases of interest, a=H/2 since the controlling length scale (the smallest length scale) will be the fracture height, and the x and z equations have been switched to reflect this geometrical consideration and keep x and y as the horizontal axes.

To estimate the leakoff disturbance, equations for the leakoff into natural fractures have been taken from Carslaw and Jaeger[11] and Howard and Fast[15] and summarized in Warpinski and Teufel[14] as:
a) infinite joint, same leakoff and reservoir fluids;

$$P = P_o + (P_o - P_\infty)\operatorname{erfc}\sqrt{\frac{\varphi\mu_\ell c Y^2}{4kt}} \qquad (10)$$

b) infinite joint, evacuated;

$$P = P_o - (P_o - P_\infty)\left[\frac{Y}{Y_f}\right], \qquad Y_f = \sqrt{\frac{2k(P_o - P_\infty)t}{\varphi\mu_\ell}} \qquad (11)$$

c) finite joint of length d, same leakoff and reservoir fluids;

$$P = P_o - \frac{4(P_o - P_\infty)}{\pi}\sum_{n=0}^{\infty}\frac{1}{2n+1}\exp\left[-\frac{(2n+1)^2 k\pi^2 t}{4\varphi\mu_\ell c d^2}\right] \cdot\sin\left[\frac{(2n+1)\pi Y}{2d}\right] \qquad (12)$$

d) finite joint of length d, evacuated;

$$P = P_o + \frac{8(P_o - P_\infty)}{\pi^2}\sum_{n=0}^{\infty}\frac{(-1)^n}{(2n+1)^2}\cdot \exp\left[-\frac{(2n+1)^2 k\pi^2 (t-t_o)}{4\varphi\mu_\ell c d^2}\right]\sin\left[\frac{(2n+1)\pi Y}{2d}\right] \qquad (13)$$

for

$$t \geq t_o = \frac{\varphi\mu_\ell d^2}{2k(P_o - P_\infty)}. \qquad (14)$$

For $t<t_o$, Equations 11 apply as the treatment fluid will not have reached the end of the crack.

Leakoff into the matrix will not generally be considered in this paper, but an approximate answer can be obtained by using a Green's function approach[16] for a time averaged length. This approximation can be done many ways, but an exponential averaged length yields

$$P = P_\infty + (P_o - P_\infty)\frac{2y}{\pi}\int_0^{0.582L}\frac{dx}{\left(x^2+y^2\right)}\exp\left\{-\frac{\varphi\mu_l c\left(x^2+y^2\right)}{4kt}\right\} \qquad (15)$$

In all cases, φ is the porosity of the fracture or matrix, c is the compressibility of the fluid, μ_l is the liquid viscosity, P_∞ is the far-field reservoir pressure, k is the permeability, Y is the distance into the natural fracture, Y_f is the location of the leakoff front (for an evacuated crack) within the natural fracture, L is the hydraulic fracture half length, y is the distance orthogonal to the hydraulic fracture face, and x is the distance along the hydraulic fracture as measured from the wellbore.

Of primary interest for this study is the leakoff into natural fractures in relatively low-permeability formations, as the slippages occur along natural fractures and such natural fractures also allow the leakoff disturbance to be transmitted much farther into the formation than through leakoff into the matrix alone. Since Equations 11-14 calculate the pressure distribution as a function of distance along the natural fracture, if the natural fracture is oriented at some angle, β, to the hydraulic fracture, then the pressure perturbation at some point, Y, is located at $y=Y\sin\beta$ in the formation.

Back stresses for hydraulic fractures in gas reservoirs are generally neglected, and they are in this analysis. For liquid reservoir and leakoff into the matrix alone, Smith's analysis[17] can be used and further linearized.[14] For liquid reservoirs with leakoff primarily into natural fractures, back stresses are ignored. Back stresses will not be further considered here.

The results from the previous equations can all be combined to evaluate the slippage condition, given as

$$\frac{1}{2}\left[\sigma_1+\sigma_x-\sigma_3-\sigma_y\right](\sin 2\beta+\mu\cos 2\beta)- \frac{1}{2}\left[\sigma_1+\sigma_x+\sigma_3+\sigma_y-2P\right]=\tau_o \qquad (16)$$

These equations can also be modified to account for horizontal slippage planes by appropriate switching of the stress values. For oblique planes, a full 3-D transformation is required.

An example calculation is shown in Figure 91, for the same parameters as given in Table 8 and with the additional parameters in Table 9. This calculation is also for a fracture at about 5000 ft in a normally pressured reservoir, but the reservoir is naturally fractured and the maximum leakoff extent occurs through the natural fractures. The failure function, F, is plotted versus orthogonal distance from the fracture face, for three different natural fracture orientations (15°, 30°, and 45°) and two different reservoir fluids. It is immediately obvious that gas reservoirs have a narrow slippage zone because the leakoff disturbance does not extend far into the reservoir. However, a liquid reservoir (oil or geothermal) will see these effects for distances that may extend several hundred feet (over 100 m). As with the previous mechanism, certain orientations of natural fractures will experience much greater activity than others depending on the formation and treatment conditions.

Table 9. Additional parameters for leakoff calculations

natural fracture permeability	500 md	34.5 MPa
natural fracture porosity	0.2	0.2
leakoff fluid viscosity	1 cp	0.001 Pa s
leakoff fluid compressibility	3.3×10^{-6} psi^{-1}	4.8×10^{-4} MPa^{-1}
Poisson's ratio	0.2	0.2
Overburden stress	5000 psi	34.5 MPa

It is also worth noting that if the hydraulic fracture intercepts relatively short natural fractures, then the natural fractures can fill up with leakoff fluid and the pressure disturbance around the hydraulic fracture will be greater (although it will not extend as far). In this case, the failure function is likely to be positive for the entire length of the natural fracture, thus extending the active zone further into the reservoir.

10.1.3 Tensile Failure at Tip

A significant amount energy is involved in the actual fracturing of the rock at the hydraulic fracture tip, but there does not appear to be any clear indication that tensile failures at the tip have been monitored in previous microseismic tests. Daneshy[18] shows that the usable work to create a hydraulic fracture in a previously unfractured rock is equally partitioned between the work of fracture and the work of deformation when there are no in situ stresses. However, where in situ stresses are large relative to the net treatment pressure, the energy associated with deformation can be an order of magnitude larger than the energy needed to fracture the rock. In addition, lab tests of discrete fracture propagation[19] have resulted in acoustic emissions at very high frequencies (30-300 kHz) which cannot be detected by current borehole receivers, and attenuation at these frequencies is expected to limit the distance at which such signals could be detected. At present, it is not clear if tensile signals are ever recorded during hydraulic-fracture microseismic monitoring tests. If these signals are present, they will likely be within the shear-generated signal zone, and only be of additional interest if they can be distinguished from the shear failure signals.

10.1.4 SPE paper on modeling results

The results of section 10.1 have been included in a SPE paper (SPE 27985) presented at the University of Tulsa Centennial Conference. Also included in the paper are some tiltmeter studies published in a previous annual report.

10.2 Finite Difference Location Analysis for GRI/MWX Site

Microfracture events at the M-Site were recorded with four three-component borehole instruments sited within several hundred feet of the sources, which should lead to high quality data and reliable locations. However, standard ray-tracing locations assuming a half-space model and using S - P times for distance and P particle motions for direction are troublesome: S - P times and azimuthal directions are consistent amongst the instruments, but the angles of incidence are not. We believe that this is an indication that significant bending of the ray paths has occurred due to strong velocity contrasts in the vertical direction, an idea that is well supported by the sonic logs in both the receiver and the treatment holes and by the P velocity tomogram between the holes. Clearly, to get better results more realistic velocity models must be used.

It is possible to modify basic ray-tracing techniques for the effects of layered models, but as the number of layers increases this problem becomes increasingly difficult and any small change in the model requires a new derivation. A better approach, we have found, is to use the finite-difference location technique of Nelson and Vidale (1990), which can handle an arbitrarily complicated model as easily as a half-space and which will always find the correct first arrival from a source point to a receiver, whether it is a straight ray, a refracted ray, or a head-wave. A brief description of the technique is given below.

10.2.1 The Finite Difference Technique:

The basis of the technique comes from an algorithm developed by Vidale[20] which uses the finite difference method to solve the eikonal equation in a gridded medium. Figure 92 shows a wavefront calculated using the algorithm. Wavefront contours are shown for a source (*) approximately 900 feet from the receivers (X) superimposed on the layered velocity model for which the contours were calculated. The numbers on the contours are centiseconds travel time from the source.

The eikonal equation comes from the equation of motion and it completely characterizes the wavefront, thus its solution for a disturbance in a gridded medium will yield first arrival times to all grid points. To understand how the eikonal solver is used in the Nelson and Vidale[21] location technique, let us consider a location problem with 4 receivers. The location proceeds as follows:

1. P velocity model is specified (generally as a set of constant velocity polygons) and this is used to generate a grid file of velocity points. If both P and S times are to be used in the location, a separate S grid file will be generated in the same way. Note that these files need only be generated once to be used in the next step.
2. Using the P gridded velocity file, the eikonal solver is run once for each receiver, using the receiver location as the source point, to generate a file with travel times from the receiver location to each grid point. A total of 4 files are generated. If S times are to be used as well, then the process is repeated using the S gridded velocity file to generate 4 more files giving a grand total of 8 files. Note that these time files also need only be generated once and can be used again and again for the actual location in the next step. The only reason to generate new files is if the velocity model used for location is changed. Note that the first two steps can be completed prior to any fracturing experiment if the velocity structure is known, estimated or assumed.
3. Now the actual location process begins. For each grid point, residual time differences are calculated between the observed time at each receiver and the calculated time (P or S) to the grid point which is stored in the files generated above (note that by reciprocity the travel time from grid point to receiver is the same as for receiver to grid point), and these differences are averaged to get a best fit origin time. If only P times are used then 4 time differences are averaged, if P and S then 8 differences are averaged. The calculated times are now added to the best fit origin time and then again subtracted from the observed times to get the true residual time at the grid point. The type of residual (L1 = mean of absolute values; L2 = root mean square) is a changeable parameter.
4. This process is repeated for all the grid points, and the point with the minimum residual is selected as the location of the event.

To those unfamiliar with the technique, it may be useful to point out a few simple features. First, as mentioned above, the technique relieves the user of the task of trying to understand where the first arrival has come form (i.e. is it a direct wave or a head wave?). Second, unlike many inversion techniques, this technique will be guaranteed to always find the absolute minimum rather than a local minimum. Third, the

eikonal solver, which is the slowest part of the system, is only run once to generate the time file(s), and this could be done on a powerful machine after which the time files could be copied to other machines such as PC's which could run the actual location code (the performance of which is completely dependent on the number of grid points). Thus, with a reasonable grid size, the locator should be able to run in near real time on a 486 based field system.

10.2.2 Modifications:

We have made a few minor modifications to the basic Nelson and Vidale[21] code:

1. The original code is actually set up to run a full three-dimensional grid. Because we have no reason to think that the use of a 3D structure is warranted for the M-Site, and because using a 3D grid slows down the location so much, we modified the code to run a 2D structure more appropriate for our problem (removing the modifications to go back to 3D should be simple if this proves necessary for future projects). Note that this implies that we can determine the azimuth information separately, but this is consistent with observations: the azimuths from the P particle motions are very consistent between the receivers for a given event.
2. The original code is set up to locate earthquakes and consequently expects receiver coordinates in latitude and longitude, which is not appropriate for our problem where source-receiver separations are so much smaller. We made a simple modification to input the source and receiver coordinates directly in grid points.
3. The original code supports a search over an initial coarse grid to find a preliminary location, and then interpolates the residuals to a finer scale for the final location. Unfortunately, this part of the code will not work when the grid is reduced to two dimensions so we had to disable it. In the future we plan to modify or replace this portion of the code with an algorithm which will work in two dimensions.
4. The original code can output a file of the residuals at each grid point which can then be contoured to assess the resolution of the location. For some purposes, horizontal and vertical error bars are preferable, so we modified the code to search through the residuals to find the minimum and maximum distance and depths within a specified tolerance (i.e. error bars).

10.2.3 Testing:

We used the same code that generated the gridded travel time files for the locator to generate times at the receivers for a variety of models, and in some cases we added gaussian noise to this "data". We then used the algorithm to locate these "events". Some of our observations are as follows:

1. Using a half-space model for a layered structure with strong velocity contrasts can lead to significant mislocations, as shown in Figure 93 which plots mislocation vectors for 441 grid points. The "data" were generated using the layered velocity model shown, but the events were located using a half-space model. (NOTE: In this and in all other mislocation vector plots, the very large vectors for grid points at horizontal distances of 100 feet and less should be disregarded: due to the symmetry of the model, these vectors incorrectly point to mirror image locations on the wrong side of the receivers and therefore are deceptively large.) The magnitudes of the mislocations increase with distance from the receivers so mislocations are not very significant (< 10 feet) for events within a few hundred feet of the receivers.
2. Addition of gaussian noise to travel time "data" to simulate a picking accuracy of "one or two points" does not have a significant effect if P and S data are both used but will drastically effect locations with

P data alone. Figure 94 illustrates the effects of noise on the locations. Data were generated using layered velocity model shown and then modified to fit a gaussian distribution around the true times. (a) Mislocation vectors for locations using P data only. (b) Same but with P and S data.

3. For a small aperture (a total of 50 feet) like the one used to record data at MWX, use of S data is essential to get reasonable locations regardless of the velocity model used.
4. Significantly larger aperture (>400 feet) would be needed to yield acceptable locations with P data alone, particularly if the "data" is noisy. Figure 95 shows the same plot as Figure 3, but the receiver spacing (receivers are shown as triangles) has been widened to 100 feet.

10.2.4 Calibration Shots:

After emplacement of the receivers in the borehole, calibration shots were set off in a nearby borehole (211 feet away) to determine the in situ orientation of the horizontal components. In order to evaluate the true accuracy or the location technique, we located these known events. We used both the best layered and best half-space model but found very little difference in the results, presumably because the events are so close. The results for the layered model are shown in Figure 96. Generally, the results are acceptable, though we note that the quality of the locations degrades as the ray paths become less horizontal.

Microfracture Locations:

This code will be used in 1995 to examine the "A" sand microseismic results and all additional testing at M-Site. In addition, we will begin to evaluate different ideas for using this code in a near-real-time field mode.

11.0 OTHER DIAGNOSTIC TASKS

11.1 H/Z Conversion

To implement the H/Z analysis for GRI sponsored research, Sandia contracted Craig Woerpel to modify the source codes for PC use. Craig Woerpel wrote most of the original FORTRAN code that was developed for H/Z and microseismic analyses. Final versions of these codes were received in May. In addition, Jim Fix is under contract with Sandia to aid in any H/Z analyses.

11.2 Receiver Configuration

One of the most important aspects of diagnostic technology is determining an optimum receiver configuration for fracture diagnostic measurements. It is assumed that most industry tests will have only one well available, either the treatment well or an offset within a reasonable distance (<2000 ft). Thus, most of our efforts have focused on single-well diagnostic measurements. Since the treatment well is a harsh environment with many restrictions on tool placement, initial activities have focused on offset wells where techniques can be developed.

Based upon the M-Site testing, it is clear that multi-level technology is required for accurate fracture diagnostics in a single well. In the "A" sand tests, the close spacing of the receivers made it difficult to use move-out information to locate microseismic events. As a result, we have concentrated on helping BOLT Technologies Inc develop longer interconnects for the five level system. This help has included telemetry testing of the longer interconnect distances, design of cables and cable heads, and reformatting some of the telemetry circuitry to accept and process the data from such and array. At the end of the fiscal year, a five-level, 50-ft-interconnect array was functional and will be used in upcoming M-Site experiments. Longer interconnects are currently being considered.

11.3 Industry Partner for Seismic-Based Diagnostics

GRI and Sandia have begun the process for obtaining an industrial partner to market diagnostic technology developed under this contract. Norm Warpinski, along with Steve Wolhart and Ed Smalley of GRI visited and made presentations at five service companies that expressed initial interest in becoming a diagnostic partner. Final decisions on the GRI partner will be made in 1995.

12.0 REFERENCES

1. Warpinski, N.R., Teufel, L.W., Lorenz, J.C. and Holcomb, D.J., "Core Based Stress Measurements: A Guide to Their Application," GRI-93/0270, June 1993.
2. Hill, R.E, Peterson, R.E., Warpinski, N.R., Lorenz, J. and Teufel, L.W., "Techniques for Determining Subsurface Stress Direction and Assessing Hydraulic Fracture Azimuth," GRI-93/0429, November 1993.
3. Holcomb, D. J., "Observations of the Kaiser Effect Under Multiaxial Stress States: Implications for Its Use in Determining In Situ Stress", Geophys. Res. Lett., 20, pp. 2119-2122, 1993a
4. Holcomb, D. J., "General Theory of the Kaiser Effect", Int. J. Rock Mech. Min. Sci. \& Geomech. Abs., 30, pp. 929-935, 1993b
5. Sleefe, G.E. and Engler, B.P., "Experimental Study of an Advanced Three-Component borehole Seismic Receiver," Proceedings, 61st Annual SEG Meeting, Houston, TX, pp. 30-33, 1991.
6. Fix, J.E., et al., "Development of Microseismic Methods to Determine Hydraulic Fracture Dimensions," GRI-89/0116, GRI Annual Report, 148 pp., 1989.
7. Fix, J.E. et al., "Investigation of Induced Microseismicity in Hydraulically Fractured Gas Wells, Final Report," GRI-91/0031, GRI Final Report, 128 pp., December 1992.
8. Mahrer, K.D., "Microseismic Logging: A New Hydraulic Fracture Diagnostic Method," SPE 21834, Proc. SPE Rocky Mt. Reg./Low Permeability Symp., Denver, CO, 287-298, April 15-17, 1991.
9. Albright, J.N. and Pearson, C.F., "Acoustic Emissions as a Tool for Hydraulic Fracture Location: Experience at the Fenton Hill Hot Dry Rock Site," *SPEJ*, Vol. 22, 523-530, August 1982.
10. Dobecki, T. L., "Hydraulic Fracture Orientation Using Passive Borehole Seismics," SPE 12110, Proc. 58th Annual Tech. Conf. of SPE, San Francisco, CA, October 5-8, 1983.
11. Jaeger, J.C. and Cook, N.G.W., *Fundamentals of Rock Mechanics*, 2nd Ed. Halsted Press, New York, 1976.
12. Westergaard, H.M., "Bearing Pressures and Cracks," *J Applied Mech.*, Vol. 6, A-49-A-53, June 1939.
13. Sneddon, I.N., "The Distribution of Stress in the Neighourhood of a Crack in an Elastic Solid," *Proc. Roy. Soc.*, Vol. 187, 229-260, 1946.
14. Warpinski, N.R. and Teufel, L.W., "Influence of Geologic Discontinuities on Hydraulic Fracture Propagation," *JPT*, Vol. 39, 209-220, Feb. 1987.
15. Howard, G.C. and Fast, C.R., *Hydraulic Fracturing*, SPE Monograph Vol. 2, Richardson, TX, 1970.
16. Carslaw, H.S. and Jaeger, J.C., *Conduction of Heat in Solids*, 2nd Ed., Oxford Univ. Press, Oxford, 270-272 & 370-371, 1959.
17. Smith, M.B., "Stimulation Design for Short Precise Hydraulic Fractures," *SPEJ*, Vol. 25, 371-379, June 1985
18. Daneshy, A.A., "Rock Properties Controlling Hydraulic Fracture Propagation," SPE 5752, Proc. SPE European Spring Mtg., Amsterdam, The Netherlands, April 8-9, 1976.
19. Nelson, P.P. and Glaser, S.D., "AE and Discrete Fracture Propagation in Rock," in *Acoustic Emission/Microseismic Activity in Geologic Structures and Materials*, Proc. of the 4th Conf., H.R. Hardy, Ed., Trans Tech Publications, 117-130, 1989.
20. Warpinski, N.R., "Interpretation of Hydraulic Fracture Mapping Experiments," SPE 27985, Proceedings, Tulsa Centennial Petroleum Engineering Symposium, Tulsa, OK, pp. 291-300, August 1994.
21. Vidale, J.E., "Finite Difference Calculation of Travel Times," *Bulletin of the. Seismological Society of America*, Vol. 78, pp. 2062-2076, 1988.
22. Nelson, G.D. and Vidale, J.E., "Earthquake Locations by 3D Finite Difference Travel Times," *Bulletin of the Seismological Society of America*, Vol. 80, No. 2, pp. 395-410, April 1990.

13.0 MAJOR ACHIEVEMENTS

Major achievements include:

Completion of the core-based stress measurements on the M-Site monitor well core.

Completion of the topical report on outcrop studies of Frontier outcrops. These outcrop studies provide the basis for an explanation of the fracture systems that should be expected in the Frontier formation within the Moxa Arch area.

Completion of modeling efforts on Frontier paleo-stresses.

Completion of the analyses of the multi-level diagnostic experiments in the A sand at M-Site These results provide a map of the hydraulic fractures and their time progression. Auxiliary results include the development of a P-wave tomogram for the "A" sand, and the development of multi-level processing techniques.

Successful design, ordering, assembly and installation of all monitor-well instrumentation and grouting of the instrumentation in position.

Development of processing codes for M-Site and multi-level receiver arrays.

Determination of the source of the surface noise problems at M-Site and the development of an action plan to mitigate the noise effects.

Development of mechanical models of reservoir behavior explaining the source and locations of microseisms developed during hydraulic fracturing.

Modification and application of a seismic analysis code for calculating event locations in a complex velocity field.

14.0 MAJOR PROBLEMS

Two major problems were encountered in 1994. The first problem was the leak in the tiltmeter cables, which forced a two month delay of instrument installation in the monitor well. The second problem was the noise interference found at M-Site, which was affecting all monitor-well instrumentation, but particularly the accelerometers. The sources of the noise were determined, action plans were developed to remedy the problems, and fabrication of some new instrument circuitry were designed and built. The changes to the surface data processing and acquisition system will be evaluated in early 1995.

15.0 CONCLUSIONS

Core-based stress measurements made on the M-Site monitor well "C" sand samples showed unexpected behavior. No anelastic strain recovery was observed and no acoustic emissions were found emanating from the samples. Both these results suggest that no relaxation was taking place only 8-9 hours after core recovery. However, velocity anisotropy and Kaiser effect data show significant microcrack structure and related effects. The results confirm the stress orientation at M-Site, but failed to give any information on stress magnitudes.

Natural fractures are an important element of production from tight rocks in the Moxa Arch region of the Green River basin. Stress modeling in the basin is helping to clarify stress relationships and to show the origin of the stress fields that induced natural fractures to form. The modeling results are being included in a topical report on natural fractures within the basin.

The M-site "A" sand experiment has provided the time evolution of a hydraulic fracture in a layered sedimentary sequence. These results show an asymmetric fracture that first develops within the sandstone interval, later grows upward in a circular fashion, and finally grows downward in the near wellbore region.

Single-well multi-level arrays can be used to accurately image a hydraulic fracture. Processing codes to do this automatically have been developed and are awaiting M-Site testing and optimization.

The M-Site monitor well instrumentation has been successfully installed and checked out. Thirty levels of triaxial accelerometers and 6 levels of biaxial tiltmeters are in position for fracture monitoring. Surface noise problems are currently being addressed.

Models of hydraulic fracturing show that microseisms develop as a result of two types of stress changes within the reservoir. Large shear stresses exist in the vicinity of the fracture tip and these enhanced shear stresses can cause slippage along natural fractures or bedding. Leakoff of fracturing fluid into natural fractures or bedding (or into the formation) will reduce the net normal stress across these planes of weakness, thus allowing the already available shear stress to cause slippage.

16.0 OBJECTIVES AND WORK PLANNED FOR NEXT YEAR

The first objective for 1995 is to complete the modifications of the monitor-well surface instrumentation and begin fracturing experiments.

The objectives of the "B" sand experiments, the first of the two available zones to be tested, are:

- Obtain detailed velocity survey information for event location analyses;
- Conduct multi-well, multi-level fracture diagnostic experiments and test the processing capabilities developed during 1994;
- Compare diagnostic results with model calculations
- Drill and core an intersecting well into the fractures

When the "B" sand tests are completed, the "C" sand experiments will begin with the drilling of an intersecting well prior to fracturing and subsequent fracture experiments. Specific objectives of the "C" sand tests will depend upon the results of the "B" sand experiments.

Work will continue on the optimization of the automatic processing codes for both M-Site and for the multi-level wireline system. This work will also include initial automatic S-wave processing.

Sandia will conduct a feasibility fracture experiment with Mitchell Energy Corporation and possibly with other companies. The objective is to test out the microseismic capabilities in other formations and conditions.

Sandia will work with the industry partner to foster the growth of fracture diagnostic capabilities.

Work on the Green River natural fracture topical report will be completed.

Table 3

ORIENTATION SCAN AZIMUTHS

1993 M-SITE TEST

	LEVEL 1 (TOP)	LEVEL 2	LEVEL 3	LEVEL 4
4800	0.9	-63.8	81.1	78.7
4810	4.0	-78.6	82.3	77.2
4820	1.1	-72.5	81.2	76.2
4830	-3.6	-70.0	75.3	79.6
4840	-2.8	-66.1	78.5	79.6
4850	-1.2	-67.5	79.0	91.3
4860	-2.1	-67.2	88.7	86.5
4870	-4.5	-65.8	80.4	82.1
4880	-2.5	-68.1	86.9	79.6
4890	4.4	-66.5	88.9	84.4
4900	-5.2	-68.7	88.3	81.9
4910	-0.9	-72.4	83.8	83.4
4920	-5.0	-69.3	82.4	84.1
4930	0.5	-74.0	88.3	85.2
4940	-1.0	-70.3	87.8	86.7
4950	0.7	-68.8	90.7	84.2
4960	0.9	-69.8	94.5	80.8
4970	2.2	-68.3	89.0	85.6
4980	2.5	-69.1	89.2	81.3
4990	5.7	-67.5	91.3	84.8
5000	1.3	-65.9	93.2	84.0
5010	10.3	-64.7	95.4	84.1
AVG	-0.2	-68.9	86.2	82.8
ST DEV	3.1	3.3	5.5	3.5

Table 5..Velocity structure data

Depth (ft)	P-wave velocity (ft/msec)
4520	14.45424
4540	14.92292
4560	15.1862
4580	14.48456
4600	13.731
4620	14.82712
4640	14.11968
4660	13.9454
4680	15.0866
4700	14.92232
4720	13.65736
4740	13.78788
4760	14.95732
4780	14.77272
4800	14.55048
4820	14.89892
4840	15.1826
4860	15.02352
4880	14.98412
4900	15.23664
4920	14.54124
4940	15.5742
4960	14.52232
4980	14.93552
5000	14.84224

Table 6. Reduced velocity structure

Depth (ft)	P-wave velocity (ft/msec)
4600	14.0
4670	15.0
4710	13.7
4750	15.0
4770	14.8
4790	14.6
4810	14.9
4830	15.2
4850	15.0
4890	15.2
4910	14.5
4930	15.6
4950	14.5
4970	14.5
5000	14.9

Table 7

WILCOXON RESEARCH ACCELEROMETERS
MODEL #731-20A
MAXIMUM TRANSVERSE SENSITIVITY = 2% OF AXIAL
MAXIMUM AMPLITUDE RANGE = 0.2g peak
SENSITIVITY MEASURED AT OUTPUT OF ACCELEROMETER AT 100 Hz, 0.2g, 25 C

SERIAL NUMBER	SENSITIVITY V/g	BIAS OUTPUT VOLTAGE (VDC)	RESONANCE FREQUENCY (Hz)	+or - 3dB	POD #	ORIENTATION
203	20.1	10.1	2060.0	1120.0	1	H1
217	20.3	10.2	2160.0	1140.0	1	H2
198	20.6	10.2	2140.0	1140.0	1	V
170	20.4	10.1	2220.0	1240.0	2	H1
250	20.4	9.6	2220.0	1280.0	2	H2
213	19.7	10.1	2140.0	1240.0	2	V
207	19.1	10.0	2120.0	1160.0	3	H1
218	19.2	10.2	2120.0	1160.0	3	H2
190	19.4	9.9	2140.0	1160.0	3	V
245	20.5	9.8	2200.0	1200.0	4	H1
199	20.6	10.1	2220.0	1200.0	4	H2
264	20.3	10.2	2200.0	1200.0	4	V
177	19.9	9.9	2200.0	1200.0	5	H1
173	19.9	10.2	2160.0	1200.0	5	H2
182	19.7	10.0	2220.0	1220.0	5	V
210	19.7	10.2	2160.0	1140.0	6	H1
212	19.7	10.2	2140.0	1140.0	6	H2
181	19.5	10.2	2120.0	1140.0	6	V
194	19.7	10.3	2140.0	1160.0	7	H1
189	19.7	10.1	2220.0	1160.0	7	H2
211	19.9	9.9	2180.0	1160.0	7	V
197	19.9	10.2	2180.0	1160.0	8	H1
174	19.9	10.0	2200.0	1180.0	8	H2
176	20.0	10.2	2180.0	1180.0	8	V
201	19.4	10.0	2200.0	1200.0	9	H1
254	19.4	9.7	2200.0	1200.0	9	H2
209	19.3	10.1	2240.0	1200.0	9	V
178	19.5	9.9	2200.0	1200.0	10	H1
168	19.5	9.8	2200.0	1200.0	10	H2
222	19.4	10.1	2240.0	1200.0	10	V
234	20.0	10.1	2120.0	1100.0	11	H1
214	20.0	10.2	2060.0	1100.0	11	H2
263	20.0	10.3	2120.0	1120.0	11	V
225	21.0	10.2	2120.0	1140.0	12	H1
227	21.0	10.0	2100.0	1140.0	12	H2
247	21.0	9.7	2180.0	1160.0	12	V

Table 7 (cont.)

185	20.2	10.2	2200.0	1160.0	13	H1
200	20.2	10.0	2180.0	1160.0	13	H2
206	20.1	10.0	2120.0	1160.0	13	V
205	19.5	10.1	2180.0	1160.0	14	H1
169	19.5	9.9	2120.0	1160.0	14	H2
191	19.6	10.2	2180.0	1160.0	14	V
239	20.7	9.8	2220.0	1220.0	15	H1
240	20.7	9.9	2200.0	1220.0	15	H2
249	20.6	9.8	2240.0	1220.0	15	V
244	20.7	9.4	2200.0	1200.0	16	H1
215	20.7	10.1	2200.0	1200.0	16	H2
242	20.8	9.7	2200.0	1200.0	16	V
167	20.0	10.1	2200.0	1200.0	17	H1
260	20.0	10.0	2220.0	1200.0	17	H2
186	19.9	9.9	2200.0	1200.0	17	V
252	20.0	10.2	2120.0	1160.0	18	H1
226	20.0	10.2	2140.0	1160.0	18	H2
256	20.0	10.1	2140.0	1160.0	18	V
233	21.0	9.9	2200.0	1200.0	19	H1
255	21.0	10.0	2220.0	1200.0	19	H2
262	21.0	10.0	2240.0	1200.0	19	V
230	20.0	10.2	2100.0	1140.0	20	H1
180	20.0	10.1	2120.0	1140.0	20	H2
232	20.0	10.1	2120.0	1140.0	20	V
219	20.8	10.2	2160.0	1160.0	21	H1
195	20.8	10.1	2140.0	1160.0	21	H2
166	20.7	10.3	2180.0	1160.0	21	V
172	19.5	10.1	2140.0	1180.0	22	H1
208	19.5	9.9	2200.0	1180.0	22	H2
204	19.6	10.4	2200.0	1180.0	22	V
187	19.4	10.2	2160.0	1180.0	23	H1
216	19.4	10.1	2180.0	1180.0	23	H2
202	19.2	10.2	2140.0	1180.0	23	V
231	21.0	10.2	2100.0	1180.0	24	H1
196	21.0	10.2	2160.0	1180.0	24	H2
235	20.8	10.1	2140.0	1180.0	24	V
241	19.1	10.1	2160.0	1180.0	25	H1
193	19.2	10.1	2200.0	1180.0	25	H2
246	19.0	9.7	2140.0	1180.0	25	V
259	20.3	10.1	2400.0	1160.0	26	H1
192	20.3	10.0	2160.0	1160.0	26	H2
265	20.5	9.9	2080.0	1160.0	26	V

Table 7 (cont.)

165	20.9	10.1	2200.0	1260.0	**27**	**H1**
228	21.0	10.2	2340.0	1260.0	**27**	**H2**
238	21.1	10.1	2200.0	1280.0	**27**	**V**
223	20.2	10.0	2200.0	1220.0	**28**	**H1**
236	20.3	9.8	2220.0	1220.0	**28**	**H2**
183	20.0	10.2	2200.0	1220.0	**28**	**V**
251	21.1	9.9	2200.0	1220.0	**29**	**H1**
243	21.2	9.9	2220.0	1240.0	**29**	**H2**
237	21.4	10.1	2220.0	1240.0	**29**	**V**
257	21.0	10.2	2280.0	1300.0	**30**	**H1**
248	21.1	9.9	2400.0	1320.0	**30**	**H2**
171	20.0	10.4	2320.0	1300.0	**30**	**V**
220	20.4	10.1	2180.0	1180.0	**SPARE**	
184	22.3	10.2	2200.0	1220.0	**SPARE**	
229	21.0	10.2	2402.0	1362.0	**SPARE**	
261	20.5	10.0	2140.0	1060.0	**SPARE**	
258	21.5	10.2	2220.0	1160.0	**SPARE**	
188	19.5	10.2	2160.0	1140.0	**SPARE**	
224	18.7	10.2	2200.0	1180.0	**SPARE**	
221	18.2	10.2	2080.0	1140.0	**SPARE**	
179	18.6	10.2	2280.0	1220.0	**SPARE**	
175	19.0	10.1	2220.0	1200.0	**SPARE**	
253						

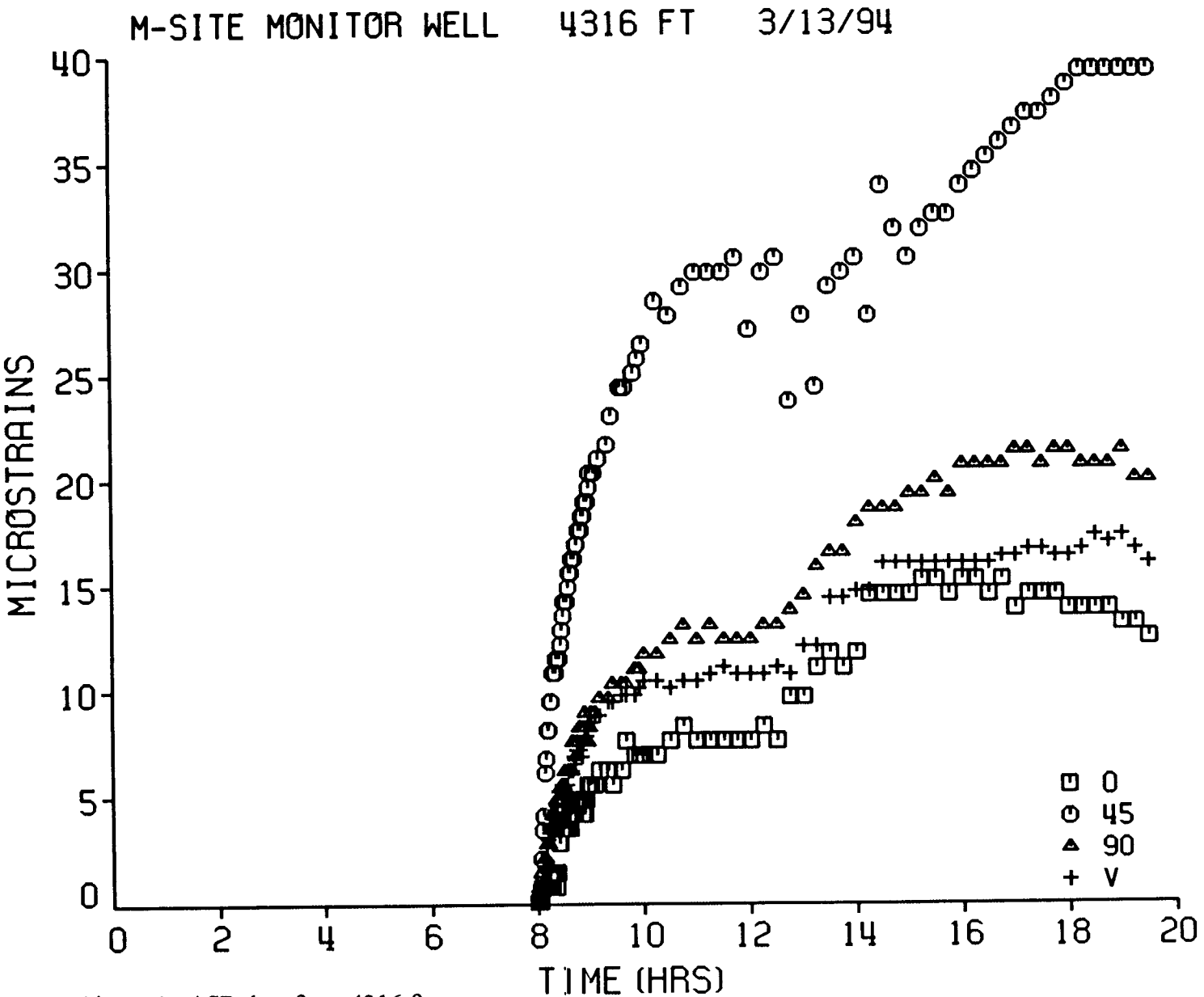

Figure 1. ASR data from 4316 ft.

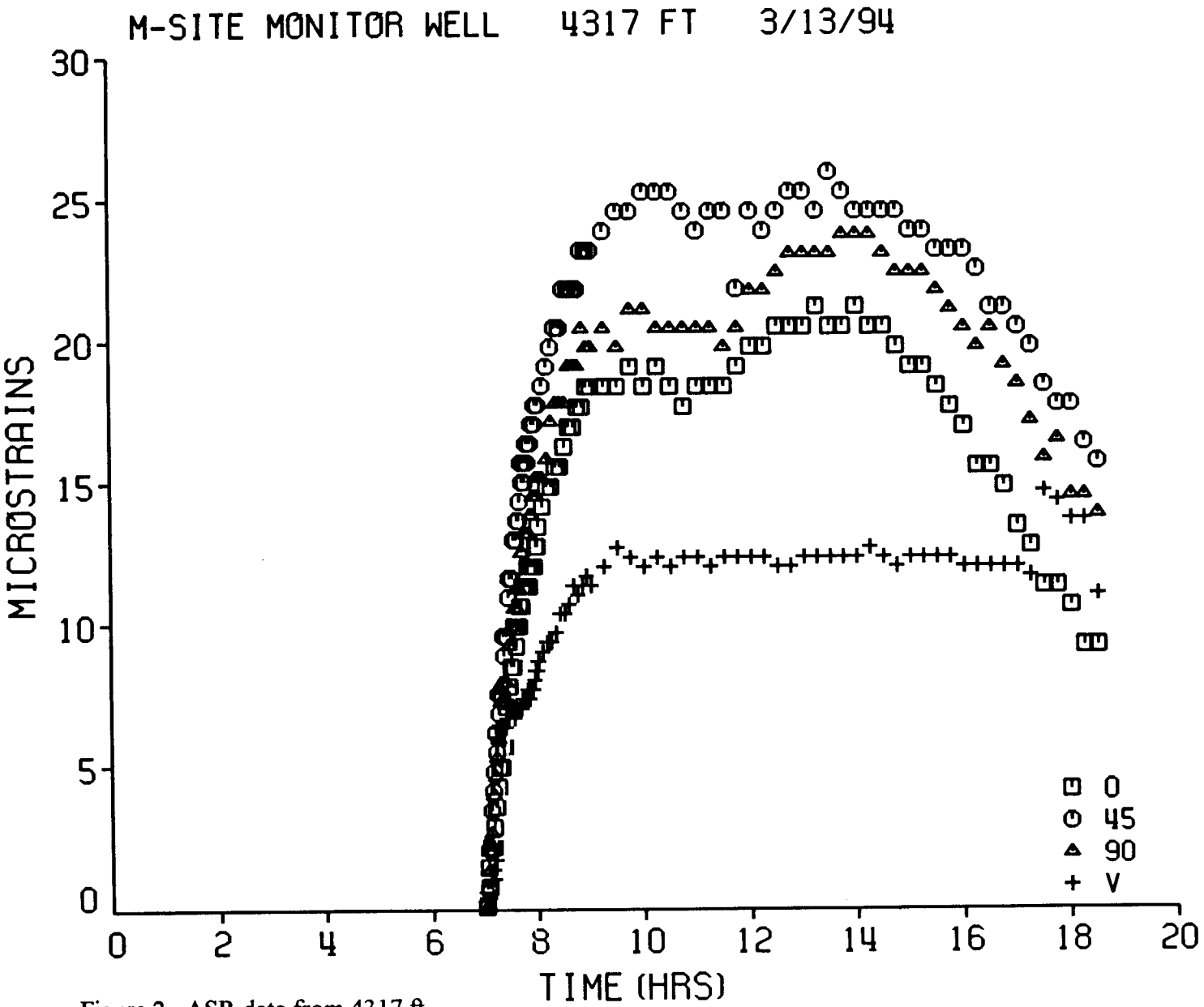

Figure 2. ASR data from 4317 ft.

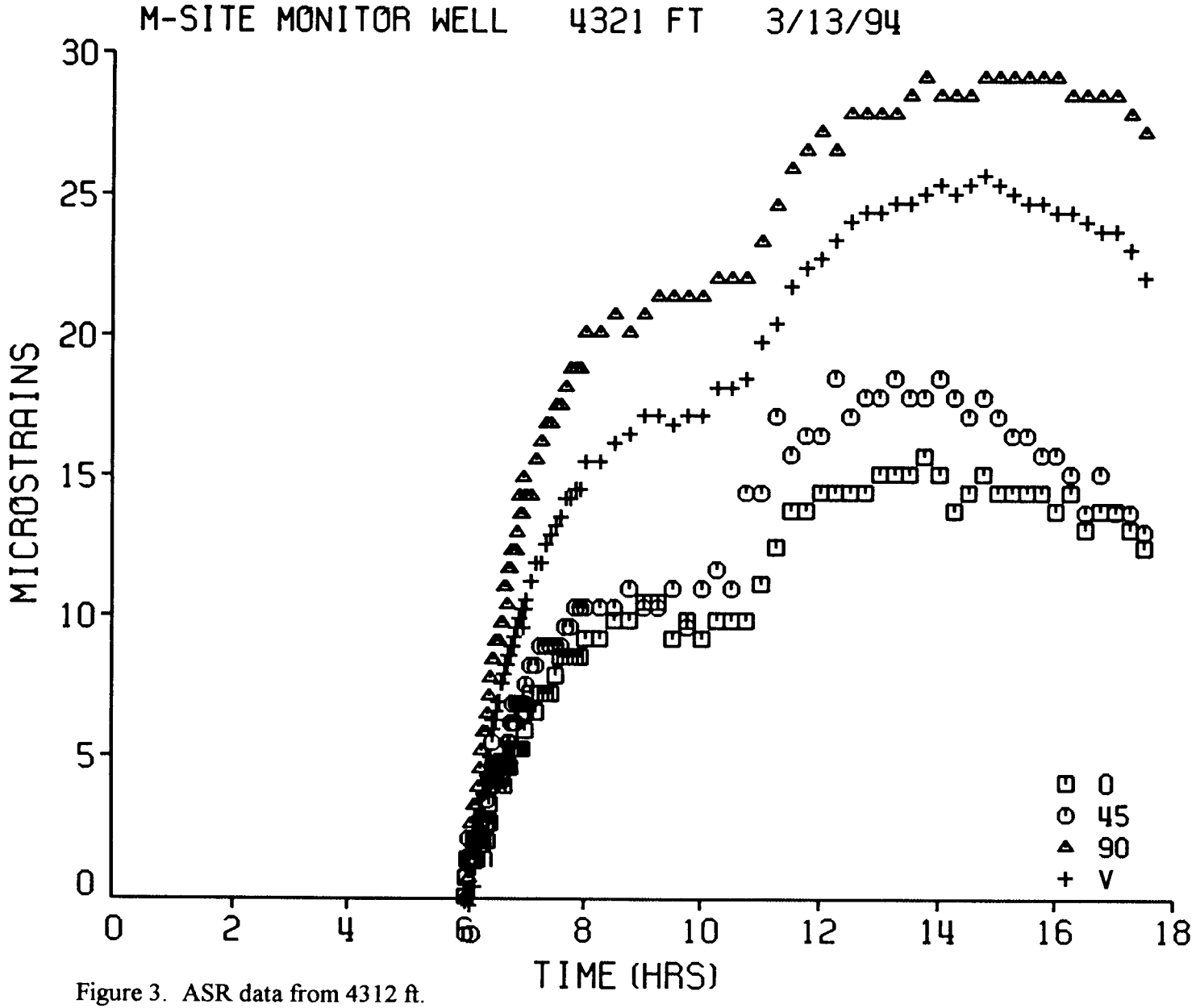

Figure 3. ASR data from 4312 ft.

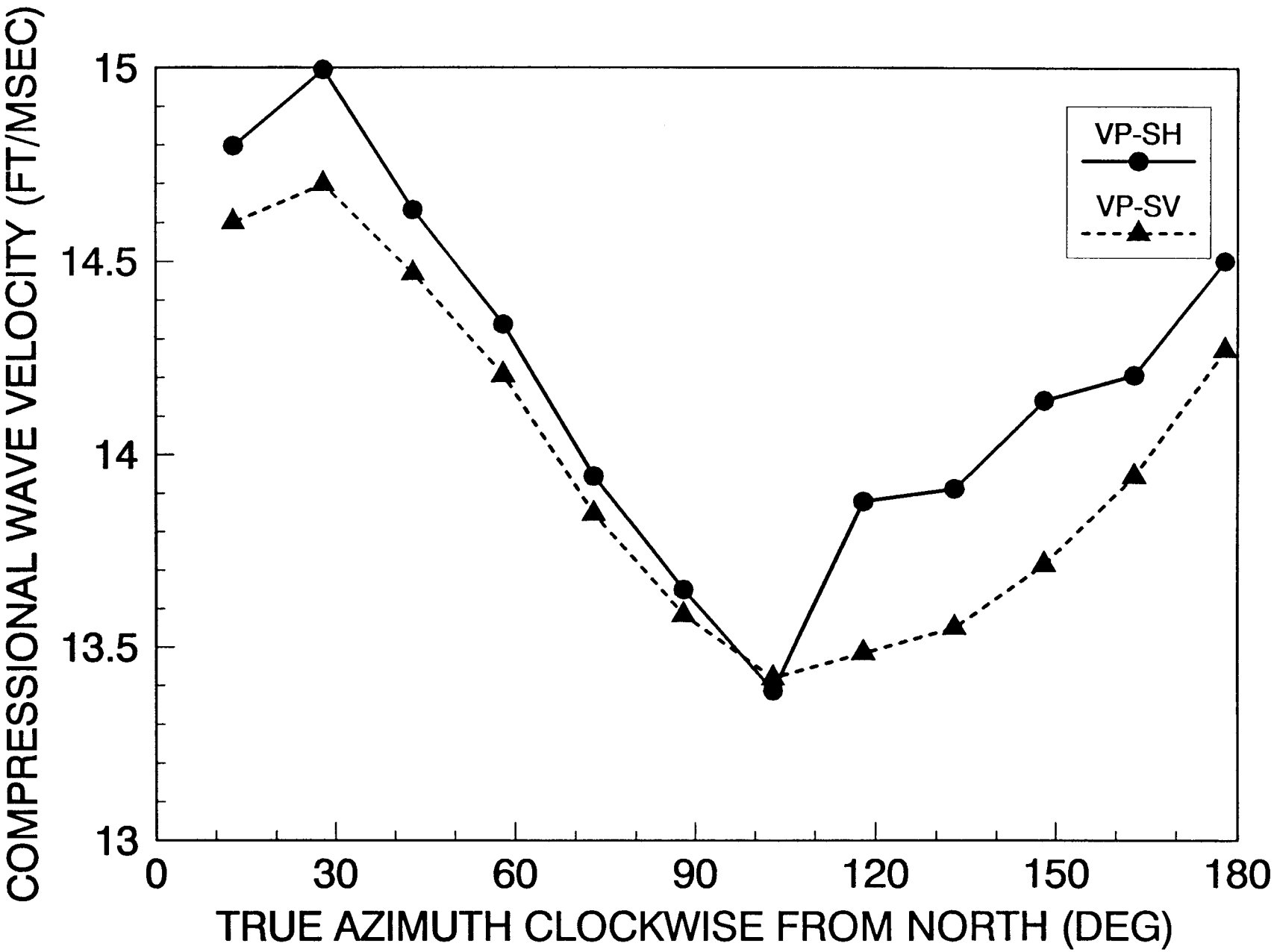

Figure 4. P-wave velocity data from sample #1 at 4314 ft.

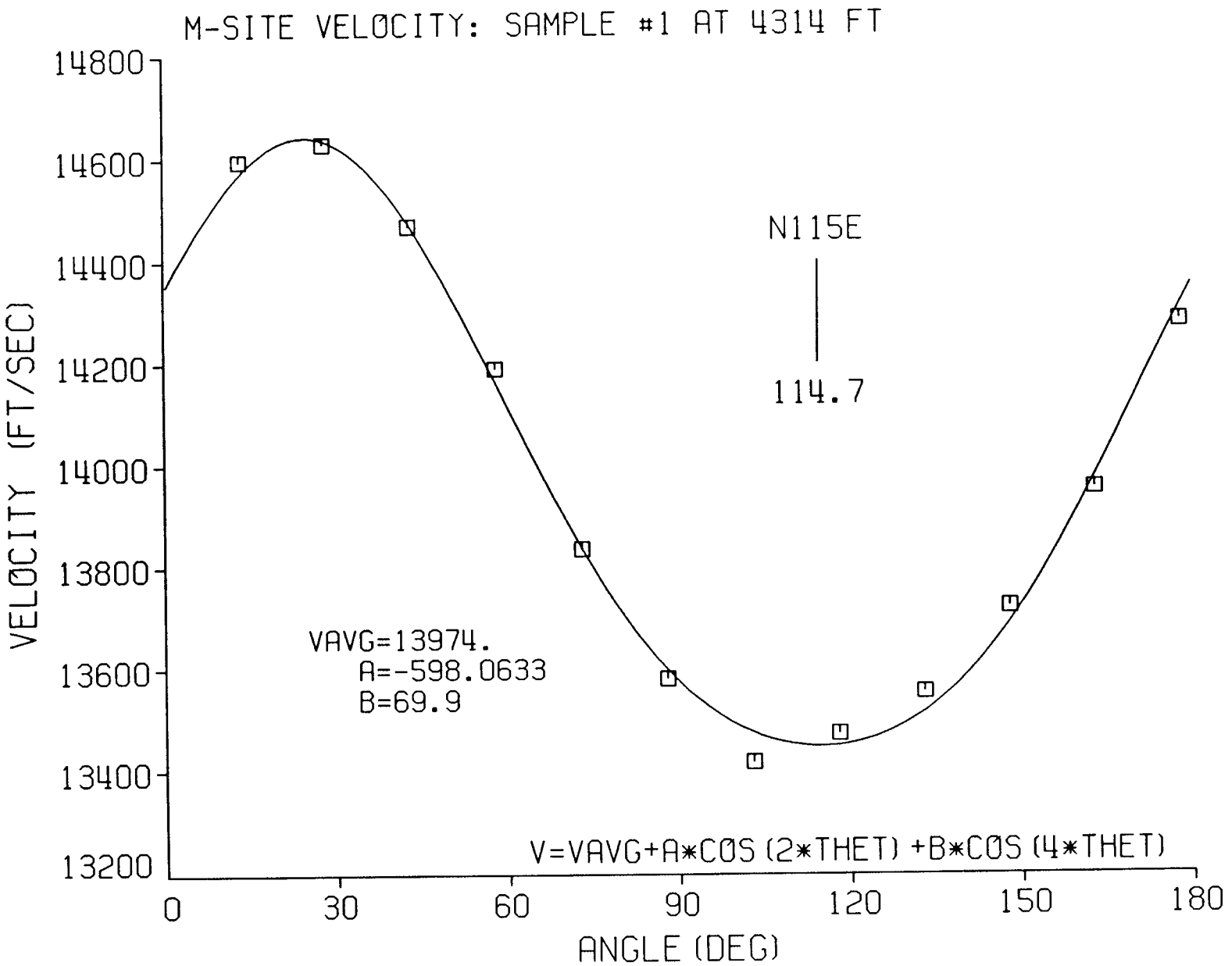

Figure 5. Least-squares fit of sample #1 data.

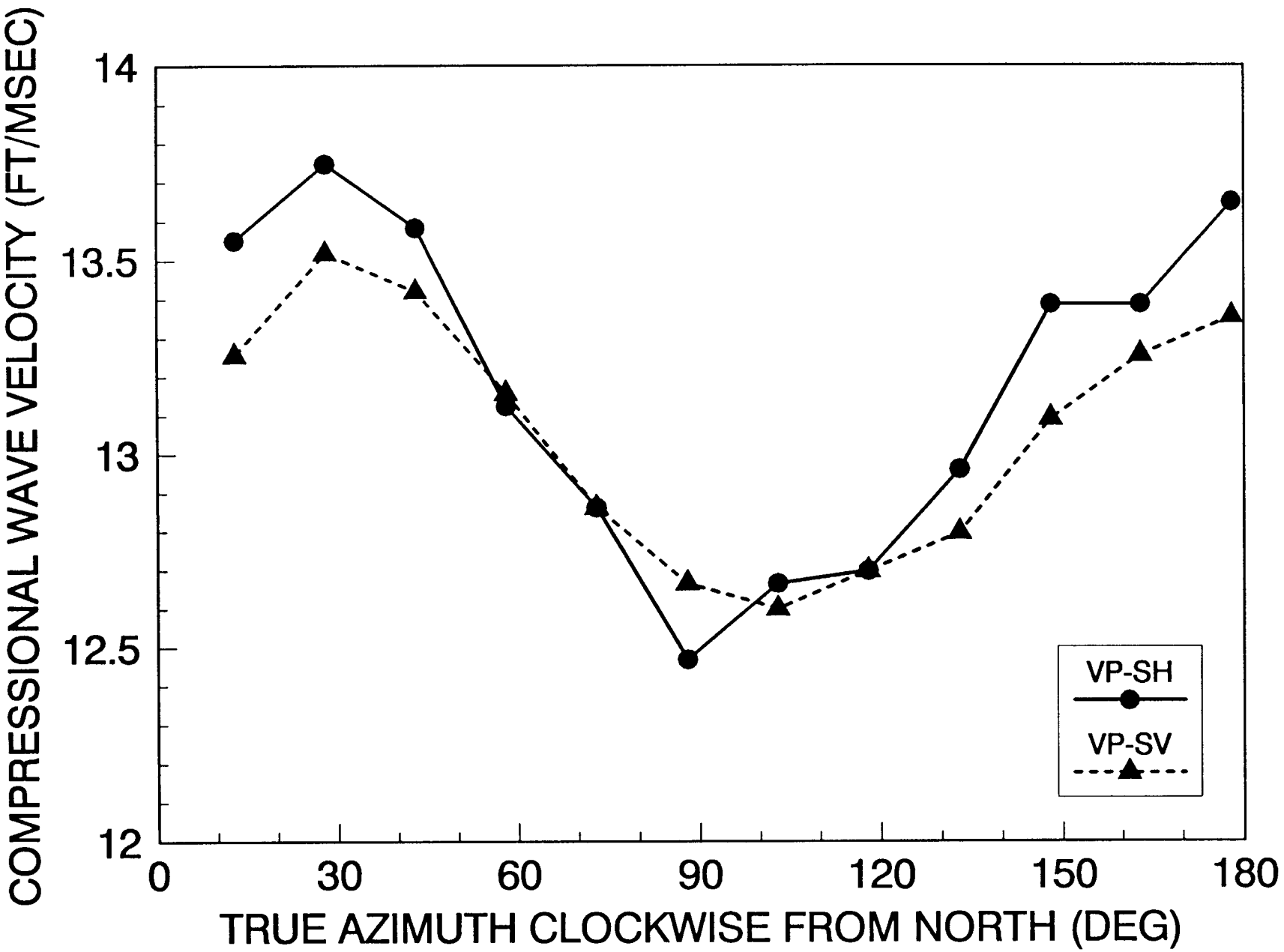

Figure 6. P-wave velocity data from sample #2 at 4314 ft.

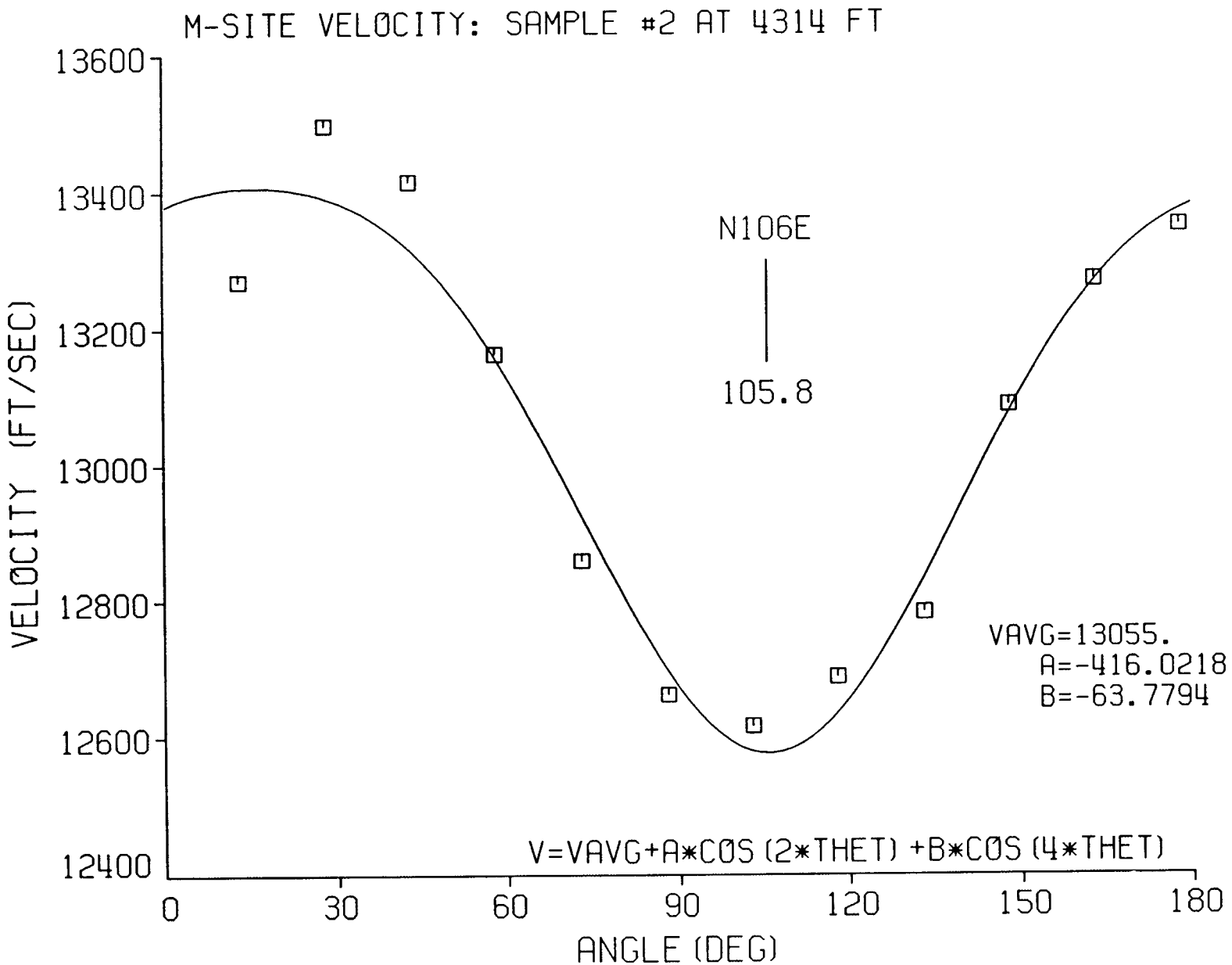

Figure 7. Least-squares fit of sample #2 data.

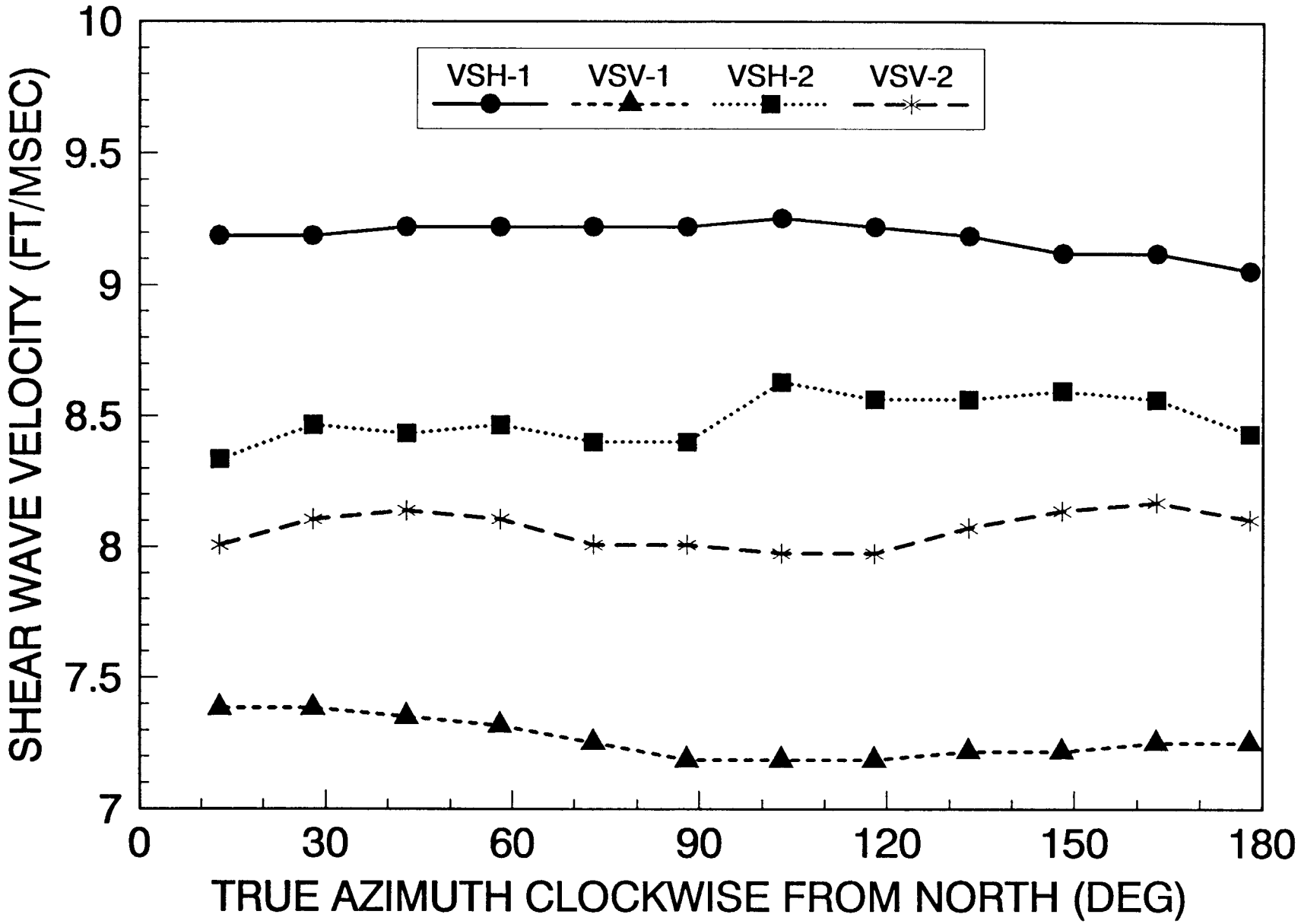

Figure 8. S-wave velocity data from both samples at 4314 ft.

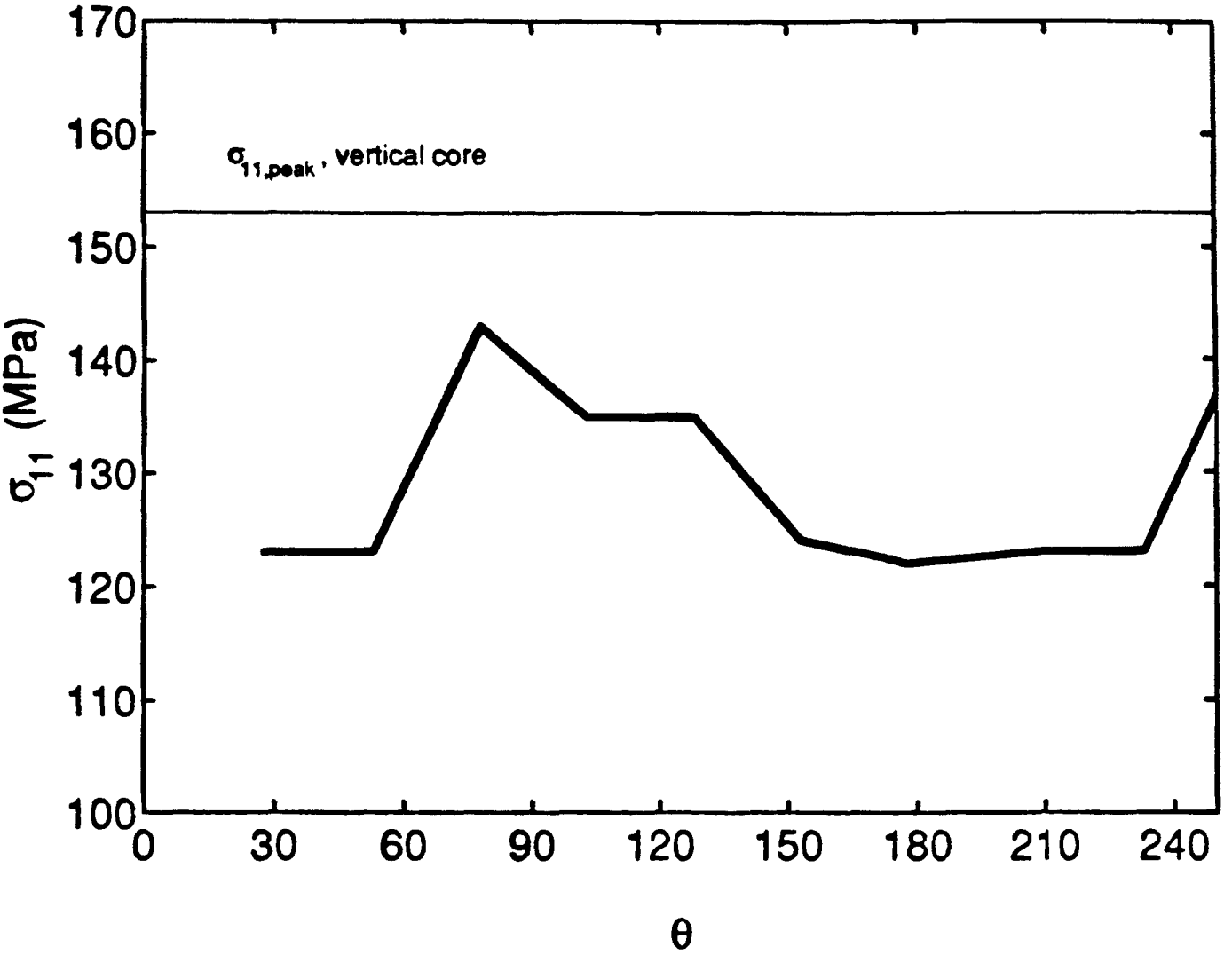

Figure 9. AE onset for uniaxial tests. The uniaxial stress at the time the AE rate began to increase is plotted for horizontal subcores as a function of the angle of the core axis relative to North. The onset stress for a vertical subcore is also shown as the horizontal line.

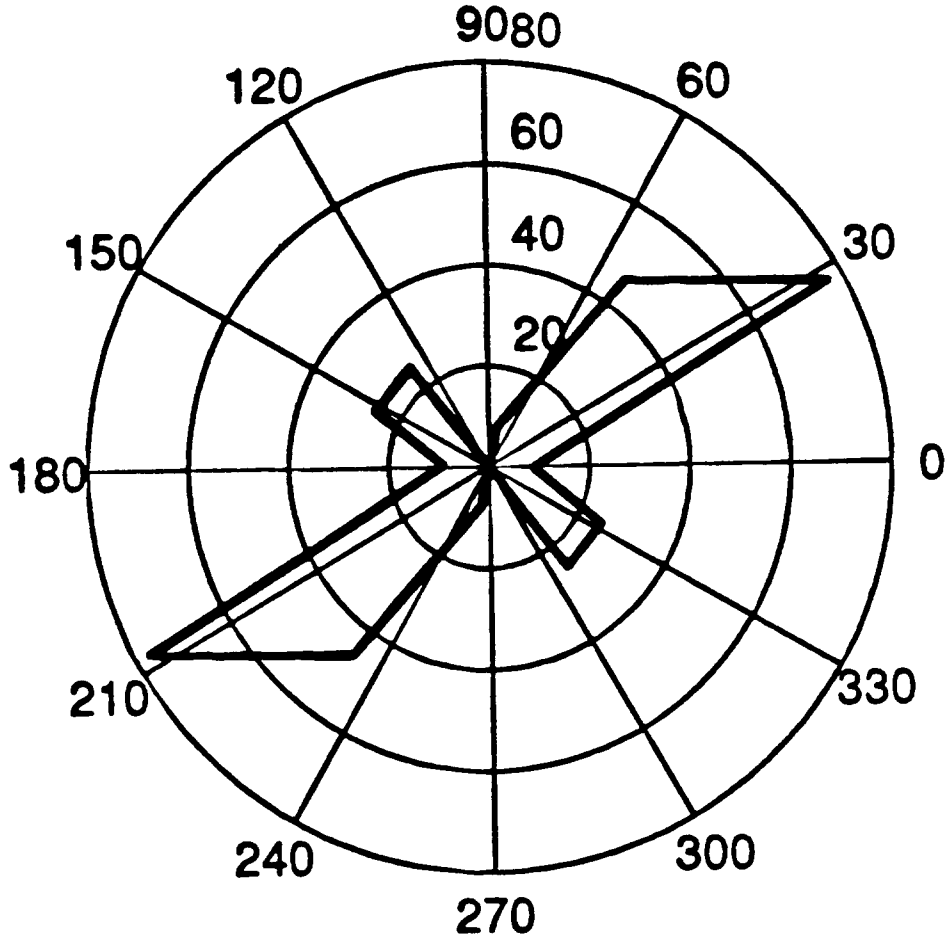

Figure 10. Data from Figure 1, replotted on a polar plot with the minimum stress subtracted off to emphasize the orientation of the anisotropy.

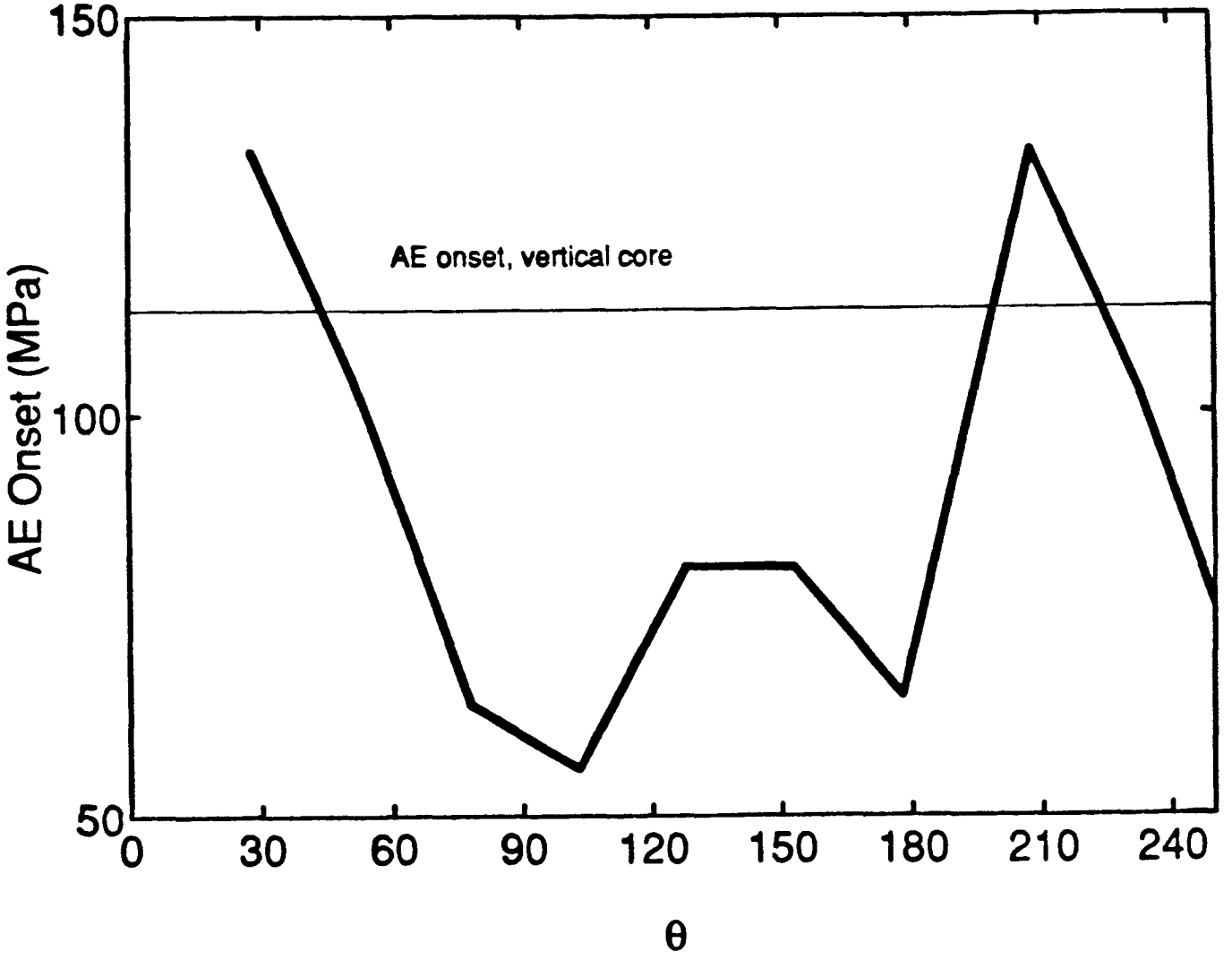

Figure 11. AE onset for extensional tests. The extensional stress at the time the AE rate began to increase is plotted for horizontal subcores as a function of the angle of the core axis relative to North. The onset stress for a vertical subcore is also shown as the horizontal line.

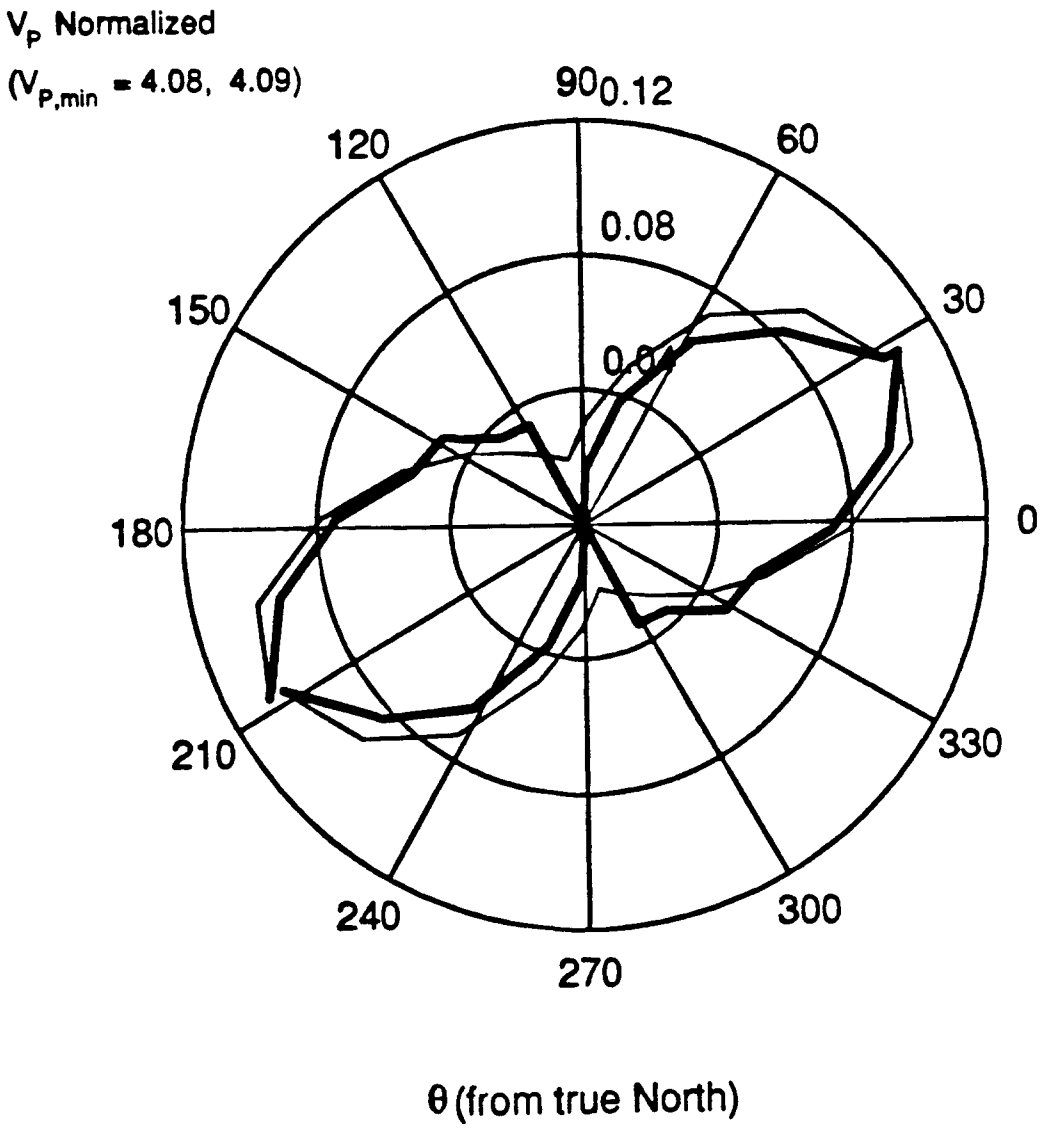

Figure 12. Data from Figure 3, replotted on a polar plot with the minimum stress subtracted off to emphasize the orientation of the anisotropy.

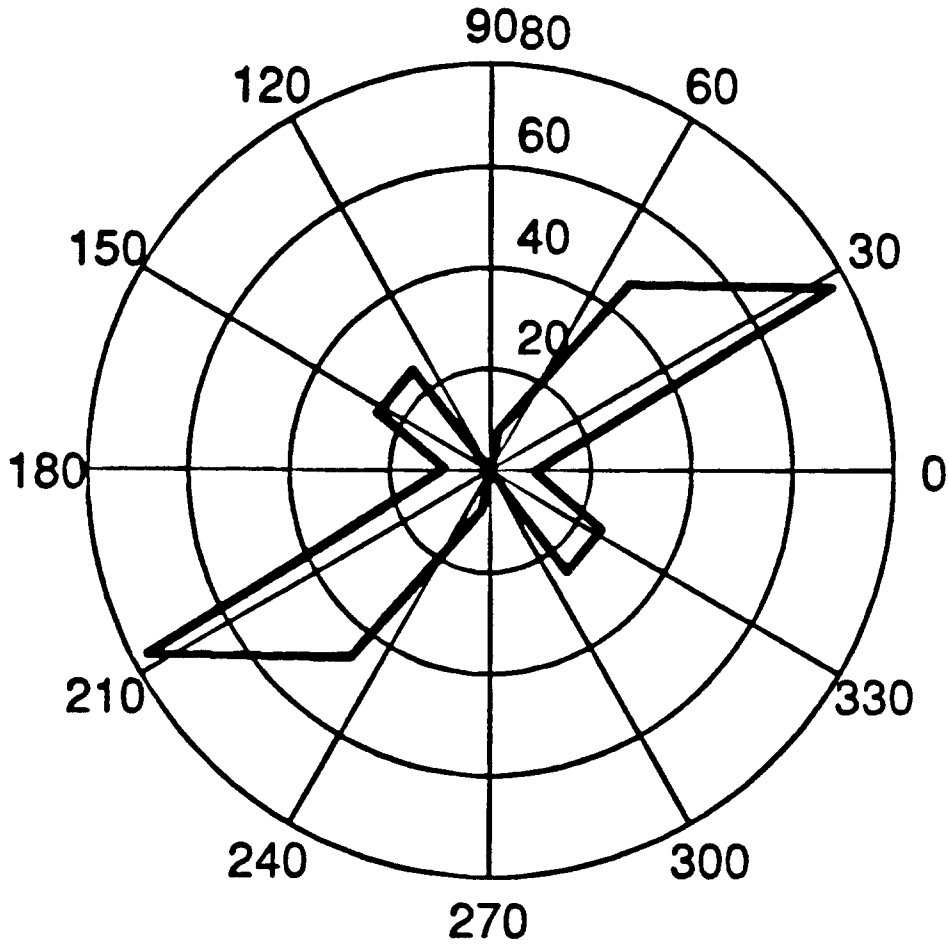

Figure 13. Two independent measurements of compressional wave velocities in the horizontal plane with the minimum velocity subtracted out to produce the characteristic figure eight shape of $cos 2\theta$ dependence. The velocities were normalized to the minimum of 4.08 km/sec. The maximum velocity was at 30 degrees.

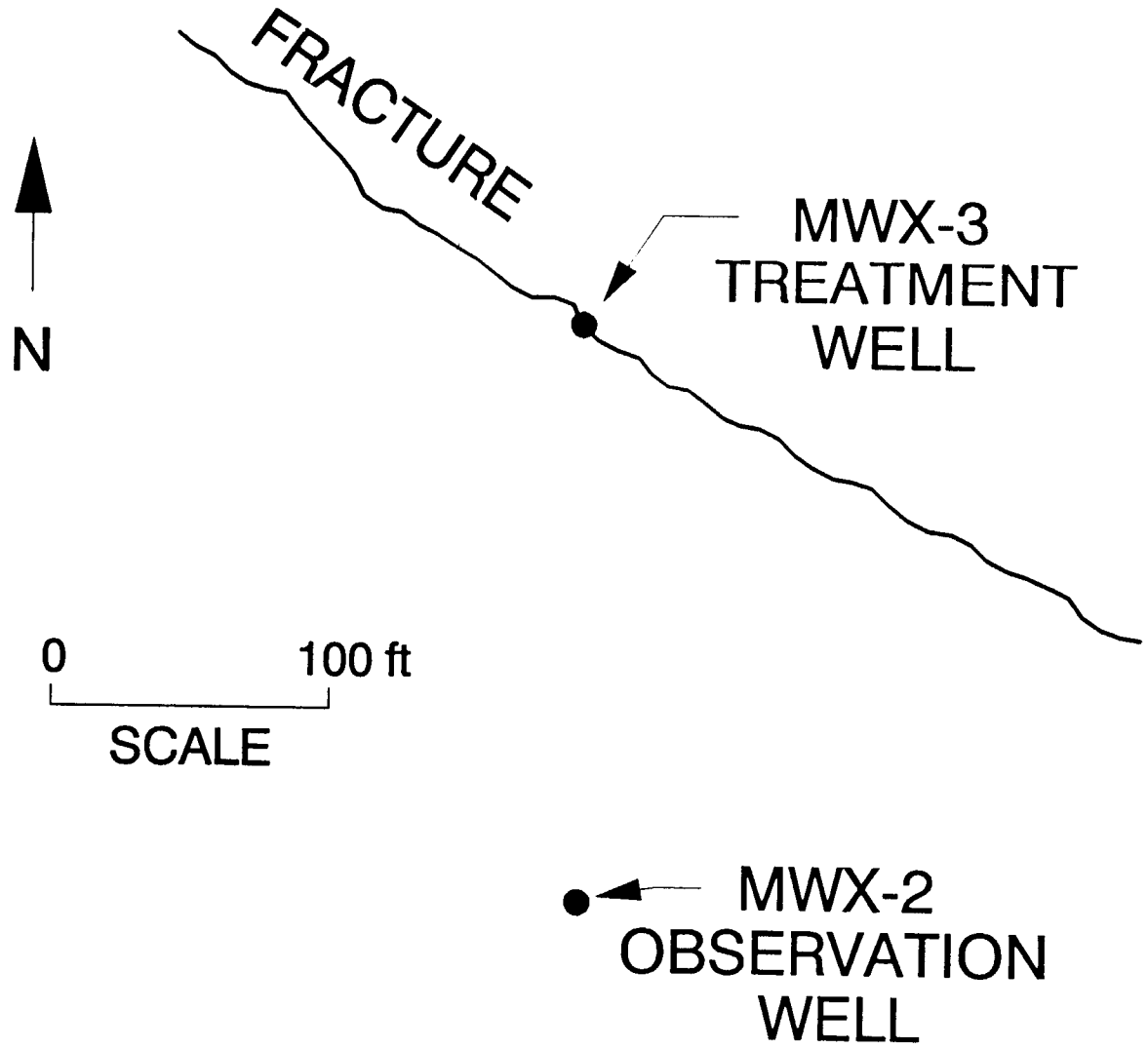

Figure 14 Well layout at M-Site

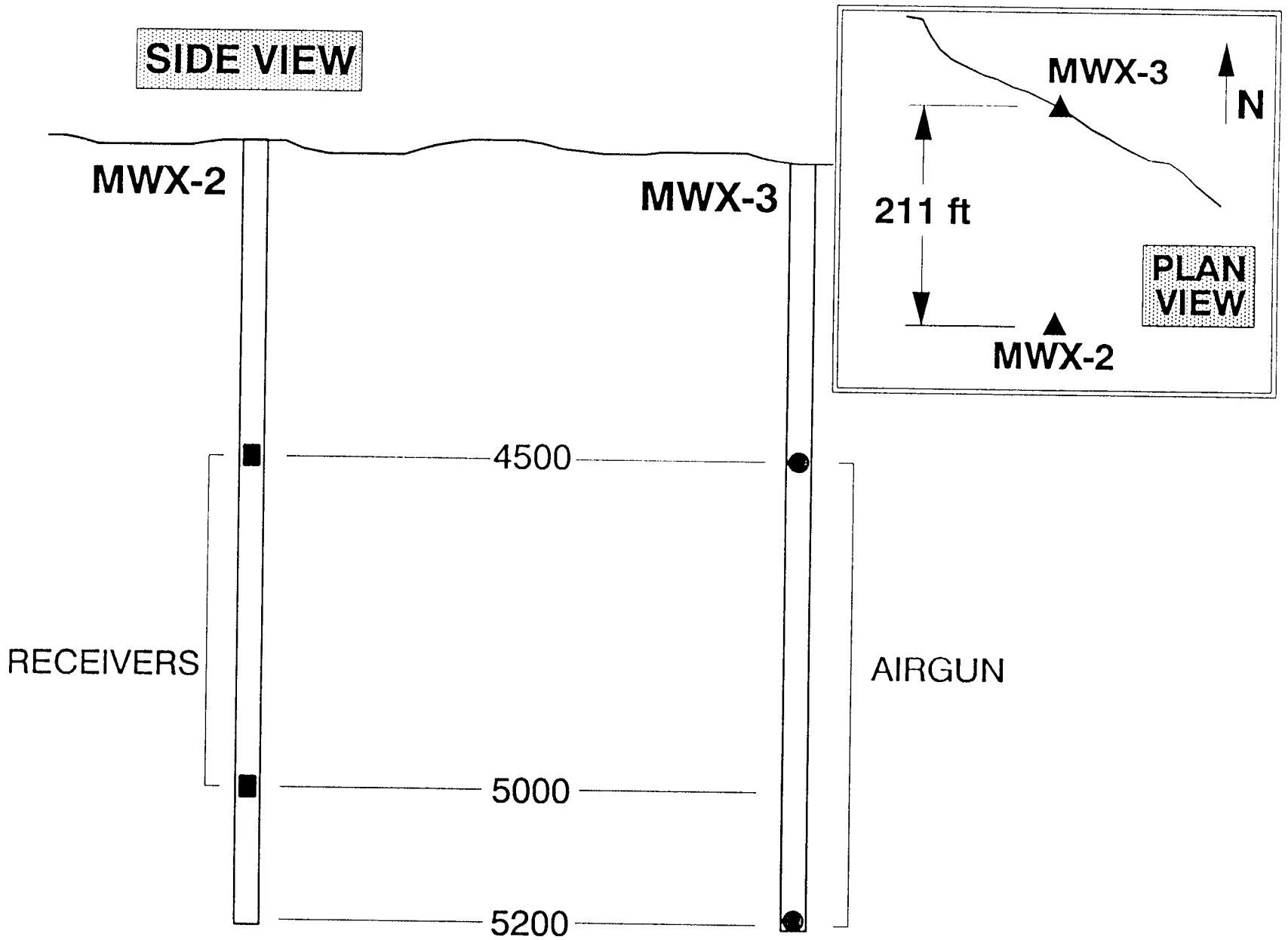

Figure 15 Configuration for velocity survey

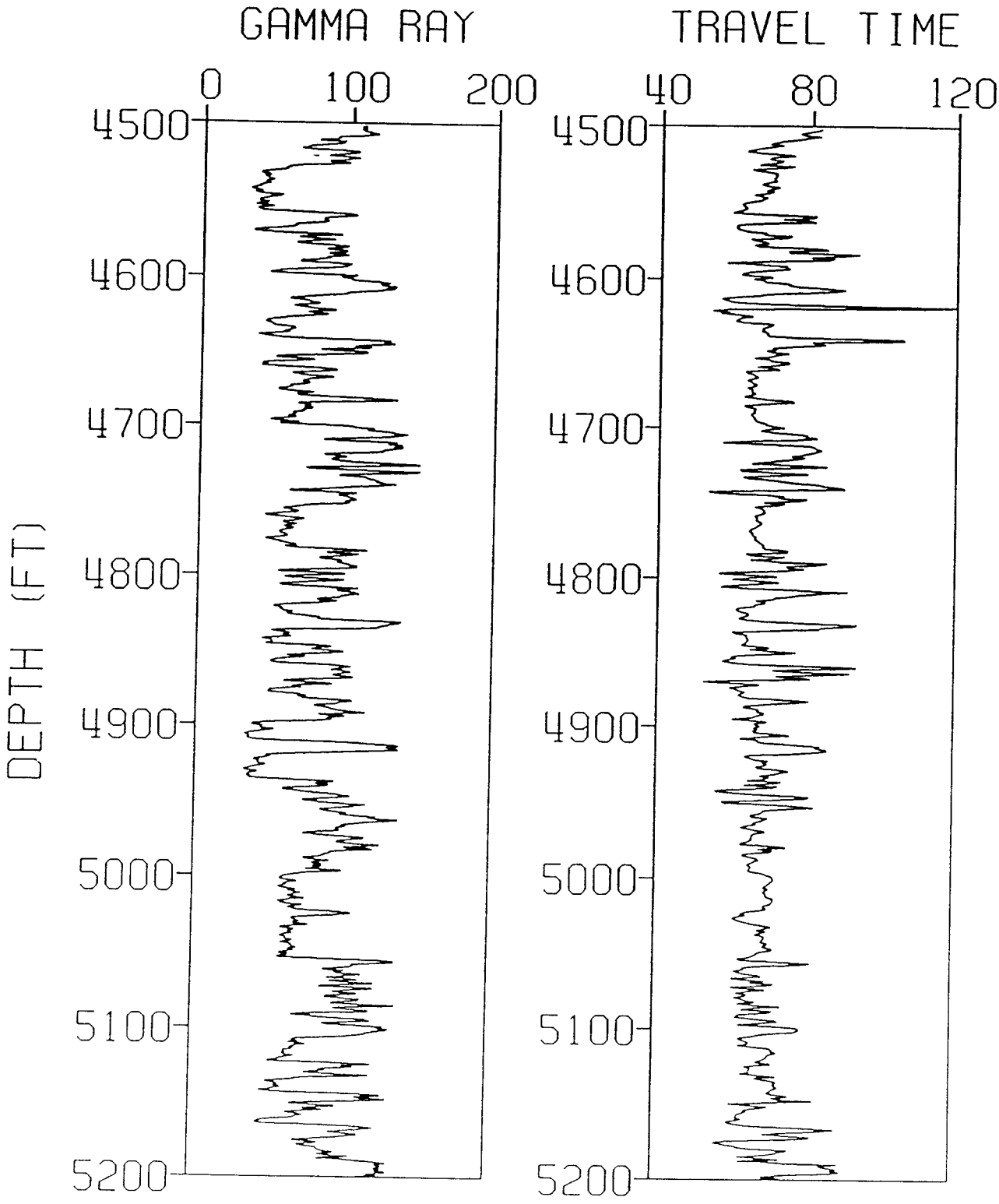

Figure 16 MWX-2 velocity data

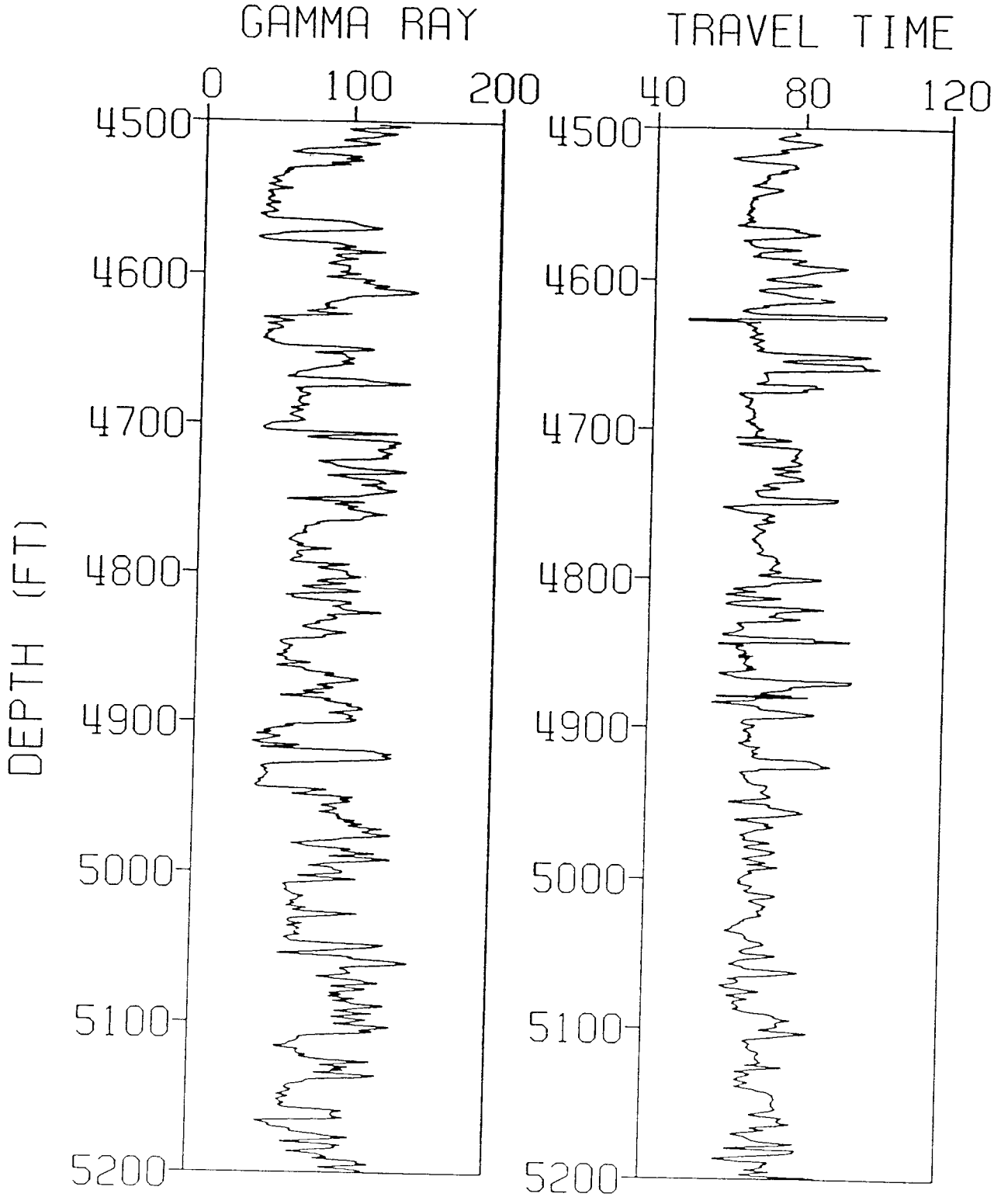

Figure 17 MWX-3 velocity data

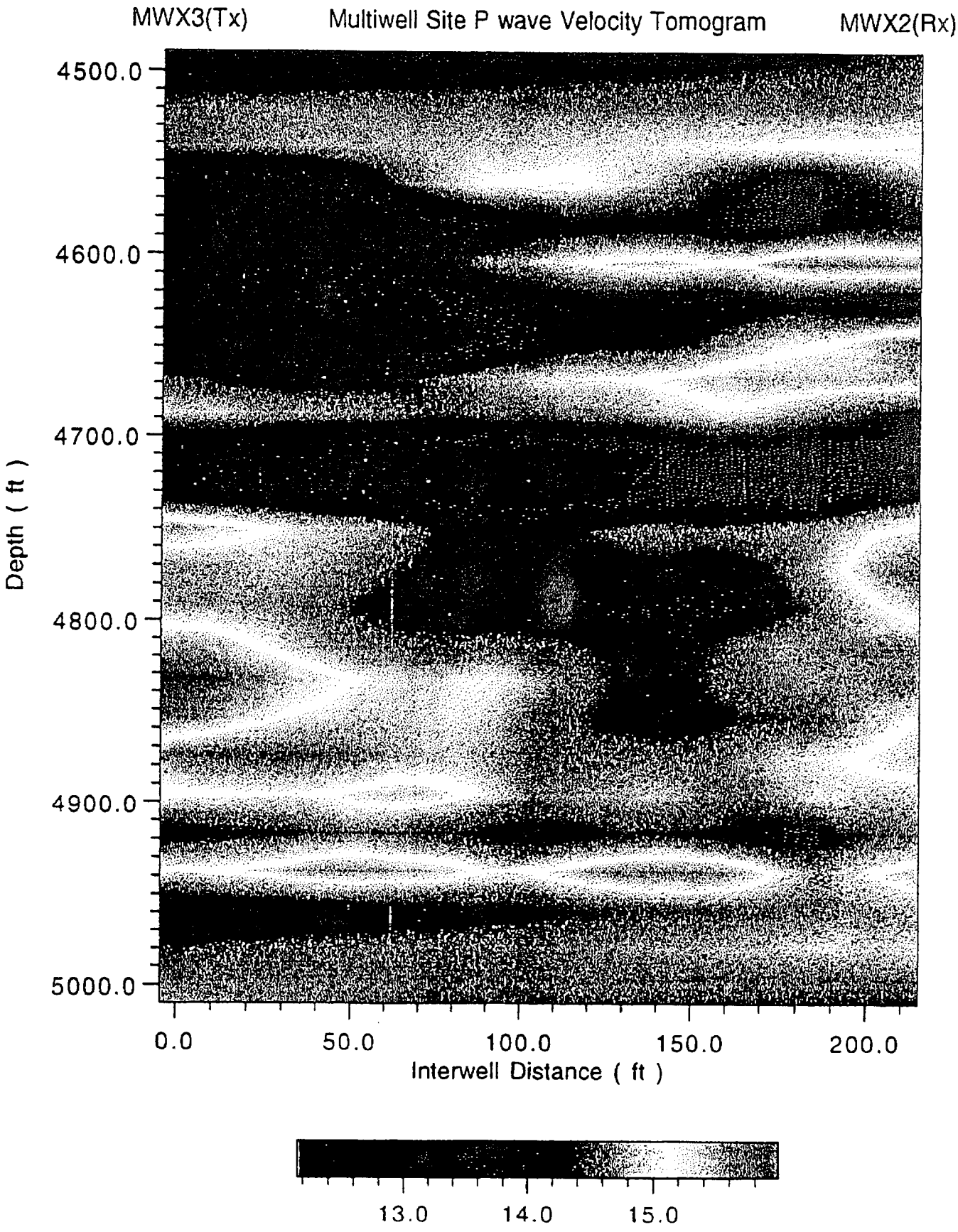

Figure 18 P-wave tomogram

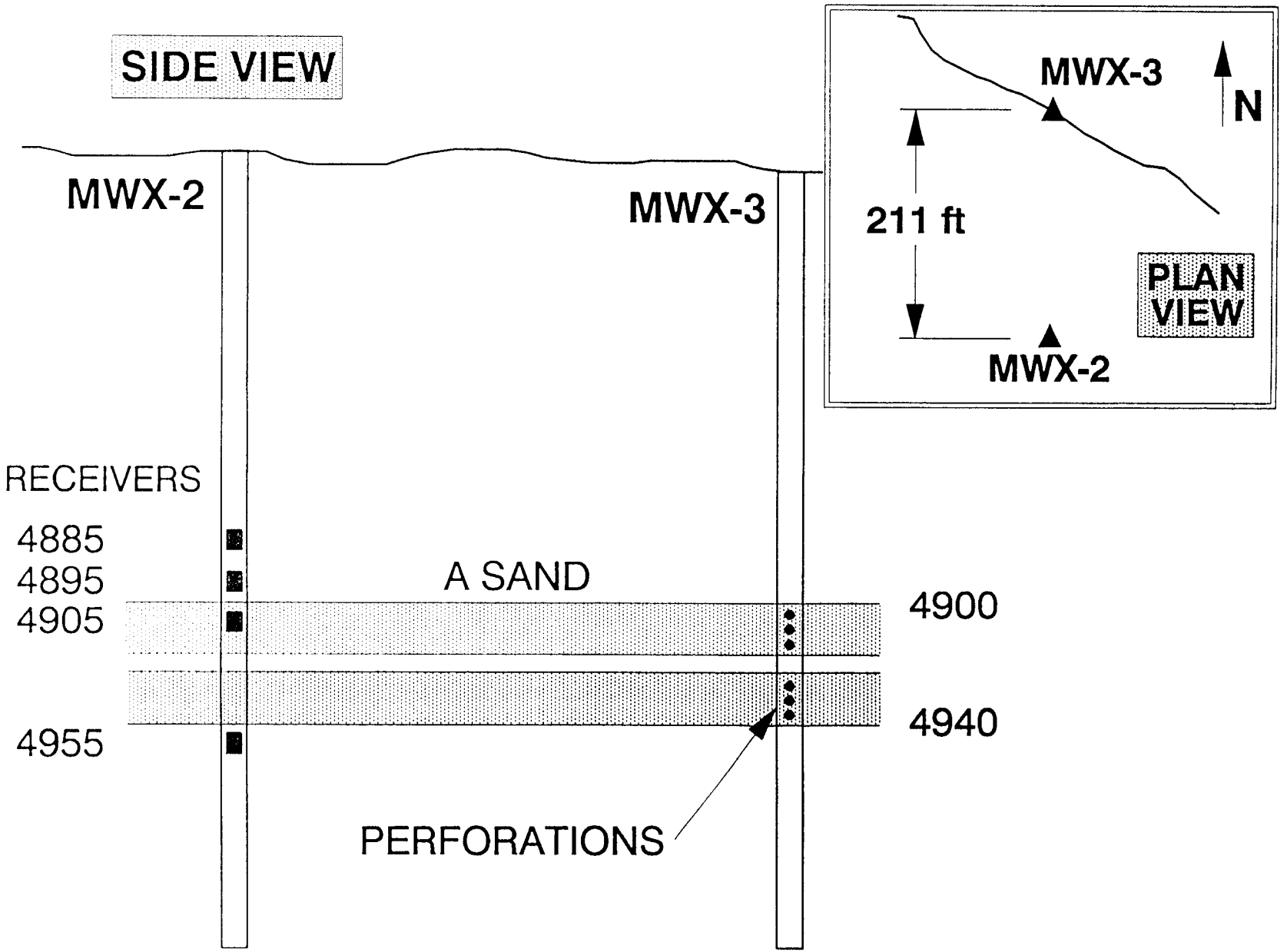

Figure 19 Receiver positions in MWX-2

Orientation Scan: Level 1 - Vertical

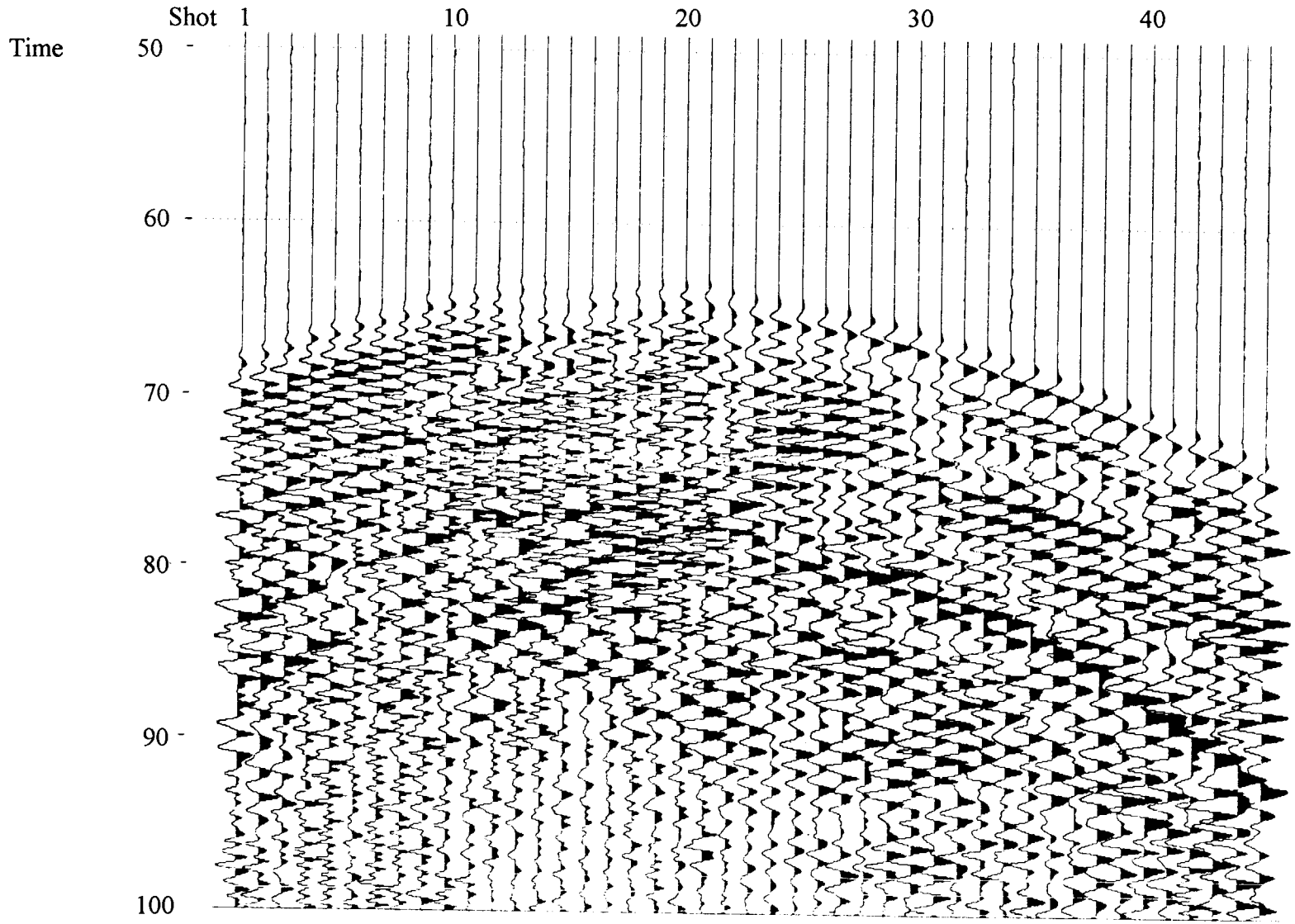

Figure 20 Orientation scan data for vertical axis

Orientation Scan: Level 2 - Horizontal 1

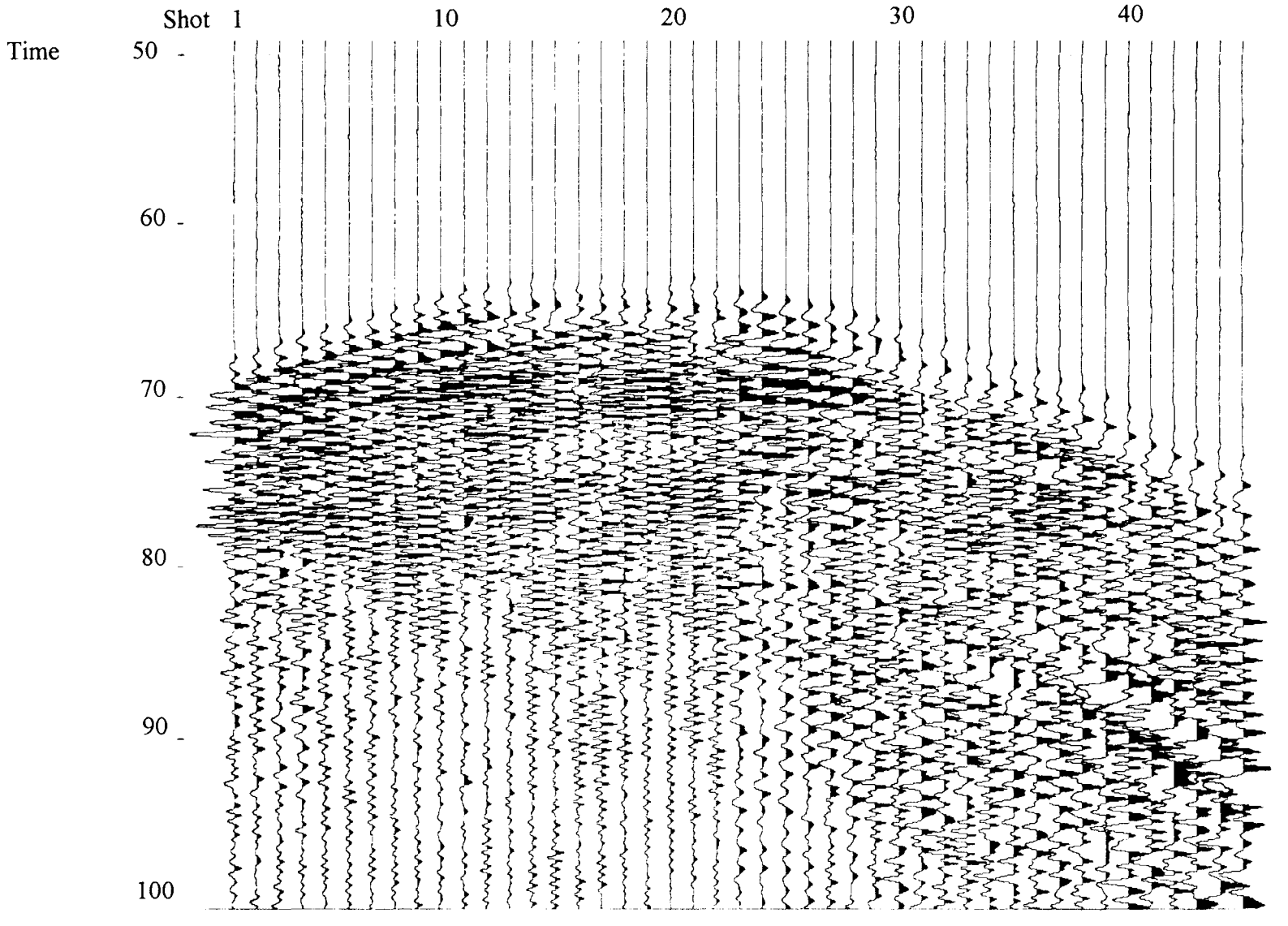

Figure 21 Orientation scan data for horizontal-1 axis

Orientation Scan: Level 2 - Horizontal 2

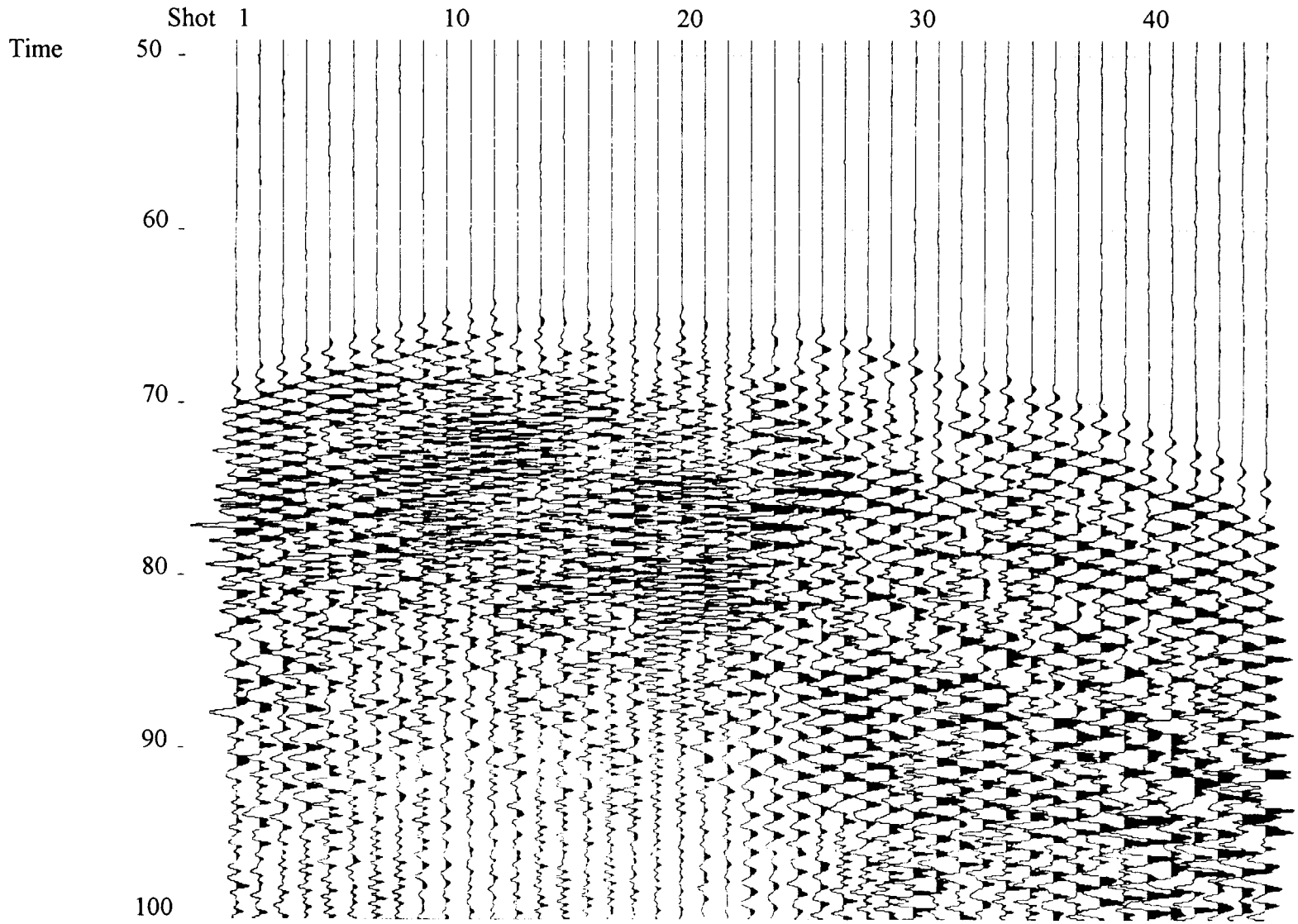

Figure 22 Orientation scan data for horizontal-2 axis

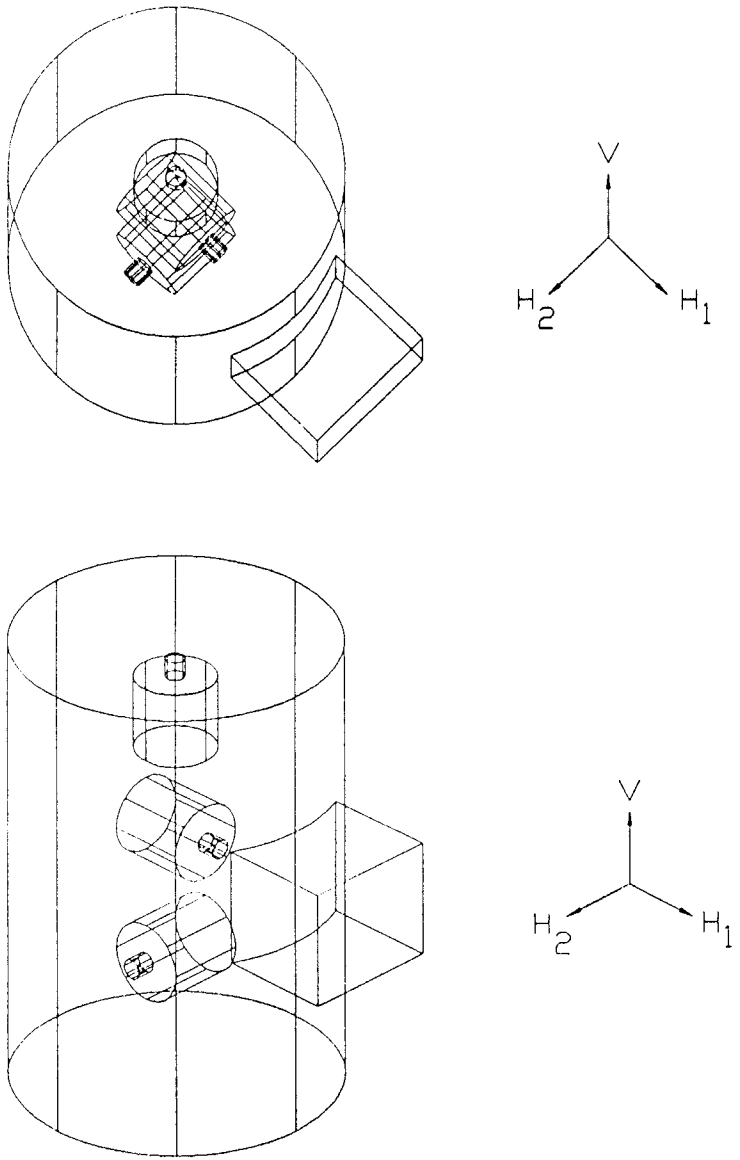

Figure 23 Mounting geometry

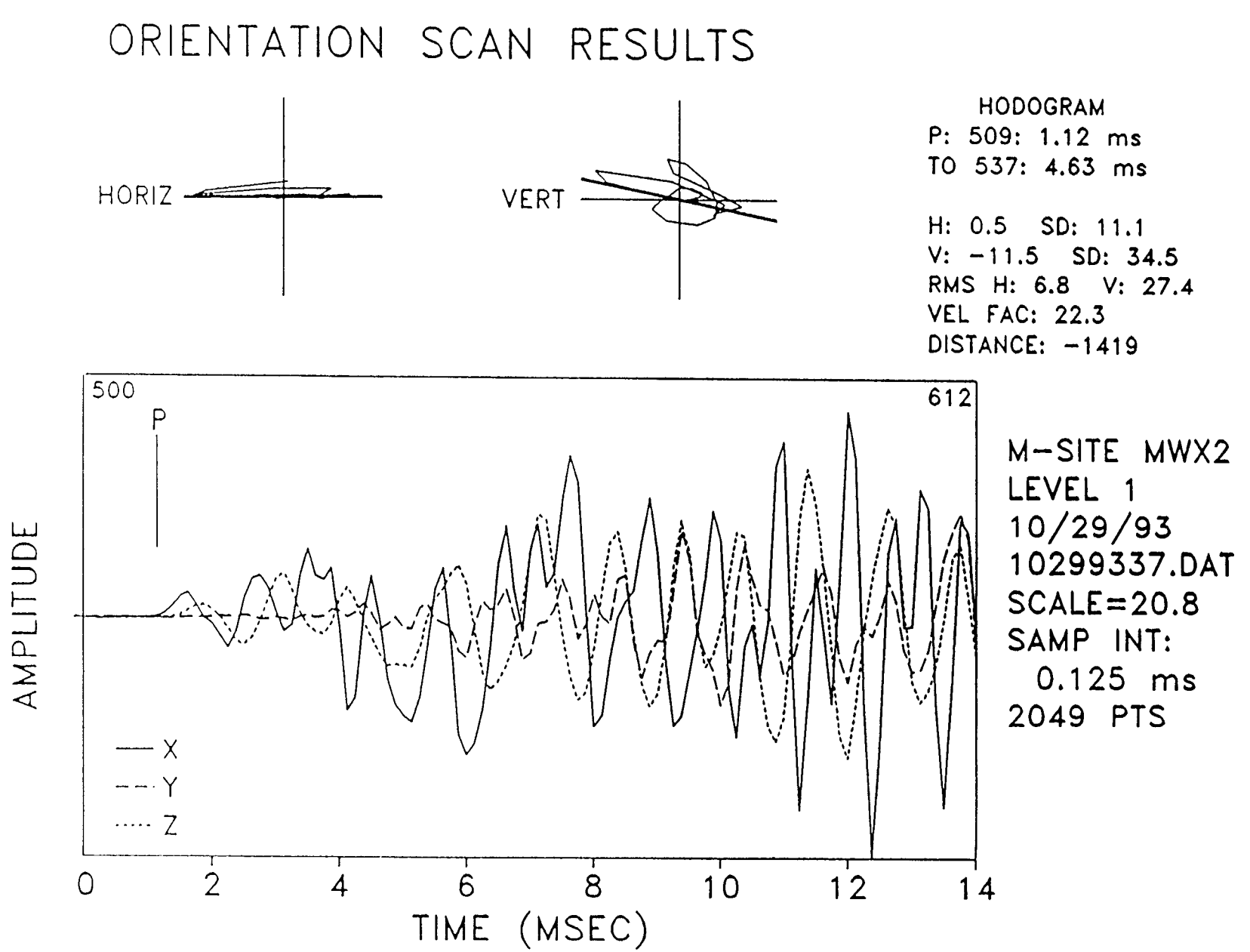

Figure 24 Example orientation data for level 1, shot at 4930 ft

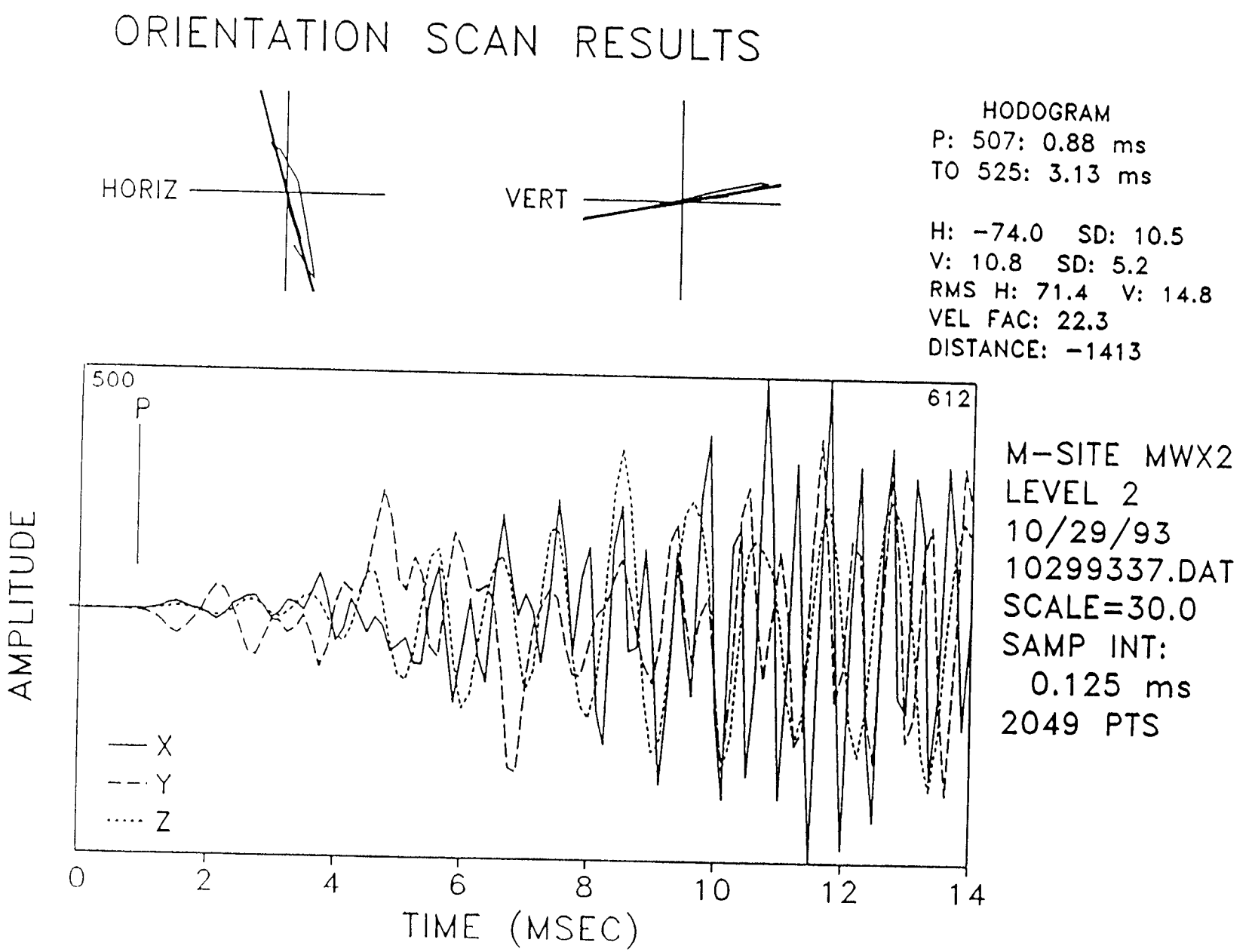

Figure 25 Example orientation data for level 2, shot at 4930 ft

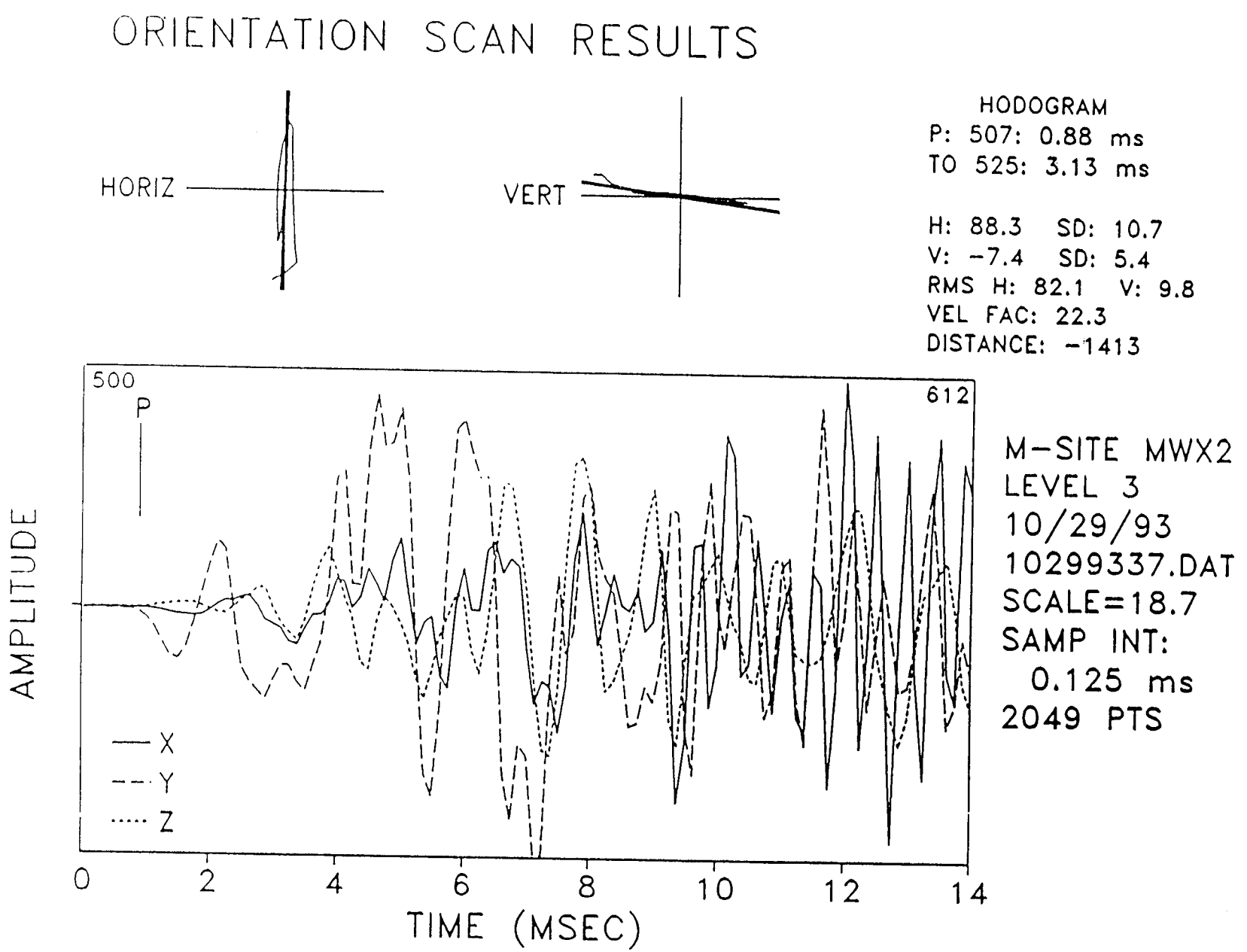

Figure 26 Example orientation data for level 3, shot at 4930 ft

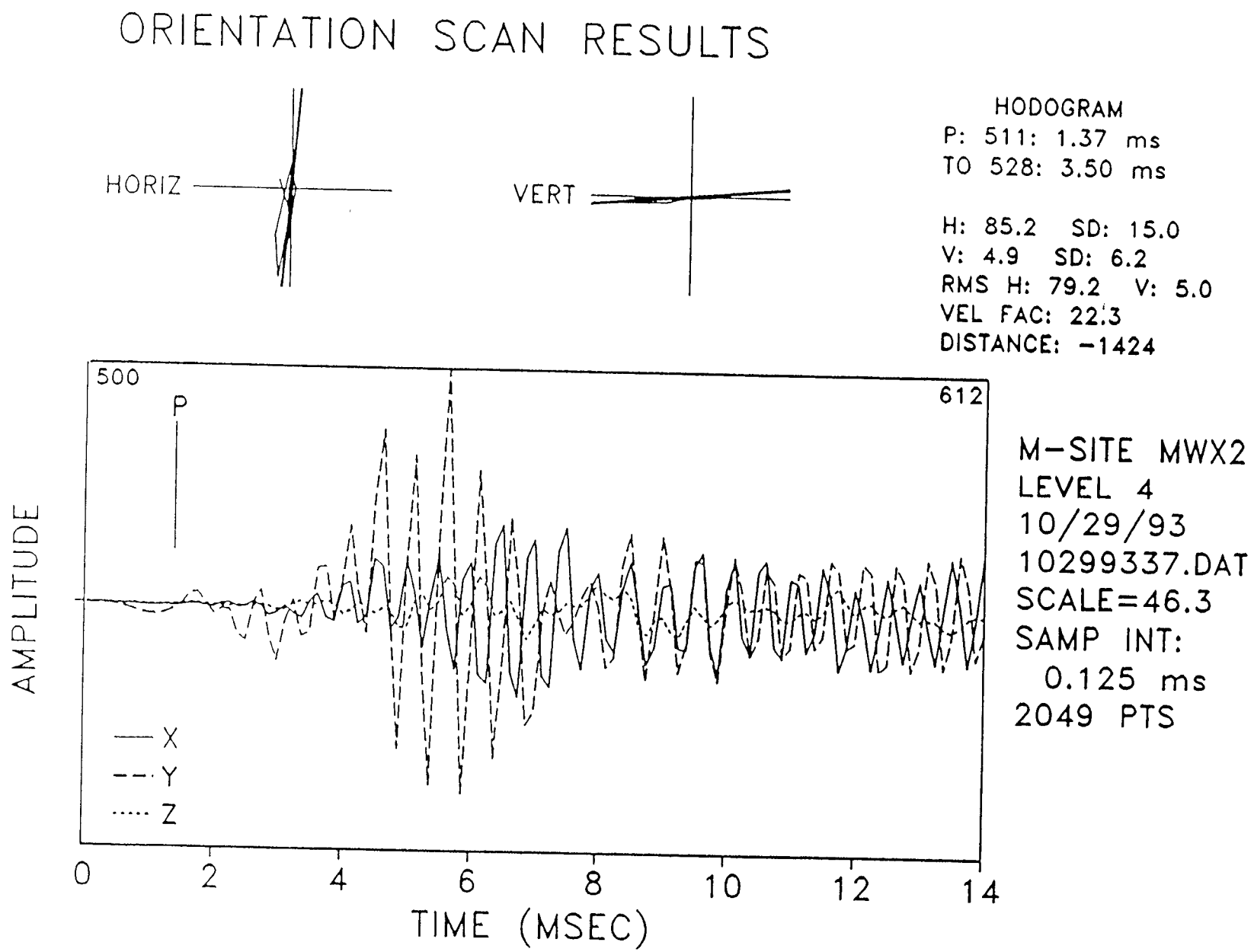

Figure 27 Example orientation data for level 4, shot at 4930 ft

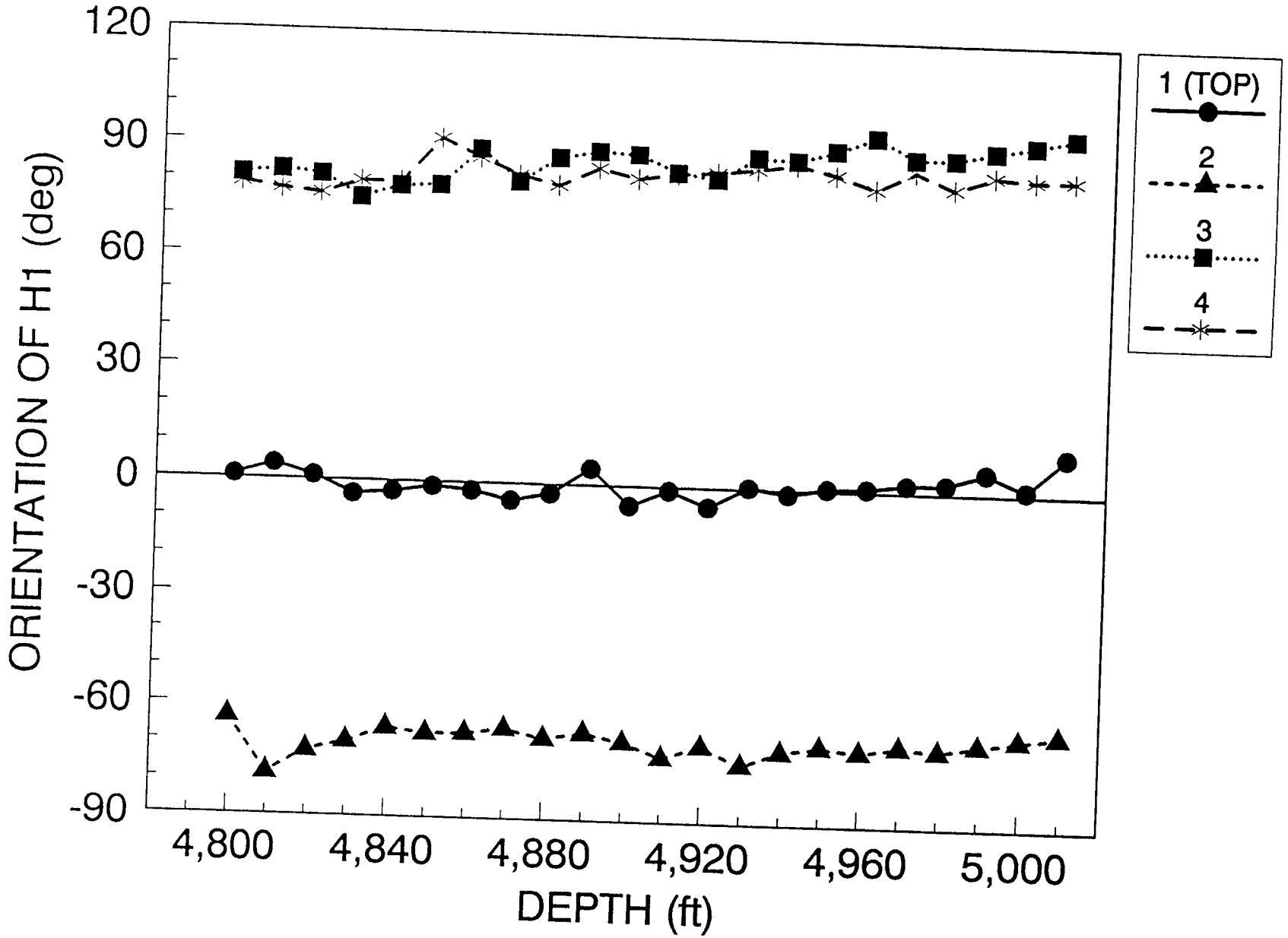

Figure 28 Orientation results

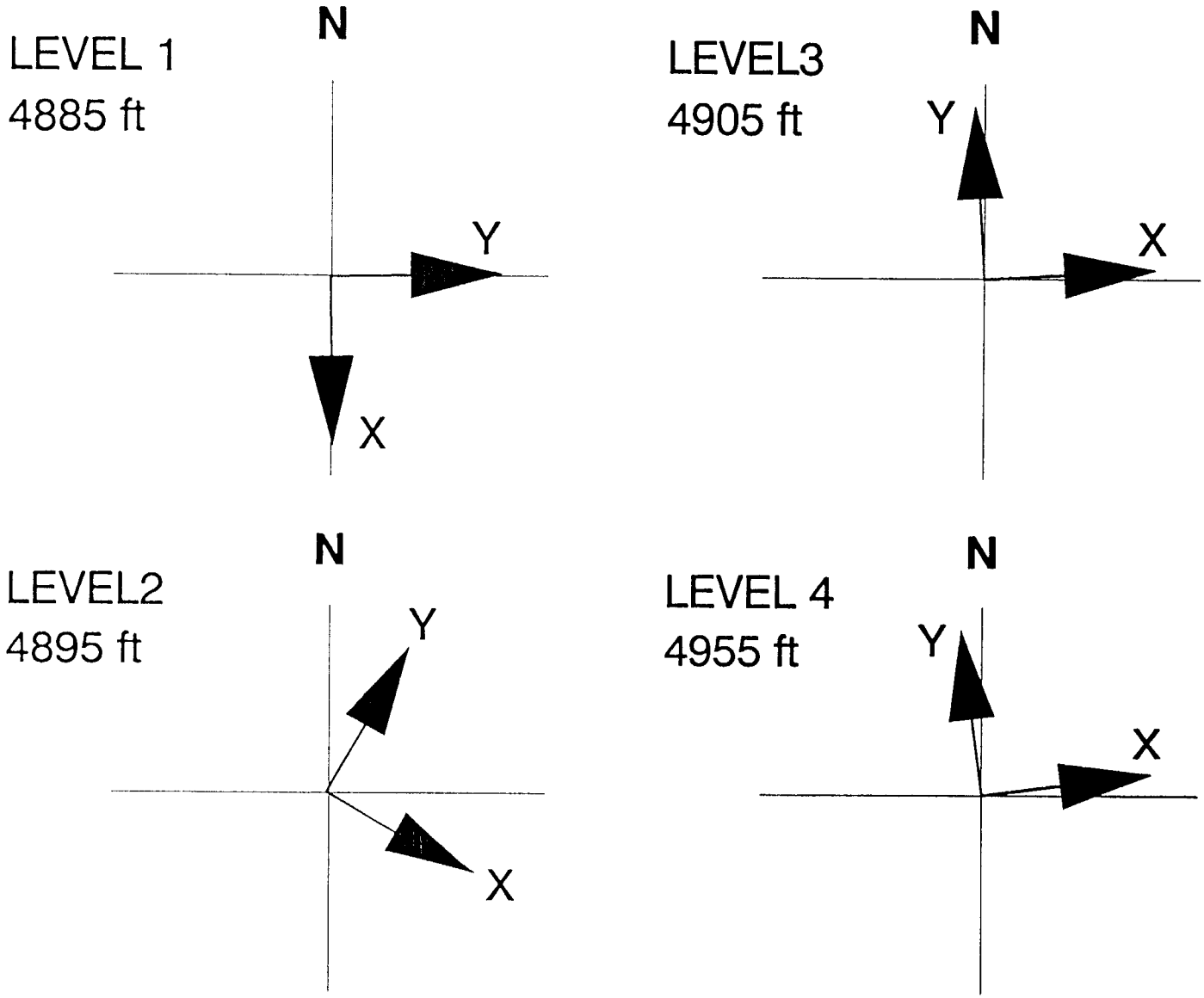

Figure 29 Orientation of individual axes

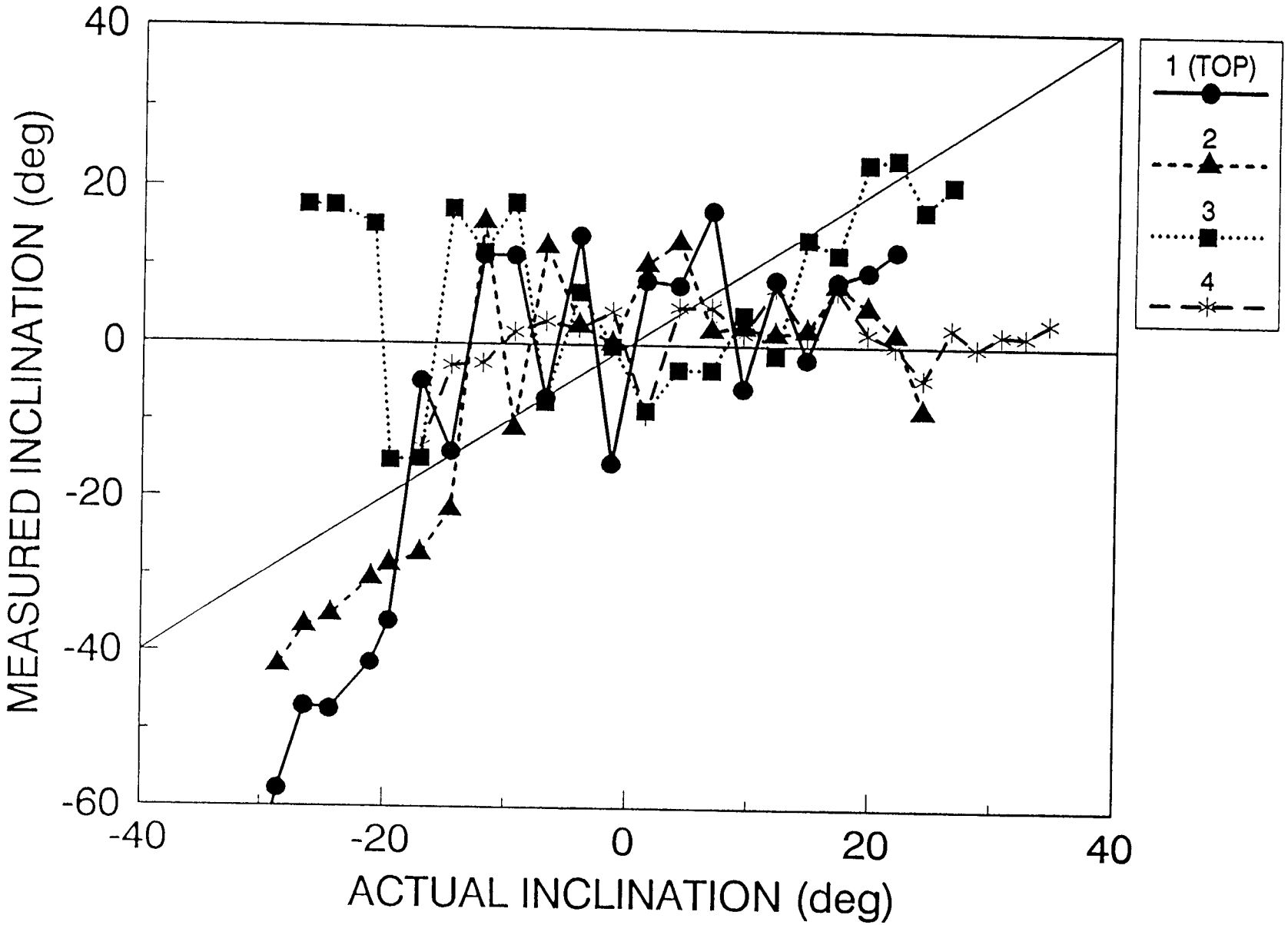

Figure 30 Inclination of each level

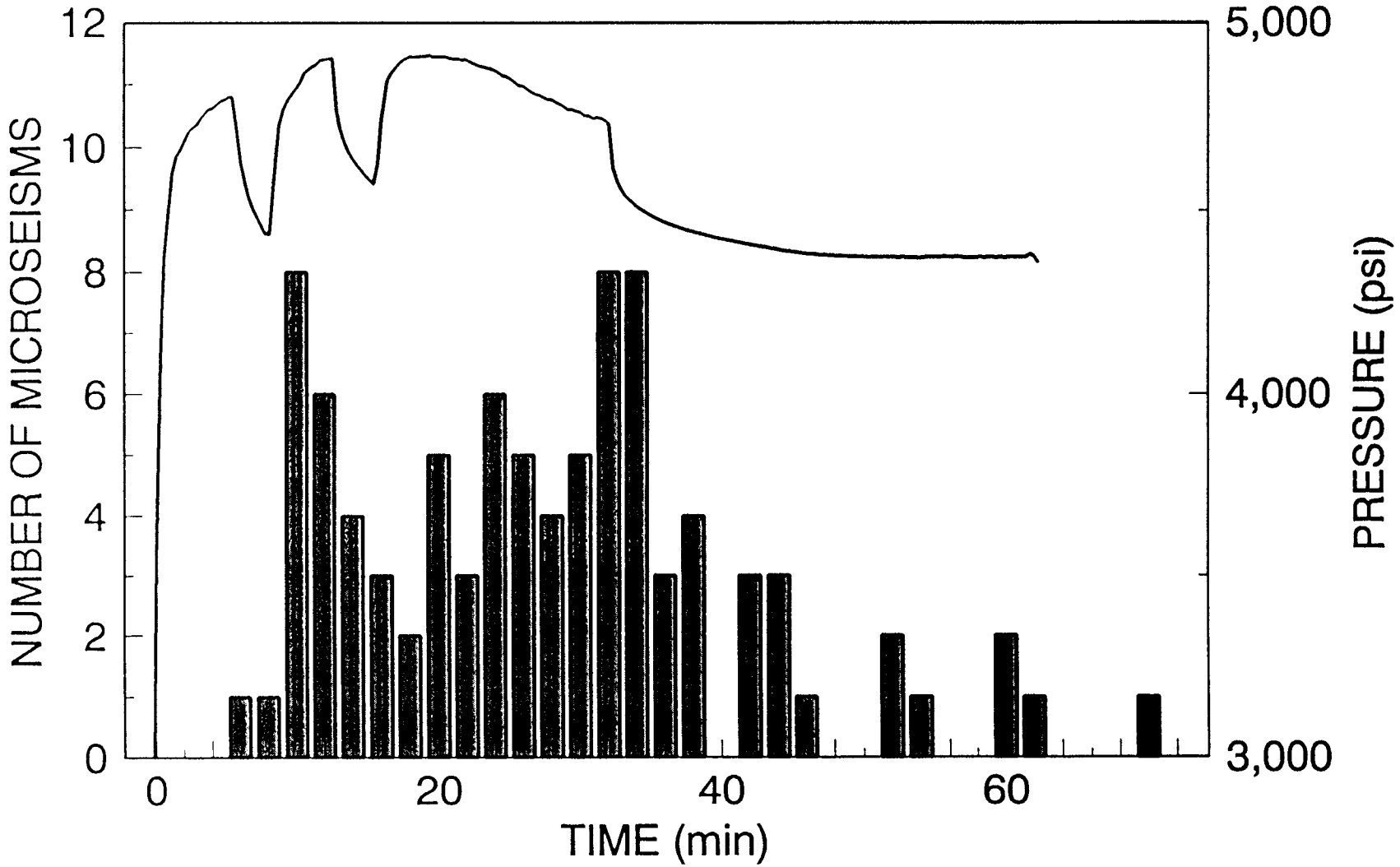

Figure 31 Histogram of events

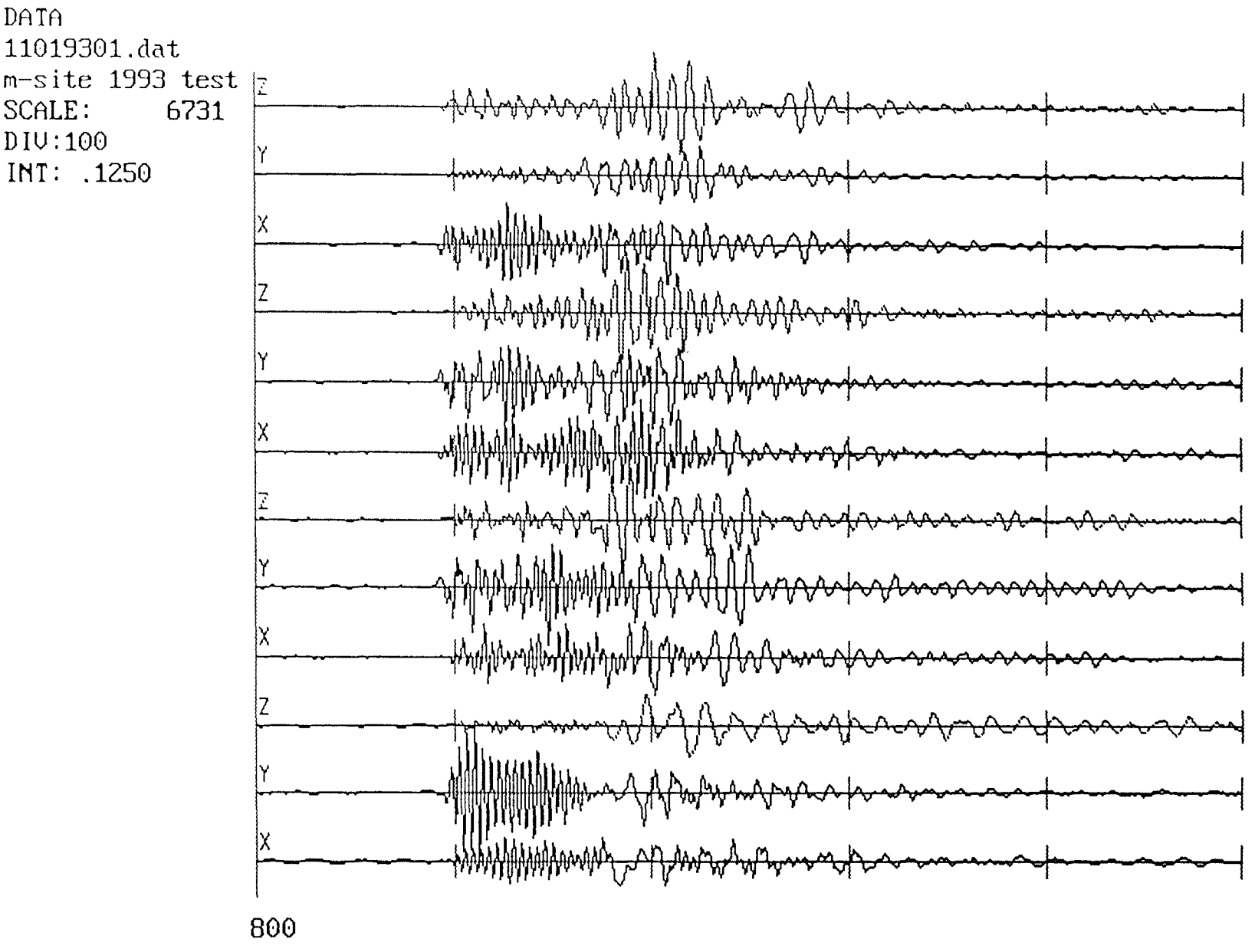

Figure 32 Example event (first event)

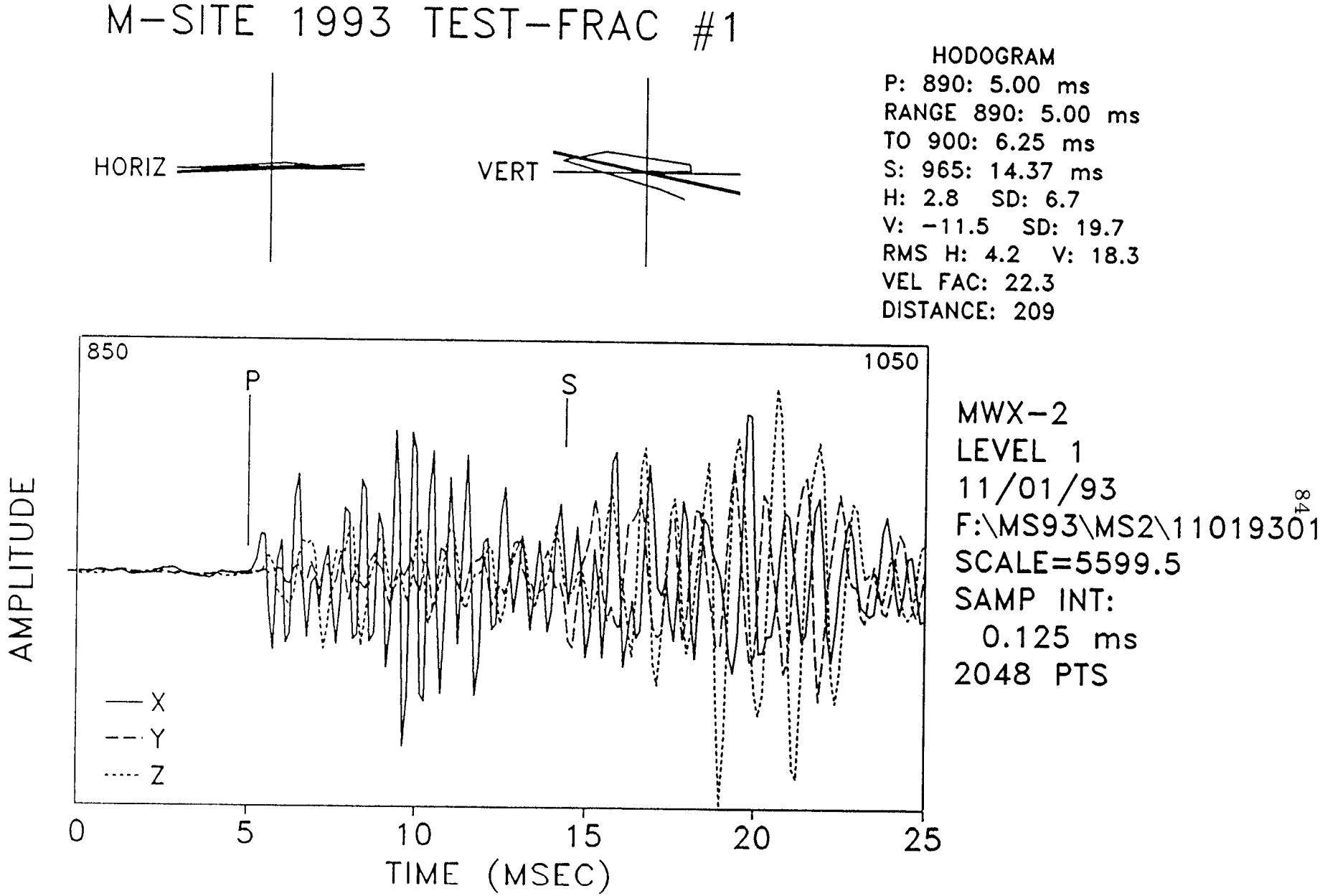

Figure 33 Traces and hodograms of first event

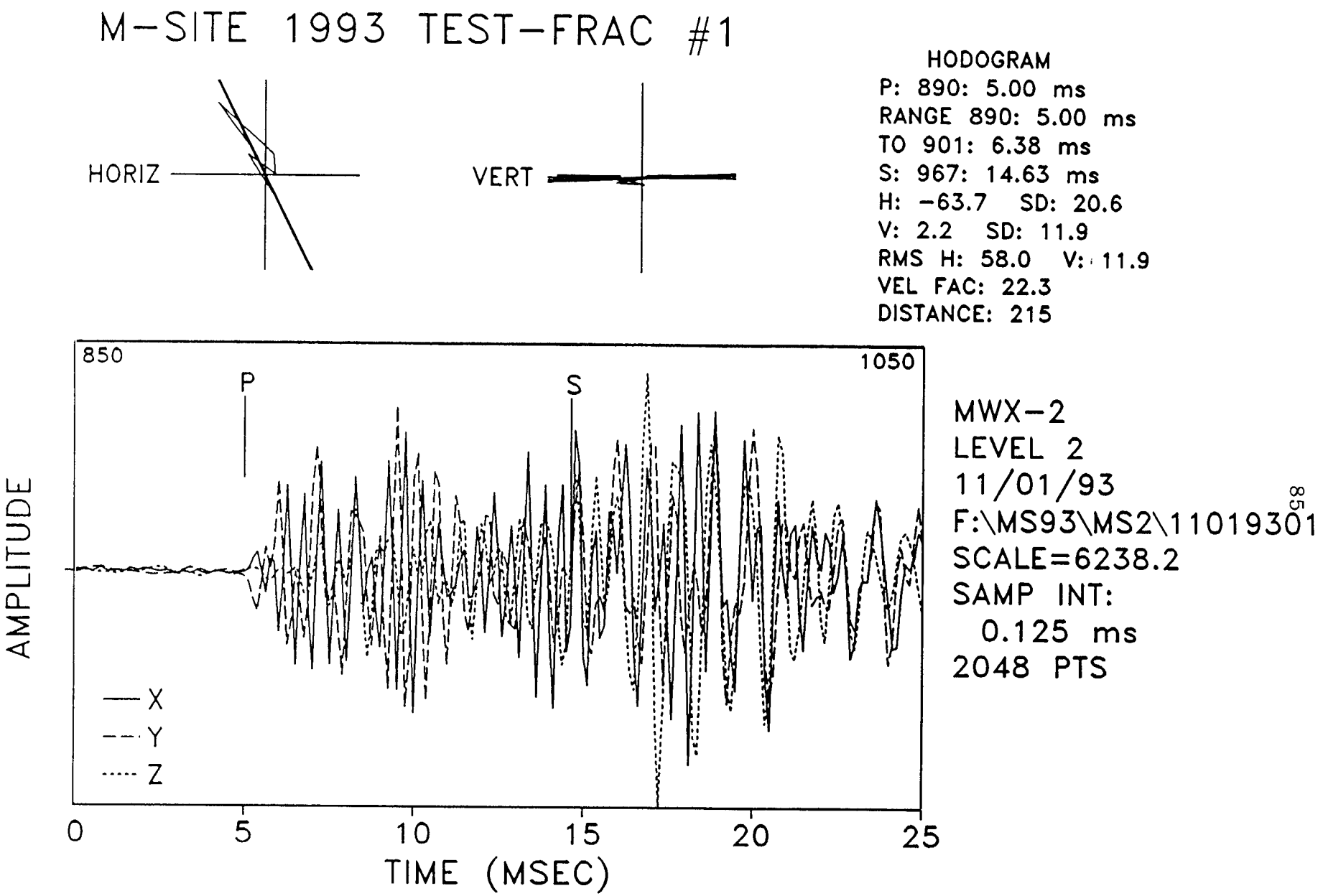

Figure 34 Traces and hodograms of first event, level 2

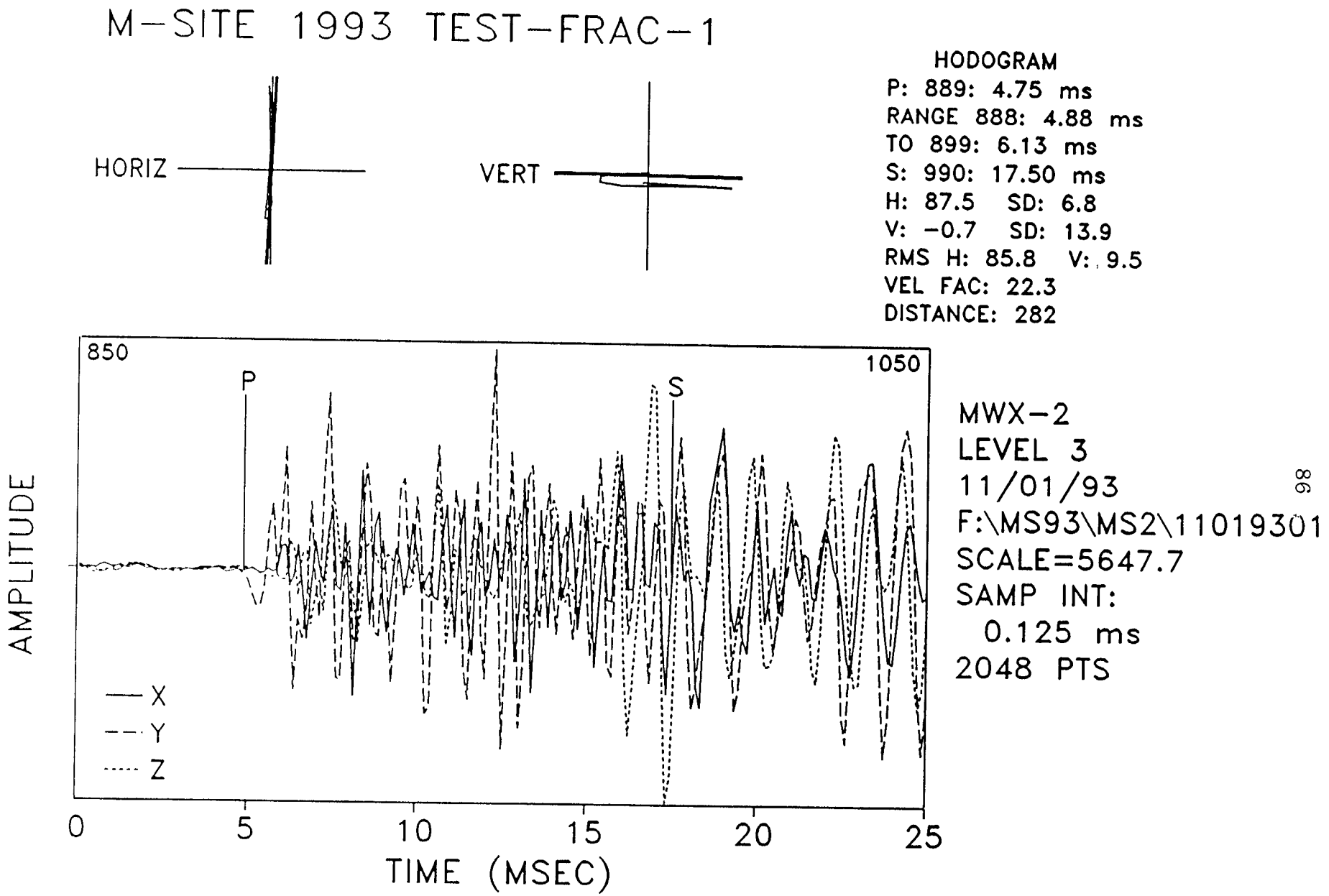

Figure 35 Traces and hodograms of first event, level 3

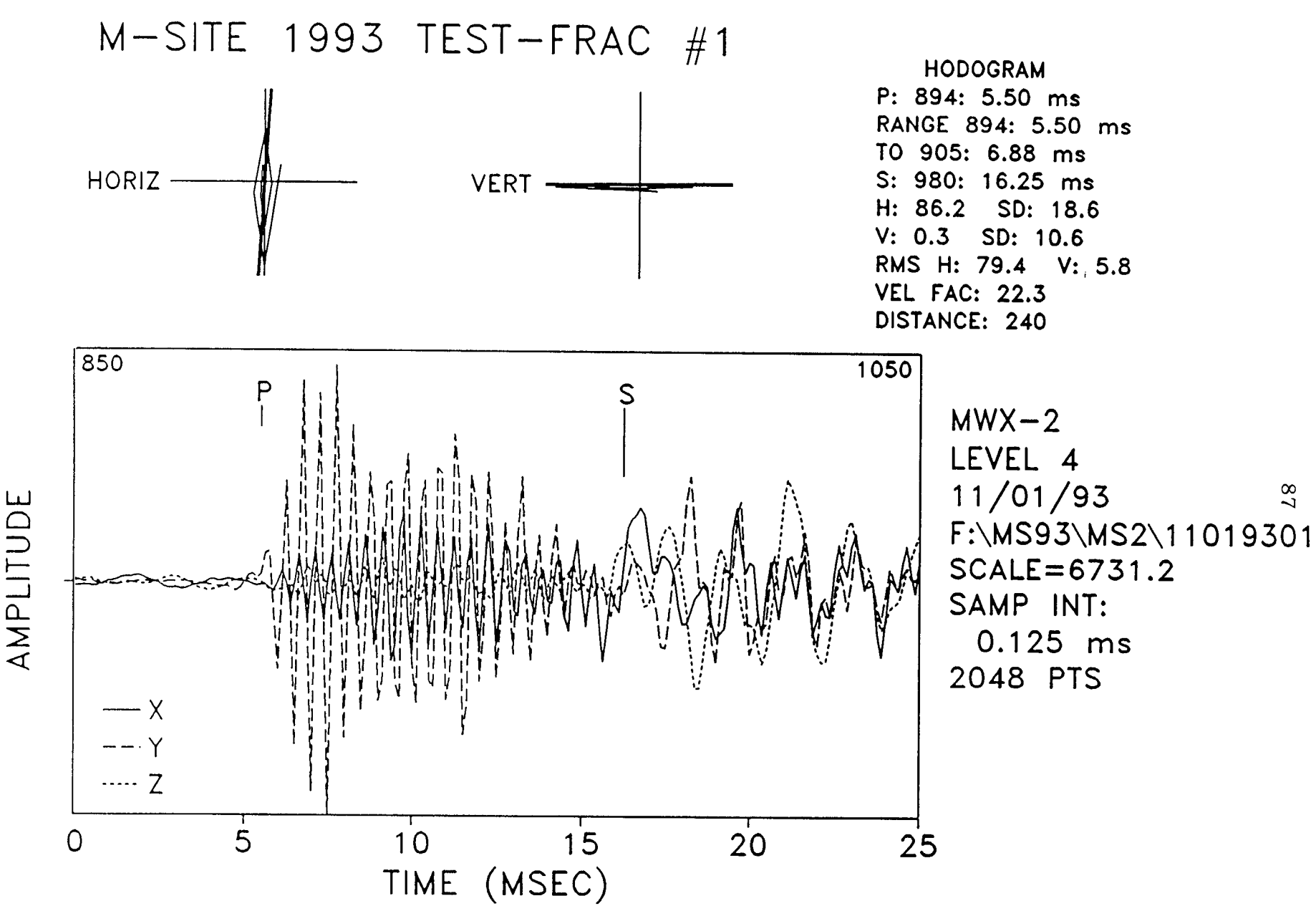

Figure 36 Traces and hodograms of first event, level 4

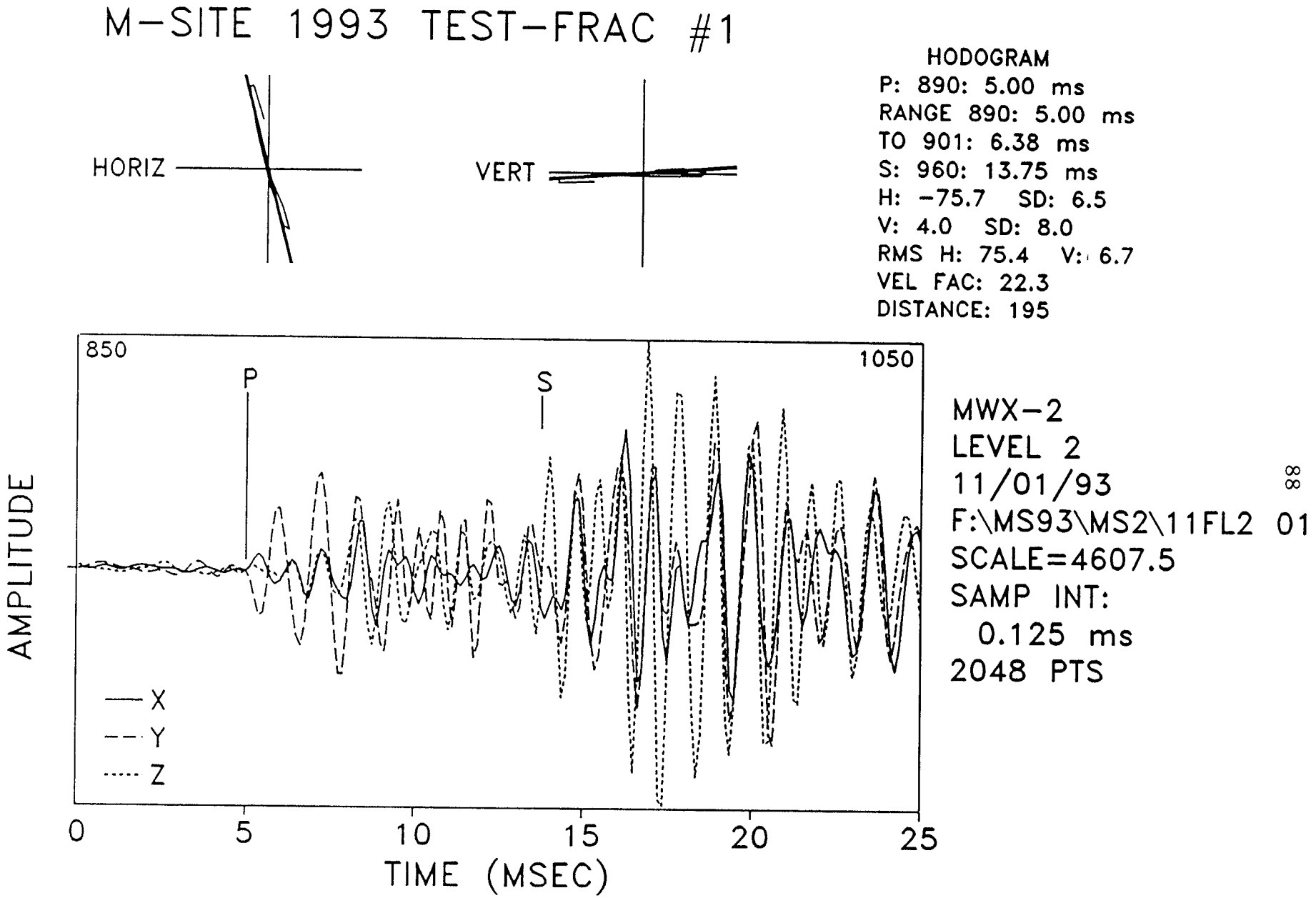

Figure 37 Filtered traces and hodograms of first event, level 2

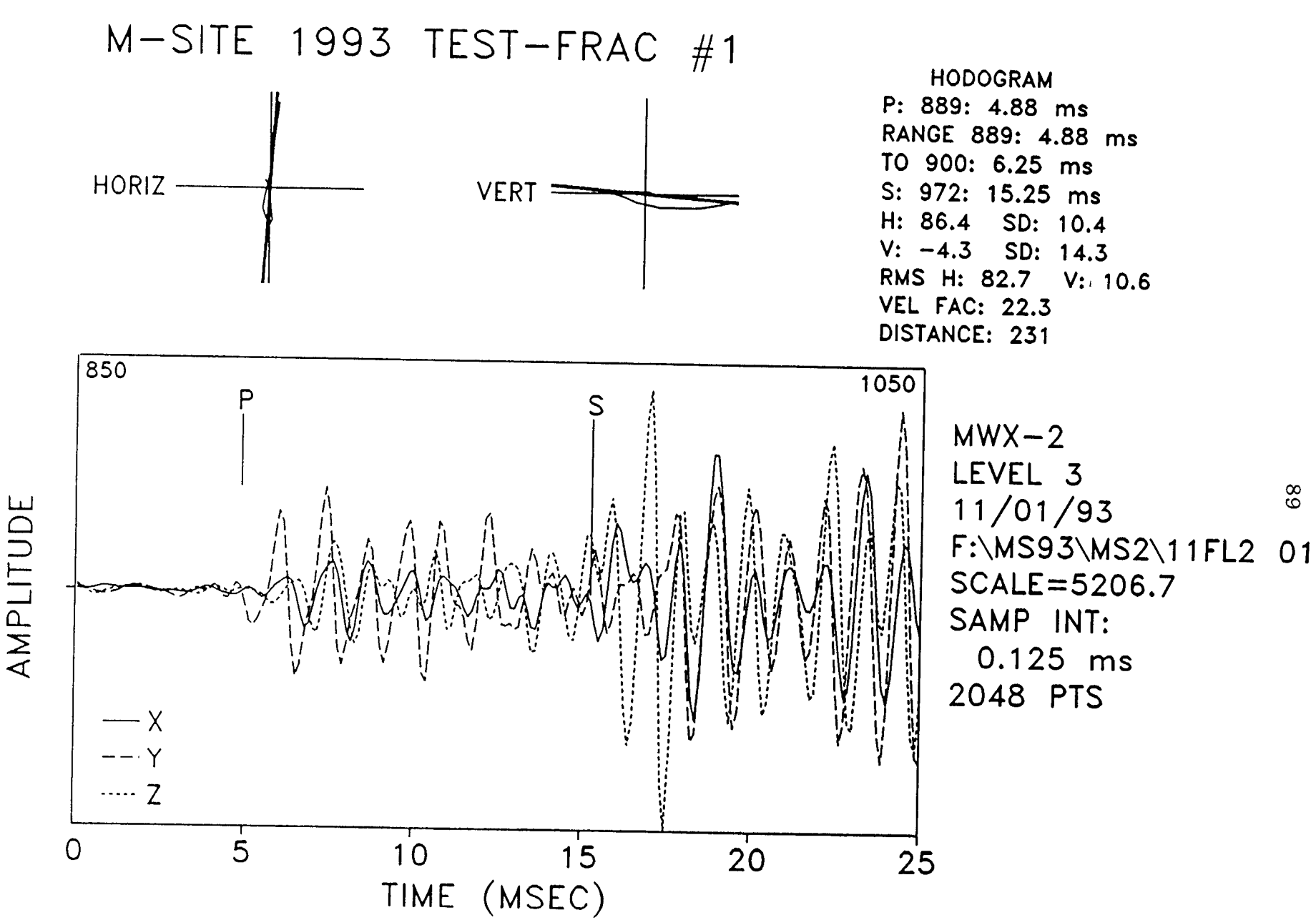

Figure 38 Filtered traces and hodograms of first event, level 3

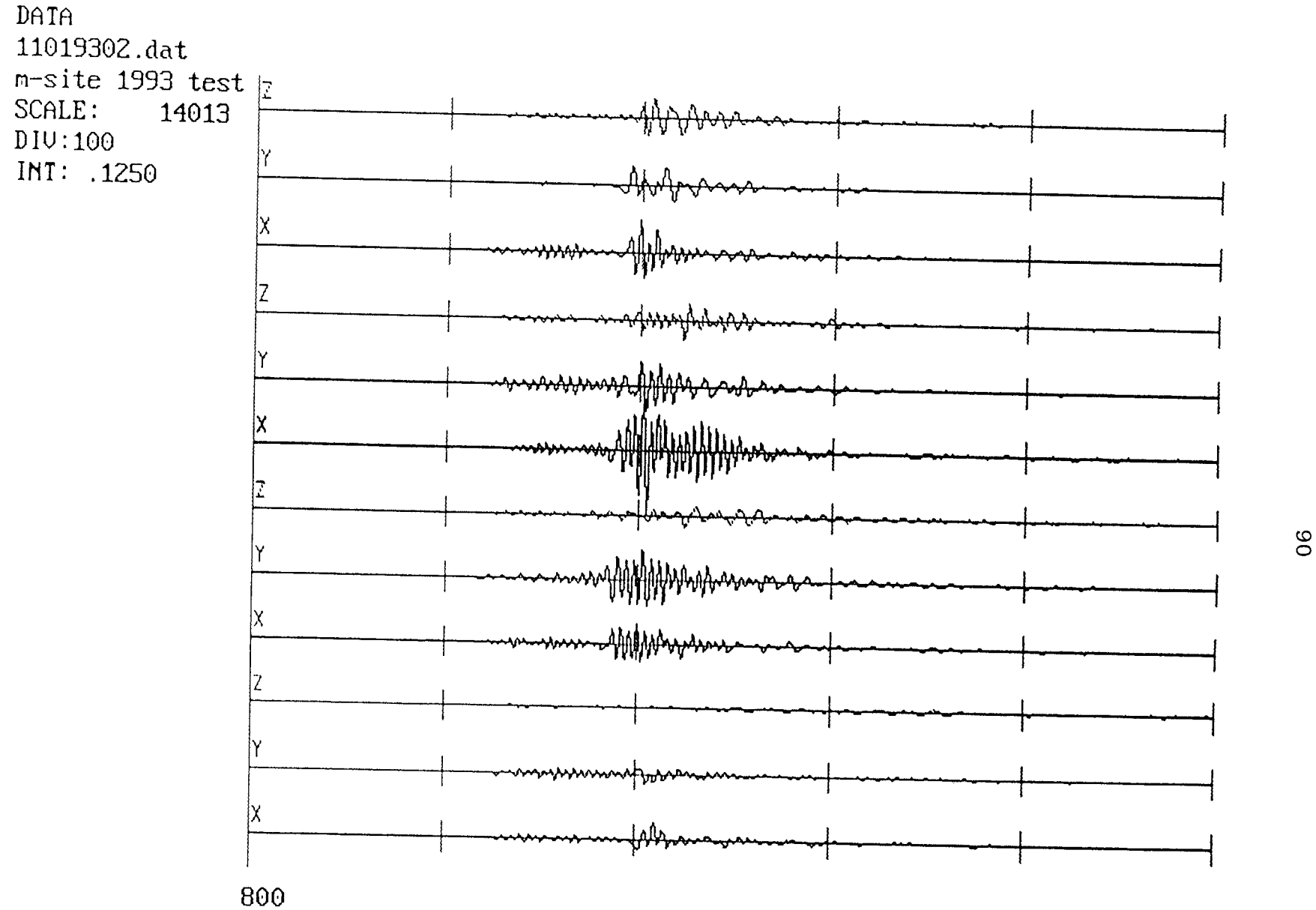

Figure 39 Second event

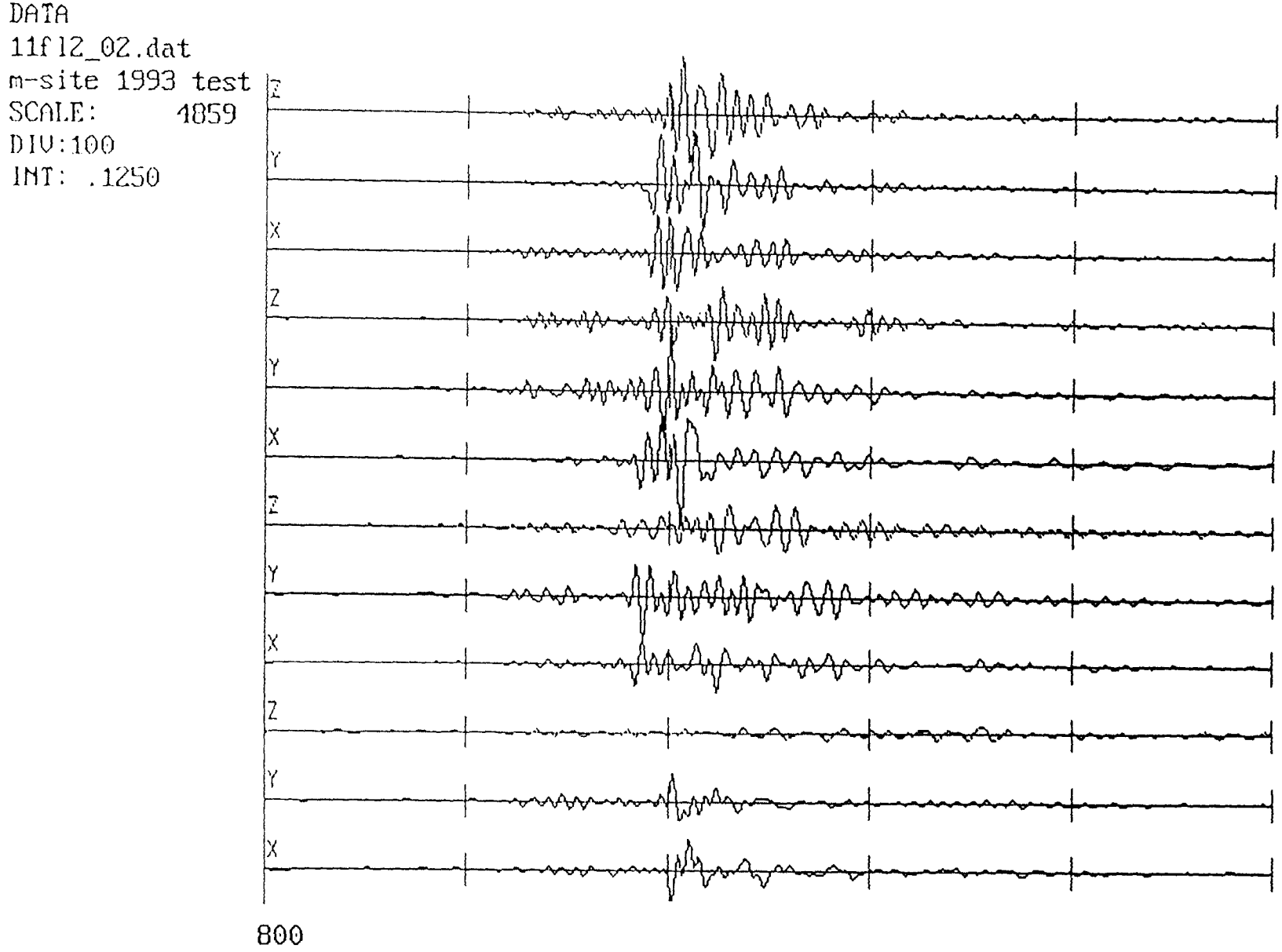

Figure 40 Second event, filtered traces

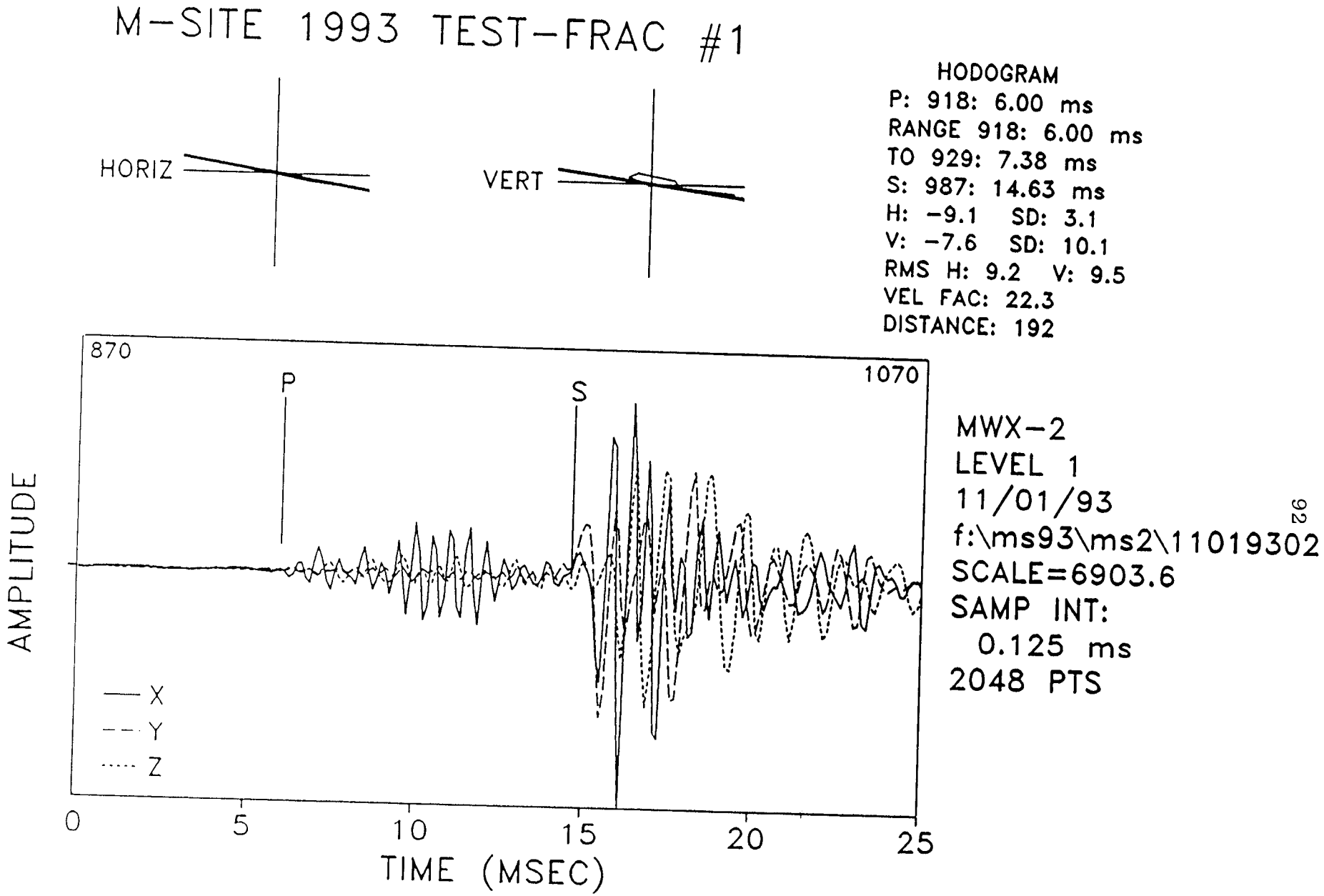

Figure 41 Traces and hodograms of second event, level 1, unfiltered

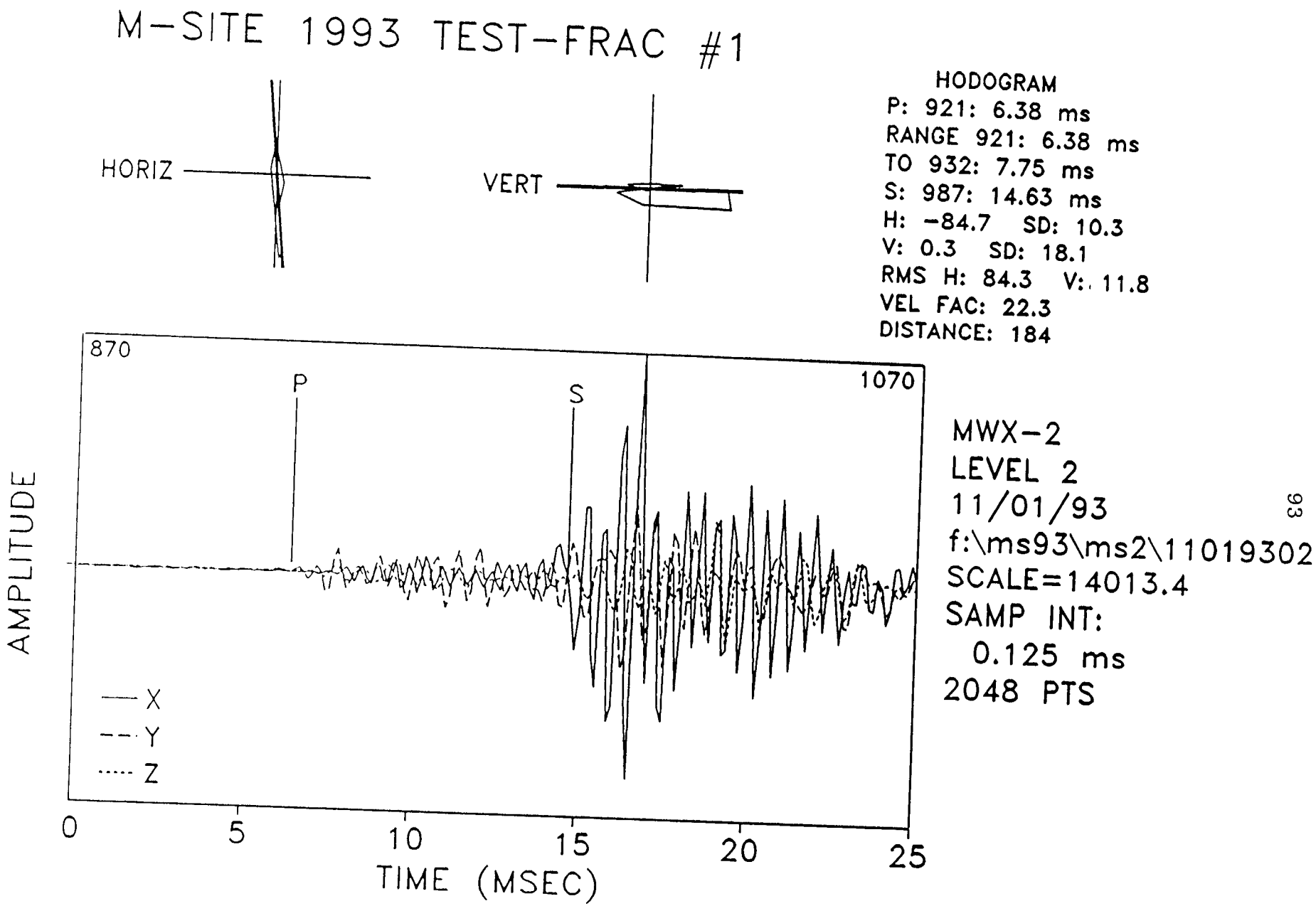

Figure 42 Traces and hodograms of second event, level 2, unfiltered

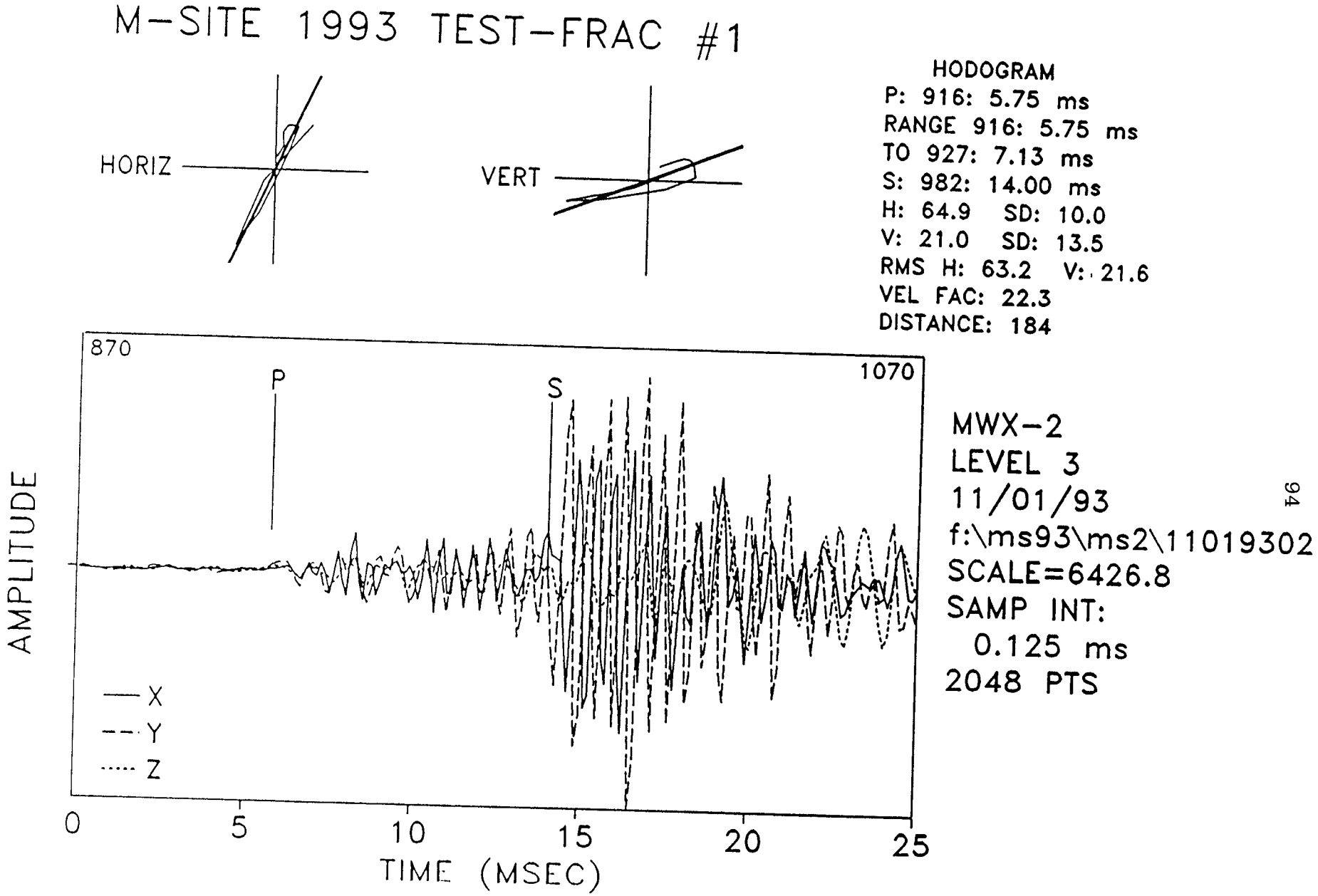

Figure 43 Traces and hodograms of second event, level 3, unfiltered

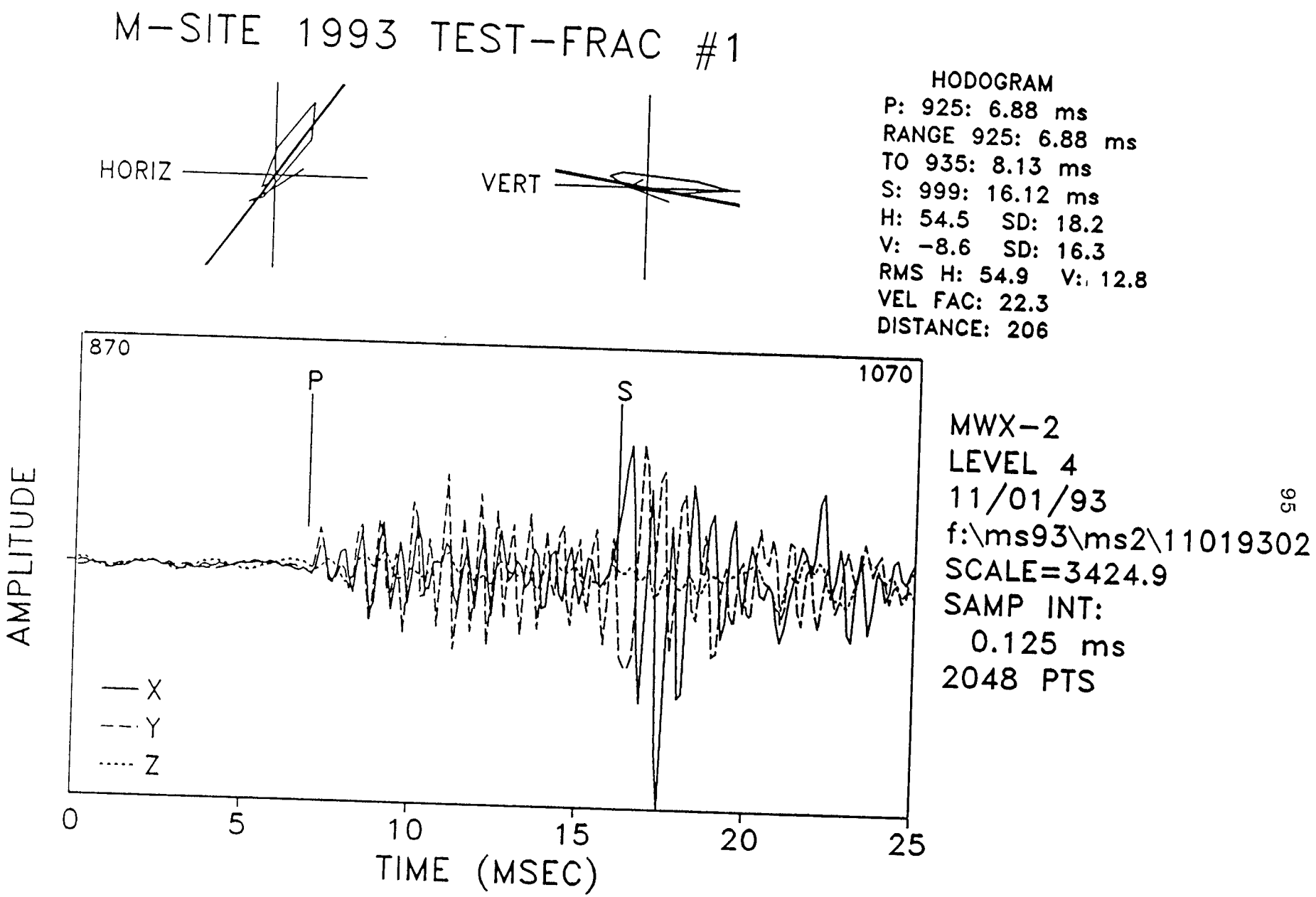

Figure 44 Traces and hodograms of second event, level 4, unfiltered

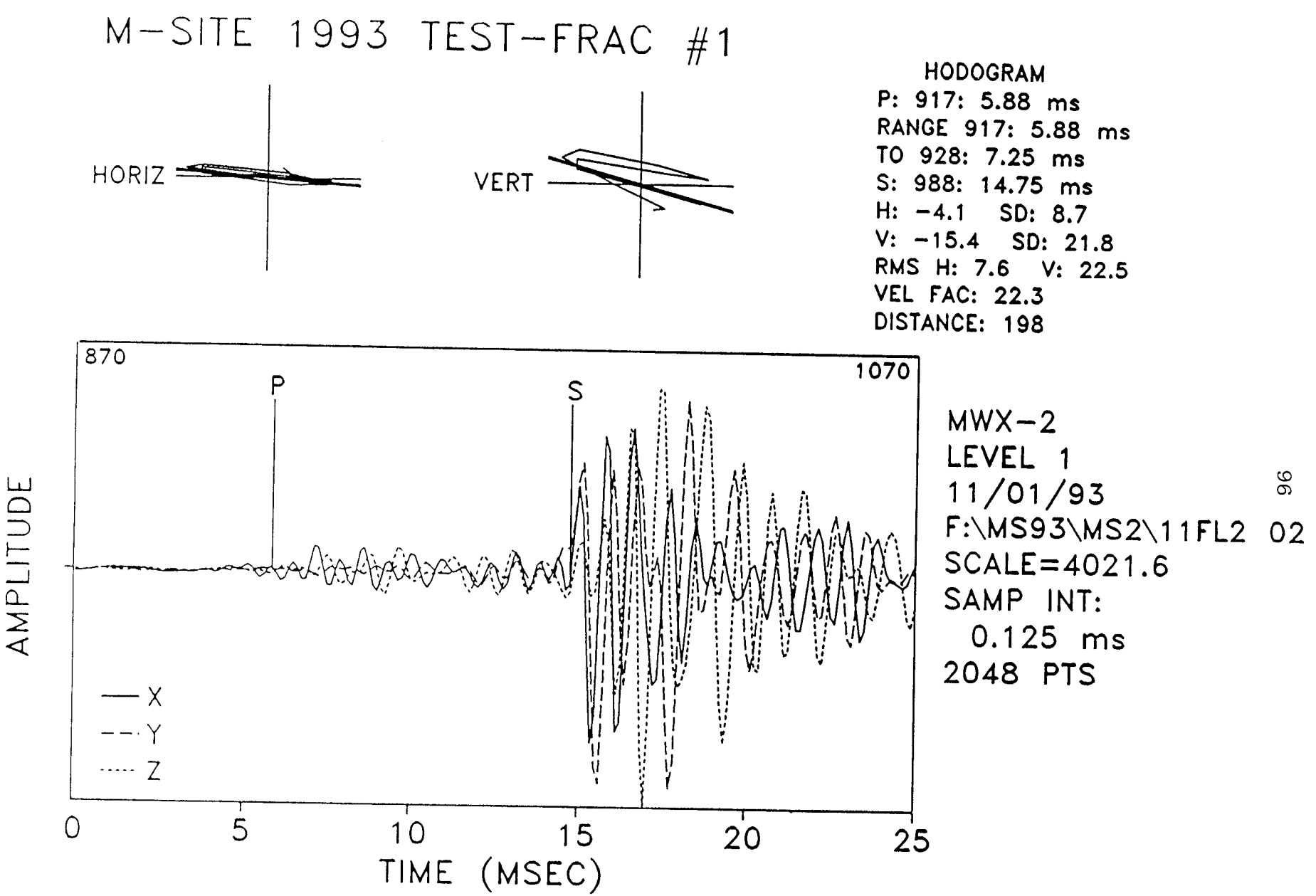

Figure 45 Traces and hodograms of second event, level 1, filtered

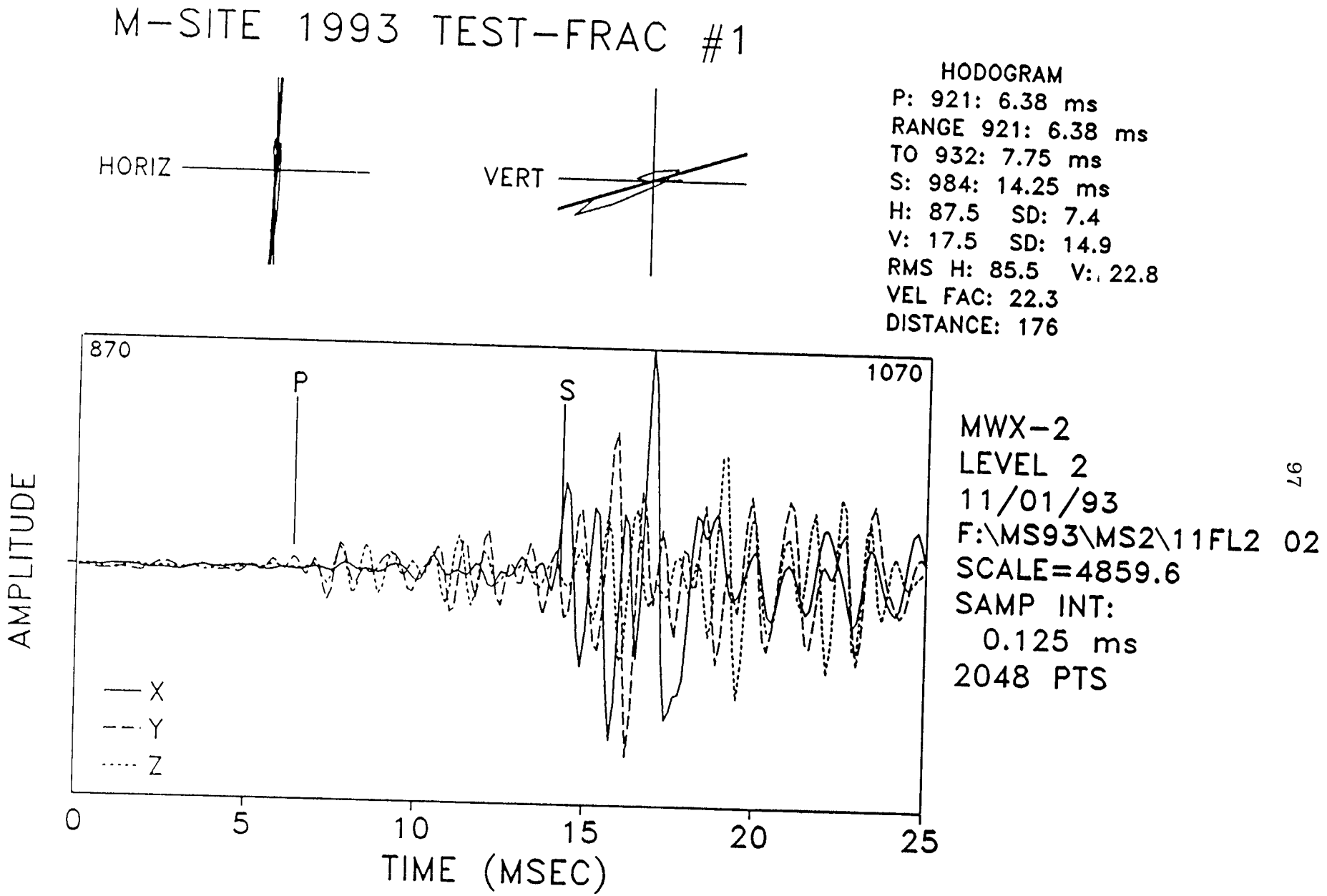

Figure 46 Traces and hodograms of second event, level 2, filtered

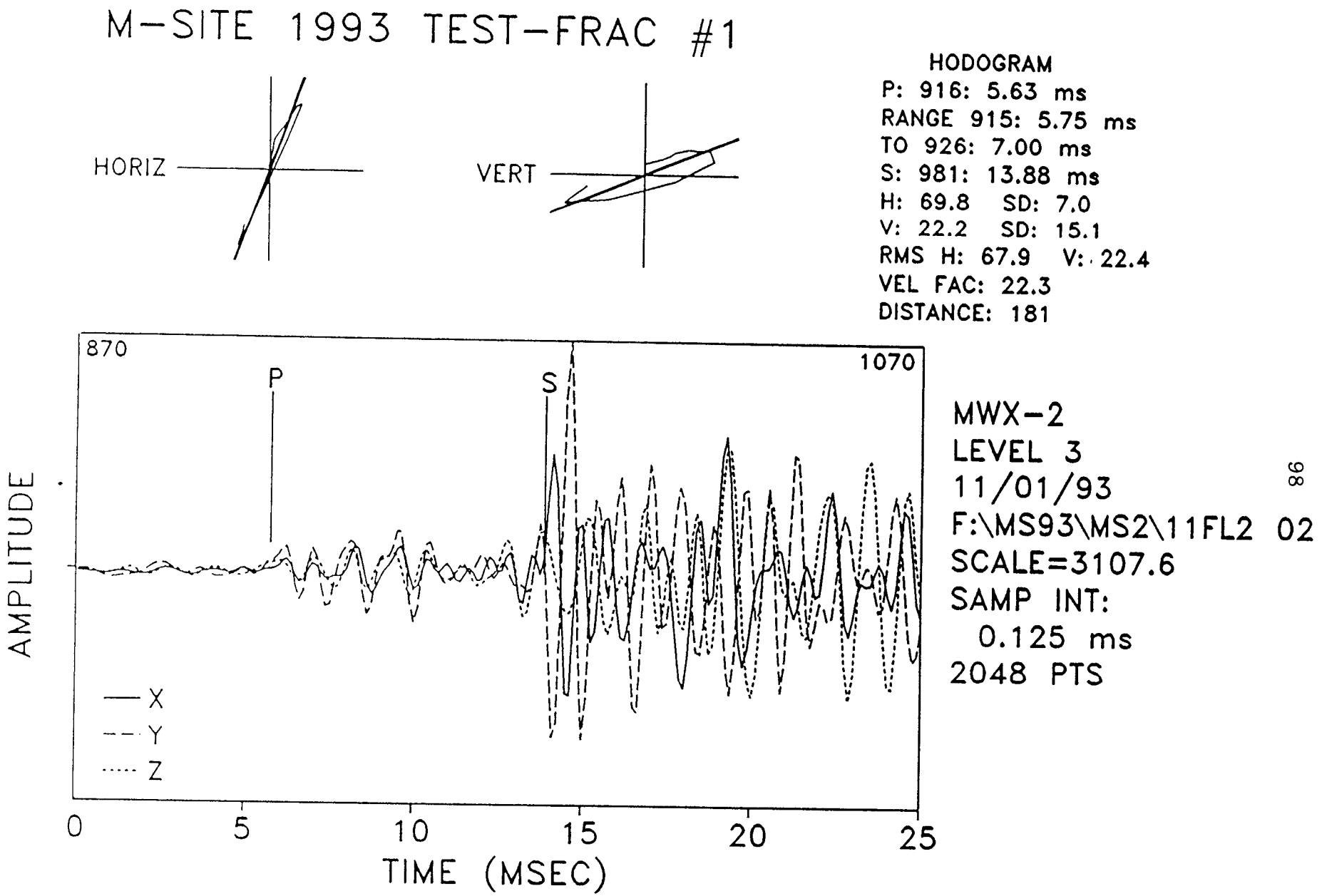

Figure 47 Traces and hodograms of second event, level 3, filtered

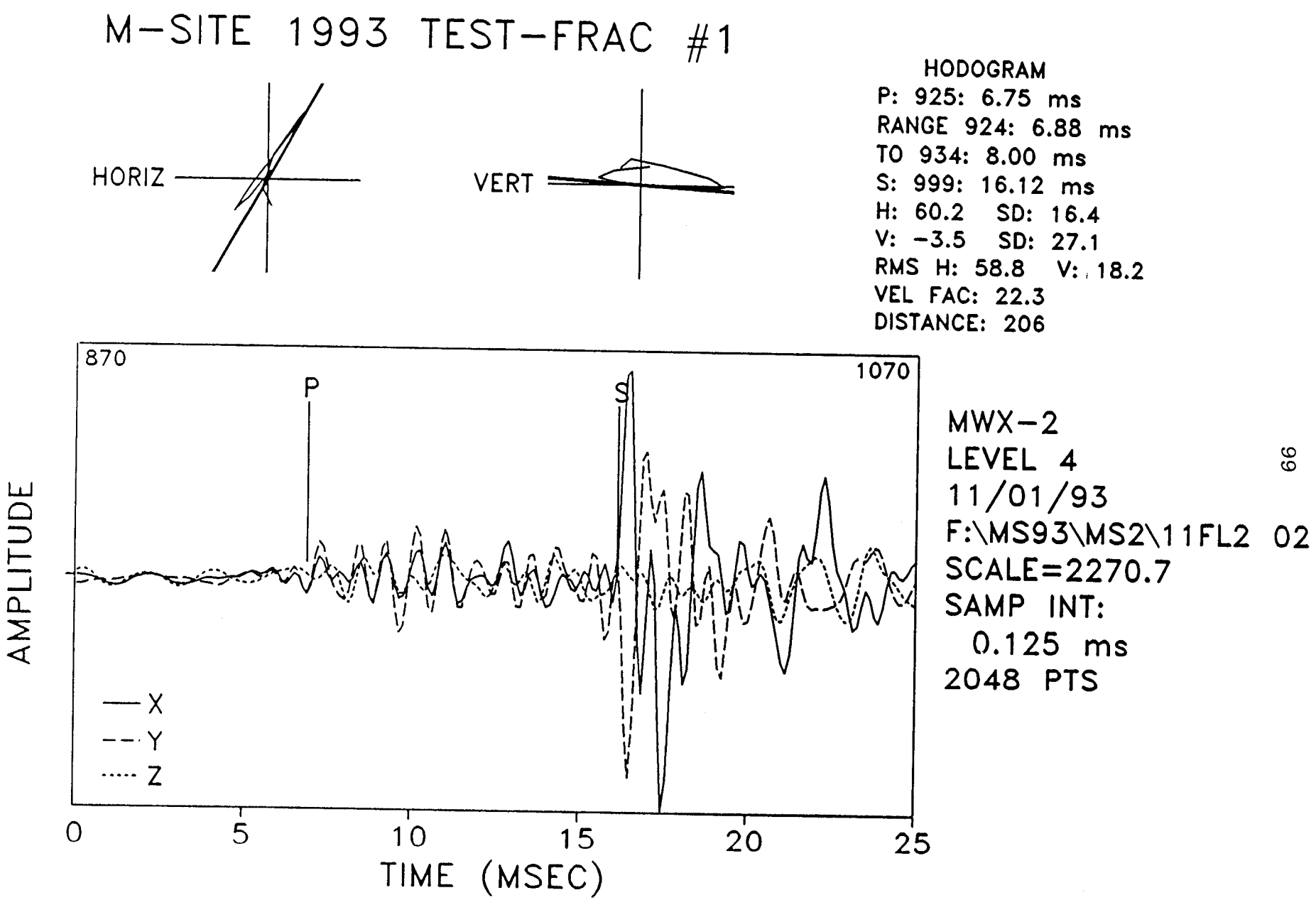

Figure 48 Traces and hodograms of second event, level 4, filtered

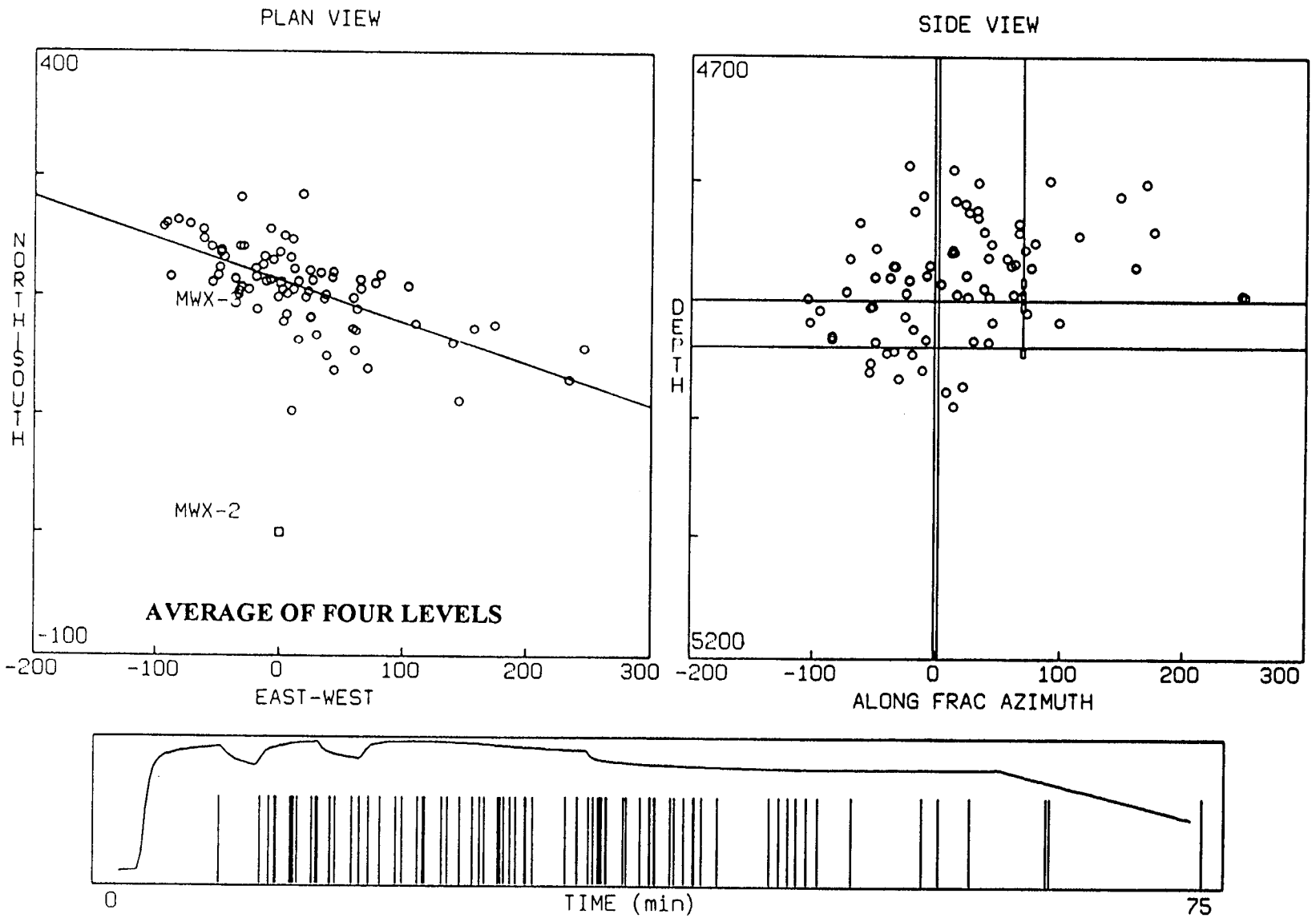

Figure 49 Map of microseisms using average of all four levels

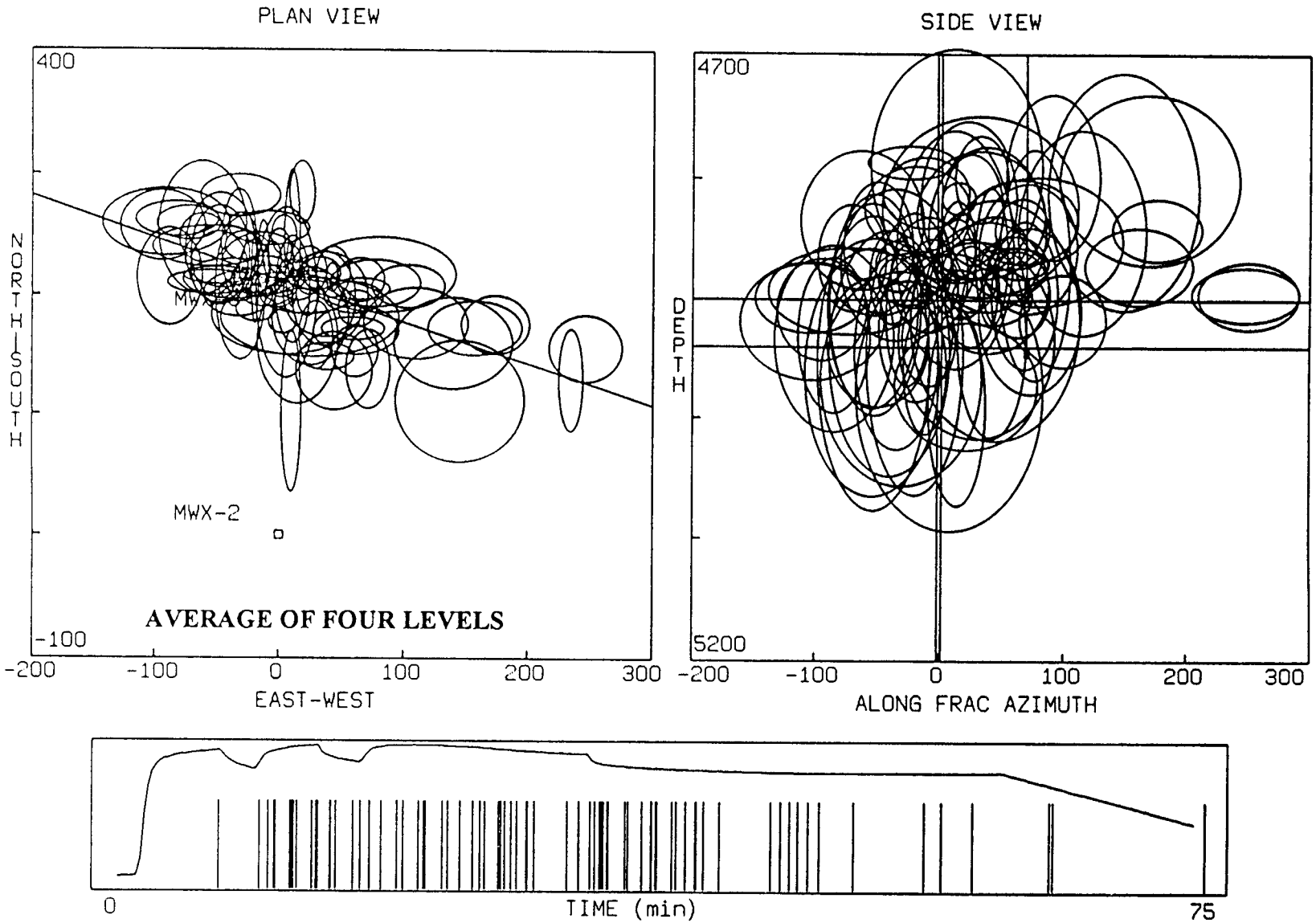

Figure 50. Uncertainty map of microseisms using average of all four levels

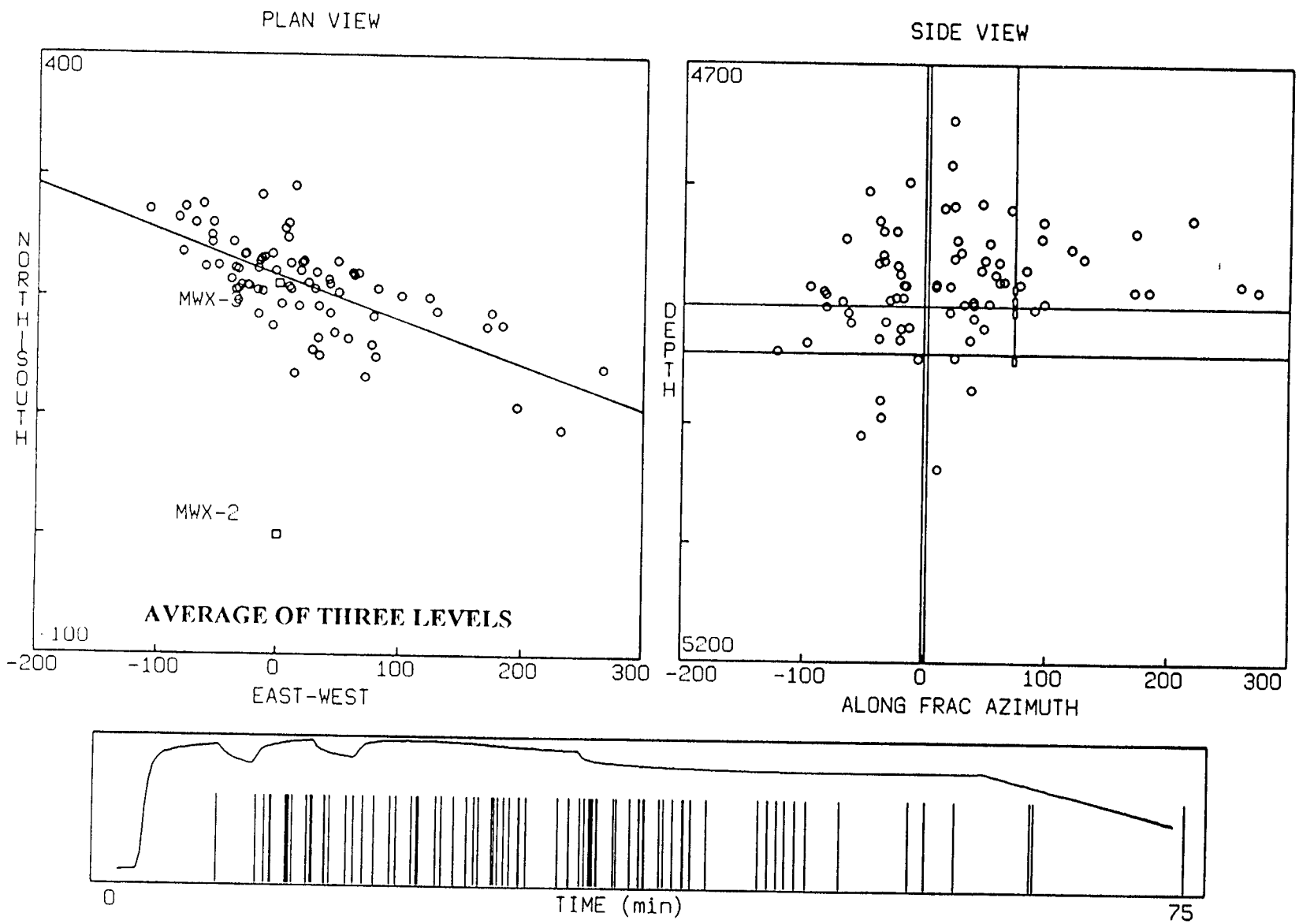

Figure 51. Map of microseisms using average of all three levels

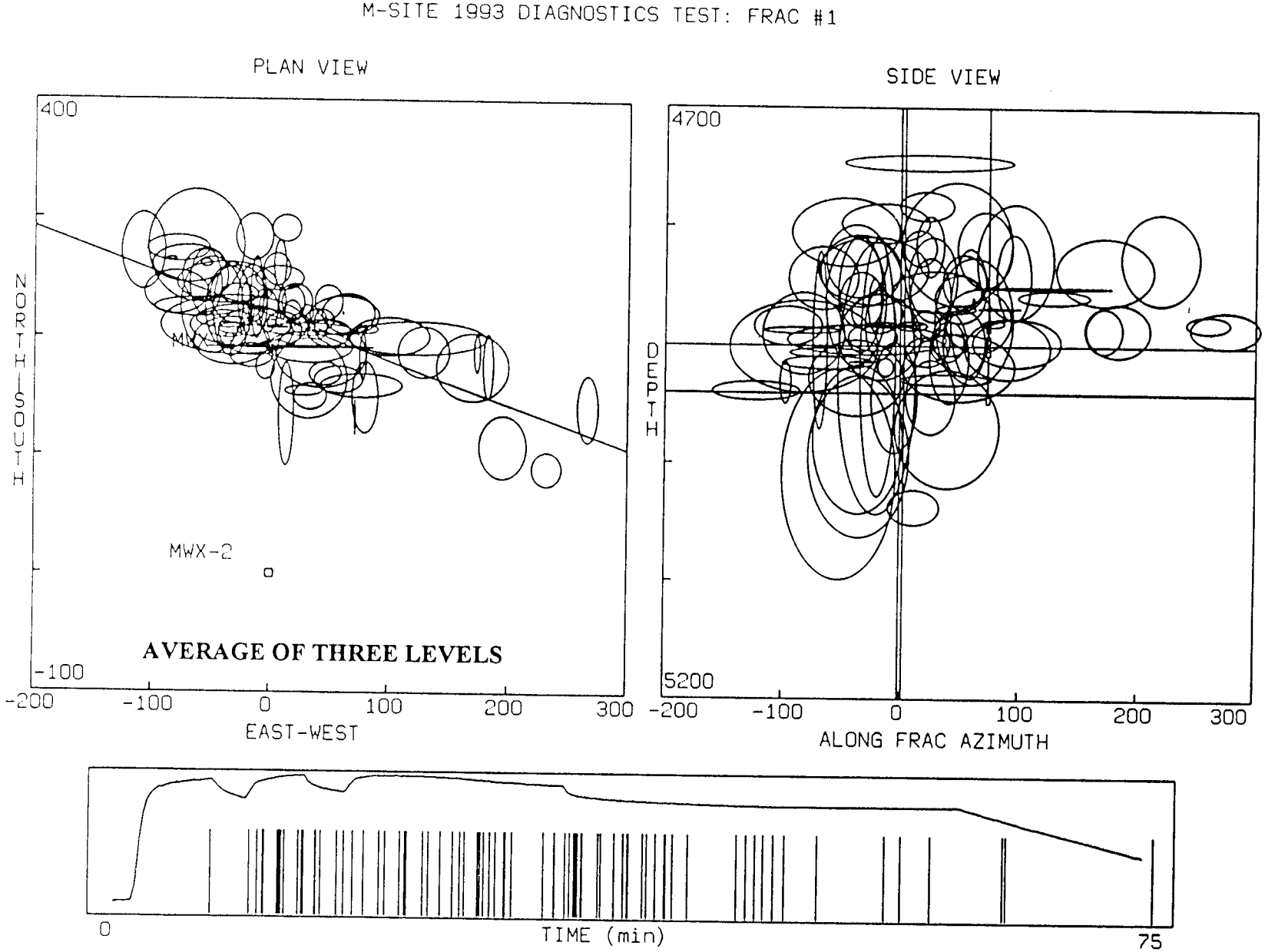

Figure 52. Uncertainty map of microseisms using average of all three levels

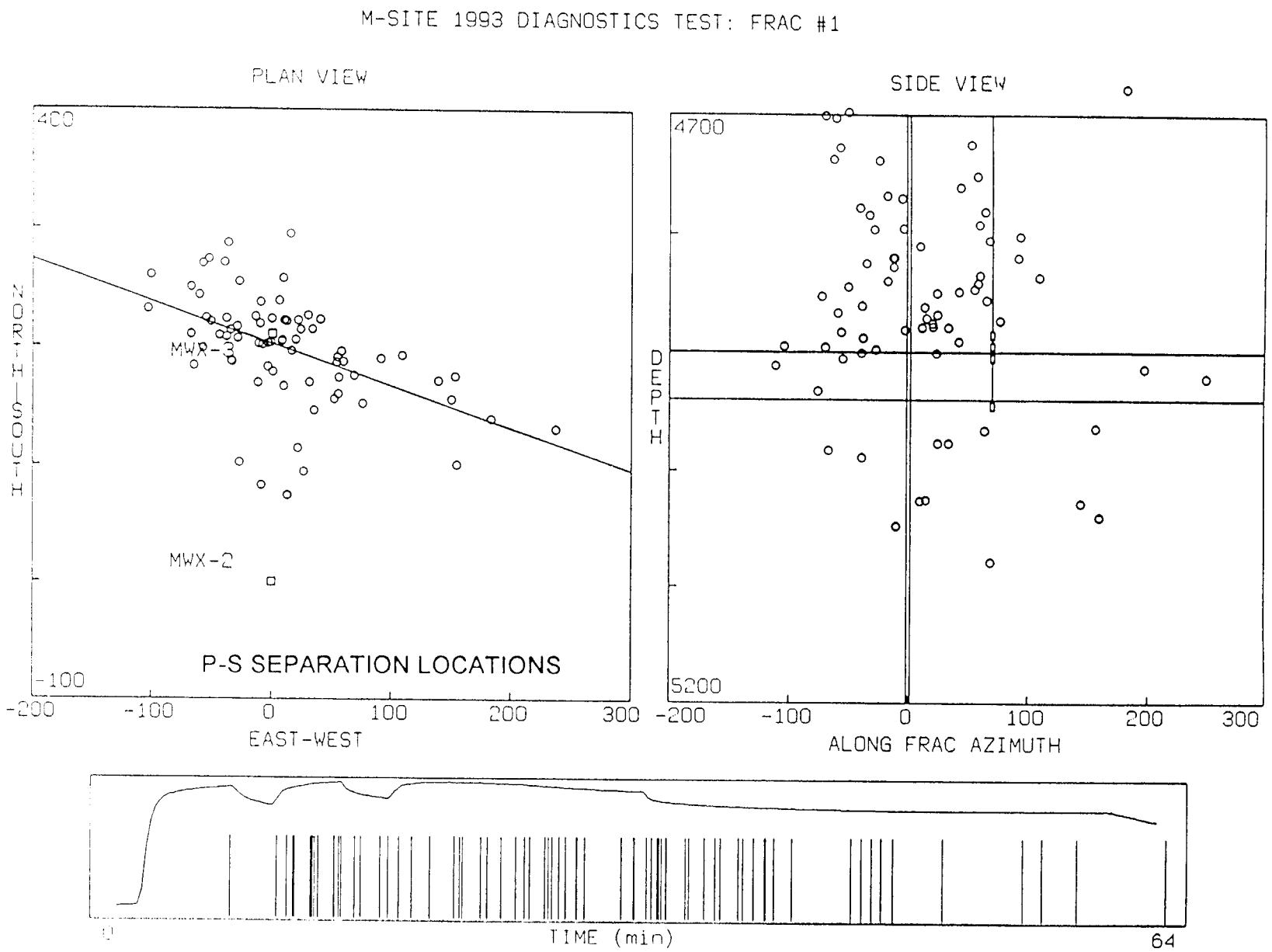

Figure 53. Map of microseisms using p-s separation only

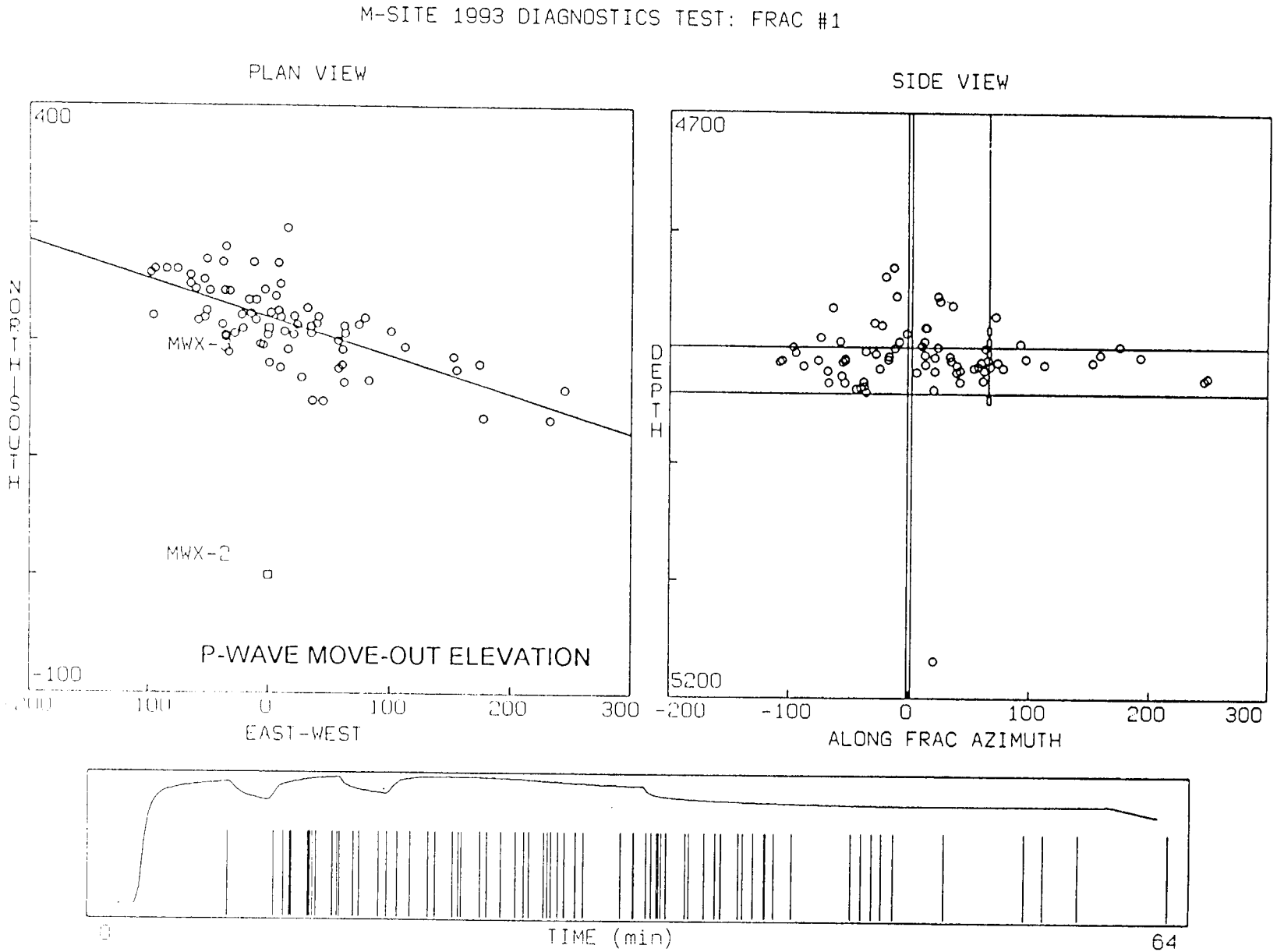

Figure 54. Map of microseisms using p-wave move out for elevation

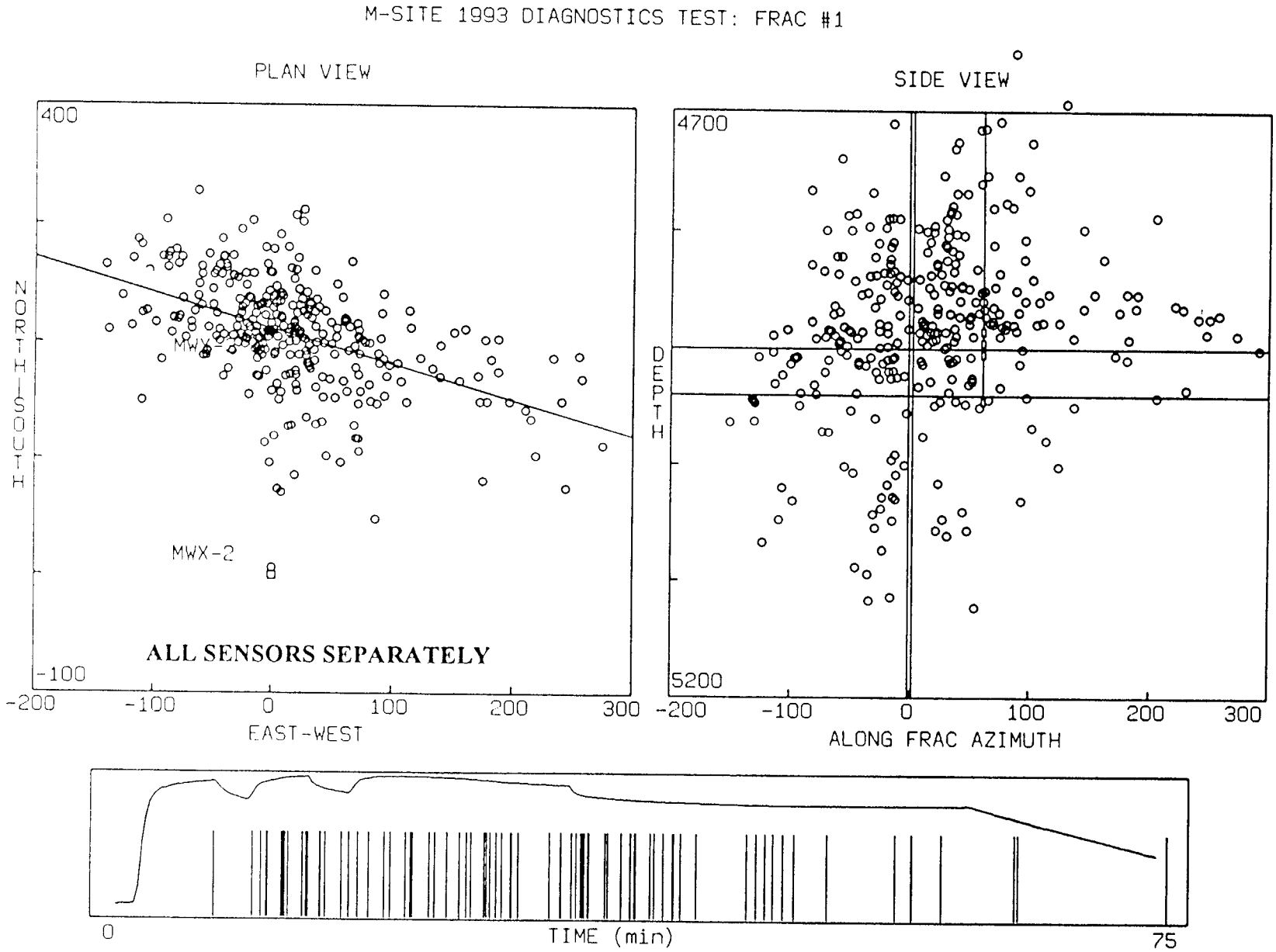

Figure 55. Map of microseisms using all levels independently

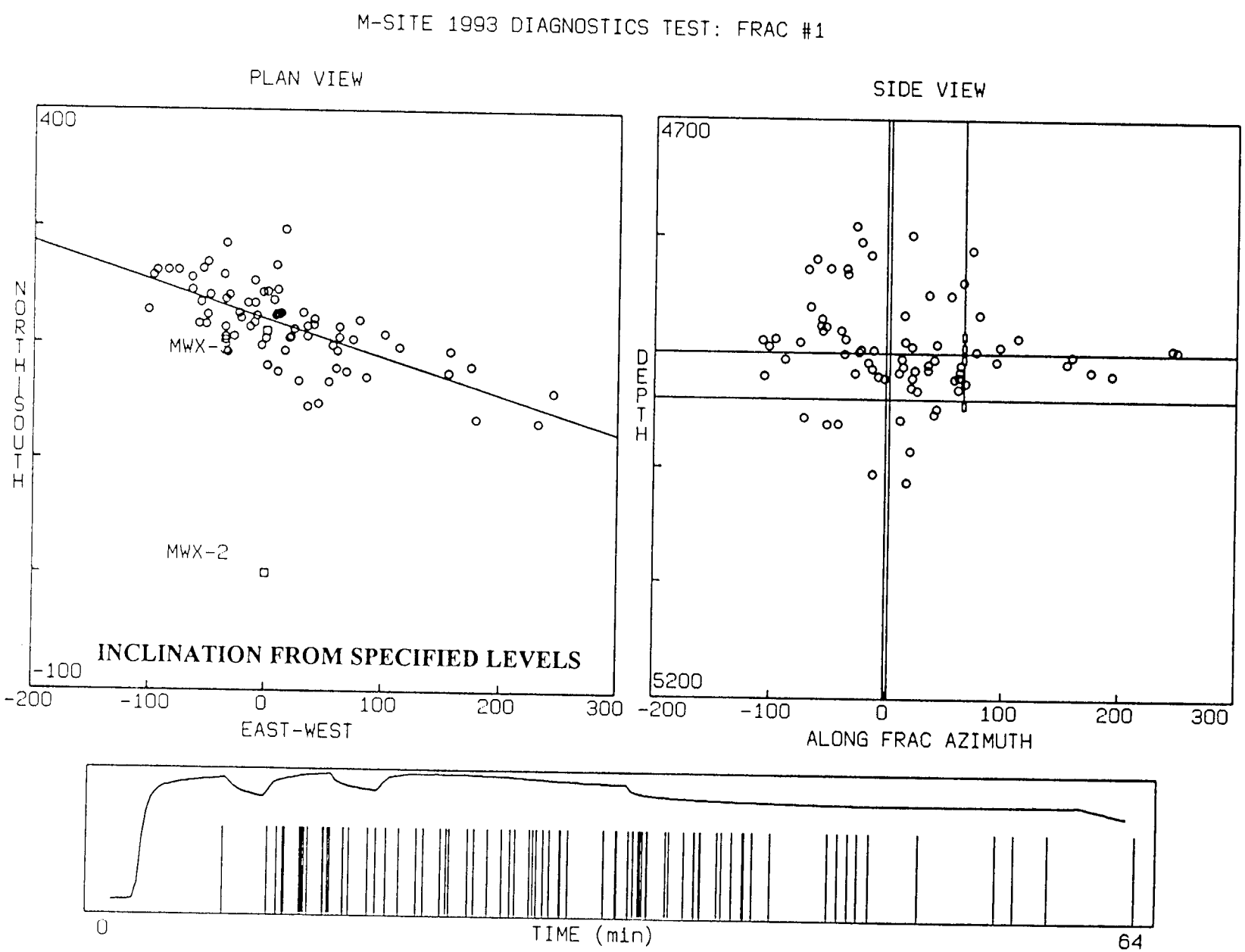

Figure 56. Map of microseisms using inclination from specified levels

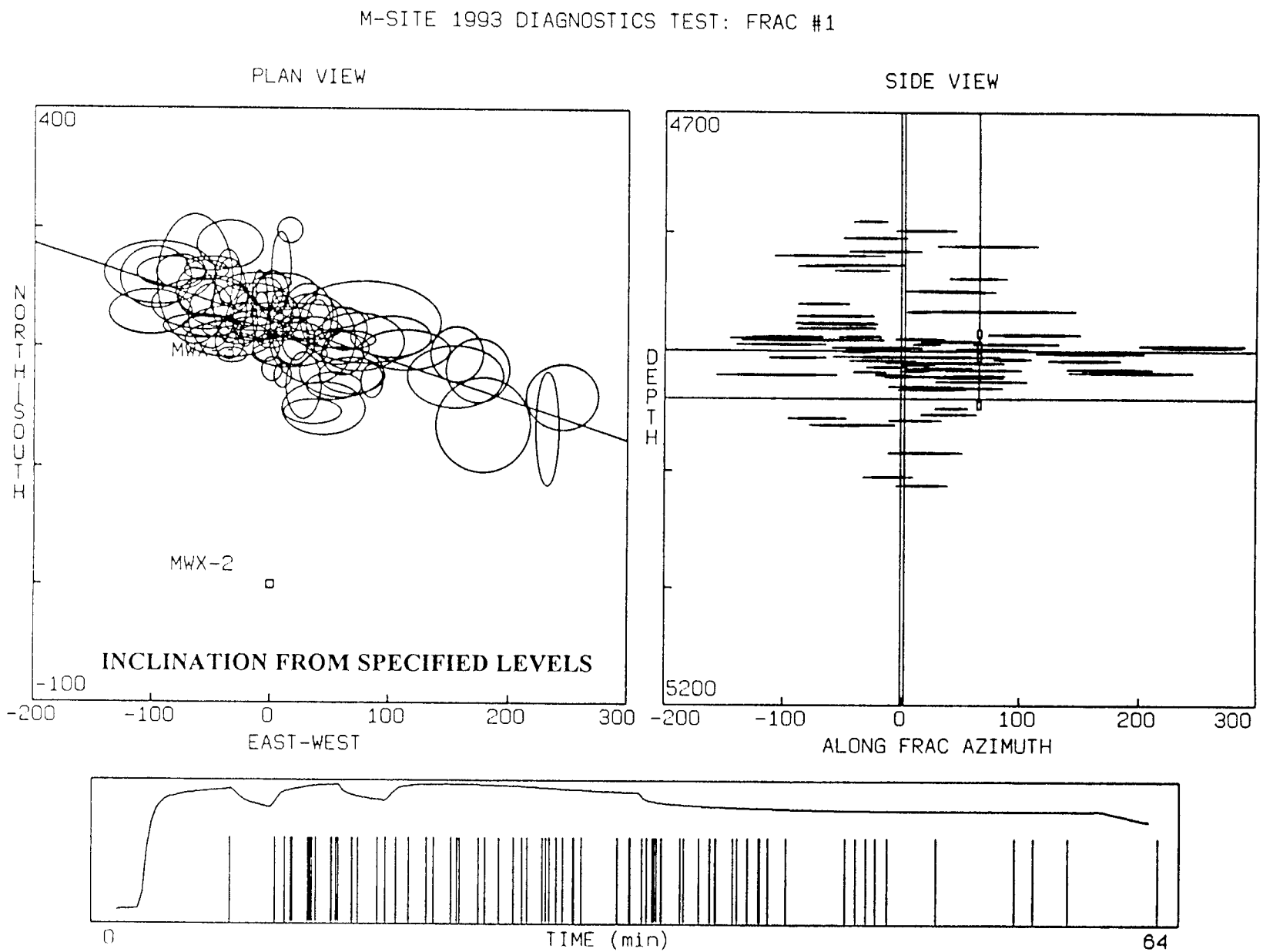

Figure 57. Uncertainty map of microseisms using inclination from specified levels

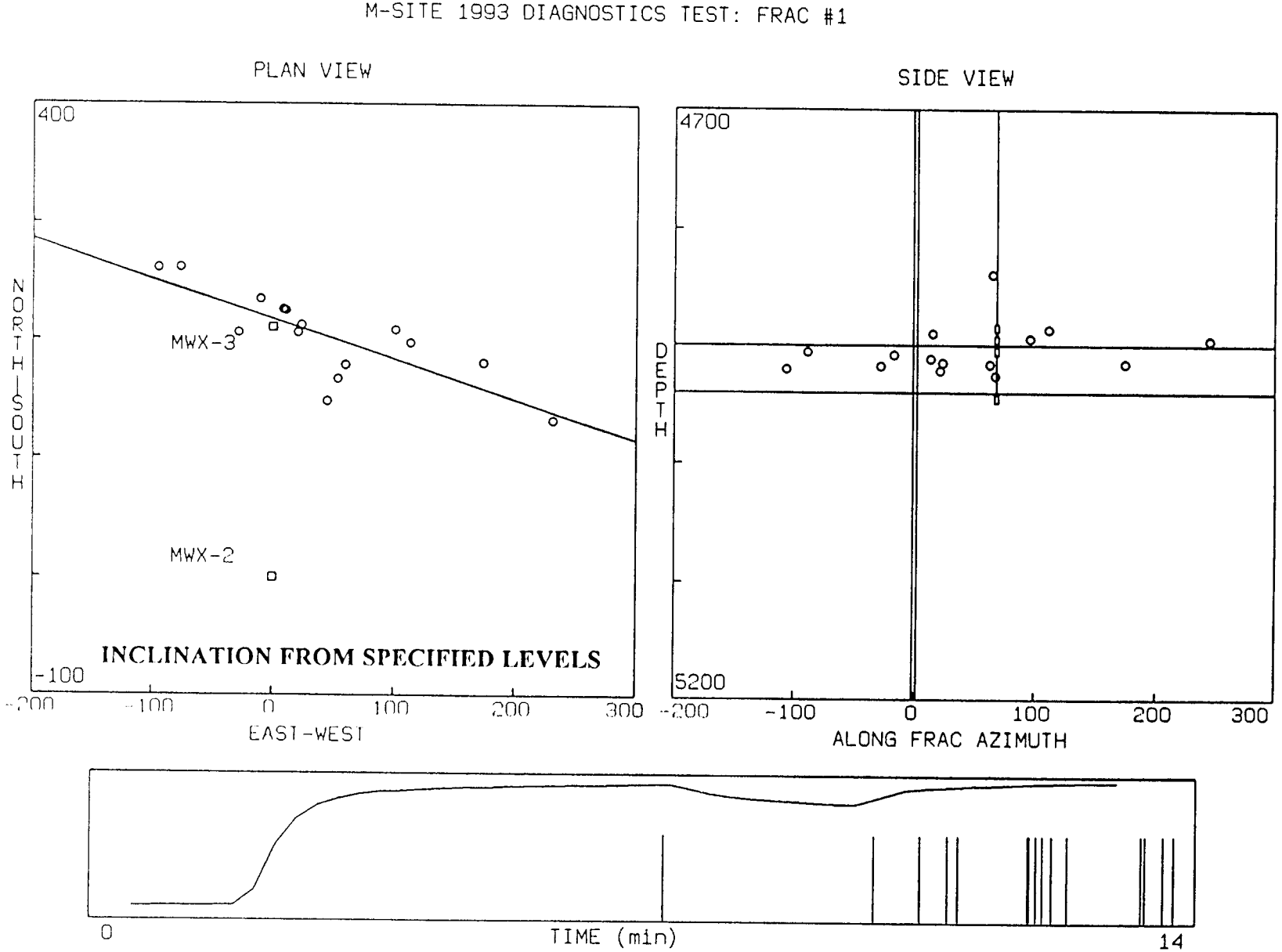

Figure 58. Map of microseisms using inclination from specified levels, time #1

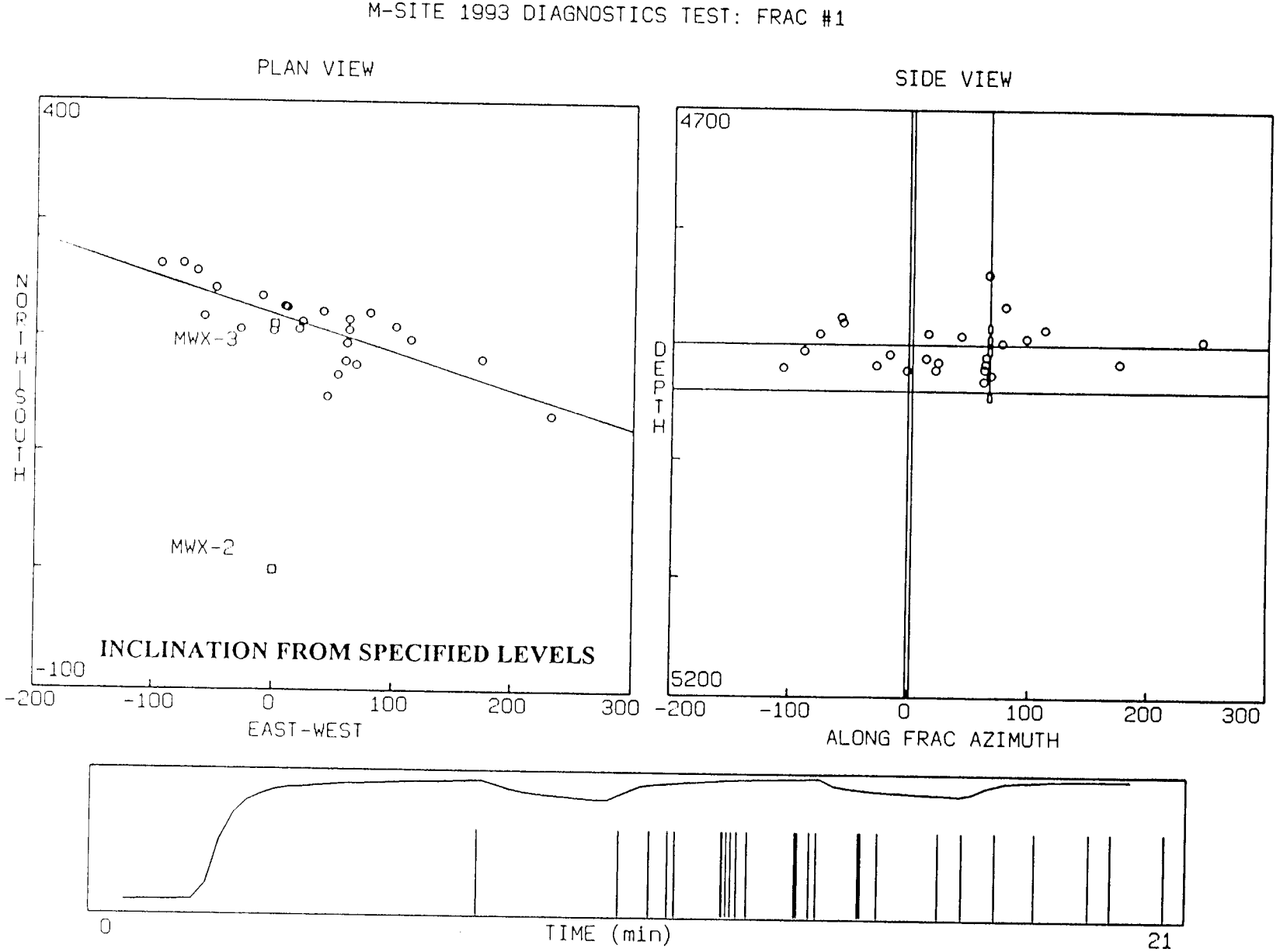

Figure 59. Map of microseisms using inclination from specified levels, time #2

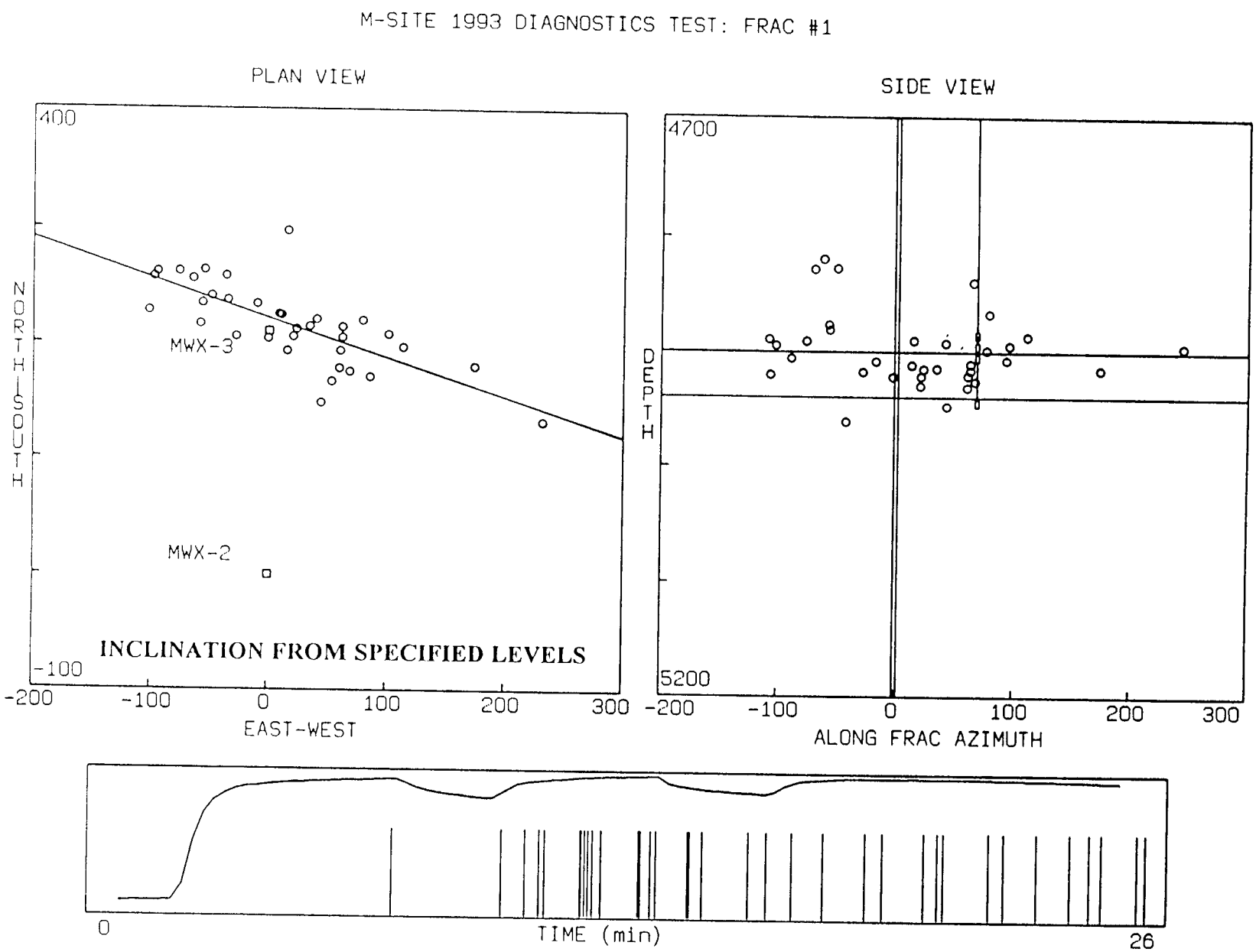

Figure 60. Map of microseisms using inclination from specified levels, time #3

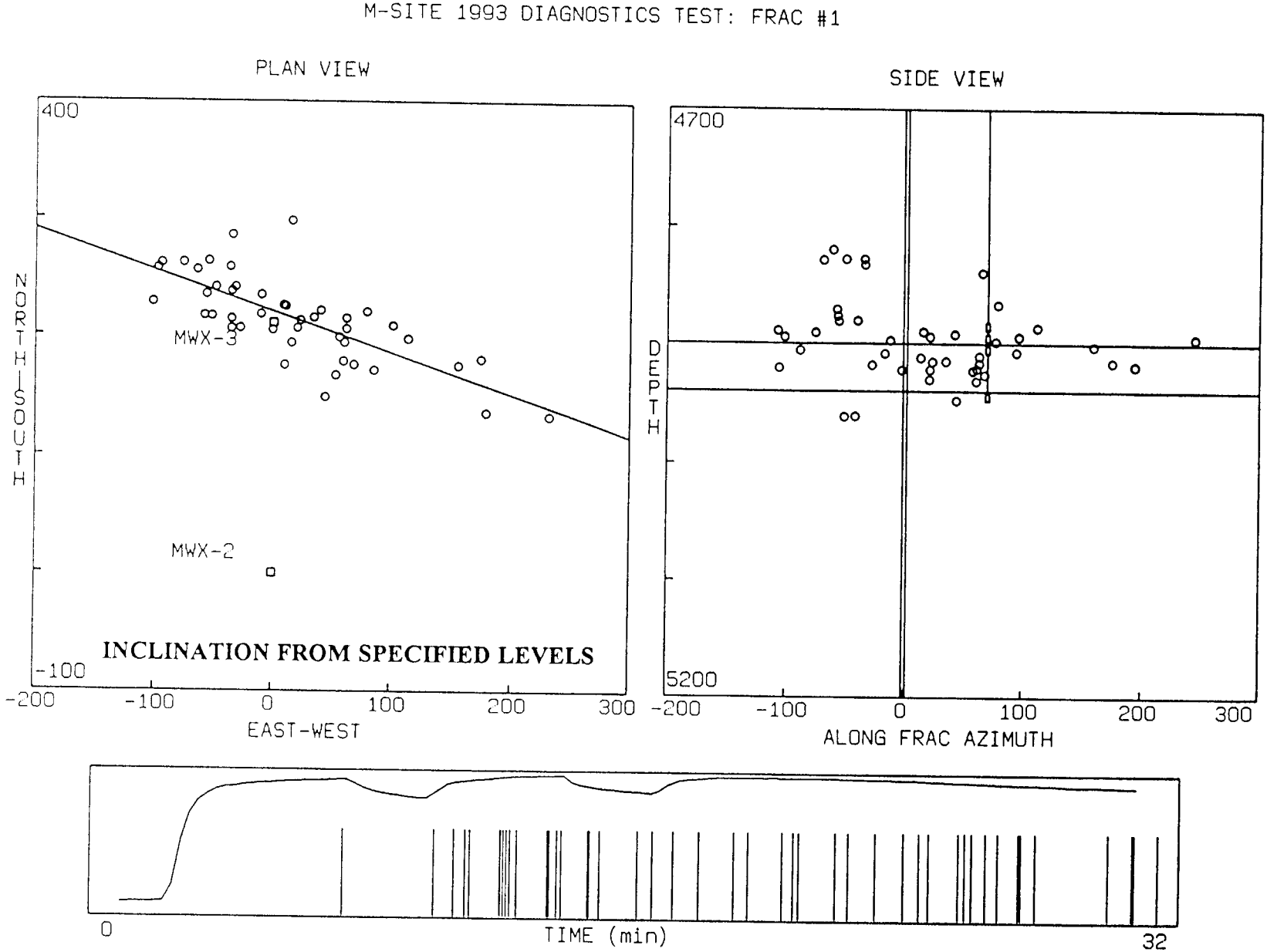

Figure 61. Map of microseisms using inclination from specified levels, time #4

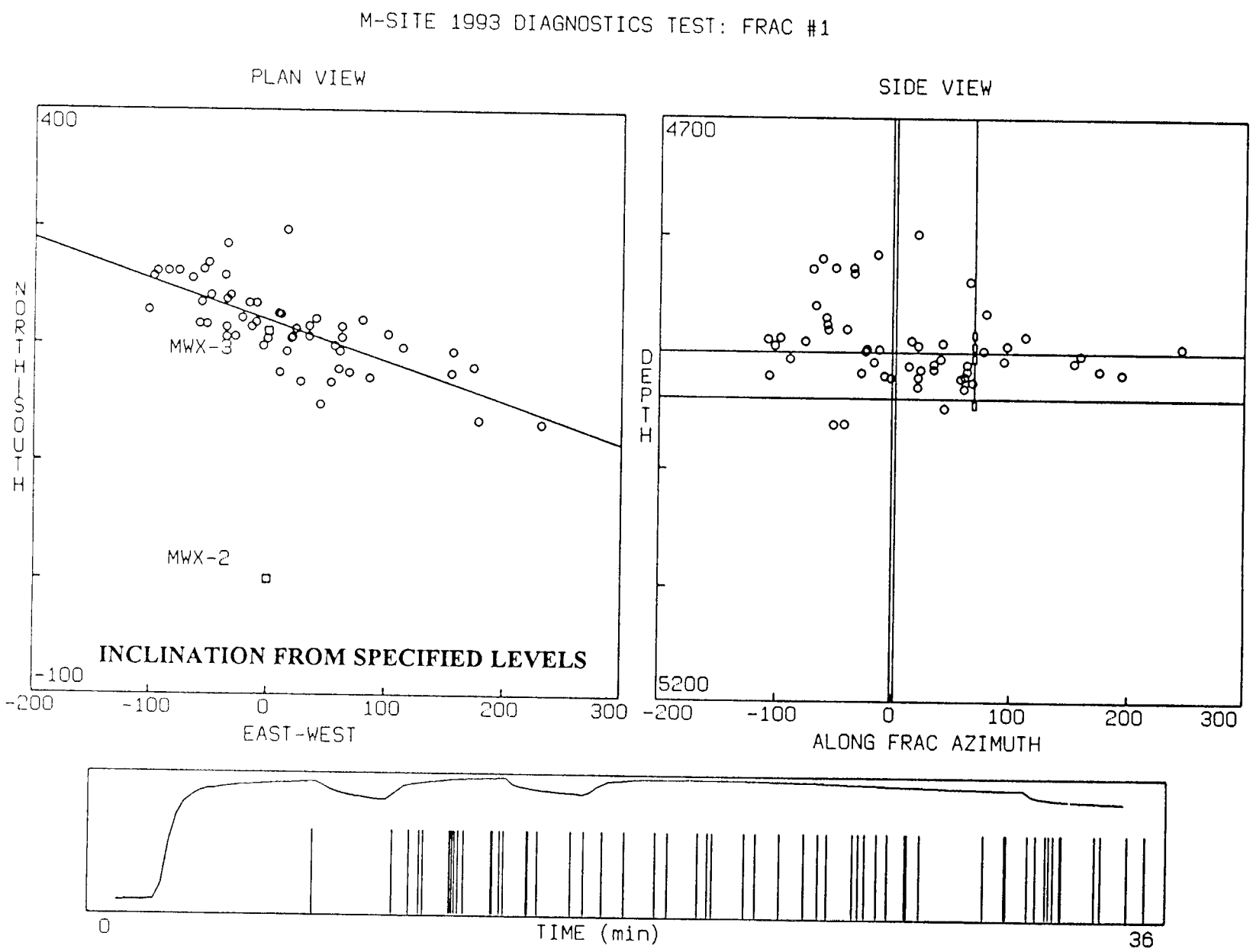

Figure 62. Map of microseisms using inclination from specified levels, time #5

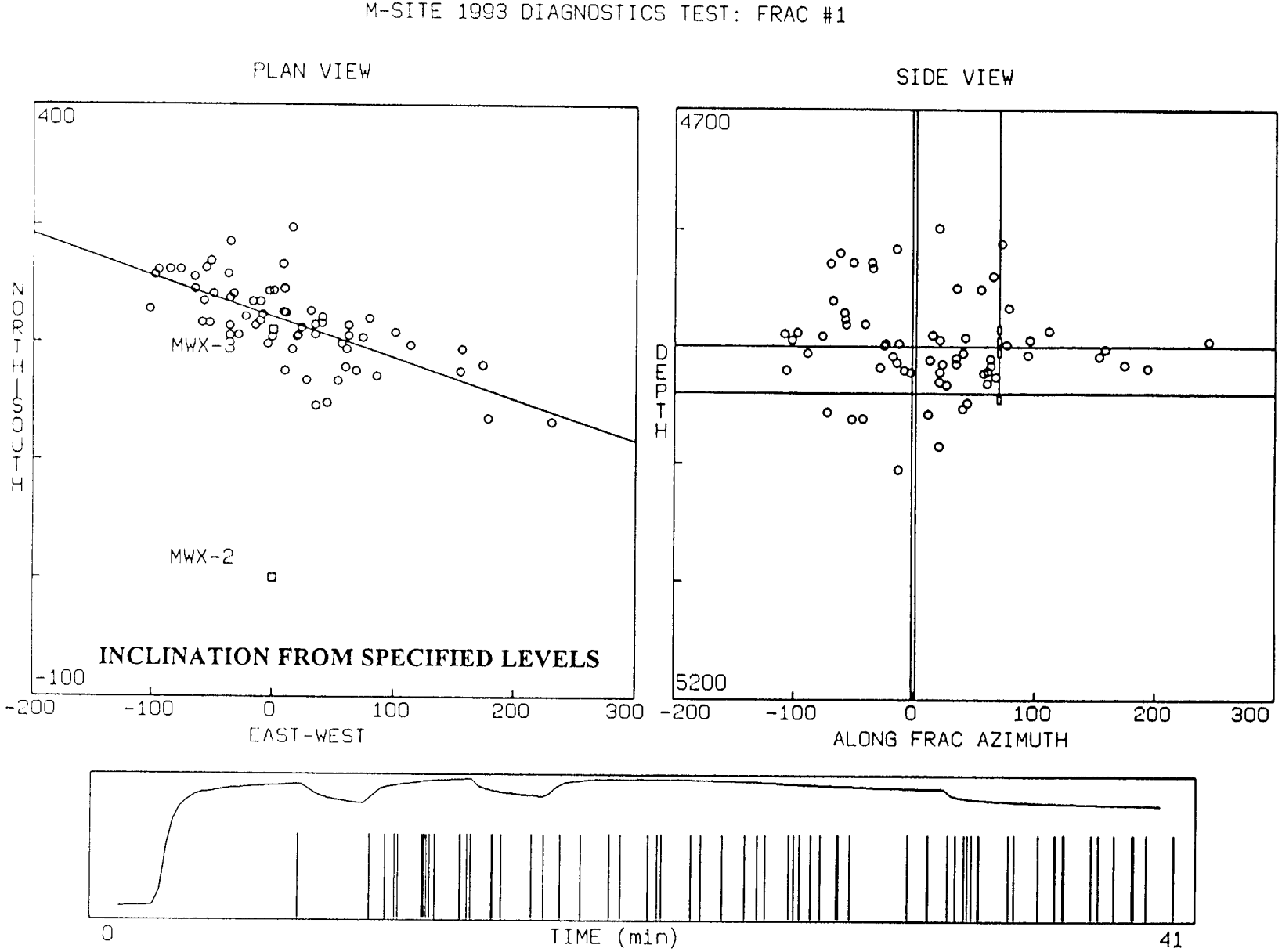

Figure 63. Map of microseisms using inclination from specified levels, time #6

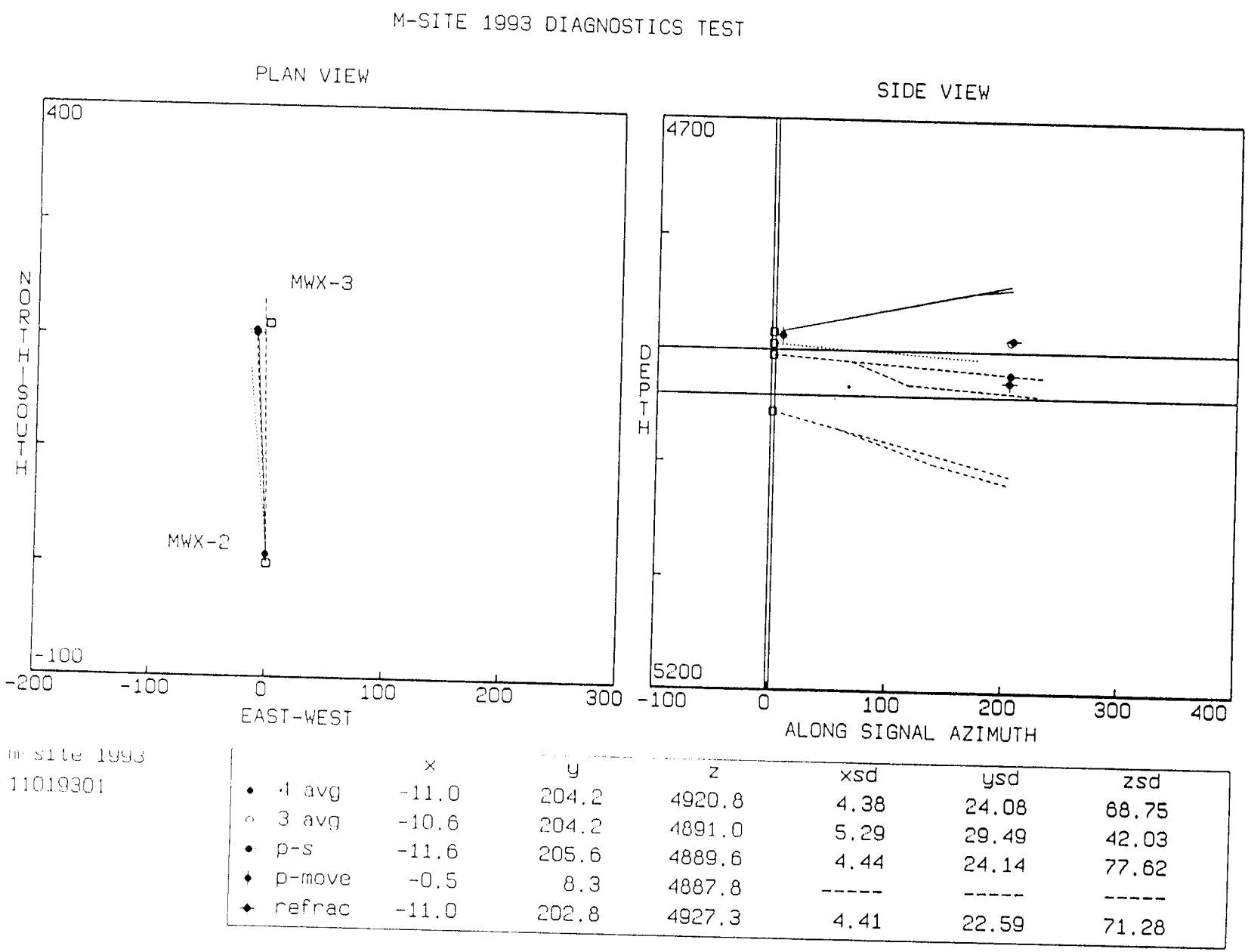

	x	y	z	xsd	ysd	zsd
1 avg	-11.0	204.2	4920.8	4.38	24.08	68.75
3 avg	-10.6	204.2	4891.0	5.29	29.49	42.03
p-s	-11.6	205.6	4889.6	4.44	24.14	77.62
p-move	-0.5	8.3	4887.8	-----	-----	-----
refrac	-11.0	202.8	4927.3	4.41	22.59	71.28

Figure 64. Refraction tracing plot, event #1

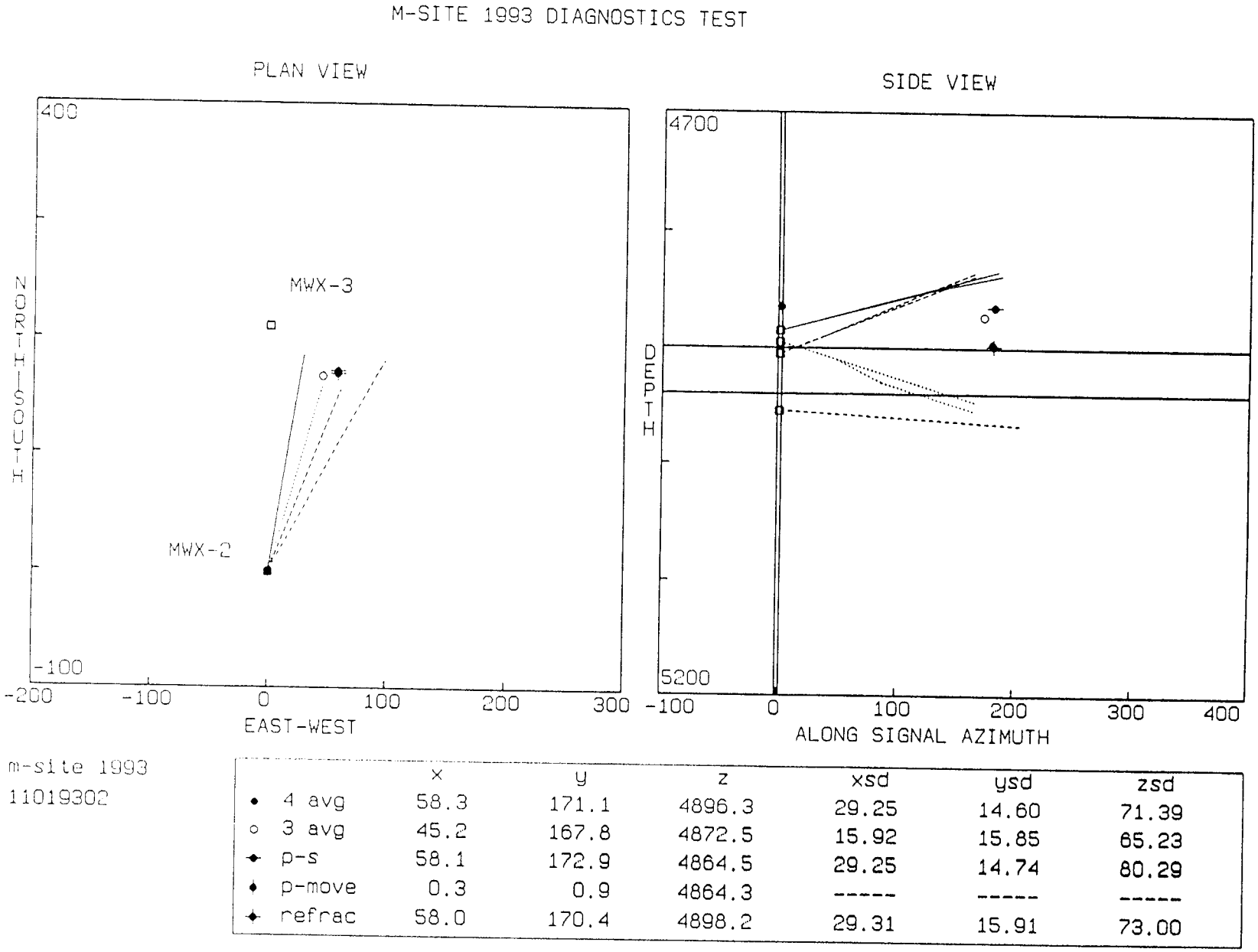

	x	y	z	xsd	ysd	zsd
• 4 avg	58.3	171.1	4896.3	29.25	14.60	71.39
○ 3 avg	45.2	167.8	4872.5	15.92	15.85	65.23
✦ p-s	58.1	172.9	4864.5	29.25	14.74	80.29
✦ p-move	0.3	0.9	4864.3	-----	-----	-----
✦ refrac	58.0	170.4	4898.2	29.31	15.91	73.00

Figure 65. Refraction tracing plot, event #2

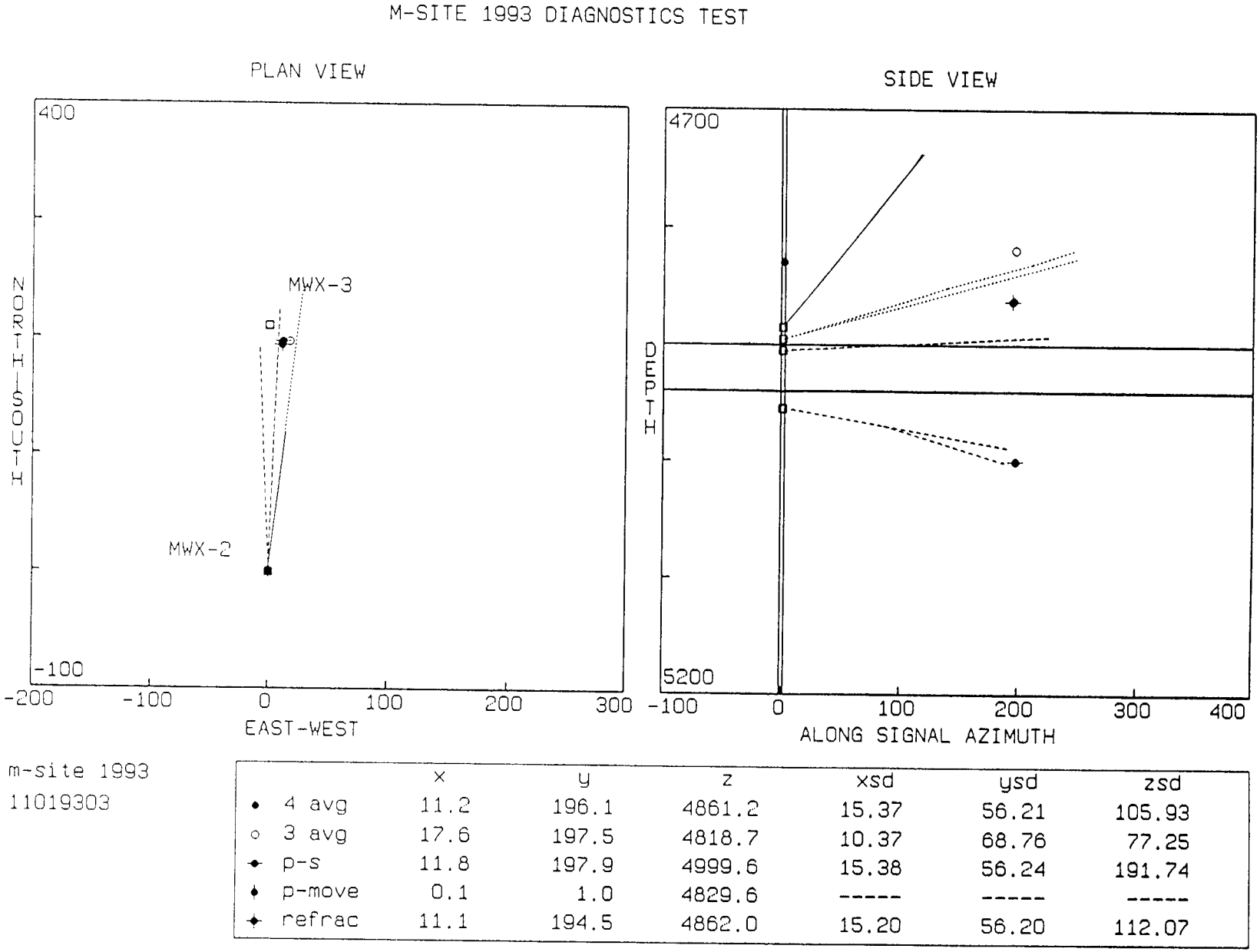

	x	y	z	xsd	ysd	zsd
• 4 avg	11.2	196.1	4861.2	15.37	56.21	105.93
○ 3 avg	17.6	197.5	4818.7	10.37	68.76	77.25
◆ p-s	11.8	197.9	4999.6	15.38	56.24	191.74
♦ p-move	0.1	1.0	4829.6	-----	-----	-----
✦ refrac	11.1	194.5	4862.0	15.20	56.20	112.07

Figure 66. Refraction tracing plot, event #3

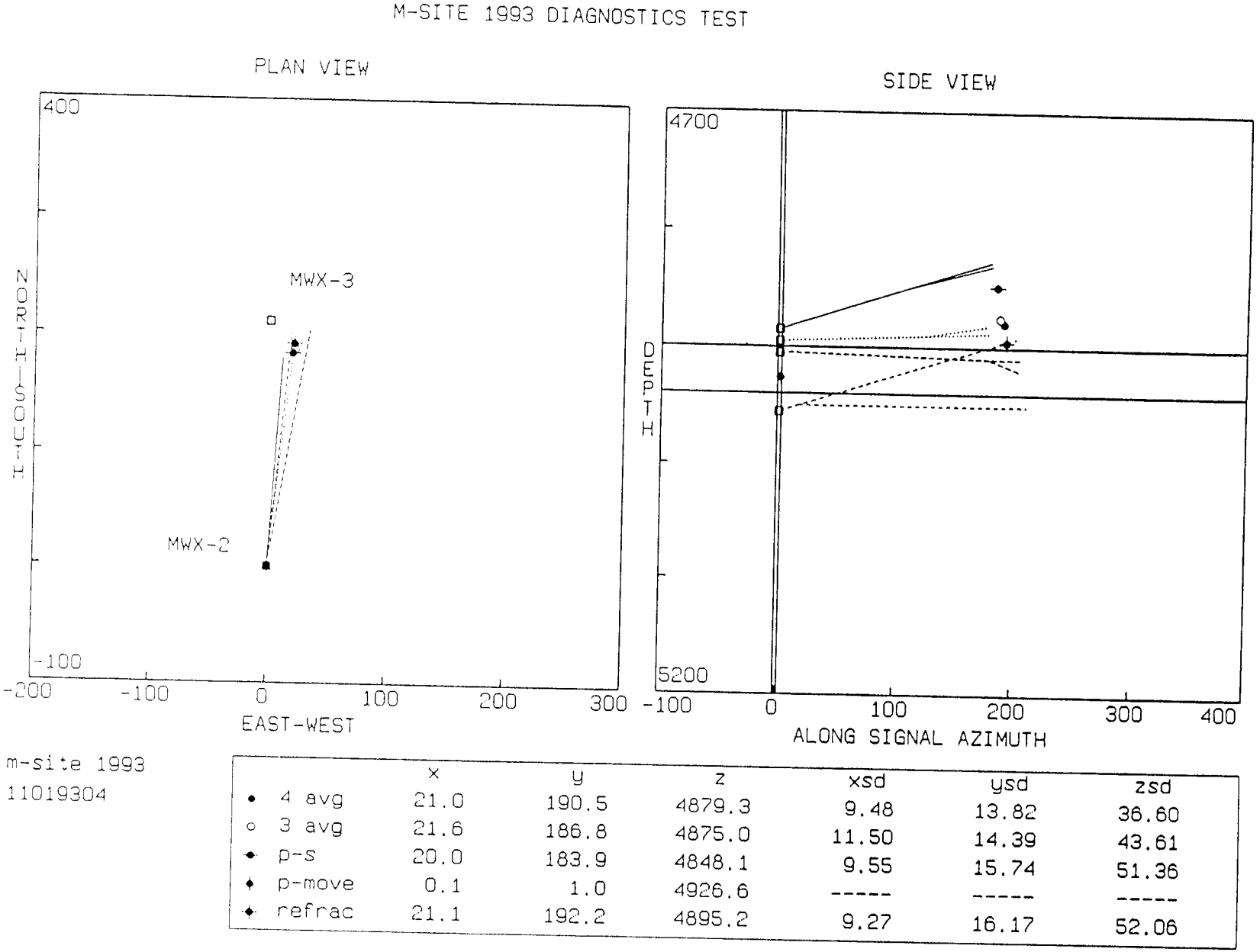

Figure 67. Refraction tracing plot, event #4

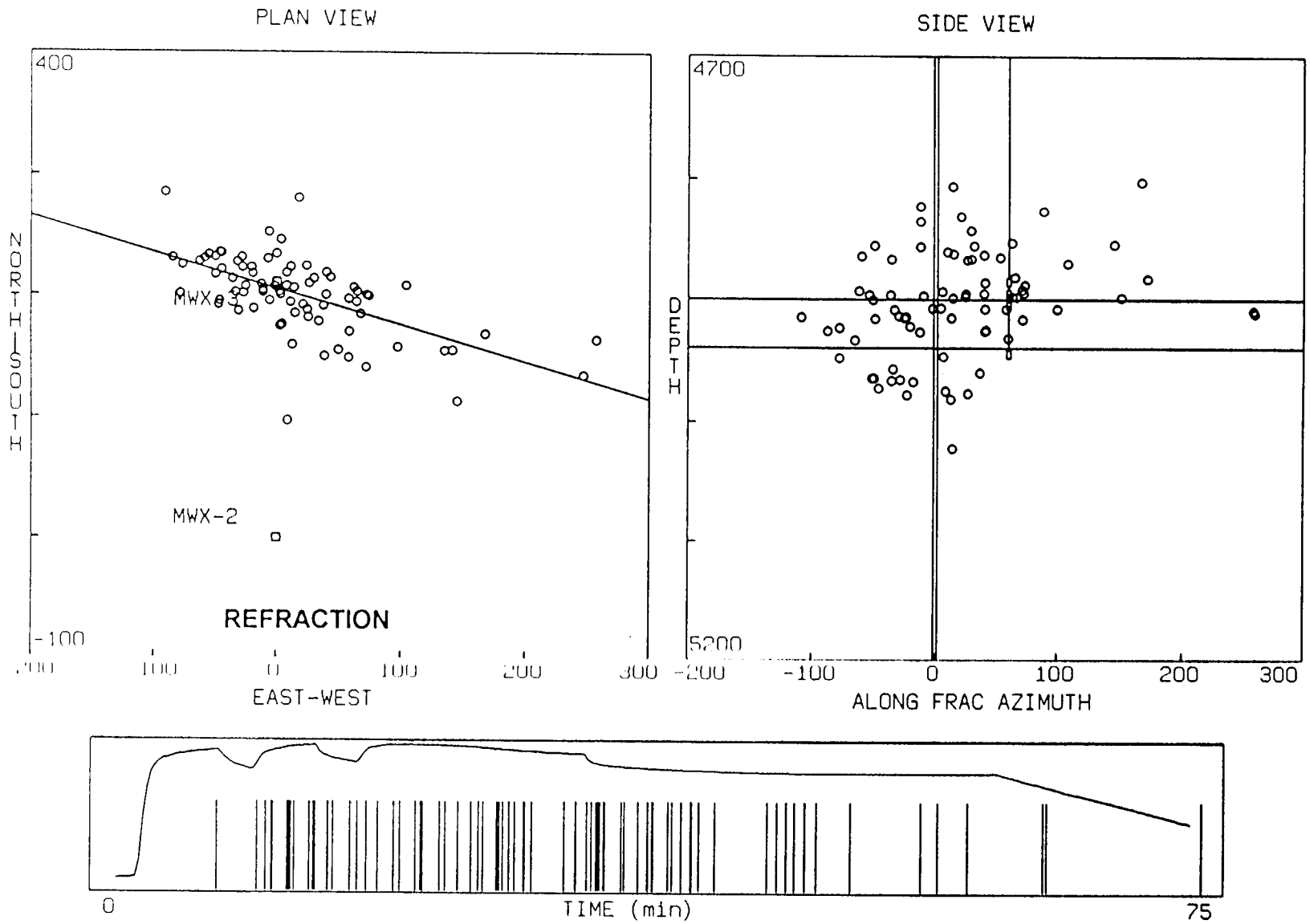

Figure 68. Refraction microseism map

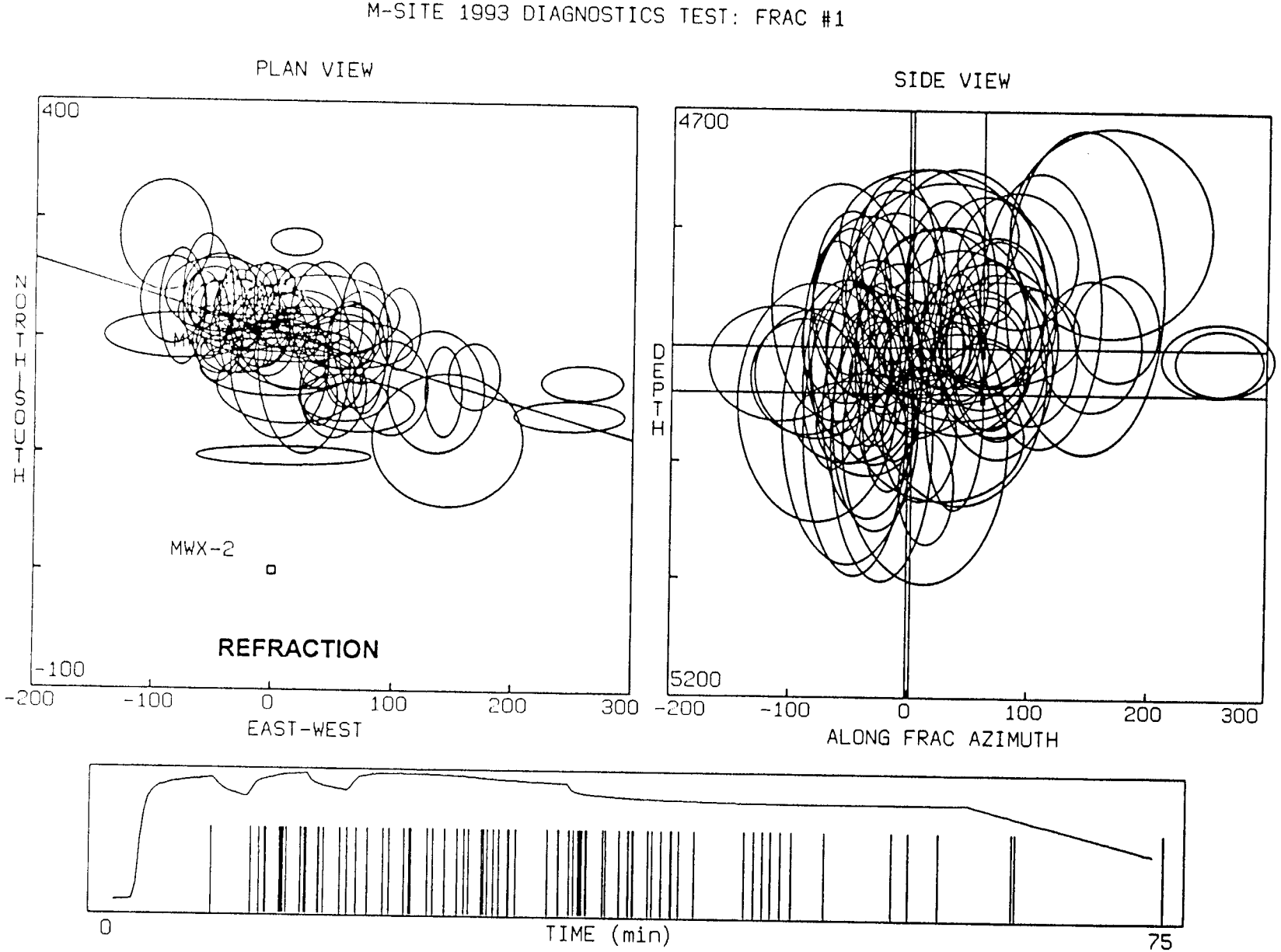

Figure 69. Refraction uncertainty microseism map

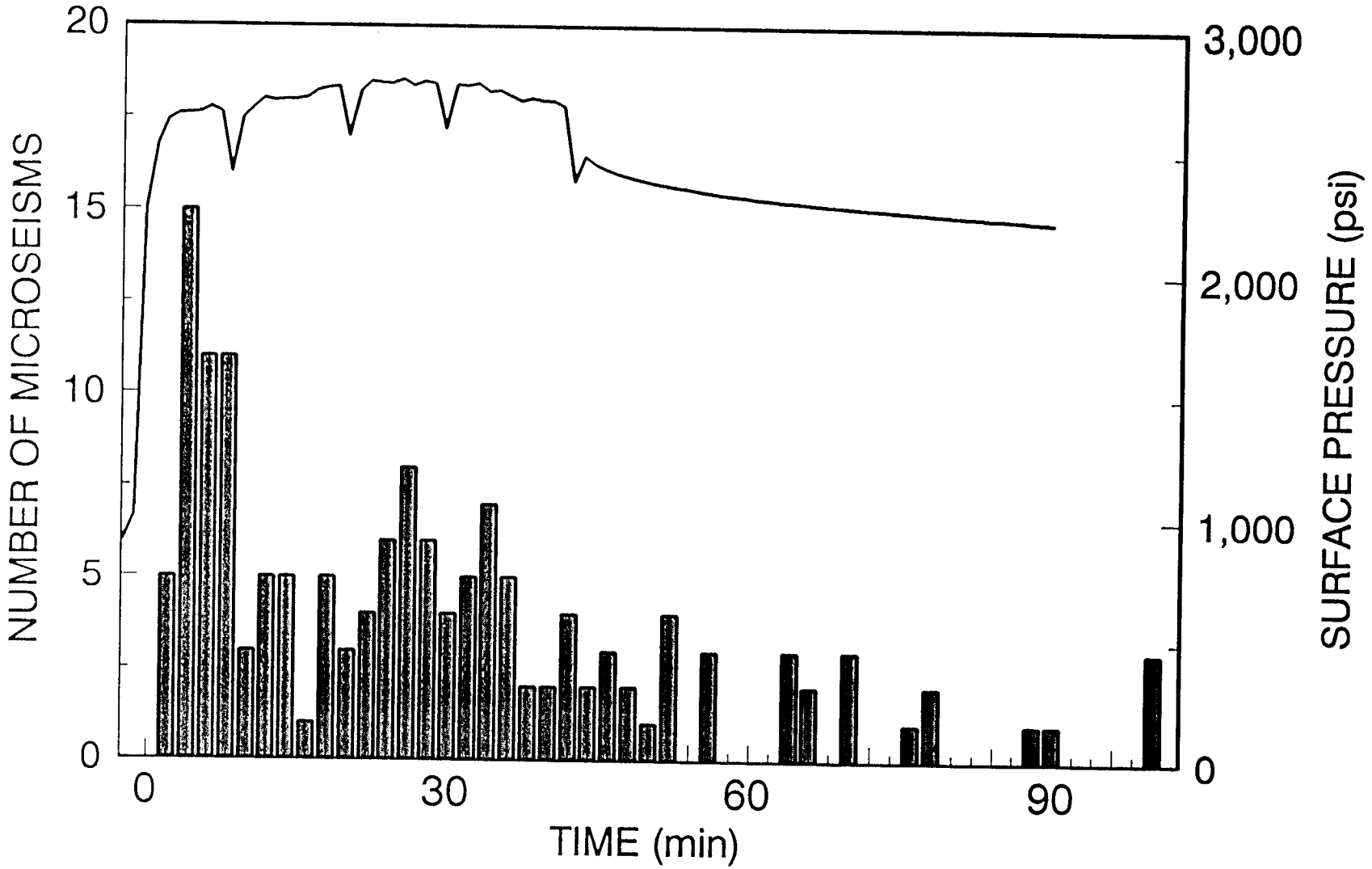

Figure 70. Histogram of events for minifrac #2

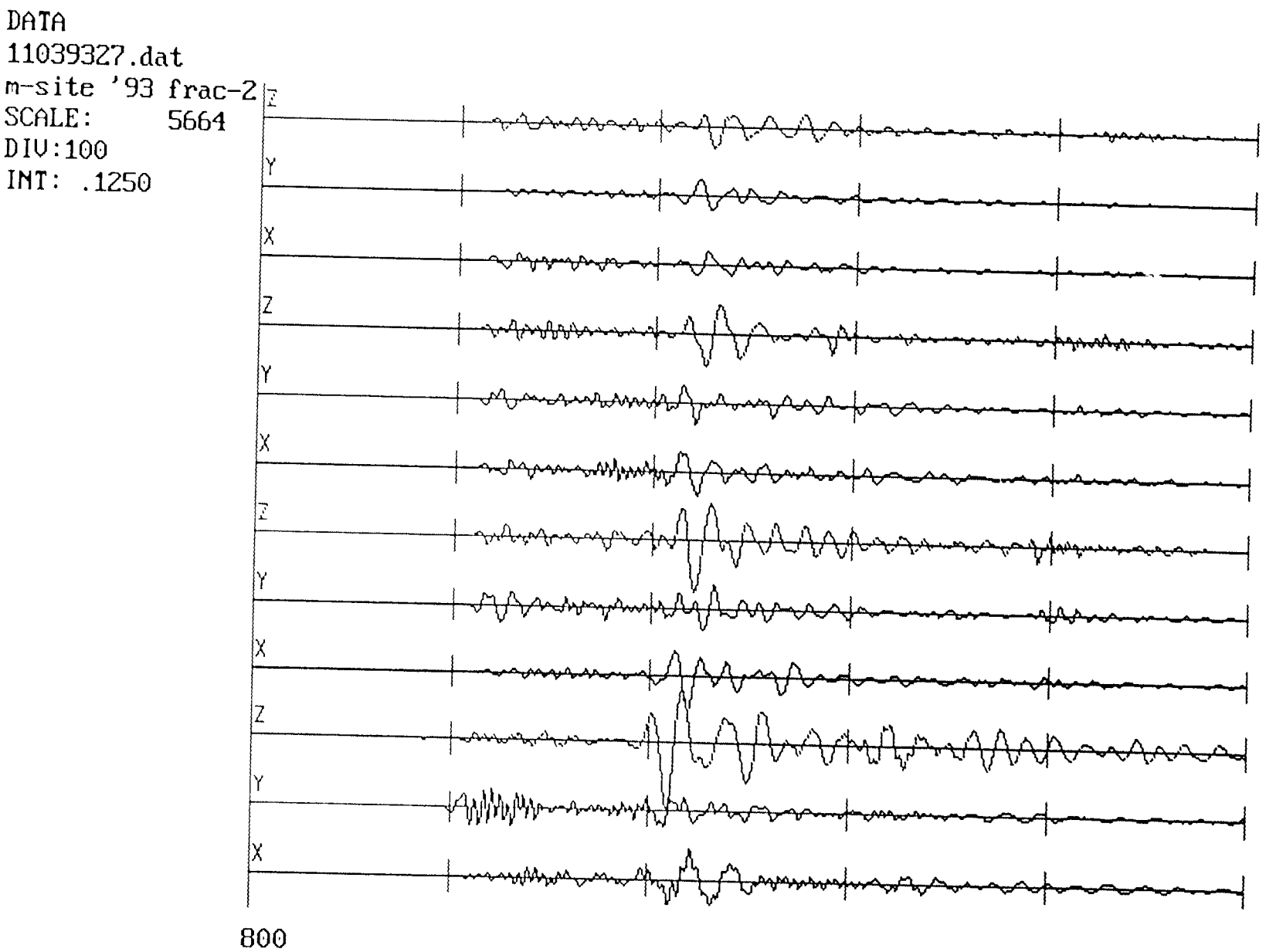

Figure 71. Example low frequency event from minifrac #2

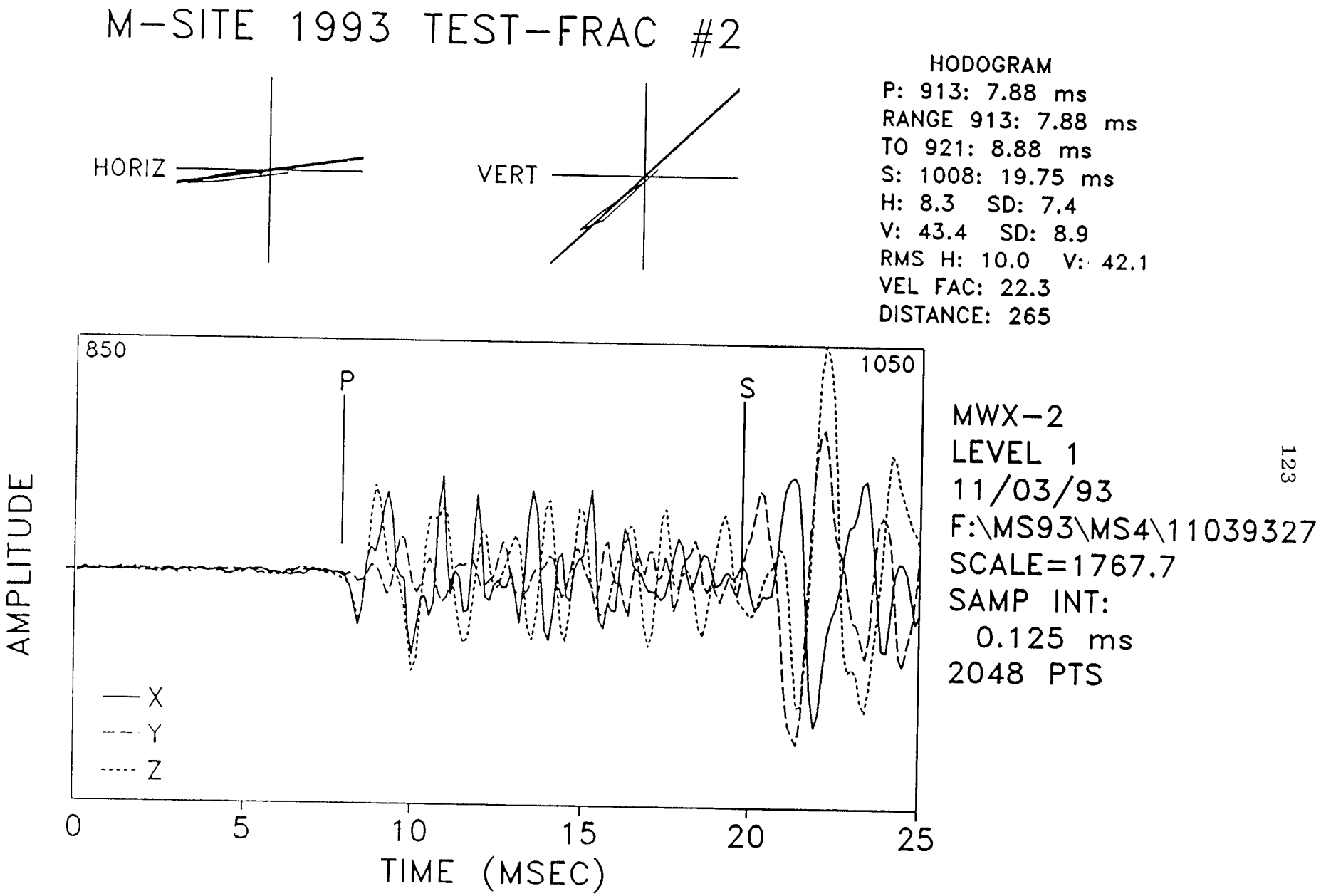

Figure 72. Trace and hodograms of example event from minifrac #2, level 1

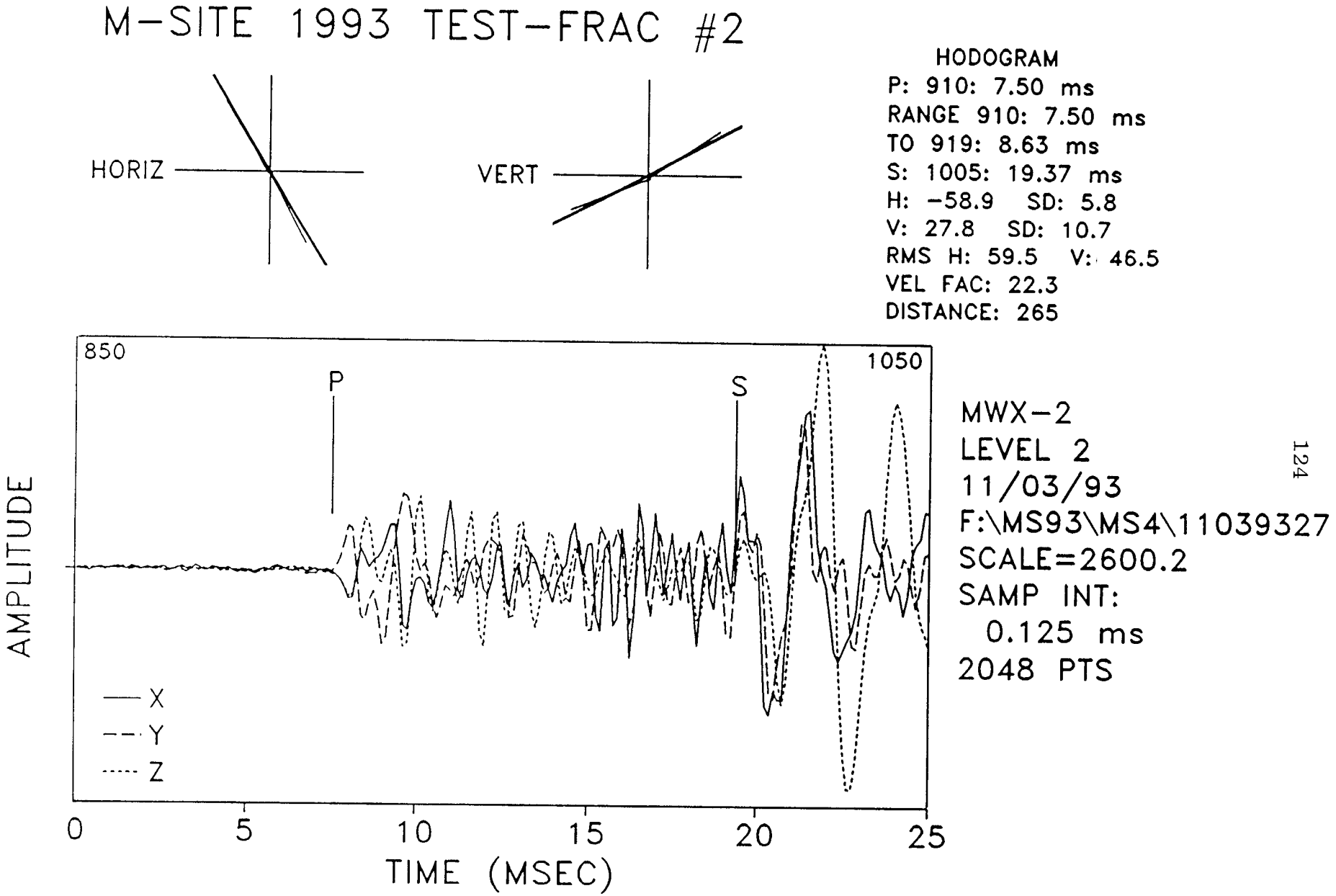

Figure 73. Trace and hodograms of example event from minifrac #2, level 2

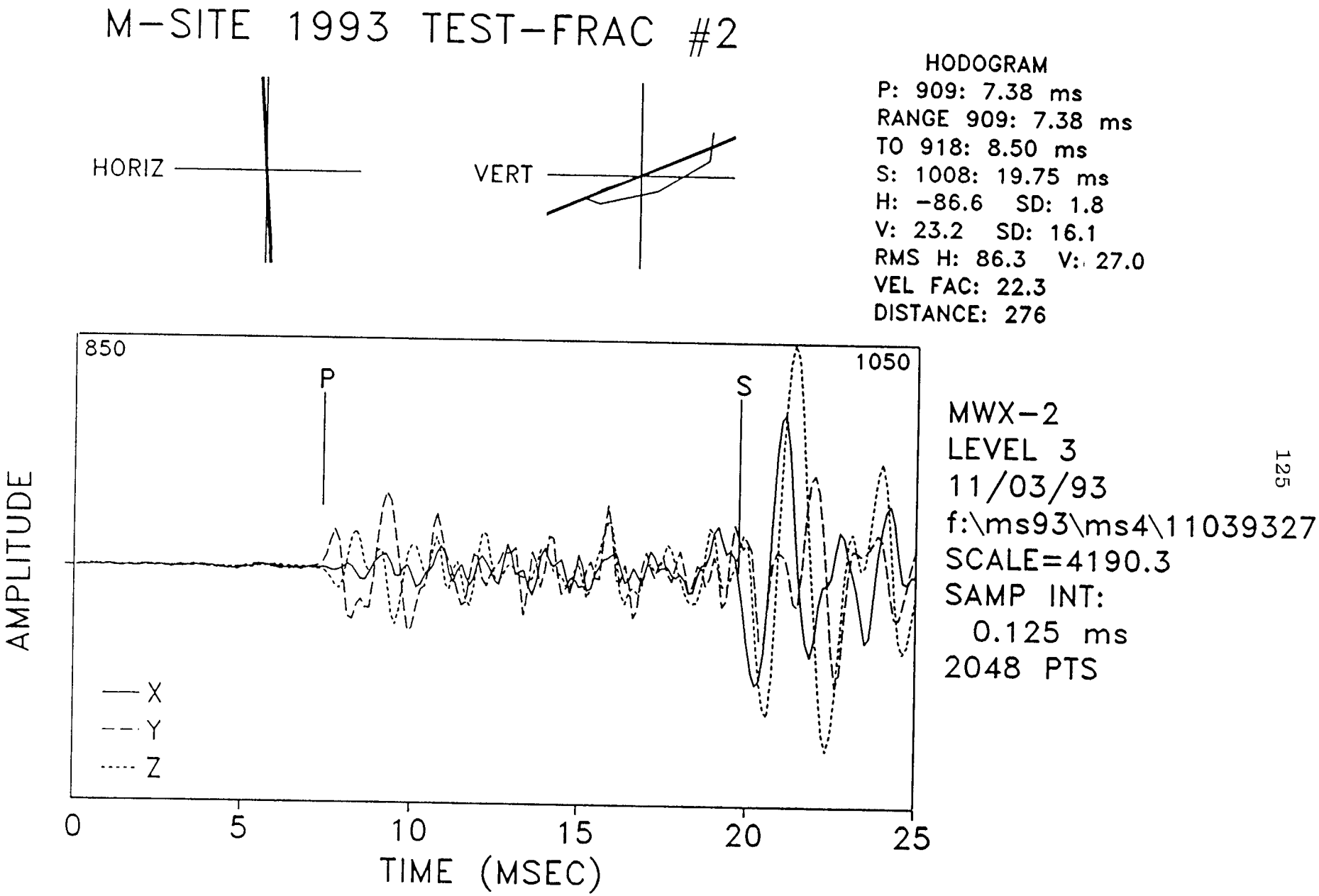

Figure 74. Trace and hodograms of example event from minifrac #2, level 3

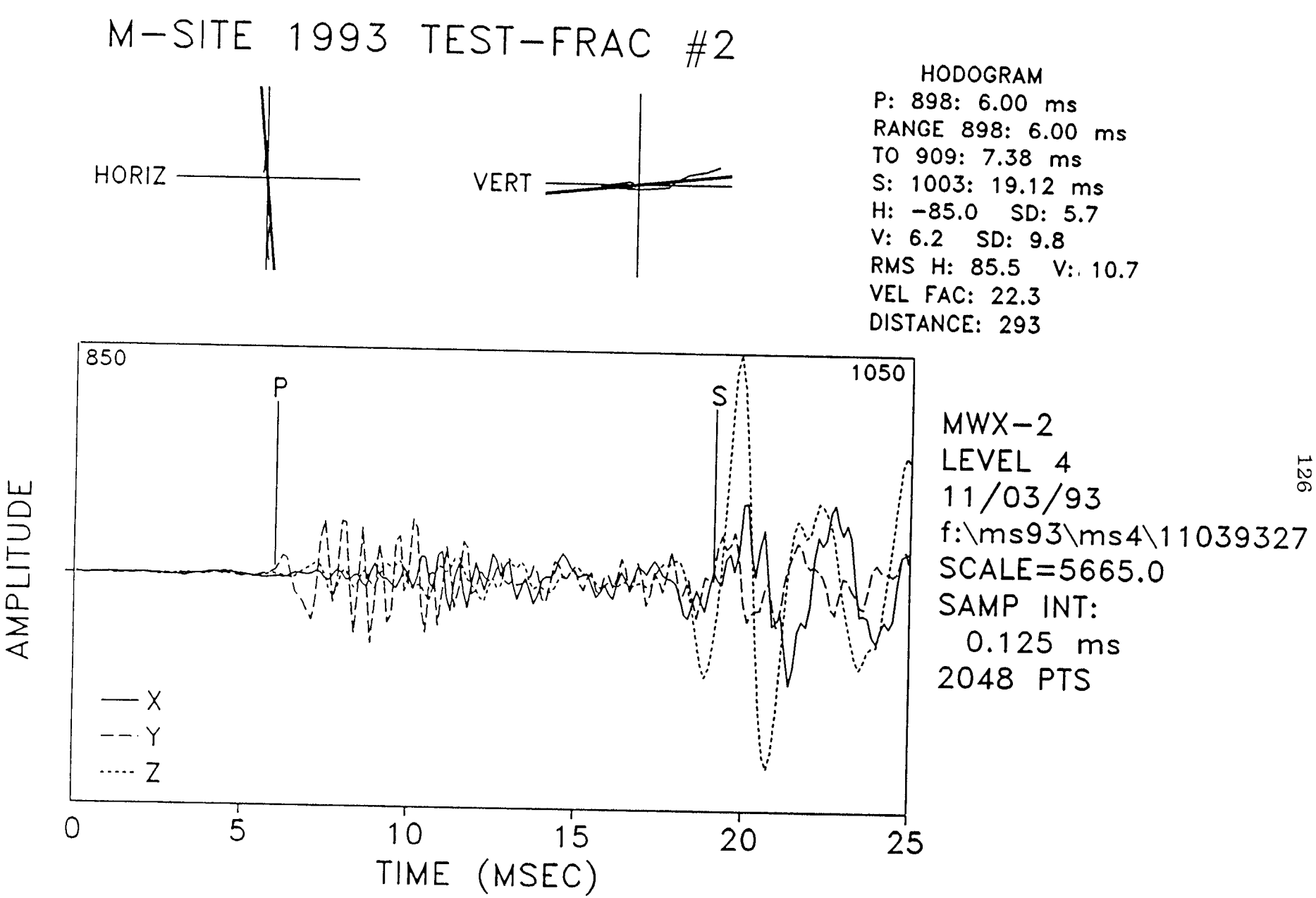

Figure 75. Trace and hodograms of example event from minifrac #2, level 4

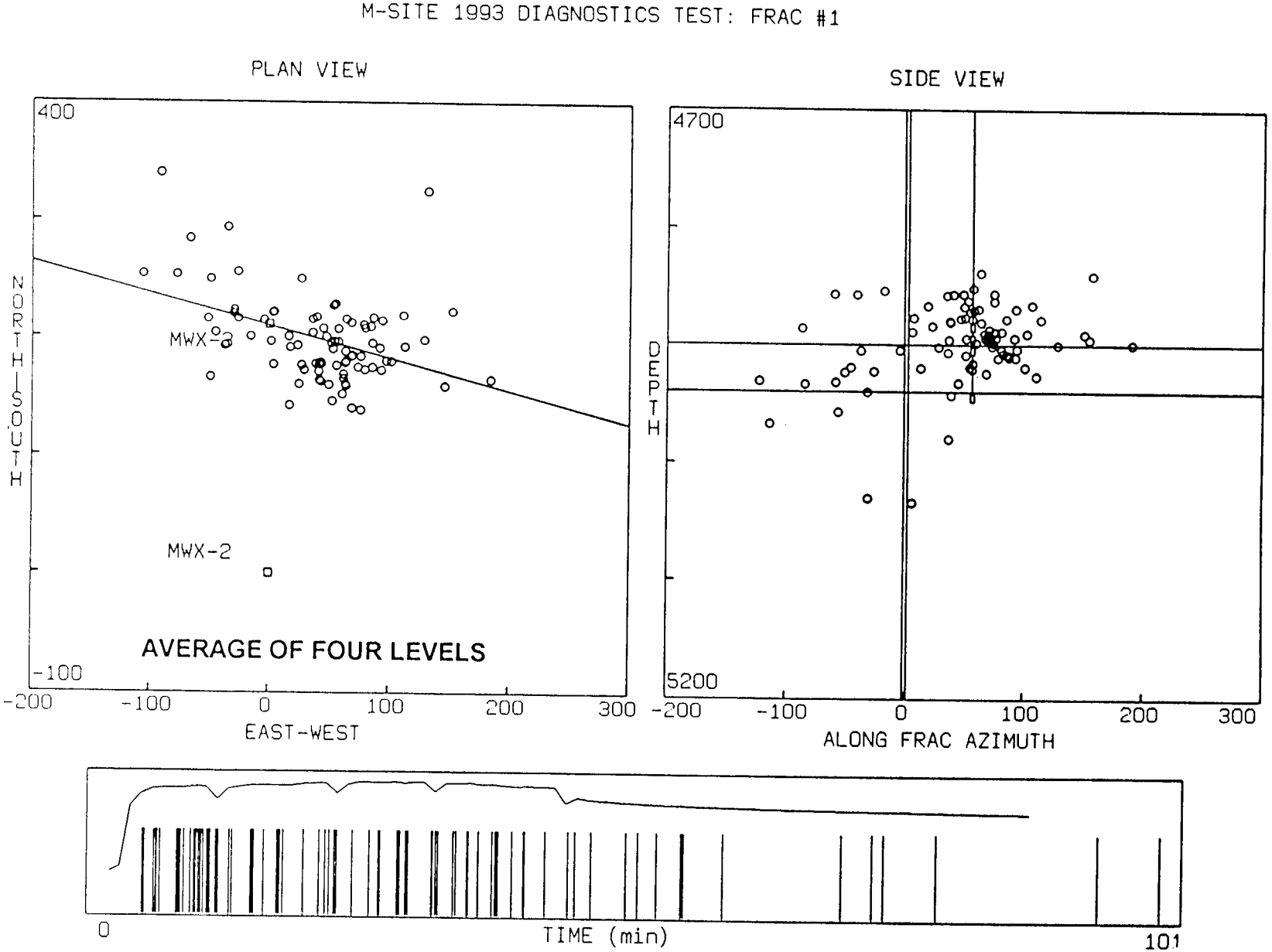

Figure 76. Map of microseisms using average of all four levels, minifrac #2

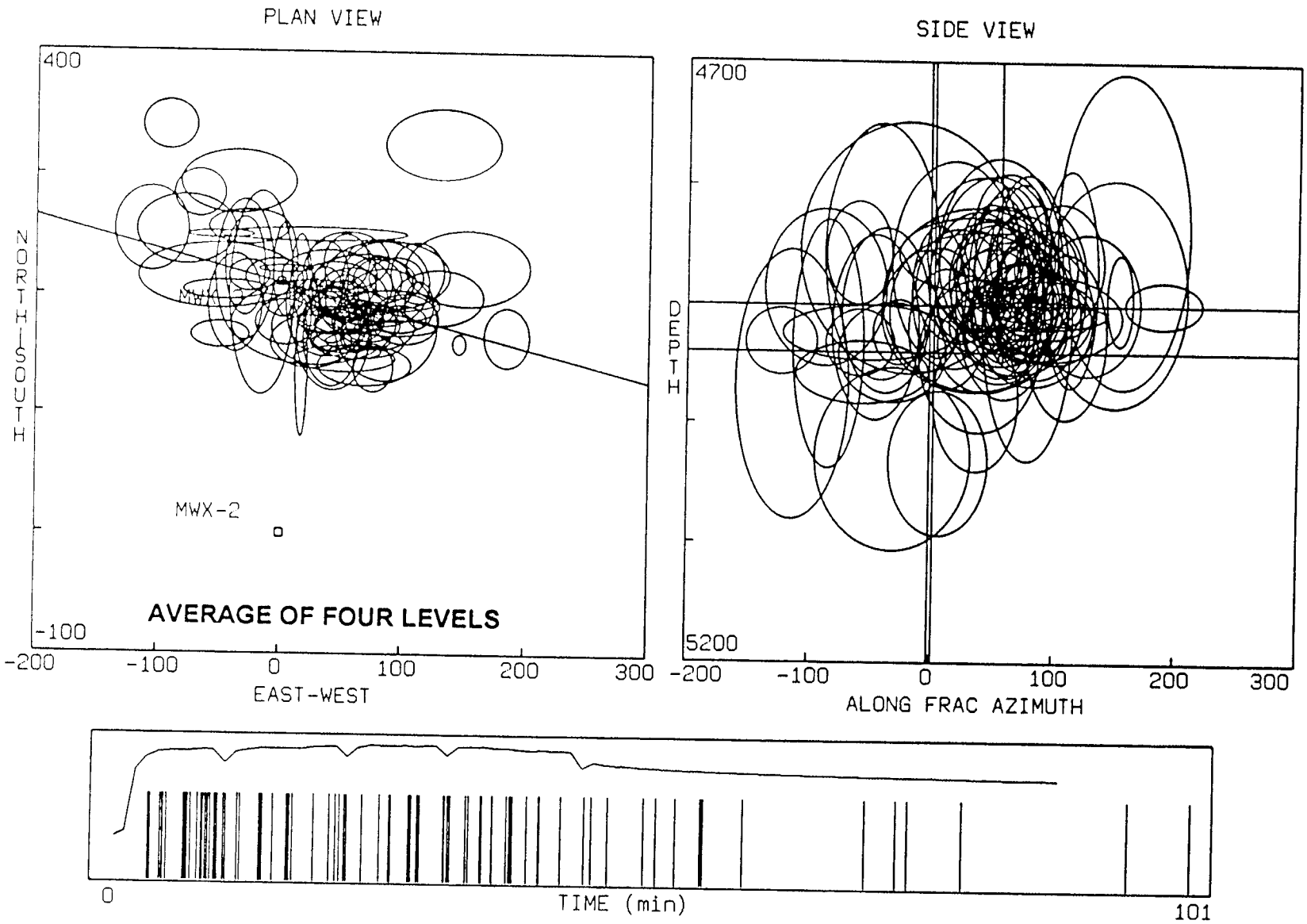

Figure 77. Uncertainty map of microseisms using average of all four levels, minifrac #2

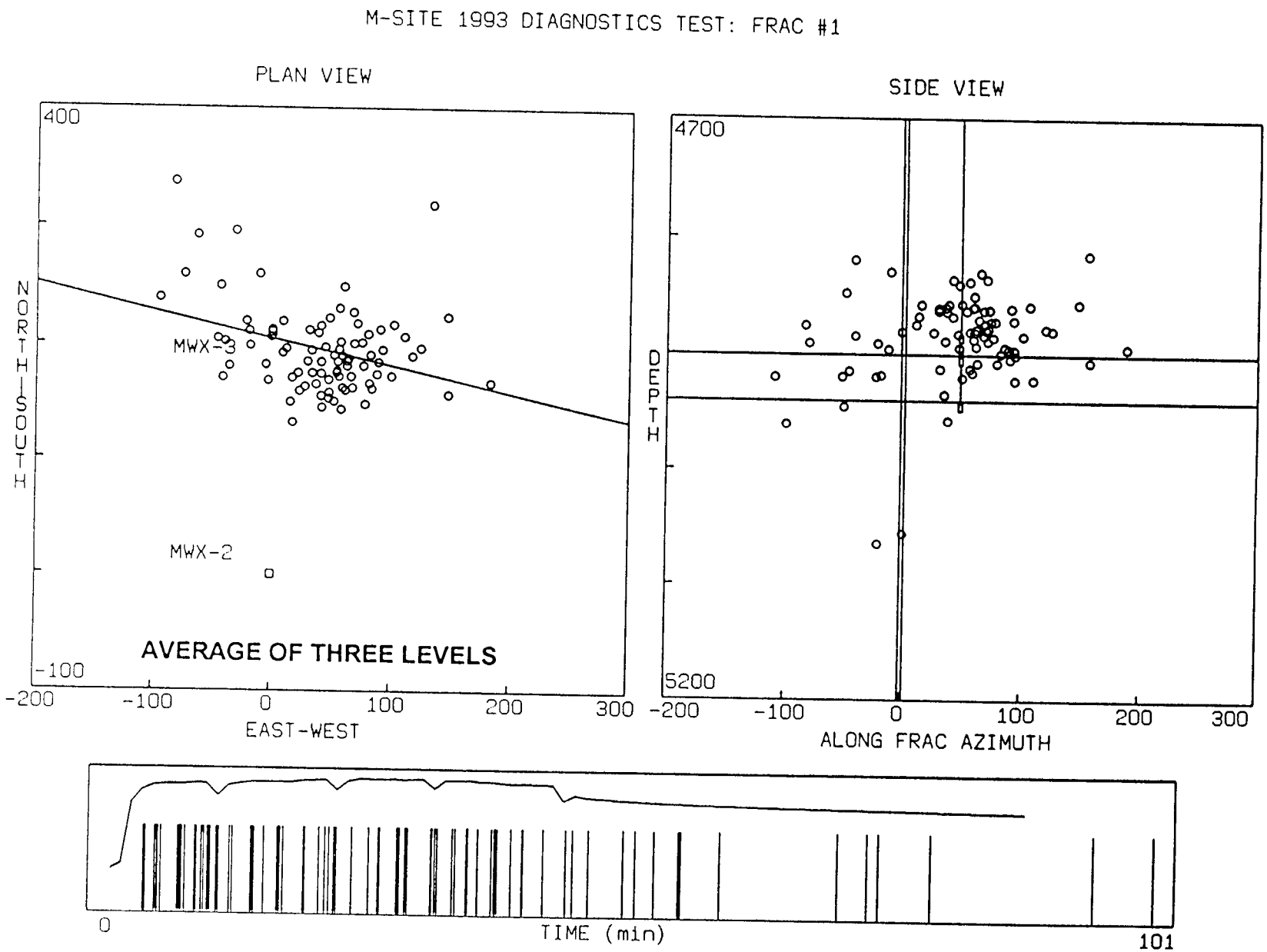

Figure 78. Map of microseisms using average of three levels, minifrac #2

Figure 79. Uncertainty map of microseisms using average of three levels, minifrac #2

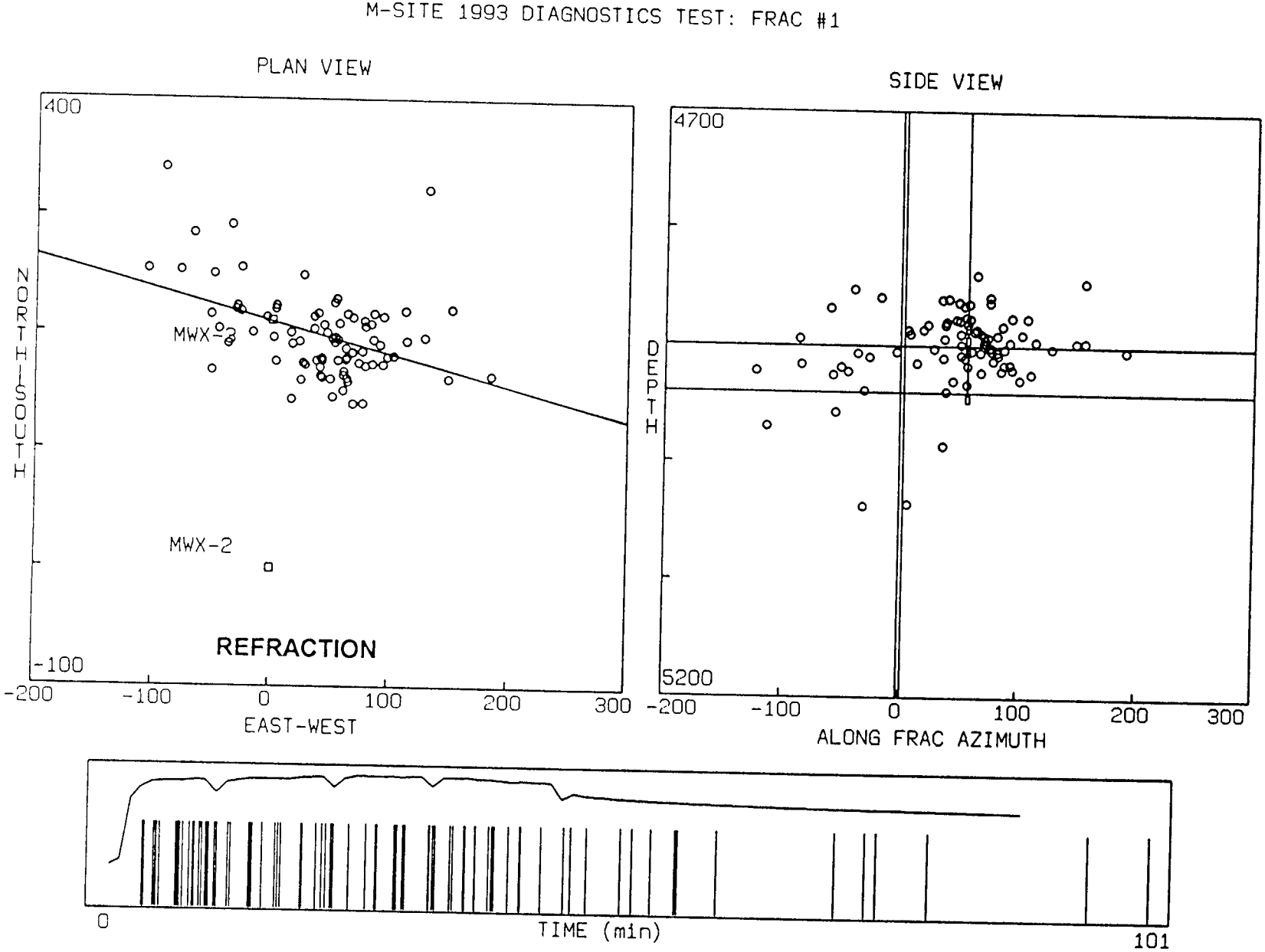

Figure 80. Refraction microseism map, minifrac #2

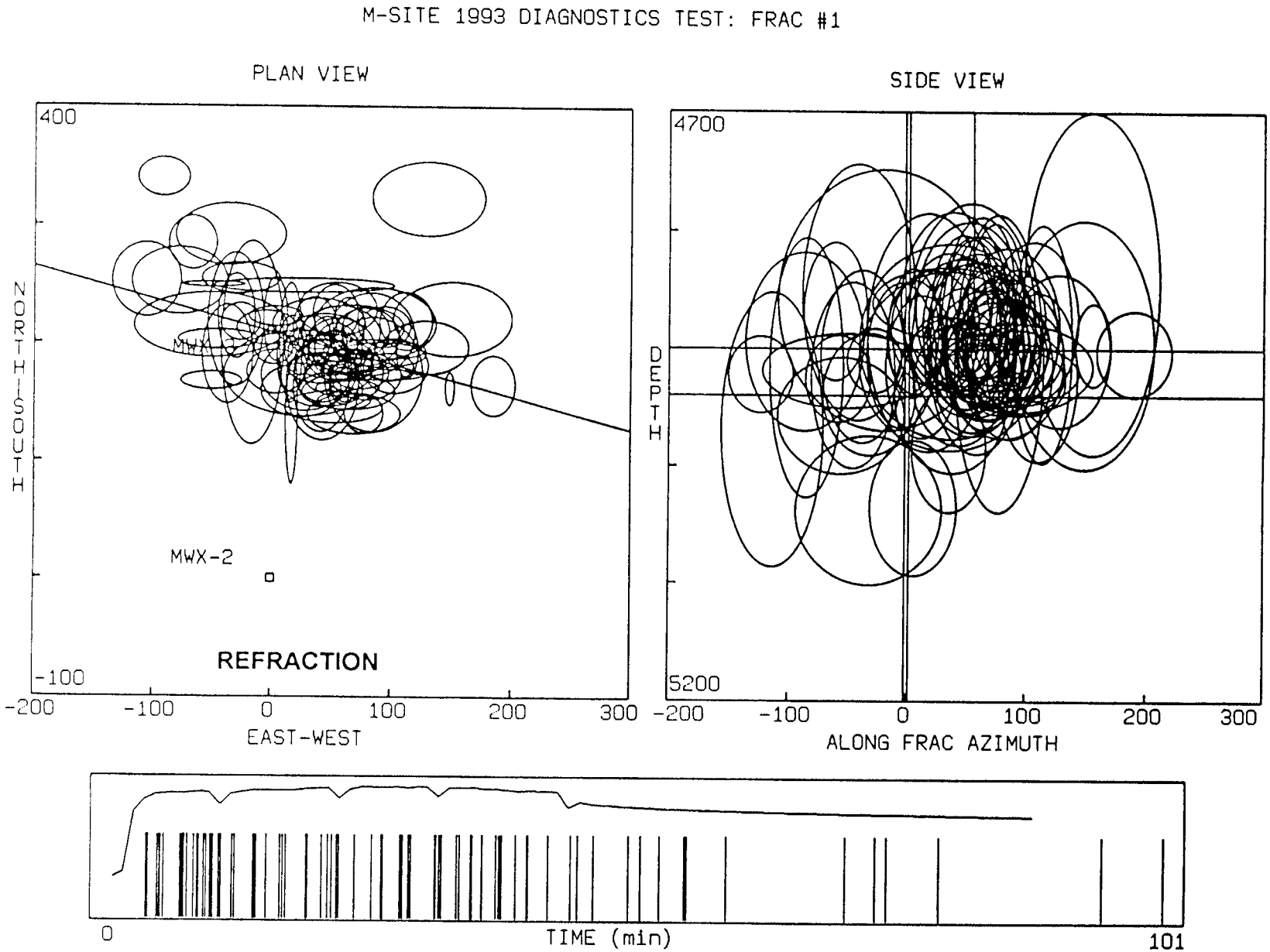

Figure 81. Refraction uncertainty microseism map, minifrac #2

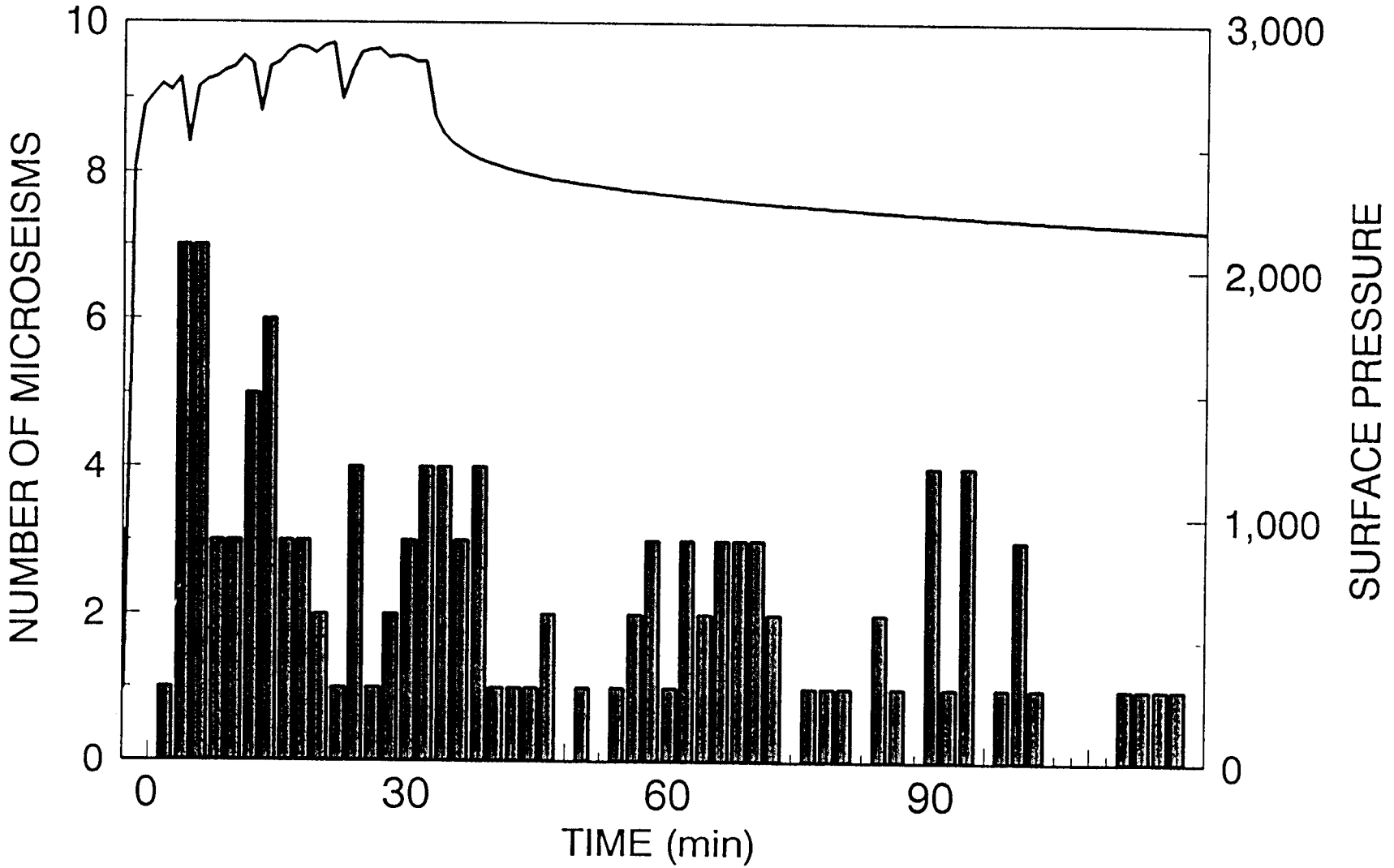

Figure 82. Histogram of events, minifrac #3

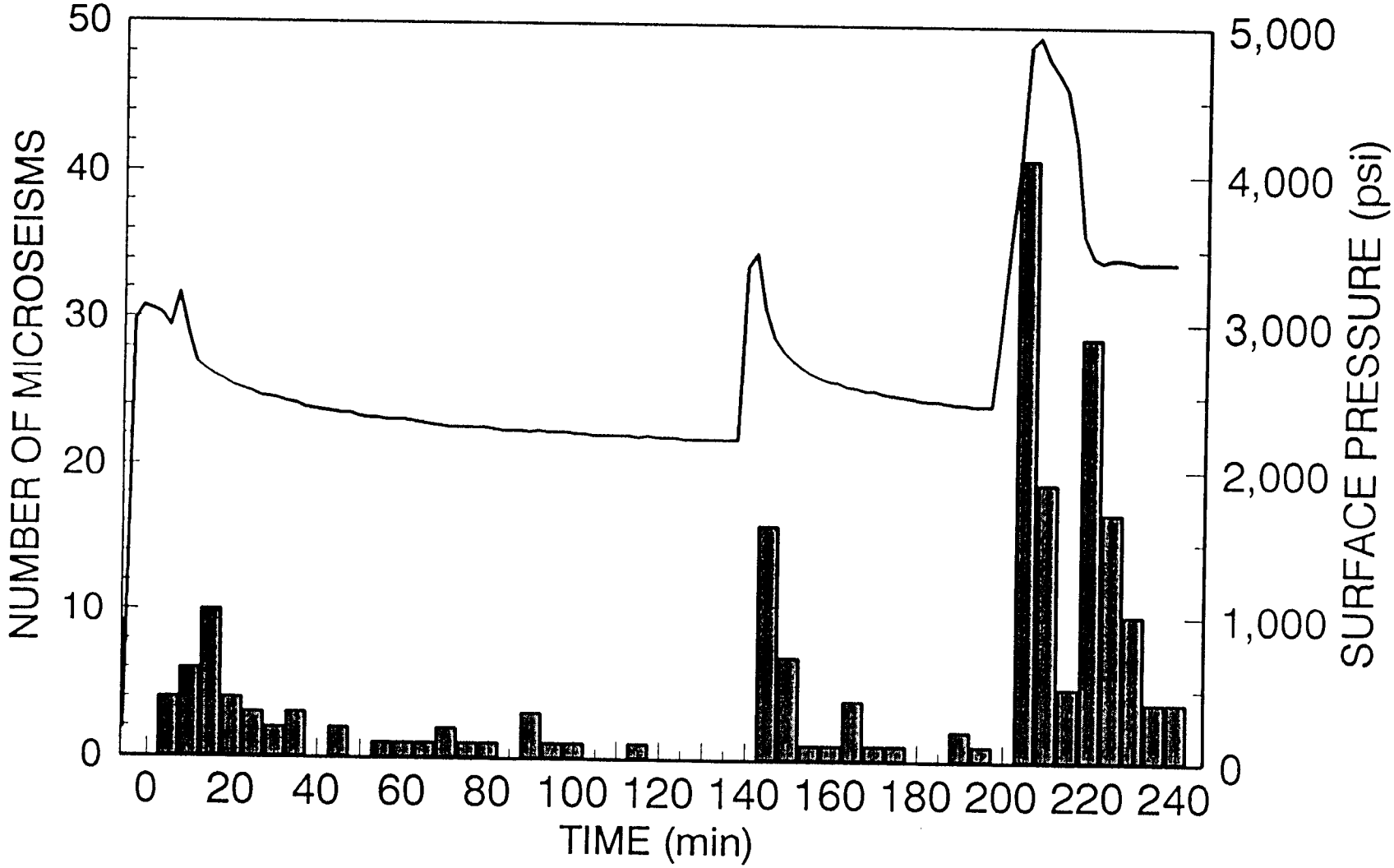

Figure 83. Histogram of events, minifrac #4

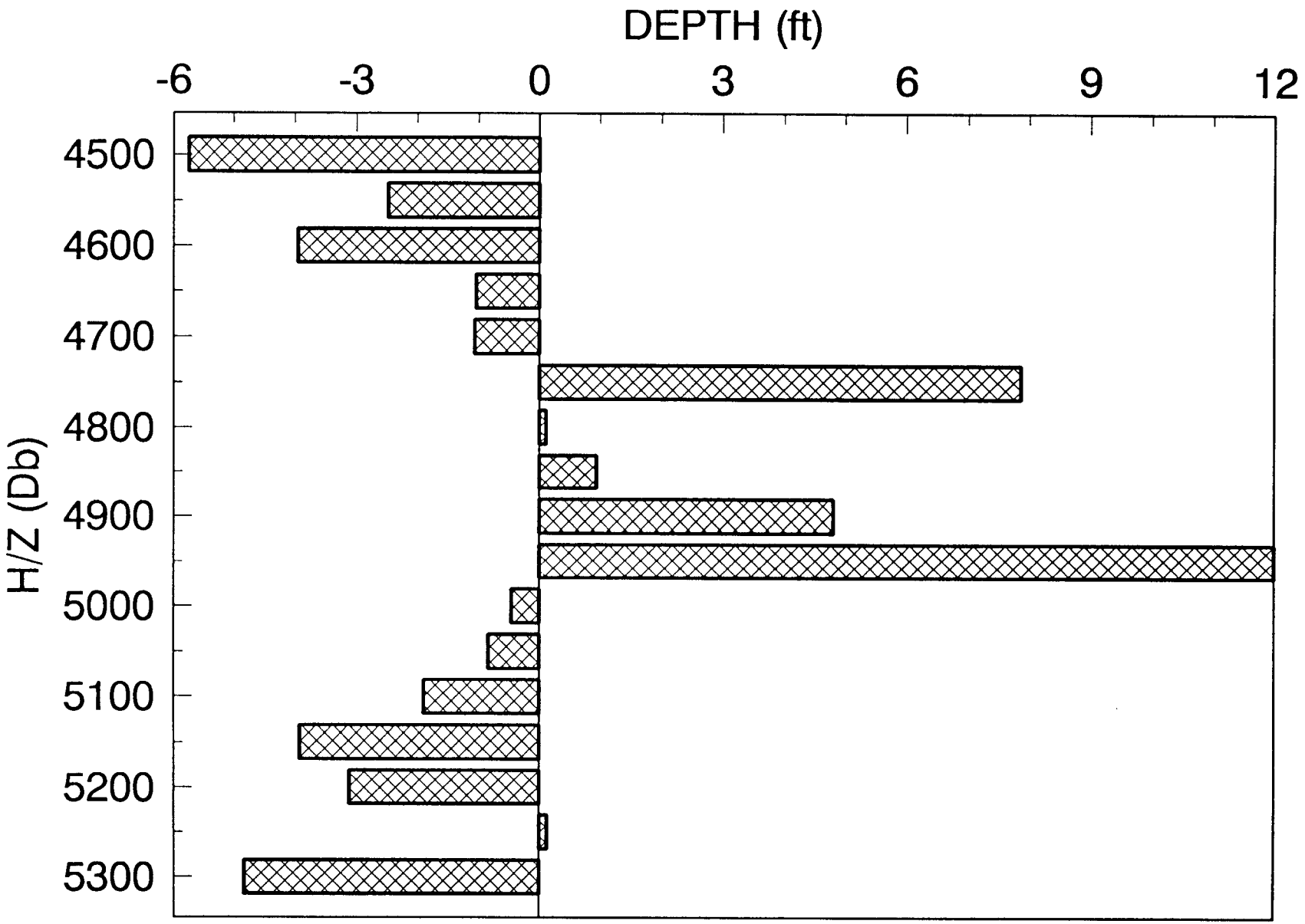

Figure 84. H/Z results for minifrac #3

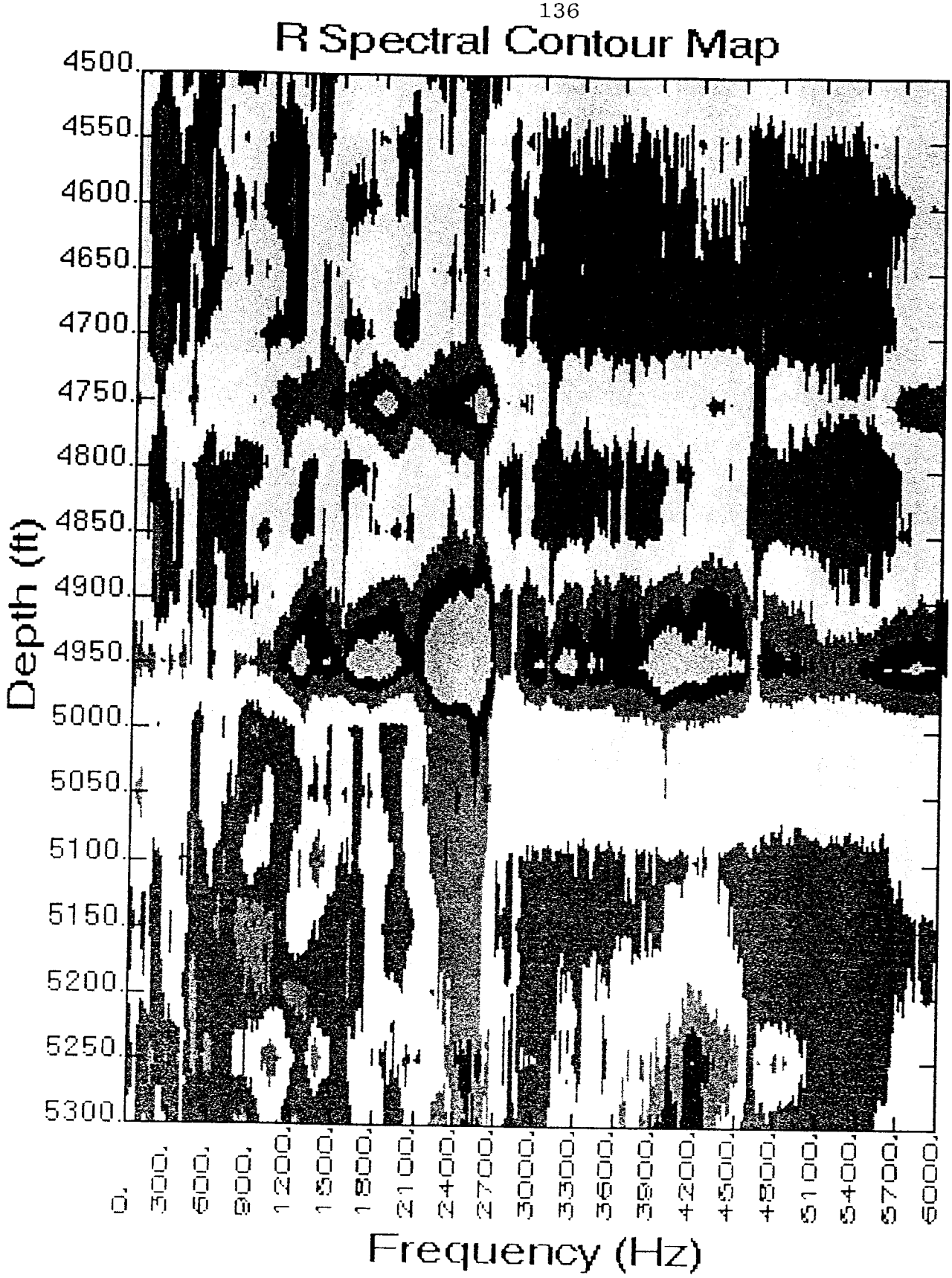

Figure 85. Spectral ratio contour results for minifrac #3

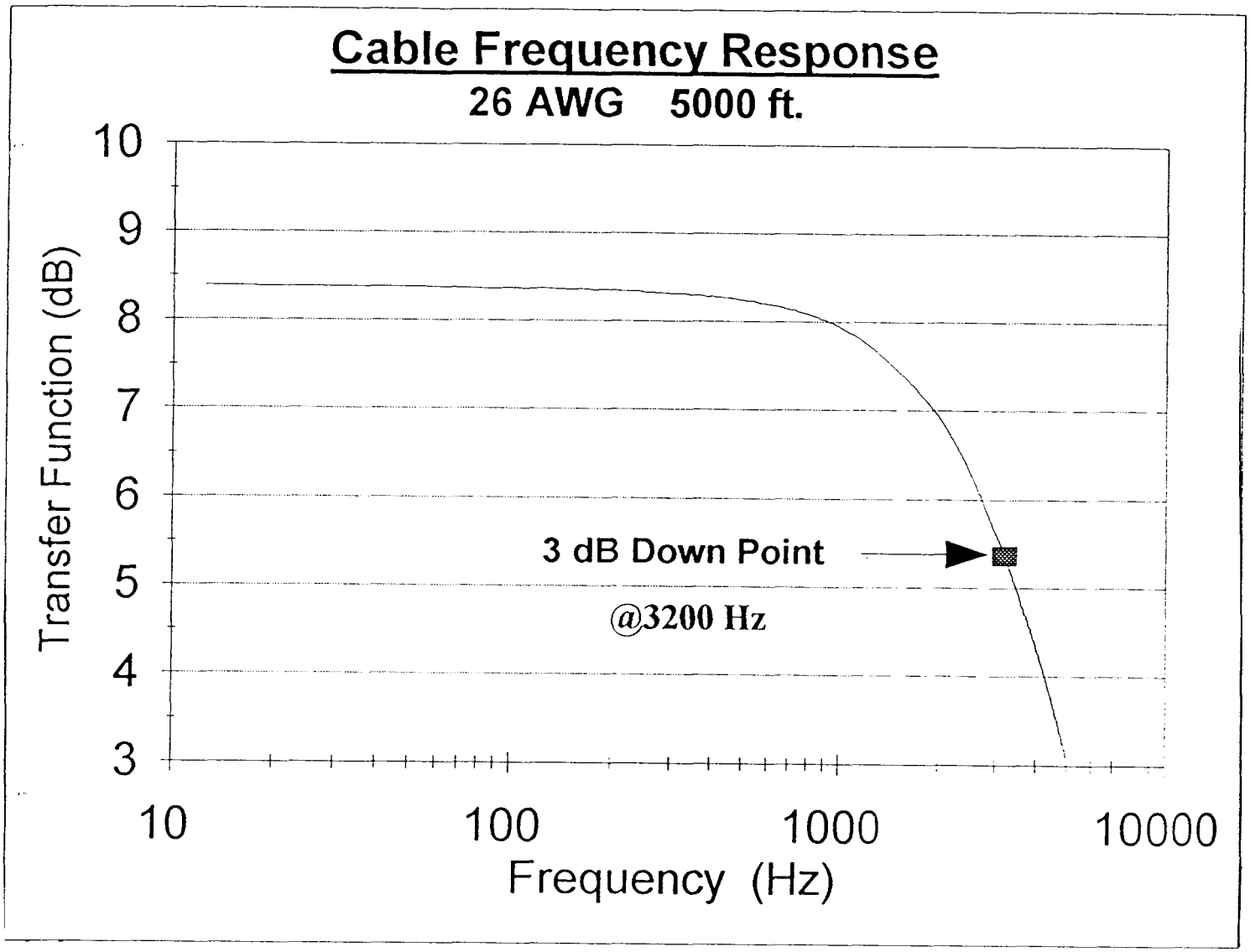

Figure 86. Cable frequency response test

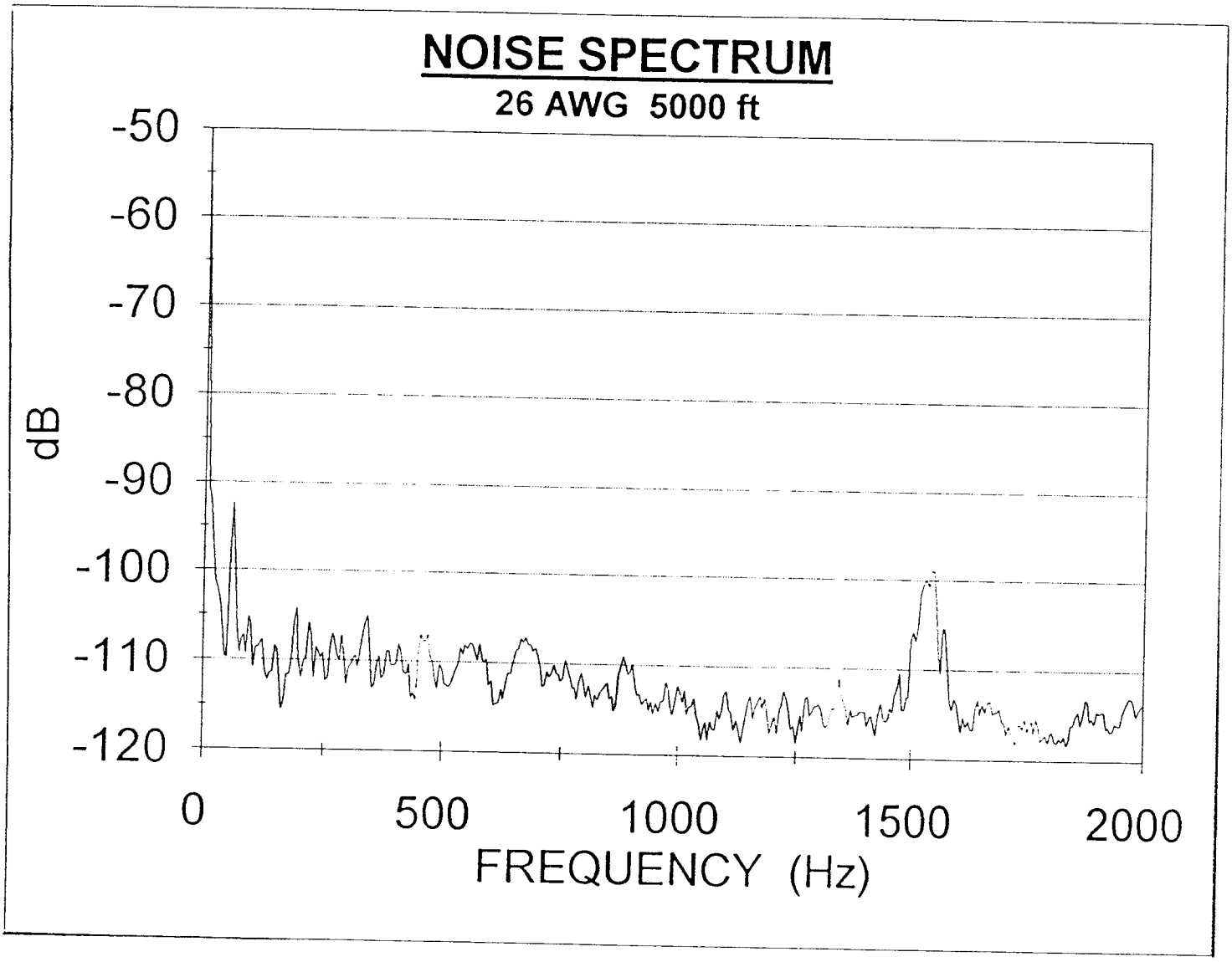

Figure 87. Cable noise characteristics

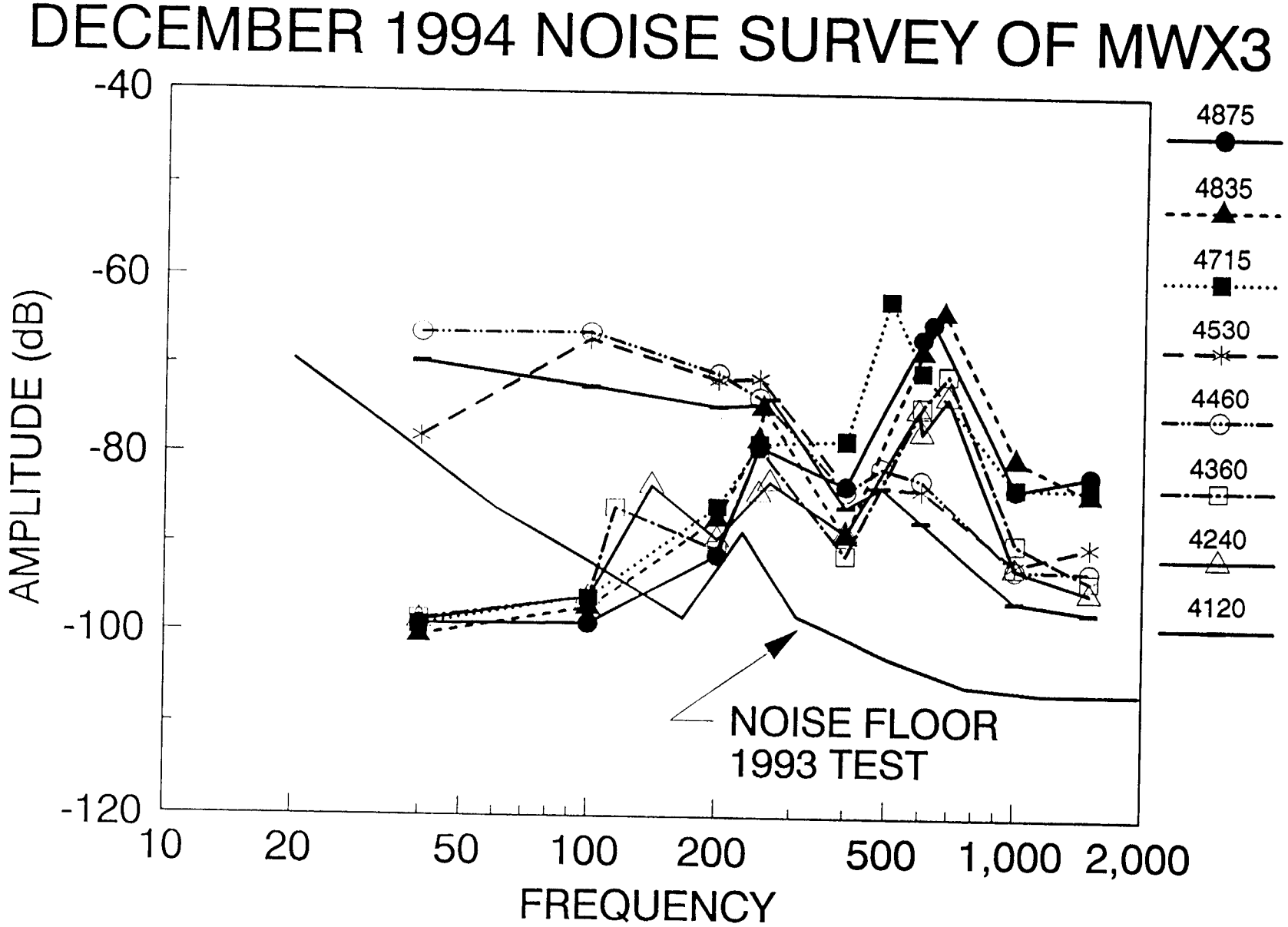

Figure 88. Noise survey of MWX-3

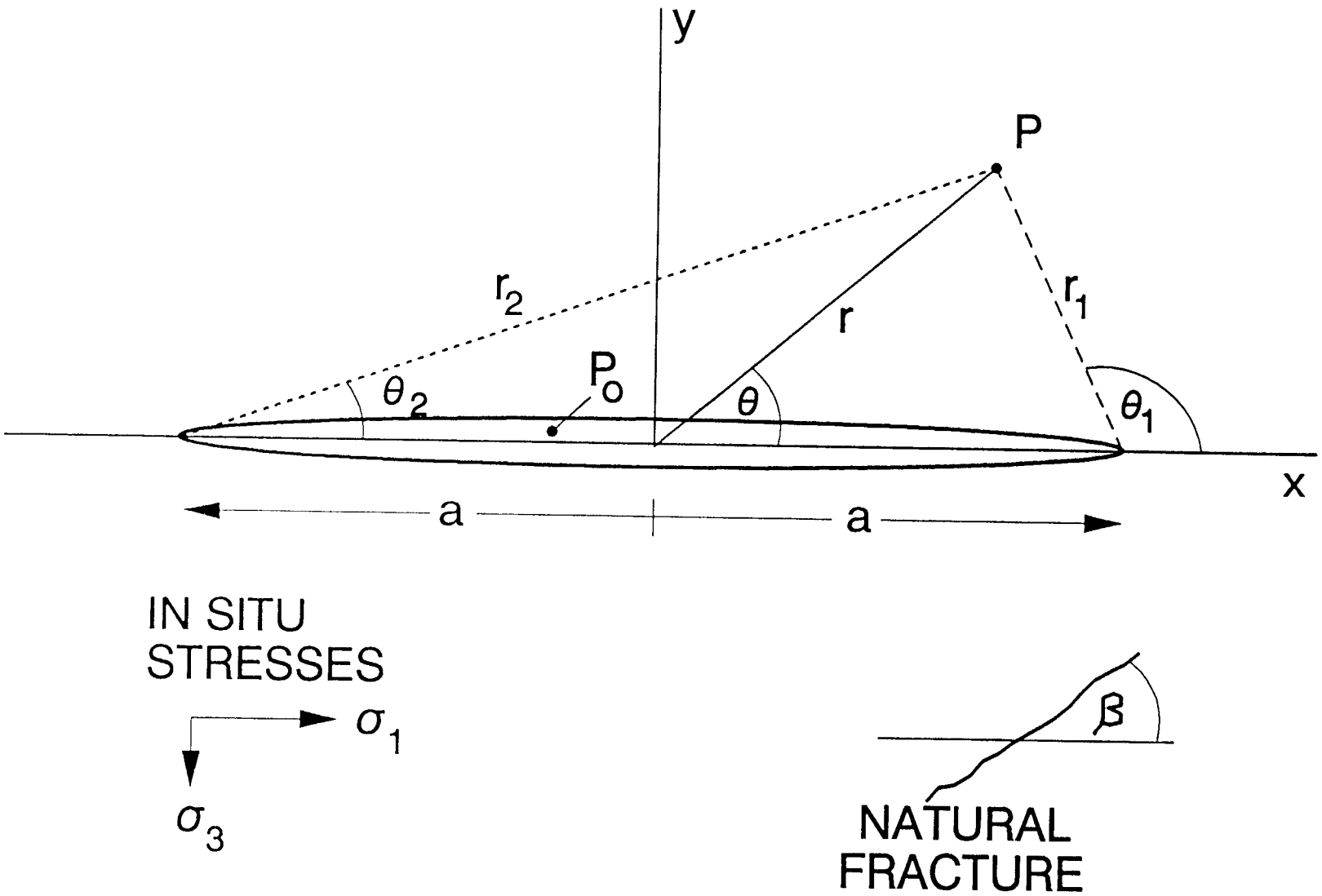

Figure 89. Parameters for Sneddon stress analysis

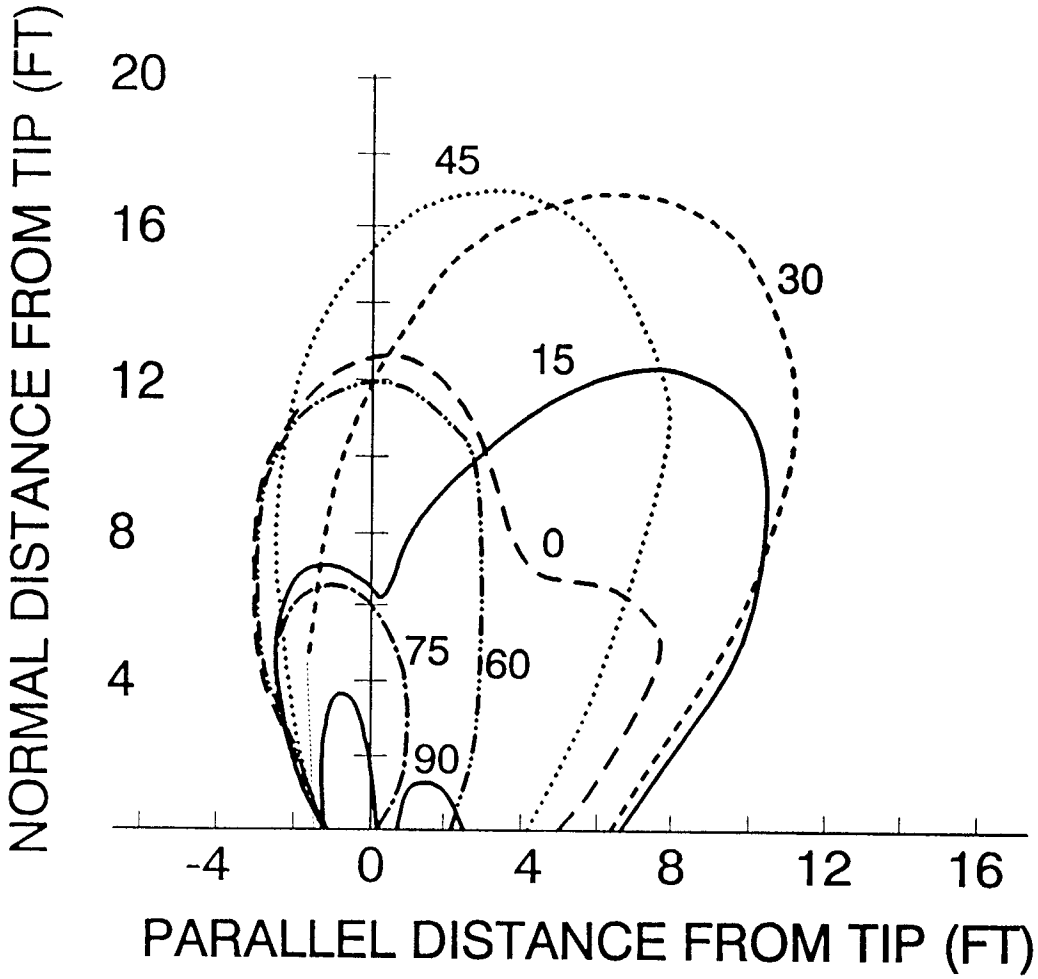

Figure 90. Zone of shear slippage around crack tip

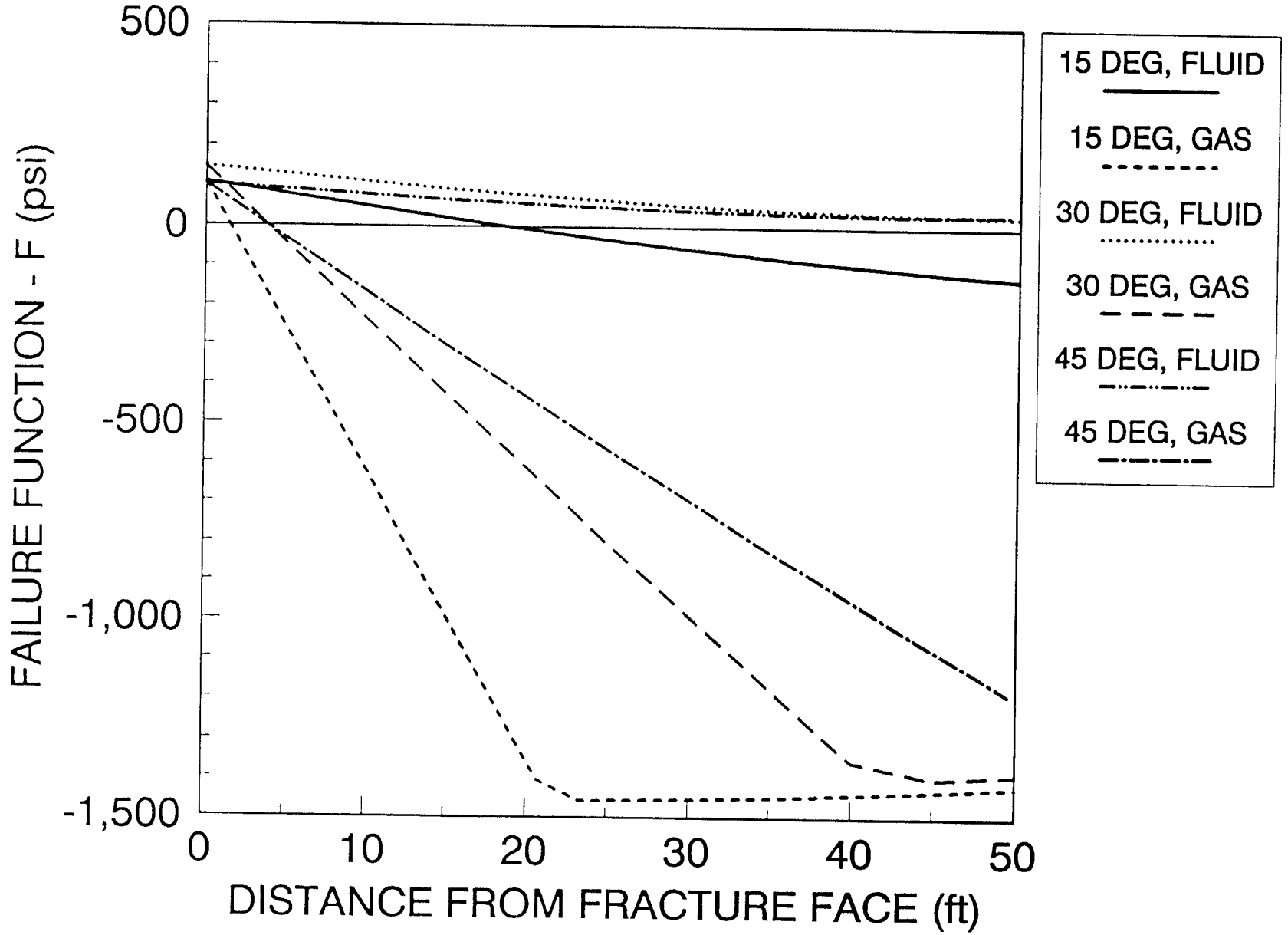

Figure 91. Leakoff induced failure function orthogonal to crack face

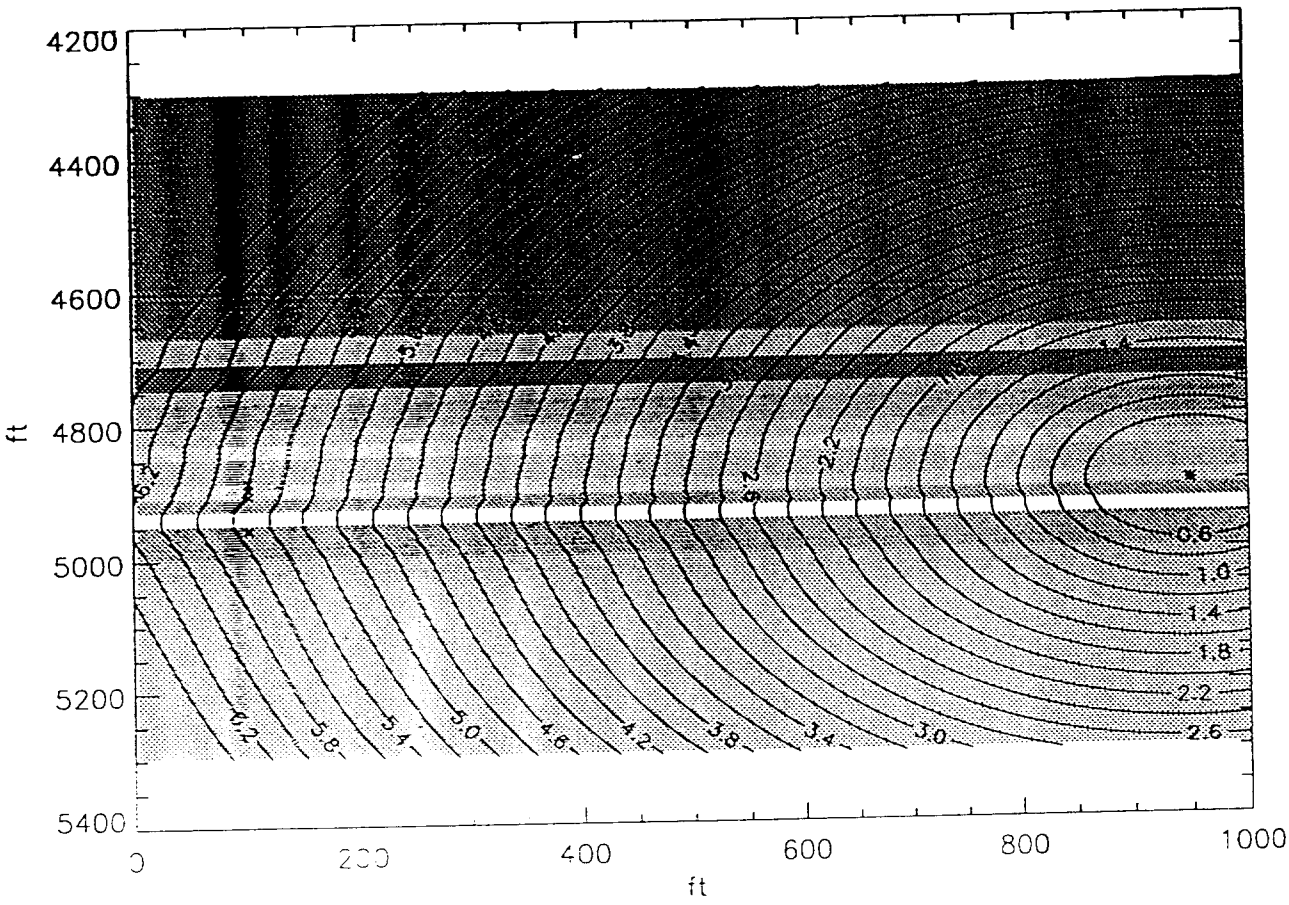

Figure 92 Wavefront contours for source 900 ft from M-Site receivers

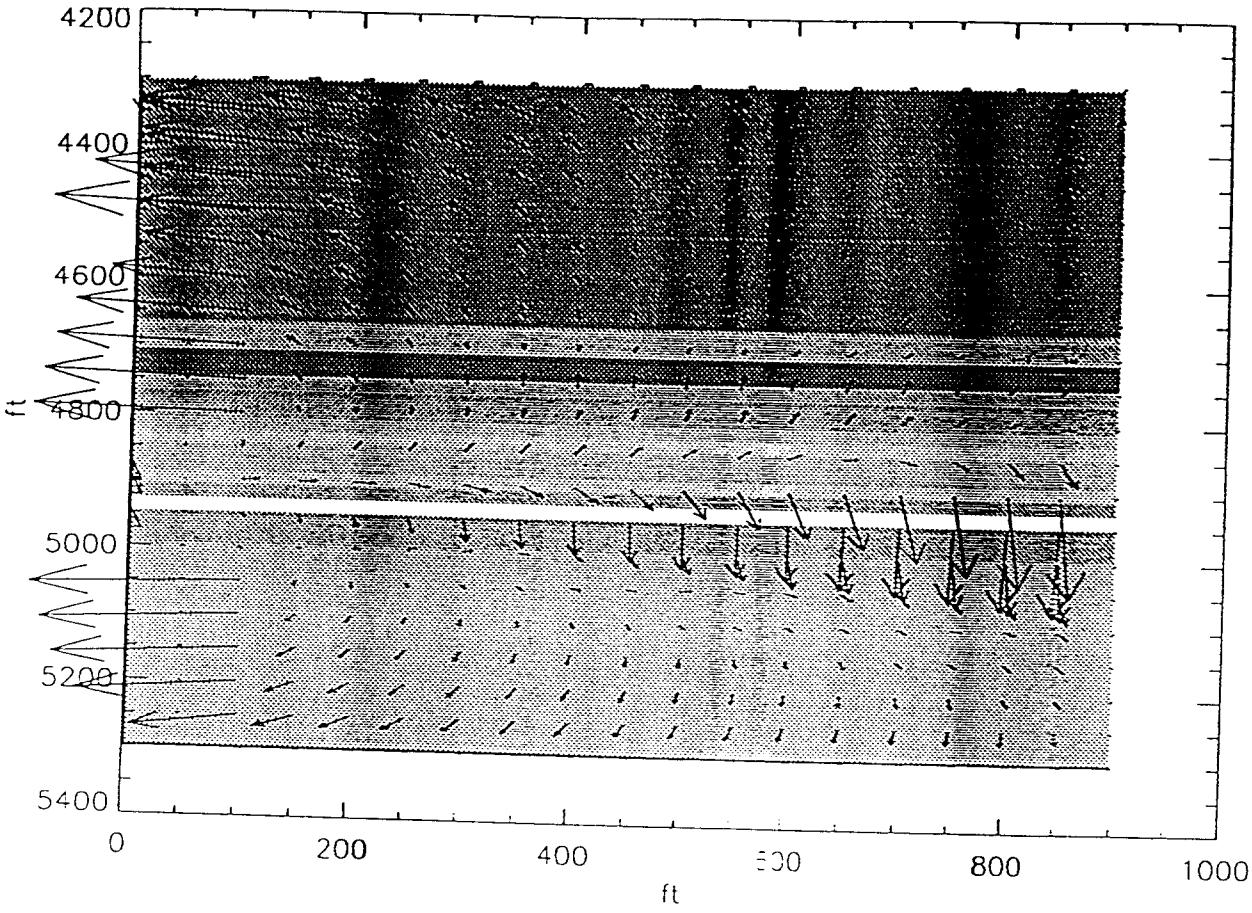

Figure 93. Mislocation vectors for 441 grid points

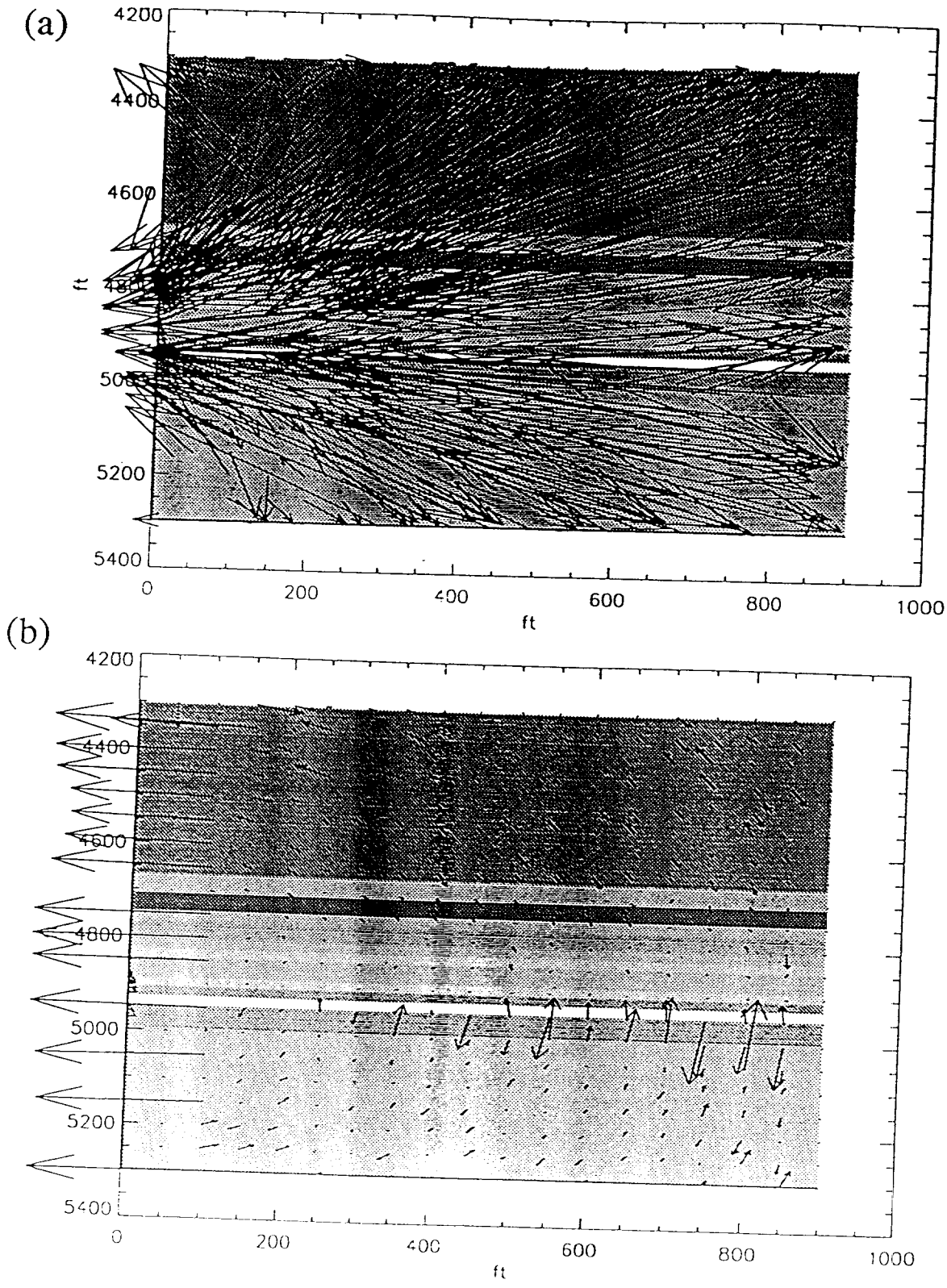

Figure 94. Effect of noise on location solutions for (a) p-wave only and (b) p and s-wave

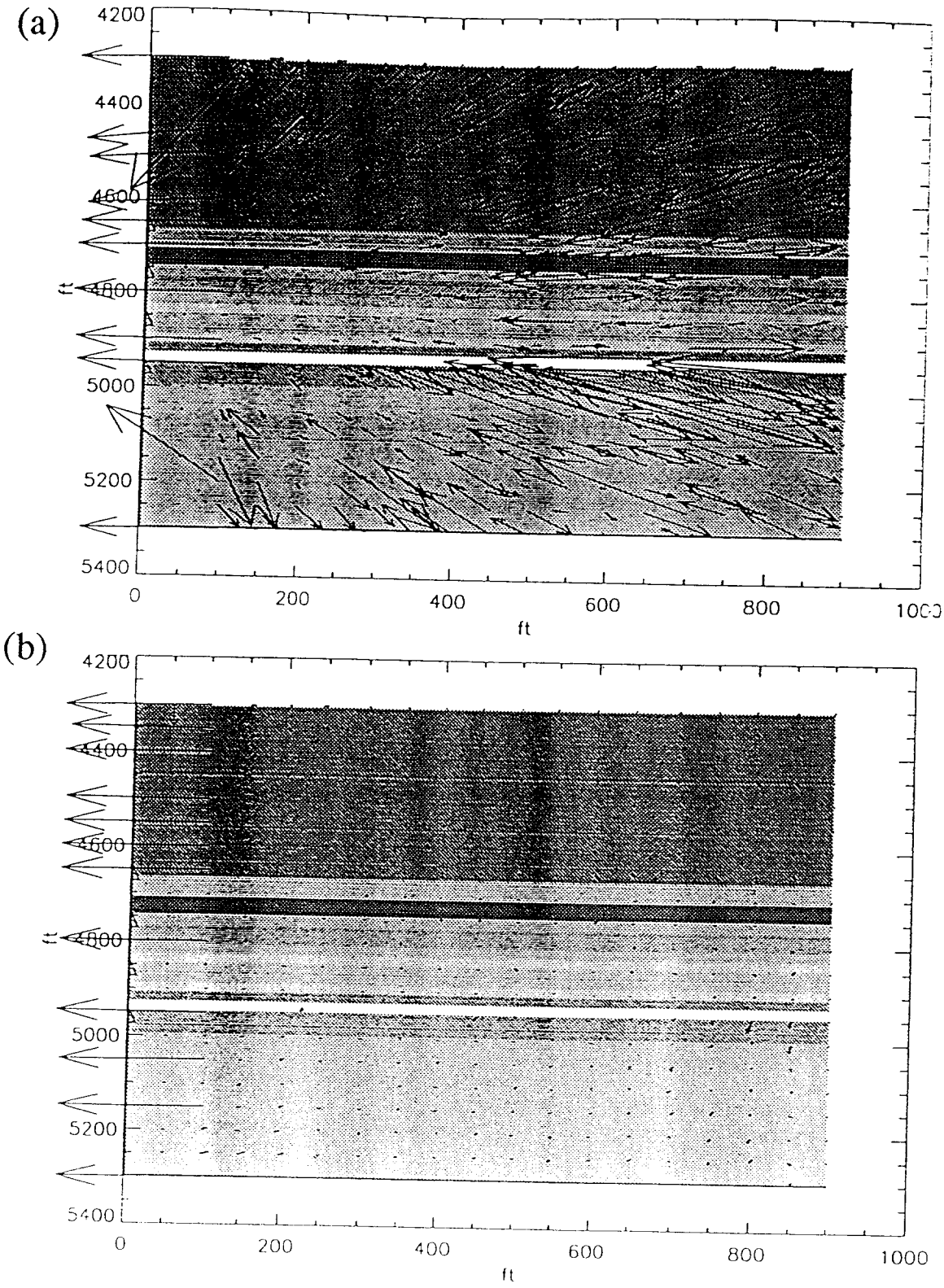

Figure 95. Effect of noise on location solutions for wider receiver spacing

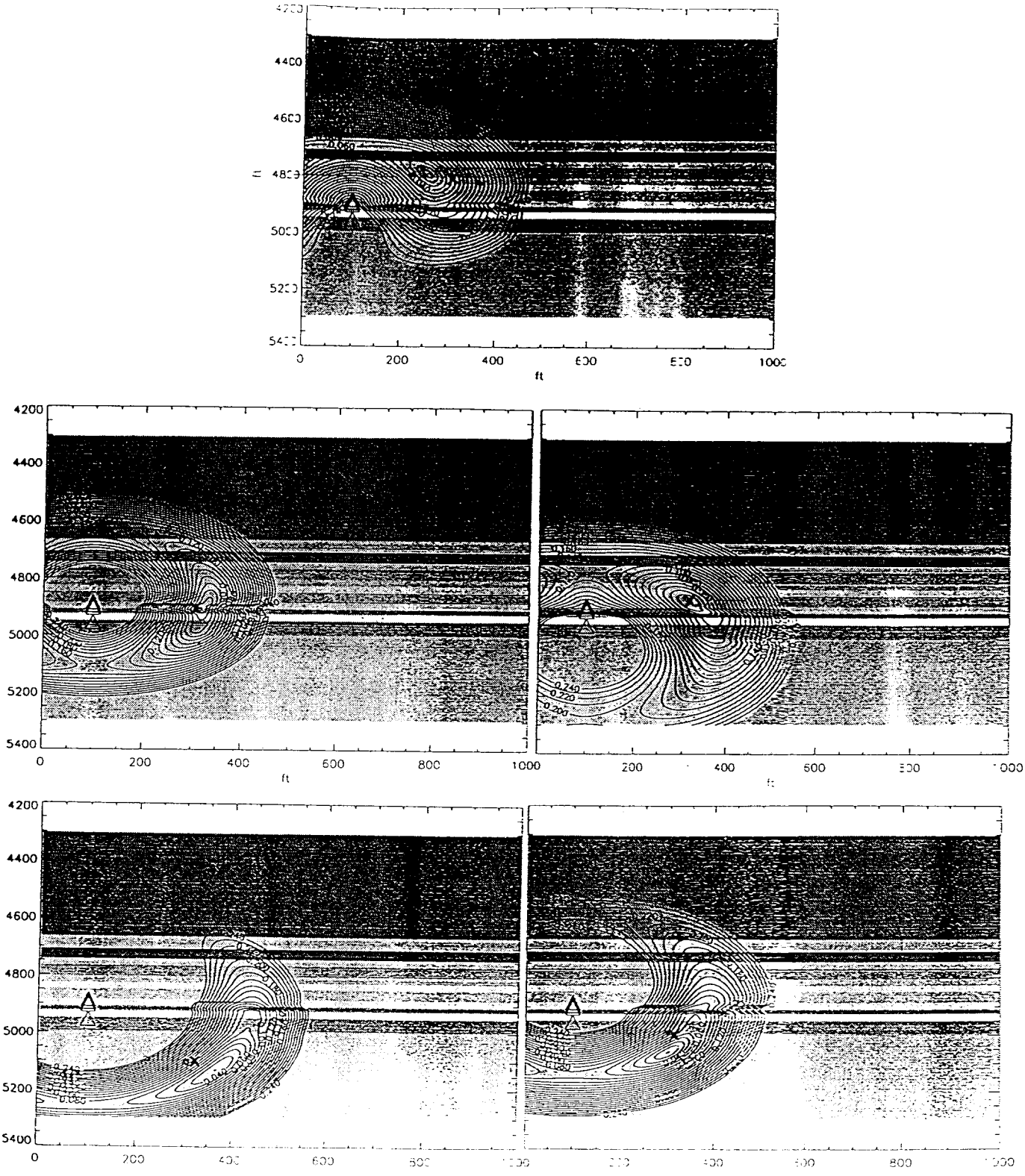

Figure 96 Calculated and actual locations for five calibration shots